

Jordan Journal of Mechanical and Industrial Engineering (JJMIE)

JJMIE is a high-quality scientific journal devoted to fields of Mechanical and Industrial Engineering. It is published by Hashemite University in cooperation with the Jordanian Scientific Research and Innovation Support Fund, Ministry of Higher Education and Scientific Research.

EDITORIAL BOARD

Editor-in-Chief

Prof. Ali M. Jawarneh

Assistant Editors

Dr. Ahmad AlMigdady

Dr. Mohannad Jreissat

Editorial Board

Prof. Tariq A. ALAzab

Al Balqa Applied University

Prof. Jamal Jaber

Al- Balqa Applied University

Prof. Mohamad Al-Widyan

Jordan University of Science and Technology

Prof. Mohammed Taiseer Hayajneh

Jordan University of Science and Technology

Prof. Mohammad Al-Tahat

The University of Jordan

THE INTERNATIONAL ADVISORY BOARD

Abu-Qudais, Mohammad

Jordan University of Science & Technology, Jordan

Abu-Mulaweh, Hosni

Purdue University at Fort Wayne, USA

Afaneh Abdul-Hafiz

Robert Bosch Corporation, USA

Afonso, Maria Dina

Institute Superior Tecnico, Portugal

Badiru, Adedji B.

The University of Tennessee, USA

Bejan, Adrian

Duke University, USA

Chalhoub, Nabil G.

Wayne State University, USA

Cho, Kyu-Kab

Pusan National University, South Korea

Dincer, Ibrahim

University of Ontario Institute of Technology,
Canada

Douglas, Roy

Queen's University, U. K.

El Bassam, Nasir

International Research Center for Renewable
Energy, Germany

Haik, Yousef

United Arab Emirates University, UAE

Tzou, Gow-Yi

Yung-Ta Institute of Technology and Commerce,
Taiwan

Jubran, Bassam

Ryerson University, Canada

Kakac, Sadik

University of Miami, USA

Khalil, Essam-Eddin

Cairo University, Egypt

Mutoh, Yoshiharu

Nagaoka University of Technology, Japan

Pant, Durbin

Iowa State University, USA

Riffat, Saffa

The University of Nottingham, U. K.

Saghir, Ziad

Ryerson University, Canada

Sarkar, MD. Abdur Rashid

Bangladesh University of Engineering &
Technology, Bangladesh

Siginer, Dennis

Wichita State University, USA

Sopian, Kamaruzzaman

University Kebangsaan Malaysia, Malaysia

EDITORIAL BOARD SUPPORT TEAM

Language Editor

Dr. Baker M. Bani-khair

Publishing Layout

Eng. Ali Abu Salimeh

SUBMISSION ADDRESS:

Prof. Ali M. Jawarneh, Editor-in-Chief
Jordan Journal of Mechanical & Industrial Engineering,
Hashemite University,
PO Box 330127, Zarqa, 13133, Jordan
E-mail: jjmie@hu.edu.jo



Hashemite Kingdom of Jordan



Hashemite University

Jordan Journal of
Mechanical and Industrial Engineering

JJMIE

An International Peer-Reviewed Scientific Journal

Financed by Scientific Research Support Fund

Volume 16 Number 4 2022

<http://jjmie.hu.edu.jo/>

ISSN 1995-6665

Jordan Journal of Mechanical and Industrial Engineering (JJMIE)

JJMIE is a high-quality scientific journal devoted to fields of Mechanical and Industrial Engineering. It is published by Hashemite University in cooperation with the Jordanian Scientific Research and Innovation Support Fund, Ministry of Higher Education and Scientific Research.

Introduction: The Editorial Board is very committed to build the Journal as one of the leading international journals in mechanical and industrial engineering sciences in the next few years. With the support of the Ministry of Higher Education and Scientific Research and Jordanian Universities, it is expected that a heavy resource to be channeled into the Journal to establish its international reputation. The Journal's reputation will be enhanced from arrangements with several organizers of international conferences in publishing selected best papers of the conference proceedings.

Aims and Scope: *Jordan Journal of Mechanical and Industrial Engineering* (JJMIE) is a refereed international journal to be of interest and use to all those concerned with research in various fields of, or closely related to, mechanical and industrial engineering disciplines. *Jordan Journal of Mechanical and Industrial Engineering* aims to provide a highly readable and valuable addition to the literature which will serve as an indispensable reference tool for years to come. The coverage of the journal includes all new theoretical and experimental findings in the fields of mechanical and industrial engineering or any closely related fields (Materials, Manufacturing, Management, Design, Thermal, Fluid, Energy, Control, Mechatronics, and Biomedical). The journal also encourages the submission of critical review articles covering advances in recent research of such fields as well as technical notes.

Guide for Authors

Manuscript Submission:

High-quality submissions to this new journal are welcome now and manuscripts may be either submitted online or email.

Online: For online and email submission upload one copy of the full paper including graphics and all figures at the online, submission site, accessed via <http://jjmie.hu.edu.jo>. The manuscript must be written in MS Word Format. All correspondence including notification of the Editor's decision and requests for revision, takes place by e-mail and via the Author's homepage, removing the need for a hard-copy paper trail

Submission address and contact :

Prof. Ali M. Jawarneh

Editor-in-Chief

Jordan Journal of Mechanical & Industrial

Engineering, Hashemite University

PO Box 330127, Zarqa, 13115, Jordan

E-mail: jjmie@hu.edu.jo

Types of contributions: Original research papers and Technical reports

Corresponding author: Clearly indicate who is responsible for correspondence at all stages of refereeing and publication, including post-publication. Ensure that telephone and fax numbers (with country and area code) are provided in addition to the e-mail address and the complete postal address. Full postal addresses must be given for all co-authors.

Original material: Submission of an article implies that the work described has not been published previously (except in the form of itstan abstract or as part of a published lecture or academic thesis), that it is not under consideration for publication elsewhere, the publication is approved by all authors and that, if accepted, it will not be published elsewhere in the same form, in English or in any other language, without the written consent of the Publisher. Authors found to be deliberately contravening the submission guidelines on originality and exclusivity shall not be considered for future publication in this journal.

Withdrawing: If the author chooses to withdraw his article after it has been assessed, he shall reimburse JJMIE with the cost of reviewing the paper.

Manuscript Preparation:

General: Editors reserve the right to adjust style to certain standards of uniformity. Original manuscripts are discarded after publication unless the Publisher is asked to return original material after use. Please use MS Word for the text of your manuscript

Structure: Follow this order when typing manuscripts: Title, Authors, Authors title, Affiliations, Abstract, Keywords, Introduction, Main text, Conclusions, Acknowledgements, Appendix, References, Figure Captions, Figures and then Tables. Please supply figures imported into the text AND also separately as original graphics files. Collate acknowledgements in a separate section at the end of the article and do not include them on the title page, as a footnote to the title or otherwise.

Text Layout: Use 1.5 line spacing and wide (3 cm) margins. Ensure that each new paragraph is clearly indicated. Present tables and figure legends on separate pages at the end of the manuscript. If possible, consult a recent issue of the journal to become familiar with layout and conventions. All footnotes (except for table and corresponding author footnotes) should be identified with superscript Arabic numbers. To conserve space, authors are requested to mark the less important parts of the paper (such as records of experimental results) for printing in smaller type. For long papers (more than 4000 words) sections which could be deleted without destroying either the sense or the continuity of the paper should be indicated as a guide for the editor. Nomenclature should conform to that most frequently used in the scientific field concerned. Number all pages consecutively; use 12 or 10 pt font size and standard fonts.

Corresponding author: Clearly indicate who is responsible for correspondence at all stages of refereeing and publication, including post-publication. The corresponding author should be identified with an asterisk and footnote. Ensure that telephone and fax numbers (with country and area code) are provided in addition to the e-mail address and the complete postal address. Full postal addresses must be given for all co-authors. Please consult a recent journal paper for style if possible.

Abstract: A self-contained abstract outlining in a single paragraph the aims, scope and conclusions of the paper must be supplied.

Keywords: Immediately after the abstract, provide a maximum of six keywords (avoid, for example, 'and', 'of'). Be sparing with abbreviations: only abbreviations firmly established in the field may be eligible.

Symbols: All Greek letters and unusual symbols should be identified by name in the margin, the first time they are used.

Units: Follow internationally accepted rules and conventions: use the international system of units (SI). If other quantities are mentioned, give their equivalent quantities in SI

Maths: Number consecutively any equations that have to be displayed separately from the text (if referred to explicitly in the text).

References: All publications cited in the text should be presented in a list of references following the text of the manuscript.

Text: Indicate references by number(s) in square brackets in line with the text. The actual authors can be referred to, but the reference number(s) must always be given.

List: Number the references (numbers in square brackets) in the list in the order in which they appear in the text.

Examples:

Reference to a journal publication:

[1] M.S. Mohsen, B.A. Akash, "Evaluation of domestic solar water heating system in Jordan using analytic hierarchy process". Energy Conversion & Management, Vol. 38 (1997) No. 9, 1815-1822.

Reference to a book:

[2] Strunk Jr W, White EB. The elements of style. 3rd ed. New York: Macmillan; 1979.

Reference to a conference proceeding:

[3] B. Akash, S. Odeh, S. Nijmeh, "Modeling of solar-assisted double-tube evaporator heat pump system under local climate conditions". 5th Jordanian International Mechanical Engineering Conference, Amman, Jordan, 2004.

Reference to a chapter in an edited book:

[4] Mettam GR, Adams LB. How to prepare an electronic version of your article. In: Jones BS, Smith RZ, editors. Introduction to the electronic age, New York: E-Publishing Inc; 1999, p. 281-304

Free Online Color : If, together with your accepted article, you submit usable color and black/white figures then the journal will ensure that these figures will appear in color on the journal website electronic version.

Tables: Tables should be numbered consecutively and given suitable captions and each table should begin on a new page. No vertical rules should be used. Tables should not unnecessarily duplicate results presented elsewhere in the manuscript (for example, in graphs). Footnotes to tables should be typed below the table and should be referred to by superscript lowercase letters.

Notification: Authors will be notified of the acceptance of their paper by the editor. The Publisher will also send a notification of receipt of the paper in production.

Copyright: All authors must sign the Transfer of Copyright agreement before the article can be published. This transfer agreement enables Jordan Journal of Mechanical and Industrial Engineering to protect the copyrighted material for the authors, but does not relinquish the authors' proprietary rights. The copyright transfer covers the exclusive rights to reproduce and distribute the article, including reprints, photographic reproductions, microfilm or any other reproductions of similar nature and translations.

Proof Reading: One set of page proofs in MS Word format will be sent by e-mail to the corresponding author, to be checked for typesetting/editing. The corrections should be returned within 48 hours. No changes in, or additions to, the accepted (and subsequently edited) manuscript will be allowed at this stage. Proofreading is solely the author's responsibility. Any queries should be answered in full. Please correct factual errors only, or errors introduced by typesetting. Please note that once your paper has been proofed we publish the identical paper online as in print.

PAGES**PAPERS**

163 - 174	No Actor is an Island: The Role of Partnerships in Sustainable Value Chains <i>Luai Jraisat, Mohannad Jreissat, Farhana Sajjad, Luciano Batista, Thaana Ghalia</i>
175 - 183	Application of Kansei Engineering and Data Mining for the Eyewear Industry in Jakarta <i>Yung-Tsan Jou, Ronald Sukwadi, Riana Magdalena Silitong, Roselly</i>
185 - 193	Advanced Multi Criteria Optimal Design of Spiral Bevel Gear Pair using NSGA – II <i>N. Godwin Raja Ebenezer , S. Ramabalan , S. Navaneethasanthakumar</i>
195 - 204	An Experimental Investigation of Double Pipe Heat Exchanger Performance and Exergy Analysis Using Air Bubble Injection Technique <i>Farhan Lafta Rashid, Shaheed Mahdi Talib, Ahmed Kadhim Hussein, ObaiYounis</i>
205 - 223	A Review of the Recent Development in Machining Parameter Optimization <i>Mohsen Soori , Mohammed Asmael</i>
225 - 245	A New Microchannel Heat Sink Design Using Porous Media Inserts <i>Hamdi E. Ahmed, Issam M.Ali Aljubury, Ammar A. Farhan, Mohammed Gh. Jehad</i>
247 - 259	Development of Water Conservation Indicators for Office Buildings Using Delphi Method <i>Sajad Sadi, Javad Gholami, Mehdi Fereydooni , Shahab Moshari</i>
261 - 274	Analysis of Elastic Stress Wave Propagation in Stepped Bars, Transmission, Reflection, and Interaction: Experimental Investigation <i>F.Y. Fraige, M.H. Es-Saheb</i>
275 - 282	Modelling and Development of Multisectional Disk Piezoelectric Transducers for Critical Application Systems <i>Ibrahim M. Aladwan, Constantine Bazilo, Emil Faure</i>
283 - 289	3D Finite Element Method Simulations on the Influence of Tool Helix Angle in Thin-Wall Milling Process <i>G. Bolar</i>
291 - 300	Flood Risk Map Using a Multi-Criteria Evaluation and Geographic Information System: Wadi Al-Mafraq Zone <i>Akram AlSukker, Marah Al-Saleem , Morad Etier</i>
301 - 307	Optimal Response of a Quarter Car Vehicle Model with Optimal Skyhook Damper Based on Preview Control <i>L.V.V. Gopala Rao, Rakesh Chandmal Sharma , V.S.V. Satyanarayana</i>
309 - 318	Effect of Inlet Swirl on Combustion Performance and Soot Formation of a Turbulent Methane-Air Non-Premixed Flame <i>Tarak Kumar Sahoo, Prakash Ghose</i>
319 - 325	Optimization of Injection Molding Simulation of Bioabsorbable Bone Screw Using Taguchi Method and Particle Swarm Optimization <i>Azizah Hadny Qurrota Ayun, Joko Triyono, Eko Pujiyanto</i>

No Actor is an Island: The Role of Partnerships in Sustainable Value Chains

Luai Jraisat^{a*}, Mohannad Jreissat^b, Farhana Sajjad^c, Luciano Batista^d, Thaana Ghalia^e

^aDepartment of Business, Talal Abu-Ghazaleh University College for Innovation, Amman, Jordan.

^bFaculty of Engineering, Department of Industrial Engineering, The Hashemite University, Zarqa, 13115 Jordan.

^cSurrey Business School, University of Surrey, Surrey, GU2 7XH, UK.

^dAston Business School, Aston University, Birmingham, B4 7EQ, UK

^eFaculty of Business and Law, University of Northampton, Northampton, NN1 5PH, UK.

Received 18 June 2021

Accepted 26 JAN 2022

Abstract

This research aims to explore key themes concerning partnerships between Business Actors (BAs) and Not-for-Profit Actors (NFPAs) along a Sustainable Value Chain (SVC). Forty interviews, as well as observations and documents representing (5) BA-NFPA collaborations, were done using a multiple-case approach. This research has identified two types of the key partnership-influencing themes: internally-focused and externally-focused partnership drivers and how they leverage the implementation of the SVC, including SVC approaches and governance forms. The innovative partnership approach is a novel contribution to the area of SVC research and helps the industry with decision making for creating successful SVCs amid the Covid-19 pandemic. Explicitly, findings regarding implementation and evaluation contribute to the theoretical and practical knowledge of value chains in the agricultural sector within emerging economies.

© 2022 Jordan Journal of Mechanical and Industrial Engineering. All rights reserved

Keywords: Partnership Approach, Sustainable Value Chain, Business Actor, Not-for-Profit Actor, Covid-19.

1. Introduction

The nature of the agriculture value chain has become complex to adapt and manage, which also creates an imbalance of bargaining power among the various actors within the chain [1,2, 3, 4]. Research highlights the importance of effective partnerships among the entities for a sustainable value chain [5,3,6]. This highlights importance of having a partnership approach in interactions between the key Business Actors (BAs) with Not-for-Profit Actors (NFPAs) and their impacts along the Sustainable Value Chain (SVC) [7,8,9,10,11, 12]. This is because, first, moving toward a sustainable partnership between both BA and NFPA calls for effective interaction within the supply chain actors' activities [13, 14,10]. Second, the content of this innovative partnership type should be formed by a multi-dimensional concept: information sharing and value creation from both actors [15, 16].

All sectors are expected to be affected by Covid-19, and agricultural sector is one of the most vulnerable, including disconnected partnerships, border disruptions and policy measures, such as quarantines, and closures of non-essential businesses impact all stages of SVCs, from input supply to production, logistics, marketing and consumption, elevating the risks of food insecurity and uncertainty [17,90]. Aday [18] carried out a study to evaluate the impact of COVID-19 in the agriculture and food sector and summarize the recommendations required to reduce and control the effect of the pandemic [78]. Prior

research has created the need to examine the role of BA-NFPA partnerships in the SVC from a multidimensional perspective [19,16, 4]. To allow practitioners and academics to identify how information sharing and value creation can be improved in these partnerships, it is necessary to identify the key internal and external themes that can be utilized to influence this association for better SVC amid Covid-19 [78]. Although there are several papers conceptualizing this association, but they have been based purely on literature reviews or limited empirical results [e.g. 20,19]. Furthermore, industries emphasize that partnership is a feasible mean for considering economic, social and environmental aspects [22]. Such partnerships have developed over time to link key actors along the value chain [16]. As the literature explaining partnership in SVCs is still at a relatively early stage, it is now time to conduct an extensive analysis to date [23,24].

Drawing from Transaction Cost Theory (TCT) [25], this research adopts governance as a key approach to further examine transactions in a sustainable BA-NFPA partnership. Governance is represented by the degree of chain actors following transactional arrangements as partnerships, which works to decreasing unwanted uncertain causes and information asymmetry in the chains [11]. This research examines the agricultural industry to develop many sustainable projects working with both local and international organizations; the industry has witnessed a growing reliance on NFPA partnerships as essential windows for better markets. This research uses extant literature as well as evidence from several case studies to examine the role of BA-NFPA partnerships in a SVC; a

* Corresponding author e-mail: LJraisat@taguci.edu.jo.

holistic conceptual framework can be proposed by interpreting possible key themes as business drivers that would help build this partnership.

This research has the following Research Questions (RQ):

RQ1. How are the key external and internal themes associated with BA-NFPA partnerships in SVCs?

RQ2. How do SAVC approaches and governance forms effectively incorporated in BA-NFPA partnerships resonate with SVCs in practice?

The paper is organized as follows. The article commences with a theoretical background to SVCs, BA-NFPA partnership and their drivers. The next section describes the research methodology followed by the key findings being presented and discussed. The managerial implications and future research avenues are explored in the last section.

2. Theoretical Background

2.1. Sustainable Value Chains (SVCs)

SVCs concept is a business context that produces value added products for a market by performing activities, transforming resources and by applying specific investment assets between actors along their economic, social and environmental supply chain [26,27,24]. This research focusses on agricultural business with sustainable value chains – a business that has grown dramatically over the last two decades [28,29,30,24]. However, improvements in production and marketing activities along the SVCs, specifically enabled by unsustainable mechanizations and unplanned collaboration in resource use and consumer added value, have led to potentially detrimental sustainability impacts [20]. These impacts are related to various pollutants (e.g. water resources, machinery usage, soil mineralization) as well as short-term

social (e.g. job security and family business) and economic (e.g. income and profitability) benefits [9,24]. Lately, research on Resilient Food Supply Chains (RFSCs) and SVCs has seen steep growth over the last decades. Prior research defined a range of strategies for building RFSCs [78,79]. Furthermore, research has indicated antecedents and consequence of risks for SVCs [90], and risk management strategies. However, survey-based empirical research investigating the underlying mechanisms amid Covid-19 that lead to the development of resilience amid exposure to supply chain risks in SVCs is still incipient, specifically in the context of SVCs [78].

Therefore, there is a need to shift from “government” to “governance” to encourage the development of SVCs that can serve the needs of both the BAs and the NFPAs towards their partnerships. This is where the NFBA needs to foster a climate of mutual respect when SVCs are developed, particularly when the BAs rely on the support programmes from their NFPAs [31]. These partnering relationships can provide considerable sustainable opportunities to engage with partners beyond simple financial support [32]. Hence, this research builds on features of SVCs such as coordination, cooperation and collaboration by linking them to approaches of corporate, intermediary, producer and hybrid driven-value chains [e.g. 33,34]. Key authors [e.g. 35, 20, 16] categorise the term SVC as a major field unto itself which has recently been identified as a key research area. Authors referring to SVCs have stressed that partnership is typically applied as one of the key terms to this field, formed by relationships that involve interactions such as coordination, cooperation and collaboration levels amongst various actors [36,30,24].

Table 1 details a classification of SVCs approaches; SVC features aim at identifying common value chain dynamics geared towards developing sustainability along the actors' value chain.

Table 1. SVCs-Approaches and Features.

SVC Approach	SVC Feature	Description
Corporate Driven-Value Chain	Coordination Level	<i>Actors:</i> Corporate buyers with small-medium producers for market linkages. <i>Driver:</i> Paramount need of the buyer to receive a certain value in quantity and quality of products for either processing or the end-customer markets. <i>Sustainable context:</i> Limited Availability
Intermediary Driven-Value Chain	Cooperation Level	<i>Actors:</i> buyers with small-medium-large producers via Heterogeneous private or public actors such as wholesalers, trade unions, NGOs etc. <i>Driver:</i> Intermediation platform to exchange value and employ sustainability. <i>Sustainable context:</i> Low Availability
Producer Driven-Value Chain	Cooperation Level Collaboration Level	<i>Actors:</i> buyers with small producers via collective organisation such as leader producer, NGOs, exogenous agent, public facilitator, etc. <i>Driver:</i> producer association or cooperative to exchange value, share costs and employ sustainability. <i>Sustainable context:</i> Medium Availability
Hybrid Driven-Value Chain	Collaboration Level	<i>Actors:</i> buyers with small-medium-large producers via local and international network such as leader private sector, government, etc. <i>Driver:</i> multi-stakeholder network and network platform to exchange value, information, share costs, share profit and employ sustainability. <i>Sustainable context:</i> High Availability

Source: Adopted from [36, 30].

To create value and improve sustainability for partners, the focus is on key outcomes of these approaches [37,29,16]. Product flow, information flow, interaction, partnership, information sharing and value creation – these hallmark concepts of SVCs underpin the key characteristics that underpin the hallmark concepts of SVCs. These concepts operate in varied strata within the market: partnering actors move from spot market via coordination to commodity markets, they move to trade relations through cooperation; or through collaboration to value chain partnerships [36, 33]. The analysis of partnership alongside the term SVC has undergone an evolution, carried out by a notable number of researchers [38,39,40, 33]. However, a conceptual overlapping exists in terms of the scholarship surrounding partnerships in SVCs. The concepts found within relevant literature are often individually considered as antecedents and/or outcomes [37,29]. Some research studies have examined associated interrelationships to understand partnerships in SVCs [41,28, 24]. Therefore, capturing the relevant concepts in a holistic framework from the perspective of NFPAs and applying sustainability in an empirical context [e.g. 19,8,11, 12] proved to be a formidable challenge, strengthening in the process, the rationale for this research.

2.2. BA-NFPA Partnerships

A partnership is defined as “a tailored business relationship based on mutual trust, openness, shared risks and shared rewards that yields in a competitive advantage resulting in greater performance” [42]. From a value basis, partnership can be divided into three types [43]: a) the symbiosis is a relationship that occurs when partners have different competitiveness to create value by themselves; b) the commensalistic relationship where one partner creates value and the other partners share the value. This should include coordination of activities of participants in the chain requires intensive exchange of information, while c) the parasitic relationship is when partners mutually offset the created value. It is important to develop a fair distribution of surpluses among all participants in the value chain. This is based on parasitic supply chain model that assumes the implementation of outsourcing strategy for partners.

One of the key themes in operations management and business literature is the focus on the dynamics of SVC and their actors [35, 16]. While many classifications of SVCs for actors exist, the focus is on the widely accepted classification of primary and secondary actors [22,12]. The term secondary actor is used to refer to partners such as NFPAs. Particular attention has been paid to primary actors such as BAs, while a large body of research has been built around multi-actor platforms and cross-sector partnerships between the two types [35,44].

Current literature suggests that NFPA is used as a broad term which also represents non-profit organizations (e.g. NGOs and international donors) in business for better knowledge transfer and value creation for partnership [38]. Teegeen [7] explains that NFPA is based on the resource-based perspective, with four types of resources being taken into consideration: financial (e.g. profit and income), intangible (e.g. knowledge and reputation), organizational (e.g. structure and culture) and physical (e.g. equipment

and machine) benefits. BAs tend to process these four benefits but with a lack of reputation and legitimacy as well as environmental and societal trends [20,8]. Therefore, interactions between BAs and NFPAs come across as an interesting link to manage resources as a governance approach to problem solving [45]. With this evolution of SVC, NFPAs have become a facilitating hub since they connect their organisations to BAs for better long-term activities between buyers and sellers [11]. NFPAs help the BAs in management functions, capacity building, agricultural technology, gender groups, market information and trade activities [10]. This can be facilitated in the form of collaborative resources and management flows in order to interact with those BAs in a conducive scenario within agricultural value chains [46]. These partnerships focus on the value that can improve activities based on innovation features to offer sustainable development for economic growth and poverty mitigation along multi-stakeholder networks [47,10,48]. While NFPAs have become important partners in local and global plans, they need to support poverty reduction plans and business development [47]. This research goes on to posit that NFPAs will play fundamental partnership roles in SVCs.

In this study, key interest lies in understanding the phenomena of BA-NFPA partnership, designed to enable NFPAs improve Bas strategies to form SVCs approaches and features; this in turn stimulates effective interactions with sustainability to strengthen specific drivers along their chains.

2.3. Drivers of BA-NFPA Partnerships and Transaction Cost Theory (TCT)

Over time, BA-NFPA partnerships have been steadily challenged by keydrivers of partnership such as themes of information sharing and value creation [12,18, 4]. These themes require key actors of BAs and NFPAs to be more open to partnerships that have been supported by sources of information and added value, with information providers including focal actors and value actors [49,50]. Such partnerships emerged from the innovative role performed by private sector and civil society actors to form creative connections such as sustainability development of economic, social and environmental results [9,31]. These types of partnership are among several approaches adopted by NFPAs to promote as well as derive sustainability from the BA-NFPA governance scenario [12].

In fact, such a partnership has not been explored in detail and it remains an empirical question. An analysis of representative themes for innovative partnership in SVCs should identify both internal and external-focused partnership drivers (Table 2). These drivers highlight how a partnership is focused on managing governed relationships between BAs and NFPAs within actors' value chain activities for improving economic, social and environmental elements [51,11].

TCT suggests that a partnership can reduce opportunistic behaviour, information searching cost and integration cost in the process of chain interactions to facilitate integrated capabilities [25]. For example, partnerships amongst non-market mechanisms can help

market actors reduce transaction costs and be dynamic towards transaction risks [57].

Williamson [25] suggests that when value created via asset specificity is linked to idiosyncratic investments, opportunism raises a key risk. Hence, high levels of asset specificity within partnership interactions linked to information symmetry can be governed via hierarchies, medium levels via hybrid modes and low levels via markets for a specific product flow.

Given the inconsistencies within the discussion of TCT in extant literature, examining the role of governance in BA-NFPA partnerships can bring key insights into the development of TCT in supply chain research. Hence, a particular focus is placed on the governance approach in SVCs where taxonomy of governance forms is proposed where the BA-NFPA partnerships can be involved as follows:

Markets: are characterised by low asset specificity and offer a low level of complexity in transactions. They typically consist of partnerships at local spot markets where products of typical value are exchanged at the price negotiated and commanded by buyers at the spot.

Modular value chains: involve low asset specificity and offer a low level of complexity in transactions. They also involve partnerships at commodity markets through coordination level when producers are able to supply products of specific value to customers based on informal agreements [58,16]. *Relational value chains:* display medium asset specificity and offer a high level of complexity in transactions. Partnerships at trade relation markets via cooperation level when producers are highly able to supply products of specific value to customers based on informal agreements or contracts. However, the producers and customers have difficulty arranging the product specifications and conditions due to their willingness to create mutual dependence [55,29,15]. *Captive value*

chain: is linked to high asset specificity and offers a high level of complexity in transactions.

Thus, it is linked to partnerships at value chain markets via collaboration level when producers are not able to fully supply products of specific value to customers based on formal agreements or contracts. However, the customers are usually large buyers who apply a high degree of monitoring and traceability over producers [10]. *Hierarchy:* is linked to high asset specificity and offering a high level of complexity in transactions. Thus, it is linked to partnerships at value chain markets via collaboration level when producers are not able to supply products of specific value to customers based on informal and/or formal agreements or contracts. However, a neutral third actor (e.g. NFPA) coordinates the suppliers' network and drive the lead buyer to take full and direct control of production and logistics over producers [59,11, 60].

3. Methodology

3.1. Research Design

This study employs inductive qualitative methodology [63,61, 62]. The case study method is a rich source for exploring complex emergent phenomena [64]. Both case study selection and protocols were applied in this research [74]. The cases are partnerships in the context of SVC and are identified as sustainable partnerships by renowned NFPAs such as the UN and the World Bank. This sampling selection was based on a list of 20 organizations that was then shortlisted to five by putting them through the following criteria: satisfactory achievement records, positive email responses, and an initial interview.

Thus, the unit of analysis is individual partnerships (BA-NFPA), as presented in Table 3.

Table 2. Drivers of BA-NFPA Partnership in SVC, their definitions and key supporting author.

Key theme "Drivers"	Definition (Present research)	Key supporting authors
<i>Internal-focused partnership drivers</i>		
Interaction	A powerful wheel of cooperation, coordination and collaboration for value assessment moving towards partnership and for speeding sustainable results in the value chain	52,22
Information Sharing	An approach for interaction between actors for long term collaboration which leads to the improvement of their partnership's competitive advantage	53,39
Value Creation	A positive strategic agreement between the actors in their collaborative interaction for the expected growth of their partnership to highlight extreme sustainable benefits.	15
<i>External-focused partnership drivers</i>		
Information flow	Both effective formal and informal interactions for information management where actors working at cross-purposes with a focal actor to develop cohesive strategy for information sharing, essential for partnerships.	15
Product flow	Both direct and indirect interactions for relationship management where chain actors working at cross-purposes with a focal actor to exchange products along the value chain forming a link between demand and supply for partnerships.	54,55, 56

Table 3. Case Study in the Context of SVC.

Case	Partnership	Age	Partnership Description
A: Producer & International Agency 1	A1	3	For improving production, managing logistics, and collaborating with local factories. The agency provides training and workshops, equipment and technology for production development, quality control, and reasonable financial support for animal feeds and visit tours.
	A2	5	
B: Product supplier & International Agency 2	B1	5	For improving processing, reaching advanced technology, collaborating with local retailers. the agency provides training and workshops, equipment and technology for processing development, quality control, and reasonable financial support for exhibition and visit tours.
	B2	7	
C: Supplier & International Agency 3	C1	3	For improving production and processing, using better packaging, collaborating with local and international buyers. The agency provides training, equipment and technology for processing development, quality control, and reasonable financial support for exhibition and visit tours.
	C2	3	
D: Processor & Local Agency	D1	4	For improving processing, using advanced technology, collaborating with local and international retailers. The local agency provides training and workshops, specific equipment and technology for processing development, quality control, and support for exhibition and visit tours.
	D2	4	
E: Supplier and Local NGO	E1	10	For improving production, building better logistics, collaborating with local and export markets. In this relationship, the local actor provides membership for those suppliers, training and workshops, various projects, quality control, certification body, social networks, database, and reasonable exhibition and visit tours.
	E2	15	

The case protocol is applied for all cases for better research reliability [64]. Ten BA-NFPAs were identified in the context of agricultural sector in emerging economy. The basis for cases was semi-structured interviews with four staff members at each BA-NFPA. Managers were asked to identify a sample of relationships with the BAs in their agricultural value chains, which they highly believed included partnerships in information sharing and value creation for three years at least. Thus, two relationships of the same type for each case were explored using the same protocol. This is where semi-structured interviews, five observation days and document collection are applied for each relationship. Many countries have agreements and initiatives with international agencies and NFPAs' such as FAO, UN, EU, World Bank, IFAD, ILO, etc. to support rural development, agricultural industries and also new sustainable agricultural value chains (see reports e.g. 9).

3.2. Data Collection

A triangulation approach is applied by the use of existing research studies and case studies to ensure construct validity [62]. In previous research such as [73,75], the case study method has been instrumental in generating rich theoretical and practical insights especially in the fields of partnerships in SVCs [e.g. 28,29,16]. A triangulation approach was applied using existing research and case studies to ensure construct validity [62]. Previous research such as [75,73, 4], the case study method has been instrumental in generating rich theoretical and practical insights especially in the fields of partnerships in SVCs [28, 29,16].

Over 40 interviews ranging from one to two hours were obtained from the managers (four different managers\same actors in a relationship) involved in 10 partnerships in 2018. The aim was to answer the following questions; 1) how many partnerships are involved in information sharing and value creation? 2) what are the roles of information sharing and value creation within the value chain? 3) how do those actors cooperate, coordinate and collaborate for better interactions? 4) and lastly, how do they ensure that better information and product flows augment the supply & demand process? To obtain reflective practitioner inputs, several contacts were made with those managers with specific clarifications involving emails, phone calls and document exchanges that created

trust and mutual benefits [64]. Interviews were conducted and recorded by two authors in person with all the participants who were asked about the same questions using a comprehensive case protocol. The interviews were also transcribed and then sent to the managers for revisions. The approved interviews were used to develop the case studies that were analysed through cross-case analyses [63]. At the same time, the other two authors attended meetings that were organized between the BAs and NFPAs. This was when each author, as a silent observer, attended one meeting at five different scenarios. Finally, key documents (e.g. annual reports) were also obtained about each relationship for a triangulation purpose [62].

3.3. Data Analysis

Transcripts and key associated dimensions have been used to analyse the data where a thematic analysis was applied to summarize themes that constituted a piece of text [63]. A thematic analysis method is adopted, and this is defined as "identifying, analyzing, organizing, describing and reporting patterns (themes) within a data set" [76,p.6]. So it is considered a thematization that begins with a set of themes based on the existing literature and/ or the themes emerge from the data [77]. Themes refer to patterns across the existing data set that are most important to the description of various aspects of the phenomenon being observed. This included the following stages: a) initial codes were generated from themes amongst the literature review, for data reduction and display for each case using interview transcripts and other sources such as observations and archival documents b) selected themes were refined into non-repetitive themes wherein each case was explored using key themes and representative quotes to support the development of propositions with the literature evidence [64] and c) a cross-case comparison for data explanation was conducted to enhance replication logic amongst the cases providing both the BA/NFPA level-focused themes [62].

This analysis resulted in nine first-order themes, which were subsequently coded into three second-order themes and associated to one overarching theme "partnership" to establish the association for the conceptual framework.

To summarise, two approaches were followed: the first is the nested approach to analyse data gathered from each

case [65, 64] by multiple sources from two managers/relationships as opposed to a single case (four managers, two relationships) for a better opportunity to examine partnerships (Five cases A, B, C, D, E) in SVC. The second is the cross-case approach to analyse the commonalities between the five cases (62). The process was iterative, moving backward and forward in time, exploring what their value chain was like before the partnership, how and why they started to change. The benefit of this method was to allow the development of insights into key themes associated with the five NFPAs and to help to clarify the conceptual framework. This research has achieved quality validity and reliability (Table 4)[64].

4. Results and Discussion

4.1. Characteristics of BA-NFPA Partnerships

The selection of themes for the initial conceptual framework was guided by the literature review, which identified a number of initial themes as influencing the BA-NFPA partnerships. According to Porter [52] and Walters and Lancaster [43], the concept of the “value chain” epitomized the unilateral role of the actor in

interaction based on information sharing, information flow and product flow for creating value. These initial themes were then developed through each exploratory case. The themes that were matched to analyse the data from the exploratory cases were: management interaction of BAs and NFPAs involving information sharing; value creation, information flow; and product flow towards partnerships. The key findings further revealed that the BA-NFPA partnership with other functional themes appears to contribute to improved sustainability for many actors in SVC. However, it was unclear how these key themes would interrelate or their relative importance. According to Walters and Lancaster [43], the characteristics of the value chain framework dominate as a tool for the strategic analysis of firm value creation and information transfer and as a conceptual map for the description of activities that BAs perform in inter-firm relations. The SVCs for a BA-NFPA partnership amongst actors in an industry should be embedded in a more significant stream of activities that we term the “value wheel” in the present research (54,35). The value wheel includes the value chain of several BAs and NFPAs under the explored topic [14, 28,10]. Thus, the approaches and features of SVCs, actor types of BA-NFPA partnerships, and governance forms are presented for case studies (Table 5).

Table 4. Research Quality

Validity and Reliability	Research design	More related stage
Construct Validity	- Building trust with interviewees. - Multiple source of evidence at data collection: interviews; observation (meetings); documents. - Chain of evidence at data collection: two relationships for each case and use the same case protocol. - Transcripts are refined by the interviewees	Research design Data collection
Internal Validity	- Explanatory approach: develop a theoretical association. [at both Case level/ Cross case level] - Chain of evidence at data analysis: key theme matching and coding via support of key literature and key interview quotations. [at Case level] - Chain of evidence at data analysis: key proposition development. [at Case level] - Data triangulation: comparing quotes from interviews with observations and document material. [at Cross Case level]	Data analysis
External Validity	- Multiple cases: replication logic/10 partnerships for five cases. - Analytical generalization: building a new holistic framework.	Research design
Reliability	- Case study protocol is the same for all cases - Case database: interview quotes, meetings, and documents. - Key themes guided propositions and discussions - External review: final case report was validated by uninformed experts (Policy makers).	Data collection

Table 5: Approaches and Features of SVCs, Actor Types of BA-NFPA Partnerships and Governance Forms.

Case: BA-NFPA partnership	SVC Approach	SVC Feature	Actor Types	Governance Form
A (A1, A2) Producer & International agency 1	Producer Driven- Value Chain	Cooperation Level Collaboration Level	NFPA links buyers with small milk producers via collective organisation such as leader producer, NGOs, exogenous agent, public facilitator, etc.	Captive value chain
B (B1, B2) Supplier & International agency 2	Hybrid Driven- Value Chain	Collaboration Level	NFPA links buyers with small-medium-large dairy product supplier via local and international network such as leader private sector, government, etc.	Hierarch
C (C1, C2) Supplier & International agency 3	Intermediary Driven- Value Chain	Cooperation Level	NFPA links buyers with small-medium-large pickling supplier via Heterogeneous private or public actors as wholesalers, trade unions, NGOs etc.	Relational value chain
D (D1, D2) Processor & Local agency	Corporate Driven- Value Chain	Coordination Level	NFPA links corporate buyers with small-medium fruit processors for market linkages.	Modular value chain
E (E1, E2) Supplier and local NGO	Intermediary Driven- Value Chain	Cooperation Level	NFPA links buyers with small-medium-large FFV supplier via Heterogeneous private or public actors such as wholesalers, trade unions, NGOs etc.	Relational value chain

4.2. Cross-Case Patterns for Drivers of BA-NFPA partnerships

The analysis of BA-NFPA partnerships in SVCs has thoroughly investigated typical themes based on internal and external partnership factors. These drivers highlight how partnerships focus on managing relationships between BAs to link supply and demand within actors' value chain activities [11], as well as linking focal actors (for example, BA), with service providers serving as NFPAs for better SVCs for economic, social, and environmental activities [11]. Consequently, these drivers are broadly consistent with the findings of previous key representative authors, who identified interaction as a key theme for internal-focused partnership drivers [36,14,10], as well as product flow and information [36,14,10]. Therefore, these drivers are broadly consistent with the findings of the previous key representative authors, who identified the concepts of interaction as a key theme for internal-focused partnership drivers [36,14,10] and the concepts of product flow and information flow as two key themes for external-focused partnership drivers [24]. The analysis shows that business relationships are based on themes, such as information sharing, value creation as well as internal-focused partnership drivers; these themes form BA-NFPA partnerships in SVCs [33].

Internal-focused partnership drivers. The managers in the five cases reported that the interaction of the BAs need to be efficiently managed since these interactions exist as an important strategy in their BA-NFA partnerships.

Cases A, B, C and D display evidence of interactional collaboration as a newly-emerged theme from the NFPAs, vital for the development of trust and mutual objectives. Both relationships in Case E show little evidence of collaboration in exchange information and value assessment; these relationships were the least effective in partnerships in SVC.

All cases indicate that both BAs and NFPAs recognize the importance of developing strong information-sharing as exchange links, which in turn, support interaction management thereby benefitting their partnerships.

Cases A and B indicate that information sharing is used by the BAs as a hub of knowledge including value, resources, types and sharing methods. The concept of the hub is a newly-emerged theme enhanced by an efficient information flow between BAs along the SVC. The managers in all five cases agreed that value creation provides highly sustainable benefits for both BAs and NFPAs; also, their partnerships involve information to share and value to add for the use of all BAs in the SVC.

Cases A, B, C and D indicate value creation as equal benefits for all BAs within SVC. This is an emerged theme that reflects minimizing costs and equal distributions of revenue for BAs as a result of their activities.

External-focused partnership drivers. The NFPA has become a facilitating body that connects their organisations to BAs for better long-term activities in the SVC.

Managers in all five cases agreed that information flow is a facilitating tool that helps BAs in interaction management, capacity building, technological know-how, employee classifications, as well as market activities. This

can act as a collaborative resource in combination with management flow for an effective interaction with BAs in situations where partnerships exist in SVCs.

All managers in cases A, B and C add that information flow is seen as a visibility tool where BAs within the value chain can gain the same level of information. This visibility is indirectly supported by NFPAs to enrich the relationships between the BAs for better sustainable approaches by learning from each other in the normal situation or during covid-19.

There was a strong evidence in all cases that partnerships cannot be formed without the link between demand and supply, such that product flow from the main supplier to end-customer exists. To have an ideal conceptualisation of BA-NFPA partnerships, all managers acknowledged that BAs and NFPAs tend to be highly dependent on a strong flow of products between BAs as a transactional tool that ensures manageable transaction costs, a good reputation and clear legitimacy.

Overall, this study identifies nine major antecedents to BA-NFPA partnership:

1. Two key themes namely, *important strategy* and *interactive collaboration* integrated into a longer-term form can inform the level of interaction;
2. The two themes of exchange links and information-sharing hub of knowledge
3. The two themes of sustainable benefits and equal benefits for value creation
4. The two themes of *facilitating tool* and *visibility tool for information flow* (that could help develop partnerships between various types of actors) and
5. The two themes of *transactional tool* and *links of supply and demand for product flow* (that could be managed for better supply and demand linkages along the value chain).

All managers from the NFPAs interviewed - in all cases among the ten relationships - highlight the importance of *interaction*, *information sharing* and *value creation* as three key themes for internal-focused partnership drivers [36,10]; both concepts of *product flow* and *information flow* are highlighted by the managers as the two key themes for external-focused partnership drivers [11,24]. This is also supported by the minutes of the meetings between focal BAs and their NFPAs, including the annual reports.

Both the literature review and the cross-case findings support that interactive collaboration is the key between BAs and NFPAs's interactions. Findings from cross cases highlighted that BA level-focused and NFPA level-focused usually interact for a long term, and this interaction reflects a positive partnership approach. The important findings show that both actors in all relationship for cases A, B, and C identify high antecedent effects in creating BA-NFPA connections in SVC. Cases D and E, on the other hand, reveal that the antecedents have a low to medium impact on the formation of BA-NFPA collaborations.

As can be seen in the overall scores of cross cases A, B, C, D, and E that reflect high effects of the antecedents in forming these partnerships, interactive collaboration, exchange links, a hub of knowledge, equal benefits, and links of supply and demand sides towards partnership are the most significant antecedents. The remaining

antecedences represent the antecedents' medium effects in building these SVC relationships.

These findings are consistent with works by [36, 20,28,47,10, 4]who have indicated that many of these themes drive partnerships in SVC context. However, case E offers weak support for these findings in other cases. In this case, the NFPA is a local NGO which provides very limited partnership activities such as a membership for the focal suppliers (e.g. producers of fresh fruit and vegetables), training and workshops within specific projects, links to the certification body, exhibitions and visit tours for local and export markets. This finding gives a similar framing to those developed by Van-Der-Vorst et al. [67] and Mikkola [66].

4.3. A Tentative Conceptual Framework for BA-NFPA Partnerships

The present research explores the keydrivers “themes” jointly and extends extant literature by focusing on the SVC context.

Previous research, such as [36, 67, 66,24], has examined these themes individually and has not uncovered associations fully amongst the identified key themes in the agricultural value chain. This work provides a new conceptual framework based on the literature review and case studies (See Figure 2). For enhanced validity and reliability, a case method based on BA/NFPA level-focused themes was adopted for both individual and cross-case comparisons. These findings contribute to value chain literature by emphasising the theoretical link between the indicated antecedents and SVC cooperation.

Many authors now see interaction as a powerful method for advancing collaboration and accelerating sustainable value chain benefits [21, 68]. All managers demonstrated strategic plans between themselves and the BAs. A few relationships showed little evidence of interaction in exchange information and value assessment, and these relationships were the least effective within SVC partnerships. Interactive collaboration highly leads to information sharing among value chain partners [69]. [41] have identified that active collaboration may be enhanced by joint planning and problem solving. For example, partners can support collaborative actors in natural capital (e.g. water management), physical capital (e.g. infrastructure for road and quality system), financial capital (e.g. loans) and human capital (e.g. technical; market information)[66]. Partnering collaboration has become a vehicle for reducing costs and increasing customer value propositions established on sharing information and value creation [21].

The exploratory cases found that the four managers' types of the five cases explained that they apply the concept of joint planning with the BAs entirely, and most of their partners are aware of efficient interactive collaboration for reintegrating the business functions. Literature and the case studies indicate that *important*

strategy and interactive collaboration are essential to establishing a partnership based on information sharing and value creation for SVC, and there are synergies between interaction and the other themes.

The exploratory findings highlighted how information flow promotes interaction, and that effective internal formal interaction (meetings and conferences), and informal interaction (casual contacts) are used to develop cohesive strategies as well as to break down functional silos [21]. The dissemination of information across all actors in value chains aids partnerships based on equal visibility of information for all [15]. The findings indicate that all five NFPAs recognized the importance of developing strong information flow links, which include facilitating tools and visibility tools for the BAs. At the same time, the two partners: BA and NFPA can share tactical information (e.g. operations) and strategic information (e.g. market information) (Hsu et al., 2008) in order to incorporate more benefits in SVC. An efficient information flow enhances information sharing towards establishing better value chain relationships for better decision making [24]. Information flow is this process of disseminating and facilitating tool for sharing information, which is believed to indirectly underpin partnership between the two key actors in a visible way within the SVC.

Chain members change their operations in order to include relationship paradigms and information management [11]. This is due to external directions, such as uncertainty, economic issues, off-season supply and demand and environmental regulation [70, 22], as well as internal directions, such as weak organizational structure (e.g. no expertise, insufficient information visibility). These directions have led BAs to bond with international actors in order to gain support for better transactional tools and to link supply with demand[56] against such product-related ambiguities. The benefits of partnership on which value to create and what information to share, for instance, are already apparent due to increased collaborative quality control (e.g. certificates of HACCAP, Global GAP etc.) and legal framework (e.g. international body) [69]. The manner in which BA- NFPA value chain is governed is significant for Bas since this brings access solutions to the market with support from transactional activities amongst the BAs and the way suppliers are linked to customers. To overcome the situation during and after Covid-19, Firstly, in all cases there was a shift toward shorter SVCs facilitated by multiple aspects of adaptive capacity, particularly social organization in the form of social networks. Secondly, emphasizing the risks of overreliance on the global and local trade and calls for balancing economic portfolios with better-developed local supply chains and networks, Thirdly, emphasizes that BA and NFPA to support adaptation need to be in place before a macroeconomic shock hits COVID-19 and associated mitigation measures have disrupted small-scale SVCs.

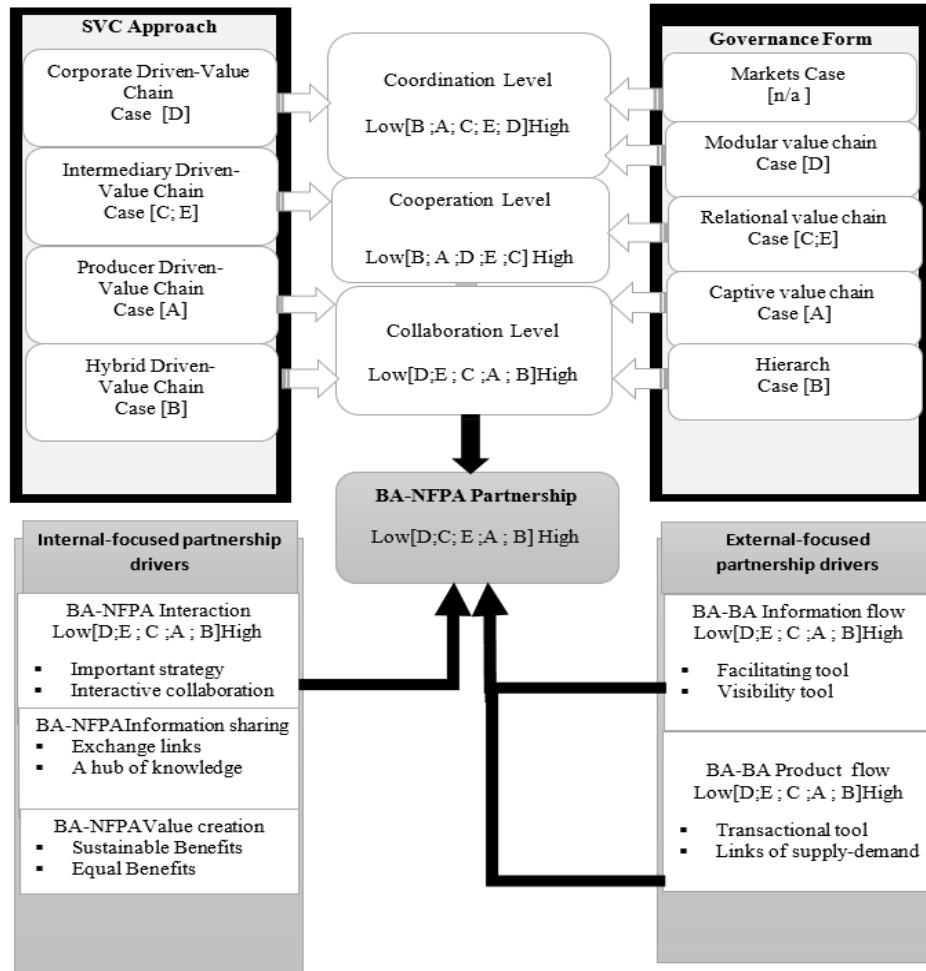


Figure 2. A conceptual Framework of Innovative BA-NFPA Partnership.

At the cross case level, we explain how and why these key drivers or themes are effectively linked to partnership in practice and how SVC approaches and governance form contribute to develop BA-NFPA partnerships. This indicates that the key themes identified should be categorized into three wheels:

1. Wheel 1-interaction of important strategy and interactive collaboration toward partnerships between BAs and NFPA. This wheel is affected by information sharing of exchange links and a hub of knowledge and by value creation of sustainable benefits and equal benefits between BA and NFPA for end-customers.
2. Wheel 2-information flow of facilitating tool and visibility tool between BAs but supported from NFPA and
3. Wheel 3-product flow of transactional tool and links of supply and demand between BAs but supported from NFPA.
- 4.

As can be seen from Figure 3, SVC approaches contribute to their features leading to the development of the concept of BA-NFPA partnerships which will be affected by wheels 1, 2 and 3. Hence, BA-NFPA partnerships rely on multi-stakeholder network and network-platform to exchange value, information, share costs, share profit and employ sustainability. These controllable activities may be used by top management to improve the information sharing and value creation

interface between BAs and NFPA. These activities include information flow and are considered to be sharing mechanisms that can be put in place quickly to support interaction of activities, and management of supply and demand for the product flow between BAs but supported from NFPA. In fact, among these, wheel 1 has become the central wheel that is surrounded by wheels 2 and 3 and influenced by SVC approaches and governance forms. The BAs are several actors surrounded by the focal actor as a supplier. For example consumers pull their “demand perspective” as a consumer value into a focal supplier in order to add input to the value chain approach and feature based on specific governance form as seen in Table 3. A supplier firm which provides inputs to a focal supplier of the value chain. The focal supplier’s product often passes through its channels’ value chains via key buyers on its way to the end-customer. Finally, the product as a perceived consumer value reflects a supply perspective to push a purchased output to the value chains to perform final customer expectations. Hence, the NFPA are the service provider actors that find “the right fit” for BA-NFPA partnerships to create the SVC for all BAs.

5. Conclusions

This study attempts to fill the gap in SVC literature in the agricultural context. Literature suggests the importance of actor involvement throughout the supply chain [6,4].

Recent literature,[17, 18] has conducted research that aims to discuss the effect of COVID-19 on socio-economic implications and the impact of lockdown on the food supply chain and agri-business. The study also summarizes the suggestions needed to control and deduce the impact of COVID-19. The study has reported some supply chain barriers caused by COVID-19 including national lockdown lack of labor availability, changing in customer behavior, delay in activity, and role of social media during the pandemic. However, there is limited research on operationalising the encouragement of an interactive partnership approach; this study endeavours to validate the constructs of value creation, information-sharing, product flow, and information flow as facilitating factors for a better partnership approach in the context of sustainable agricultural value chains.

5.1. Theoretical Contributions

The proposed theoretical framework based on an innovative partnership approach contributes to the background theory of SVC in an agricultural context and highlights avenues for further research within the value chain environment. This theoretical framework can help scholars understand underlying complexities of relationship research within value chains, thereby extending knowledge in the area. Without adequate empirical research on the partnership approach to an SVC, researchers and practitioners would be left without a SVC-oriented effective, efficient decision making tool.

5.2. Contributions to practitioner knowledge

This research contributes to practitioner knowledge that would benefit managers from both NFPA and BA working to improve BA-NFPA partnership in SVC. The developed framework utilises information sharing and value creation to propose systematic guidelines towards step-by-step partnership building between actors along the value chain. Research has highlighted relationship complexities among actors in the value chain who are engaged in various activities at different levels with multiple relations that create management issues and lower efficiencies [71,3]. Creating a relationship using a partnership approach that improves management and sustainability requires actors to interact based on strategic collaboration amply supported by the proper management of information and product flows.

Nine antecedents of the BA-NFPA partnership which may improve information-sharing levels between partners are highlighted, along with the information flow that leads to better value creation in their functions within the SVC. To improve information-sharing between partnering actors, managers should establish exchange links for a good source of information, classify information types, apply a variety of sharing methods and indicate the value of the information they need.

Managers may then apply the shared information (e.g., knowledge of quality control, demand, packaging) to their value generation activities along with the actor activities for sustainable value addition with the SVC. Policymakers, as well as internationally funded programs can also benefit from the current key findings. The new framework can help

them with corporate strategies and adopt the changes required for sustainable supply chain management [72].

From a strategic perspective, this research contends that partners need to interact mainly based on agreed strategies and collaborations rather than coordination and cooperation. Partners to respond to value chain complexity through interaction and lining up information visibility and product value, taking into account the uniqueness of each single function from production to consumption.

5.3. Limitations to research and future research

This research raises interesting areas of study. The conceptual framework indicates significant opportunities for future studies. Prior research has highlighted that information sharing [e.g. 15,20,69,73] and value creation [e.g. 20, 30] are needed at various levels of partnership development and improvement. Questions are raised about criteria for each level of development and improvement to support working actors in forming sustainable activities at each level. This study is qualitative in nature and the conceptual framework needs to be tested through further qualitative studies or quantitative studies involving large-scale surveys. The study considers only local value chains and, therefore, future research should consider international chains. Another potential area of study is the role of dyads (two firms) and triads (three firms) (e.g. lack of ties among partners) in partnerships from the perspective of multi-partners as actors. It remains to be verified how information sharing and value creation influence sustainable development and the chain dyad's performance especially in the field of agriculture [41,28].

References

- [1] Cho, D.W. and Lee Y.H. (2013), "The value of information sharing in a supply chain with a seasonal demand process", *Computers & Industrial Engineering*, Vol.65 No.1, pp. 97-108.
- [2] MacMillan, K., Money, K., Money, A., & Downing, S. (2005), "Relationship marketing in the not-for-profit sector: An extension and application of the commitment-trust theory", *Journal of Business Research*, Vol.58, pp. 806-818.
- [3] Janet, H., Meredith, L. and Kathleen H. (2016), "Value chain analysis: an iterative and relational approach for agri-food chains", *Supply Chain Management: An International Journal*, Vol. 21 No. 3, pp. 352-362.
- [4] Jraisat, L., Upadhyay, A., Ghali, T., Jresseit, M., Kumar, V., and Sarpong, D. (2021): Triads in sustainable supply-chain perspective: why is a collaboration mechanism needed?, *International Journal of Production Research*, DOI: 10.1080/00207543.2021.1936263.
- [5] Wu, Z., T. Y. Choi, and M. J. Rungtusanatham. 2010. "Supplier-Supplier Relationships in Buyer-Supplier-Supplier Triads: Implications for Supplier Performance." *Journal of Operations Management* 28 (2): 115-123.
- [6] Haiyan, E. L., Andrew, P., Vasco, S. R. and Helen, W. (2018) "Exploring sustainable supply chain management: a social network perspective", *Supply Chain Management: An International Journal*, Vol. 23 No. 4, pp. 257-277.
- [7] Teegen, H., Doh, J.P. and Vacchani, S. (2004), "The importance of nongovernmental organizations (NGOs) in global governance and value creation: an international business research agenda", *Journal of international Business Studies*, Vol.35, pp. 463-483.

- [8] Graf, N.F.S. and Rothlauf, F. (2012), "Firm-NGO collaborations: A resource-based perspective", *Z Betriebswirtsch*, Vol.82, pp. 103–125.
- [9] Baur, D. and Schmitz, H.P. (2012), "Corporations and NGOs: When accountability leads to co-optation", *Journal of Business Ethics*, Vol.106, pp. 9–21.
- [10] Bonney, L., Clark, R., Collins, R. and Fearn, A. (2007), "From serendipity to sustainable competitive advantage: insights from Houston's farm and their journey of co-innovation", *Supply Chain Management: An International Journal*, Vol. 12 No. 6, pp. 395-399.
- [11] Christopher, M. (1998). *Logistics and Supply Chain Management - Strategies for Reducing Cost and Improving Service*. 2nd edition, Prentice Hall.
- [12] Goodman, J., Korsunova, A. and Halme, M. (2017), "Our collaborative future: Activities and roles of stakeholders in sustainability-oriented innovation", *Business Strategy & Environment*, Vol.26 No.6, pp. 731-753.
- [13] Khan, S.A., Chaabane, A., Dweiri, F., 2020. Supply chain performance measurement systems: A qualitative review and proposed conceptual framework. *International Journal of Industrial and Systems Engineering*. Vol. 34, No.1, PP. 43–64.
- [14] Berger, I. E., Cunningham, P. H., and Drumwright, M. E. (2004), "Social alliances: Company/ nonprofit collaboration", *California Management Review*, Vol.47 No.1, pp. 58-90.
- [15] Porter, M. and V. Millar (1985), "How information gives you competitive advantage," *Harvard Business Review*, Vol.63 No.4, pp. 149–160.
- [16] Niall, P. and Rich, N. (2015), "The relationship between lean operations and sustainable operations", *International Journal of Operations and Production Management*, Vol. 35 No. 2, pp. 282-315.
- [17] Morsy, H., Salami, A. and Mukasa, A. (2021), "Opportunities amid COVID-19: Advancing intra-African food integration", *World Development*, Vol. 139 No. , pp. 1-3.
- [18] Aday, M. (2020), "Impact of COVID-19 on the food supply chain", *Food Quality and Safety*, Vol 4, No. 4, pp.167–180.
- [19] Austin, J. E., and Seitanidi, M. M. (2012), "Collaborative value creation: A review of partnering between nonprofits and businesses: Part 1. Value creation spectrum and collaboration stages", *Nonprofit and Voluntary Sector Quarterly*, Vol. 41 No. 5, pp. 726- 758.
- [20] Bailey and Francis (2008), "Managing information flows for improved value chain performance", *International Journal of Production Economics*, Vol.111 No.1, pp. 2-12.
- [21] Luzzini, D., Brandon-Jones, E., Brandon-Jones, A. and Spina, G. (2015), "From sustainability commitment to performance: the role of intra- and inter-firm collaborative capabilities in the upstream supply chain", *International Journal of Production Economics*, Vol. 165, pp. 51-63.
- [22] Amara, N., Halilem, N. and Traoré, N. (2016), "Adding value to companies' value chain: Role of business schools scholars", *International Journal of Business Research*, Vol.69 No.5, pp. 1661-1668.
- [23] Cojocaru, S. and Sfetcu, L. (2013), "Partnerships in Social Economy", *Social and Behavioral Sciences*, Vol. 92, pp. 197 – 201
- [24] Tasca, A. L., Nessi, S. and Rigamonti, L. (2017), "Environmental sustainability of agri-food supply chains: An LCA comparison between two alternative forms of production and distribution of endive in northern Italy", *Journal of Cleaner Production*, Vol.140, pp. 725-741.
- [25] Jarillo, J. C. (1990), "Comments on 'transaction costs and networks'", *Strategic Management Journal*, Vol. 11 No.6, pp. 497-499.
- [26] Almeida, A., Bastos, J., Francisco, R.D.P., Azevedo, A., Ávila, P., (2016), "Sustainability assessment framework for proactive supply chain management. *International Journal of Industrial and Systems Engineering*, Vol.24, No.2, pp.198–222.
- [27] Simatupang, T. M. and Sridharan, R. (2005), "The Collaboration Index: a measure for supply chain collaboration", *International Journal of Physical Distribution & Logistics Management*. Vol.35 No.1, pp. 44-62.
- [28] Spekman, R. E., Jr, W. K. J. and Myhr, N. (1998), "An empirical investigation into supply chain management: A perspective on partnership", *Supply Chain Management: An International Journal*, Vol.3 No. 2, pp. 53-67.
- [29] Pagell, M. and Shevchenko, A. (2014), "Why research in sustainable supply chain management should have no future", *Journal of Supply Chain Management*, Vol. 50 No. 1, pp. 44-55.
- [30] Esfahbodi, A. Zhang, Y. Watson, G. (2016), "Sustainable supply chain management in emerging economies: Trade-offs between environmental and cost performance", *International Journal of Production Economics*, Vol.181, pp. 350–366.
- [31] Skjoett-Larsen, T., Thorne, C. and Andresen, C. (2003), "Supply chain collaboration: theoretical perspectives and empirical evidence", *International Journal of Physical Distribution & Logistics Management*, Vol.3No.6, pp. 532-549.
- [32] Tachizawa, M.E. and Wong, Y.C. (2014), "Towards a theory of multi-tier sustainable supply chains: a systematic literature review", *Supply Chain Management: An International Journal*, Vol. 19 Nos 5/6, pp. 643-663.
- [33] Aggarwal, S. and Srivastava, M. K. (2016), "Towards a grounded view of collaboration in Indian agri-food supply chains: A qualitative investigation", *British Food Journal*, Vol. 118 No.5, pp.1085-1106.
- [34] Cole, R., Aitken, J., 2020. The role of intermediaries in establishing a sustainable supply chain. *Journal of Purchasing and Supply Management* 26, 100533. <https://doi.org/10.1016/j.pursup.2019.04.001>.
- [35] Acquaye, A., Genovese, A., Barrett, J. and Koh, S.C.L. (2014), "Benchmarking carbon emissions performance in supply chains", *Supply Chain Management: An International Journal*, Vol. 19 No. 3, pp. 306-321.
- [36] Fearn, A. (1998), "The evolution of partnerships in the meat supply chain: insights from the British beef industry", *Supply Chain Management*, Vol.3 No.4, pp.214-231.
- [37] McAdam, R., Hazlett, S-A. and Anderson-Gillespie, K. (2008), "Developing a conceptual model of lead performance measurement and benchmarking: A multiple case analysis", *International Journal of Operations & Production Management*, Vol. 28 No. 12, pp. 1153-1185.
- [38] Giannakis, M. (2008), "Facilitating learning and knowledge transfer through supplier development", *Supply Chain Management: An International Journal*, Vol. 13 No. 1, pp. 62-72.
- [39] Ding, H., Guo, B., and Liu, Z. (2011), "Information sharing and profit allotment based on supply chain cooperation", *International Journal of Production Economics*, Vol.133 No.1, pp 70-79.
- [40] Kembro, J., Selviaridis, K. and Näslund, D. (2014), "Theoretical perspectives on information sharing in supply chains: a systematic literature review and conceptual framework", *Supply Chain Management: An International Journal*, Vol.19 No.5/6, pp. 609-625.
- [41] Taylor, D.H. and Fearn, A. (2006), "Towards a framework for improvement in the management of demand in agri-food supply chains", *Supply Chain Management: An International Journal*, Vol.11No.5, pp. 379–384
- [42] Lambert, D.E., (2008), *Supply Chain Management: Processes, Partnerships, Performance* (3rd ed), Supply Chain Management Institute, The Hartley Press, Jacksonville.

- [43] Walters, D. and Lancaster, G. (2000), "Implementing value strategy through the value chain", *Management Decision*, Vol. 38 No. 3, pp. 160-178.
- [44] Rim, H., Yang, S-U. and Lee, J. (2018), "Strategic partnerships with nonprofits in corporate social responsibility (CSR): The mediating role of perceived altruism and organizational identification", *Journal of Business Research*, Vol. 69 No.9, pp. 3213-3219.
- [45] Andreasen, A. R. (1996), "Profits for nonprofits: Find a corporate partner *Harvard Business Review*, Vol.74 No.6, pp.47-50, 55-59.
- [46] Kim, N., Sung, Y. and Lee, M. (2011), "Consumer evaluations of social alliances: The effects of perceived fit between companies and non-profit organizations", *Journal of Business Ethics*, Vol.78 No.4, pp. 611-622
- [47] Porter, M. E., and Kramer, M. R. (2011), "Shared value: How to reinvent capitalism and unleash a wave of innovation and growth", *Harvard Business Review*, Vol.89 No.12, pp. 62-77
- [48] Mota, J., de Castro, L. M., & Brito, C. (2016). "Powered by... whom?" A network perspective on replication as strategy', *Journal of Business Research*, Vol.69 No.11, pp. 4732-4736.
- [49] Prahalad and Ramaswamy (2004), "Co-creation experiences: the next practice in value creation, *Journal of Interactive Marketing*, Vol.18 No.3, pp. 22-34.
- [50] Xue, X., Shen, Q., Tan, Y., Zhang, Y., and Fan, H. (2011), "Comparing the value of information sharing under different inventory policies in construction supply chain", *International Journal of Project Management*, Vol.29 No.7, pp. 867-876.
- [51] Wymer, W. W., Jr. and Samu, S. (2003), "Dimensions of business and nonprofit collaborative relationships", *Journal of Nonprofit & Public Sector Marketing*, Vol.11 No.1, pp. 3-22.
- [52] Porter, M. E. (1985). *Competitive advantage: Creating and sustaining superior performance*. New York: Free Press.
- [53] Cheng, J.H. (2011), "Inter-organizational relationships and information sharing in supply chains", *International Journal of Information Management*, Vol. 31 No.4, pp.374-384.
- [54] Giannakis, M. and Croom, S.R. (2004), "Toward the development of a supply chain management paradigm: a conceptual framework", *Journal of Supply Chain Management*, Vol.40 No.2, pp. 27-37.
- [55] Horvath, L. (2001), "Collaboration: the key to value creation in supply chain management", *Supply Chain Management: An International Journal*, Vol. 6 No. 5, pp. 205-207.
- [56] Flynn, B.B., Huo, B. and Zhao, X. (2010), "The impact of supply chain integration on performance: a contingency and configuration approach". *Journal of Operation Management*, Vol. 28 No.1, pp. 58-71.
- [57] Schmidt, C.G., Wagner, S.M., (2019), "Blockchain and supply chain relations: A transaction cost theory perspective", *Journal of Purchasing and Supply Management* 25, pp.100-552.
- [58] Arshinder, (2012), "Flexibility in supply chain using coordination: Issues and learnings", *International Journal of Industrial and Systems Engineering*, Vol.11, No.2, pp.308-330.
- [59] Reardon, T., Barrett, C., Berdegue, J. and Swinnen, J. (2009), "Agri-food industry transformation and small farmers in developing countries", *World Development*, Vol.37 No.11, pp. 1717-1727.
- [60] Adobor, H., McMullen, R.S., (2014), "Strategic purchasing and supplier partnerships-The role of a third party organization," *Journal of Purchasing and Supply Management* Vol.20, pp.263-272.
- [61] Denzin N. and Lincoln Y. (Eds.) (2000). *Handbook of Qualitative Research*. London: Sage Publication Inc.
- [62] Eisenhardt, K.M. and Graebner, M.E. (2007), "Theory building from cases: opportunities and challenges", *Academy of Management Journal*, Vol. 50 No. 1, pp. 25-32.
- [63] Miles, M. B., Huberman, A. M., & Salda-na, J. (2014), "Qualitative data analysis. A methods sourcebook," 3rd ed. Thousand Oaks, CA: SAGE Publications, Inc; 2014.
- [64] Yin, R. K. (2014), "Case Study Research: Design and Methods. 5th ed. Thousand Oaks, CA: Sage.
- [65] Voss, C., Tsikriktsis, N. and Frohlich, M. (2002), "Case research in operations management", *International Journal of Operations & Production Management*, Vol. 22 No. 2, pp. 195-219.
- [66] Mikkola, M, (2008), "Coordinative structures and development of food supply chains", *British Food Journal*, Vol. 110, No. 2, pp.189-205.
- [67] Van Der Rhee, B., Van Der Veen, J.A., Venugopal, V. and Nalla, V.R., (2010), "A new revenue sharing mechanism for coordinating multi-echelon supply chains", *Operations Research Letters*, Vol. 38, No. 4, pp.296-301.
- [68] Thilmany, D., Canales, E., Low, S.A. and Boys, K. (2021), "Local Food Supply Chain Dynamics and Resilience during COVID-19," *Appl Econ Perspect Policy*, Vol.43, pp.86-104.
- [69] Jraisat, L. and Sawalha, I., (2013), "Quality control and supply chain management: a contextual perspective and a case study", *Supply Chain Management: An International Journal*, Vol. 18, No. 2, 194-207.
- [70] Mohebalizadeh, M., Hafezalkotob, A., (2018), "Modelling sustainable supply chain management problem with fuzzy demand based on multi-criteria decision making methods," *International Journal of Industrial and Systems Engineering*, Vol.30, No.2, pp. 267-297.
- [71] Axelsson, B. and Easton, G. (1992), *Industrial Networks: A New View of Reality*, Routledge, London.
- [72] Johnston, A.D. and Linton, D.J. (2000), "Social networks and the implementation of environmental technology", *IEEE Transactions on Engineering Management*, Vol. 47 No. 4, pp. 465-477.
- [73] Jreissat, M., and Jraisat, L. (2019), "Sustainable Dyads in Supply Chain Management: A Qualitative Perspective." *Jordan Journal of Mechanical & Industrial Engineering* Vol.13, No. 4., pp. 277-290.
- [74] Stuart, I., McCutcheon, D., Handfield, R., McLachlin, R. and Samson, D. (2002), "Effective case research in operations management: a process perspective", *Journal of Operations Management*, Vol. 20 No. 5, pp. 419-433.
- [75] Reddya, B. Chandra Mohana, et al.(2008), "Quota Allocation to Distributors of the Supply Chain under Distributors' Uncertainty and Demand Uncertainty by Using Fuzzy Goal Programming." *Jordan Journal of Mechanical and Industrial Engineering*, Vol. 2 No.4, pp. 215-226.
- [76] Braun, V. & Clarke, V. (2006), "Using thematic analysis in psychology", *Qualitative Research in Psychology*, Vol.3, pp.77-101.
- [77] Boyatzis R. E. (1998), "Transforming qualitative information: Thematic analysis and code development", Thousand Oaks, CA: Sage
- [78] Myrto, R. (2020), "Safety of Foods, Food Supply Chain and Environment within the COVID-19 Pandemic." *Trends in Food Science & Technology*, Vol. 102, 2020, pp. 293-299.
- [79] Asamoah, D., Agyei-Owusu, B. and Ashun, E. (2020), "Social network relationship, SC resilience and customer-oriented performance of small and medium enterprises in a developing economy", *Benchmarking: An International Journal*, Vol.27 No.5, pp. 1793-1813.
- [80] Ivanov, D & Dolgui, A. (2020) Viability of intertwined supply networks: extending the supply chain resilience angles towards survivability. A position paper motivated by COVID-19 outbreak, *International Journal of Production Research*, Vol.58 No.10, pp.2904-2915.

Application of Kansei Engineering and Data Mining for the Eyewear Industry in Jakarta

Yung-Tsan Jou¹, Ronald Sukwadi^{2*}, Riana Magdalena Silitonga^{1,2}, Roselly²

¹Department of Industrial and Systems Engineering, Chung Yuan Christian University, Taiwan

²Department of Industrial Engineering, Faculty of Engineering, Atma Jaya Catholic University of Indonesia, Indonesia.

Received 18 April 2021

Accepted 26 JAN 2022

Abstract

The importance of eyeglasses is increasing in the present day. Myopia has a significant increase globally, with the highest prevalence of myopia in Asia-Pacific, East Asia, and Southeast Asia. Girls are more prone to suffer myopia and have more risk factors than boys in Asia. As eyeglasses' uses started to be more progressive at age 6 to 22 years, the purpose was to identify the Kansei words and to translate them into authentic eyeglasses design that teen girls in Jakarta desire. One hundred teen girls had contributed to this study by comparing 16 Kansei words, including modern, elegant, casual, beautiful, comfortable, attractive, good quality, aesthetic, trendy, light weight, practical, durable, affordable, strong, fit to hand and ergonomic against ten eyeglasses pictures. Data mining method was applied to find the connection between eyeglasses' whole appearance and emotions captured in a shorter time. This experiment achieved decision tree classification and association rules technique with Waikato Environment for Knowledge Analysis (WEKA). The best Kansei design of eyeglass for teen girls is round shape, titanium material, light-colored, full-frame, and plain surfaces.

© 2022 Jordan Journal of Mechanical and Industrial Engineering. All rights reserved

Keywords: eyeglasses, Kansei Engineering;teen girls;data mining; WEKA.

1. Introduction

Myopia has become one of the significant issues in the public health world; it contributes to visual impairment affecting all age groups, from children to adults. Myopia is most correctable with spectacles and contact [1]. It has been accepted as an epidemic titled "The Myopia Boom," especially in East and Southeast Asia [2]. It is estimated that myopia will significantly increase prevalence globally, affecting almost roughly 5 billion people by 2050. Table 1 shows the estimated prevalence of myopia by 2050 for each region [3]. As seen in Table 1, myopia's highest prevalence is Asia-Pacific, East Asia, and Southeast Asia, meaning that a notable rise in myopia has attacked Asia. The prevalence of myopia in young adults, especially in some of the developed countries of East and Southeast Asia, is now over 80% [4].

Meta-analysis research [5] includes studies of the prevalence of myopia characteristics based on race, and Indonesian young adults aged 21 – 50 years old reached 48.5 %, which makes Indonesia's prevalence of myopia pretty high [6]. According to many studies, girls are more prone to suffer from myopia and have more risk factors than boys in Asia, mentioned in [7]; girls have a higher prevalence of myopia than boys in urban China, India, and Malaysia. The higher prevalence of myopia in girls was also stated in a study [8]. These reflect a consistent pattern that female subjects are more likely to use a pair of eyeglasses than male subjects. In order to focus on teen girls in their youth as the segmented market, the eyewear

industry must design a pair of eyeglasses beyond their functional requirement.

Table 1. The estimates prevalence of myopia between 2000 – 2050 for each decade.

Region	Prevalence (%) in Each Decade					
	2000	2010	2020	2030	2040	2050
Andean Latin America	15.2	20.5	28.1	36.2	44.0	50.7
Asia-Pacific, high income	46.1	48.8	53.4	58.0	62.5	66.4
Australia	19.7	27.3	36.0	43.8	50.2	55.1
Caribbean	15.7	21.0	29.0	37.4	45.0	51.7
Central Africa	5.1	7.0	9.8	14.1	20.4	27.9
Central Asia	11.2	17.0	24.3	32.9	41.1	47.4
Central Europe	20.5	27.1	34.6	41.8	48.9	54.1
Central Latin America	22.1	27.3	34.2	41.6	48.9	54.9
East Africa	3.2	4.9	8.4	12.3	17.1	22.7
East Asia	38.8	47.0	51.6	56.9	61.4	65.3
Eastern Europe	18.0	25.0	32.2	38.9	45.9	50.4
North Africa and Middle East	14.6	23.3	30.5	38.8	46.3	52.2
North America, high income	28.3	34.5	42.1	48.5	54.0	58.4
Oceania	5.0	6.7	9.1	12.5	17.4	23.8
South Asia	14.4	20.2	28.6	38.0	46.2	53.0
Southeast Asia	33.8	39.3	46.1	52.4	57.6	62.0
Southern Africa	5.1	8.0	12.1	17.5	23.4	30.2
Southern Latin America	15.6	22.9	32.4	40.7	47.7	53.4
Tropical Latin America	14.5	20.1	27.7	35.9	43.9	50.7
West Africa	5.2	7.0	9.6	13.6	19.7	26.8
Western Europe	21.9	28.5	36.7	44.5	51.0	56.2
Global	22.9	28.3	33.9	39.9	45.2	49.8

* Corresponding author e-mail: ronald.sukwadi@atmajaya.ac.id.

Ergonomics is an interdisciplinary science; the study of human activities in the workplace and life environment [9]. Ergonomics are not limited to controlling the workplace, but considering further domains, including product design. Responding to customer trends, needs approaches to make an appropriate connection between emotional aspects of design and products. Kansei Engineering is a multidisciplinary methodology found by Mitsuo Nagamachi that embodies product design and is appropriate with the principles of ergonomics. A Kansei product that converts the user's needs into tangible features can be ergonomic.

Many researchers are currently focusing on developing many approaches in product design, and some are known as 'voice of customers' for prioritizing customer needs [10]. Kansei Engineering is a new product development technology to identify 'voice of customers' by creating a human-oriented product and captive consumers' emotions [11]. Kansei Engineering itself has been used in many studies on product design [12]. A few prior studies of Kansei were applied to many goods and services like automatic boards [13], a recliner [14], car seat lever position [15], real estate consumer preferences [16], airline services [17], and many more. Nonetheless, because many elements compose a product, most previous studies on Kansei Engineering focused only on one item of design element to one degree of emotion. While in everyday life, consumers become aware of things as a whole rather than an individual part of a product; therefore, it might not be the most effective way to compose a KE study for each element [18]. One way to help is with Data Mining Technology.

Data mining is the process of exploration and analyzing a large quantity of data to discover basic patterns and rules formed to develop their marketing, sales, and customer support operations [19]. According to Hand et al. [20], data mining is described as analyzing massive datasets to discover the unsuspected relationship and review data more logically. It serves the desired results while in this case is to identify the relationship between a product appearance and the emotion captured by the customer after seeing it. One of the technology of data mining is WEKA, a machine learning toolkit by the University of Waikato, an easy interface to understand & access for the public. It works well for beginners [19, 21, 22].

Data mining tasks are grouped into two main categories; Predictive and Descriptive. Fayyad et al. [23] defined six primary data mining functions: classification, regression, clustering, dependency modeling (association rules), deviation detection, and summarization. Classification, regression, and anomaly detection are categorized under a predictive category, while clustering dependency modeling are categorized under a descriptive category. Predictive model forecasts use some variables in the dataset to predict unknown values of other relevant variables [21, 22, 24]. In contrast, a descriptive model classifies patterns or relationships and encompasses human understanding patterns and trends in data [25].

The combination of Kansei and data mining is to find the connection between a pair of eyeglasses' whole appearance and the emotions felt or captured by customers in a shorter amount of time. This study aims to satisfy customers' affective needs by determining the Kansei words and translating them into the actual design of eyeglasses desired by girls residing in Jakarta, Indonesia. The best combination of attributes, that form eyeglasses, to capture the potential market will be identified.

2. Methods

2.1. Step 1 – determine the subject

One hundred subjects who wear eyeglasses took part in the study. In their youth between the ages of 15 to 24, teen girls residing in a particular region, Jakarta (senior high school and undergraduate students), were selected for the field study.

2.2. Step 2 – eyeglasses images

A set of eyeglasses images were huddled from various advertising websites, including all the exterior views of the product, such as color, surface pattern, and shape. The images used in the study include 25 eyeglasses samples. They were printed in color for experts to evaluate.

2.3. Step 3 – development of the field study

An interview with four refractions opticians from Optik Melawai, Optik Seis, and Optik Tunggal as experts were done to construct the eyeglasses design elements and attributes. They have been informed about the study objectives and asked to evaluate the exterior view of 25 eyeglasses images. Then, they were asked to help narrow it down to the top 10 most likely to be bought by girls based on their experience as an optician, then identify the eyeglasses properties/design elements and attributes as shown in Figure 1.



Figure 1. Eyeglasses samples selected for evaluation

2.4. Step 4 – determine Kansei words

Firstly, Kansei words were collected by turning many websites, literature, and journals related to this field study and interviewing five girls who fell into the selected subject category. About 30 Kansei words were gathered, as shown in Table 2.

2.5. Step 5 – questionnaire 1

Secondly, the initial 30 Kansei words must be filtered to only the most important ones since 30 was still too many for each subject to evaluate. A preliminary questionnaire was distributed through google form to narrow it down. Respondents were asked to evaluate each Kansei word using the 5 points semantic differential scale of 1. The Kansei word is not a vital perception variable on eyeglasses. The Kansei word is a significant perception variable on eyeglasses to scale five. One hundred and one

subjects filled out the google form resulting average score for each Kansei word. If the average score of each Kansei word were more significant than the relative average score of all 30 Kansei words, those would be the selected Kansei words as most important (Table 3).

Sixteen most important Kansei words were selected: Modern, Elegant, Casual, Beautiful, Comfortable, Attractive, Good Quality, Aesthetic, Trendy, light Weight Practical, Durable, Affordable, Strong, Fitness to Fingers and Ergonomic.

Table 2. Kansei words are taken from the observation

Kansei Words	Sources
Modern	[22,26]
Antique/Vintage	Interview
General/Common	[12,14]
Elegant	[14,15,26, 27]
Unique	Interviews
Formal	[11,12,15, 27]
Casual	[14,15, 26]
Beautiful	[12,14,15,26]
Cute	[12, 14,15]
Fancy	[12, 14, 15]
Feminine	[26]
Masculine	[11,12, 18]
Simple	[26, 27]
Comfortable	[26, 27]
Innovative	Websites (eye-book.com)
Attractive	Websites (eye-book.com)
Good Quality	[12, 14,15]
Aesthetic	Websites (eye-book.com)
Exclusive	[12, 14,15, 18]
Eye-Catching	Interview
Young-Looking/Youthful	[18, 26]
Trendy	[18, 26]
Light-Weight	[11,12, 18]
Practical	[22,26]
Edgy	[26]
Durable	[14,15, 22]
Affordable	[14,15, 18, 22]
Strong	[14, 15, 26]
Fitness to Fingers/Hand	[14,18, 26]
Ergonomic	Interview

2.6. Step 6 – questionnaire 2

In this phase, ten selected eyewear frame pictures and 16 Kansei words were put together as the main questionnaire using a 1 to 5 semantic differential technique scale by Osgood (Figure 3). The purpose of this phase was to evaluate how teen girls felt the moment they saw the eyeglasses picture as a product sample. One hundred questionnaires were printed and distributed individually offline for teen girls residing in the Jakarta area with an age range between 15 to 24 years old. The 5-level semantic differential was managed with sixteen Kansei words in negative-positive format. For example, if a respondent filled out scale number 5 on the Kansei word Comfortable against the first picture, the respondent felt comfortable with the first configuration of product properties. However, if a respondent filled out scale number 1 on Kansei word and completed it against the first picture, the respondent would feel that the first

configuration of product properties was uncomfortable (Figure 2).

Table 3. The average score for each Kansei word

Kansei Word	Respondents	Total	Average
Modern	101	376	3.72
Antique/Vintage	101	274	2.71
General/Common	101	326	3.23
Elegant	101	385	3.81
Unique	101	322	3.19
Formal	101	307	3.04
Casual	101	390	3.86
Beautiful	101	420	4.16
Cute	101	291	2.88
Fancy	101	328	3.25
Feminine	101	304	3.01
Masculine	101	256	2.53
Simple	101	348	3.45
Comfortable	101	471	4.66
Innovative	101	361	3.57
Attractive	101	398	3.94
Good Quality	101	462	4.57
Aesthetic	101	399	3.95
Exclusive	101	330	3.27
Eye-Catching	101	237	2.35
Young-Looking/Youthful	101	353	3.50
Trendy	101	370	3.66
Light Weight	101	436	4.32
Practical	101	438	4.34
Edgy	101	357	3.53
Durable	101	451	4.47
Affordable	101	418	4.14
Strong	101	401	3.97
Fitness to Fingers/Hand	101	365	3.61
Ergonomic	101	375	3.71
Relative Average			3.61

2.7. Step 7 – data processing

In total, 100 questionnaires were sorted into datasets for each emotion or Kansei word. The datasets were then processed by applying the decision tree classification technique and then association rules mining provided through WEKA Machine Learning.

3. Results and Discussions

3.1. Sample profile

Most of the respondents were aged 18-20 years old and in detail three teen girls aged 16, 1 girl aged 17, 24 girls aged 18, 25 girls aged 19, 24 girls aged 20, 1 girl aged 21, 9 girls aged 22 and 1 aged 23. In total, 95 respondents out of 100 were university students. The respondents with minus below 1 were eight girls, minus 1-2 were 33 girls, minus 2-3 were 23 girls, minus 3-4 were 13 girls, minus 4-5 were 17 girls, and with minus more than 5 were six girls. There were 50 teen girls with Optik Melawai as their favorite store and about 49 teen girls willing to spend money on eyeglasses for IDR 1,000,000 to IDR 2,000,000. Eyewear companies and designers can take these data into account on creating eyeglasses for the intended market.

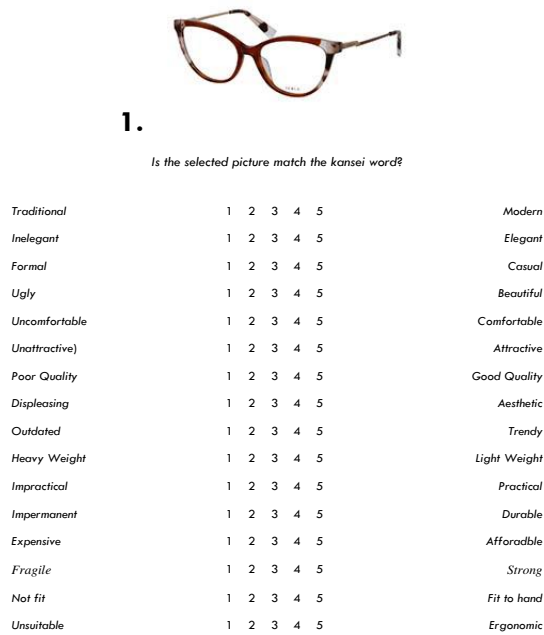


Figure 2. Kansei word questionnaire

3.2. Eyeglasses properties

The interviewees were asked to identify the eyeglasses properties/specs then to matched them with each eyeglasses image. Eyeglasses specs and sample properties are stated in Figure3 and Table 4.

1. Frame Shape	a. Pilot	b. Cat Eye	c. Round	d. Oval	e. Rectangle	f. Square
2. Material	a. Titanium	b. Plastic	c. Metal	d. Stainless		
3. Frame Type	a. Full Frame	b. Half Frame	c. Rimless			
4. Overall Color	a. Dark Color	b. Medium Color	c. Bright Color			
5. Surface	a. Plain	b. Gradient				

Figure 3. Eyeglasses properties

3.3. Decision tree

A random tree algorithm with ten cross-validations was employed in a decision tree to form a classification model in a tree shape that can be translated into a combination of eyeglasses design attributes satisfying the affective needs of teen girls in Jakarta. Random Tree was selected. Sixteen trees illustrated the set combination of eyeglasses design elements and attributes affecting teen girls' emotion significantly. The best rules are: Strongly Agree (SA) and Agree (A) due to Class: Emotion. Each tree figure contains 13 to 21 leaf nodes meaning there are 13 to 21 rules formed for each Kansei word or emotion from the root node to the bottom. For example, in Figure 4, regarding the round as frame shape, titanium as material combines with the color of bright affects teen girl's emotion aesthetic significantly.

3.4. Association rules

As stated in the theoretical background, decision tree classification is a predictive class-by-class approach, while association rules mining is a descriptive approach; it can

predict any attributes that were not formed in the decision tree. By combining those 2, we were able to put together as many rules as possible, and it can be used as a knowledge-based or like a dictionary in eyeglasses product design. Rules by decision tree classifier and association rules are listed in Table 5 and Table 6. In Table 5, one of the best rules that significantly affect teen girls' emotion of Beautiful is a pair of round-shaped eyeglasses, made of titanium, full-frame with bright colors.

While with association rules in Table 6, every rule can be measured its worth based on confidence and support degree. The best ones are the ones with the highest support degree. For instance, in Table 6, the best results from the association rules can be identified depending on the selected emotion such as a pair of eyeglasses made from titanium and plain patterned is the most related design for the emotion of attractive with the highest support degree of 0.140

4. Conclusions

Fifty final rules from the decision tree classifier and thirty-five rules from association rules mining were organized as knowledge-based to find the relationship among eyeglasses design elements, attributes, and emotions girls felt upon seeing them. This study investigated each rule from a different point of view, not from the tree or measuring the support degree, but by establishing how many Kansei words the rules satisfied. Since the grounds were to determine the best eyeglasses design with the KE approach focusing on consumer-centered way, and based on their most important Kansei words, the best design can satisfy all the basic emotions or affective needs, not just one emotion or two but more emotions and passions.

The best attributes for frame shape are round and oval. The best attributes for material are Plastic, titanium, and Metal. The best attribute for overall color is bright, and the surface is patterned. When we combine those best attributes, one possibility of the combination was already applied in Eyeglasses Sample Number 5. It is a pair of eyeglasses shaped round, full-frame, titanium, light-colored, and plain patterned on the surface. This design is suggested for eyewear companies and designers to be propagated in production (Figure 5).

This research proposes the usage of classification and association rules, which are the most common data mining methods to extract rules and predict the most appealing model. However, still, some further works are suggested (1) Other data mining methods, such as Clustering can be applied, (2) Using another Machine Learning besides WEKA for a more extensive dataset (3) and adding more sample pictures in the future study.



Figure 5. Most appealing design

5. Acknowledgement

The research was supported by Atma Jaya Catholic University of Indonesia Research Grant 2020

Table 4. Product properties of eyeglasses samples

Eyeglasses Sample	Frame Shape						Material			
	Pilot	Cat Eye	Round	Oval	Rectangle	Square	Stainless	Titanium	Plastic	Metal
Sample1		v							v	
Sample2				v					v	
Sample3					v					v
Sample4					v				v	
Sample5			v					v		
Sample6			v					v		
Sample7	v							v		
Sample8			v				v			
Sample9				v						v
Sample10			v						v	

Eyeglasses Sample	Frame Type			Color			Surfaces	
	Full Frame	Half Frame	Rimless	Dark	Medium	Bright	Plain	Gradient
Sample1	v				v			v
Sample2	v				v			v
Sample3	v					v	v	
Sample4	v			v			v	
Sample5	v					v	v	
Sample6	v			v			v	
Sample7	v					v	v	
Sample8	v				v			v
Sample9	v			v			v	
Sample10	v			v				v

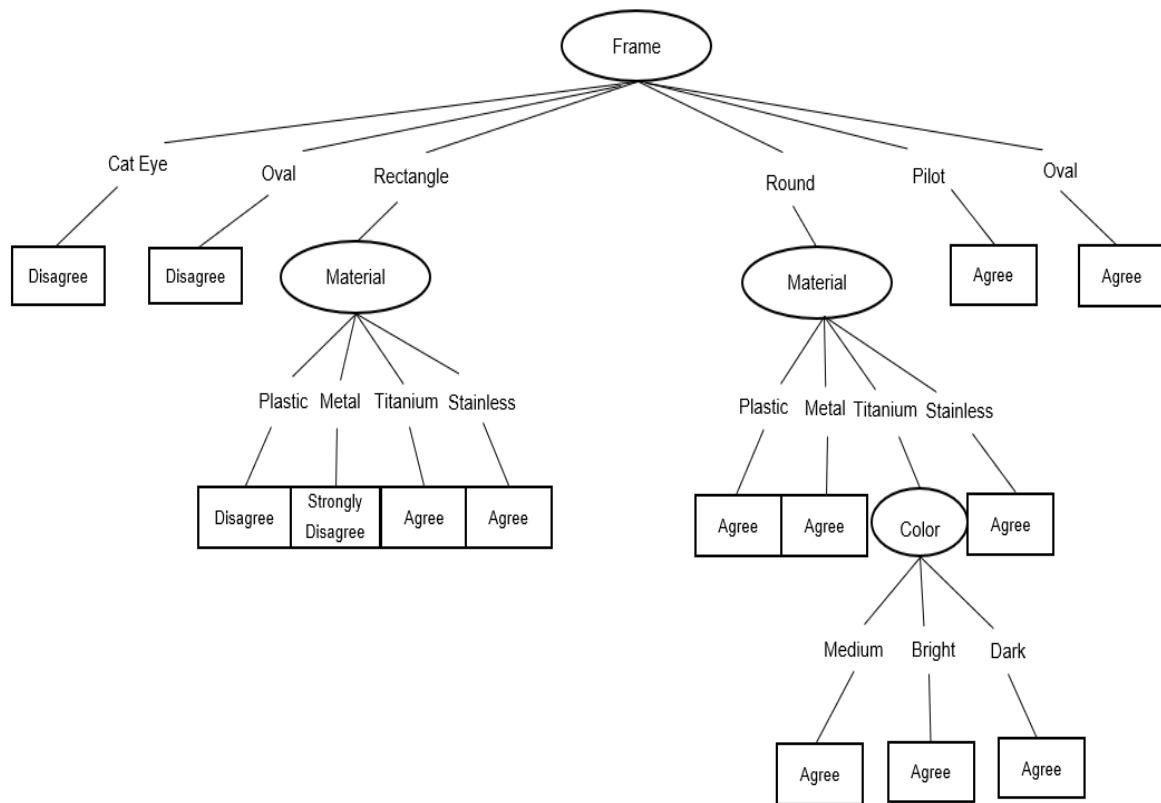


Figure 4. Decision tree for the emotion of 'Aesthetic'

Table 5. Decision tree rules

No	Rules	Result	Kansei Words
1	CatEye - Plastic - Full Frame	Agree	Beautiful, Comfortable, Durable, Ergonomic, Fit to Hand, Good Quality, Light Weight, Practical, Strong
2	Oval - Plastic - Full Frame	Strongly Agree	Attractive, Comfortable
3	Oval - Plastic - Full Frame	Agree	Attractive, Beautiful, Comfortable, Durable, Elegant, Ergonomic, Fit to Hand, Good Quality, Light Weight, Practical, Strong, Trendy
4	Rectangle - Plastic - Full Frame	Agree	Durable, Comfortable, Ergonomic, Fit to Hand, Light Weight, Practical, Strong
5	Round - Plastic - Full Frame	Agree	Aesthetic, Affordable, Attractive, Casual, Comfortable, Durable, Elegant, Ergonomic, Fit to Hand, Good Quality, Modern, Practical, Strong, Trendy
6	Pilot - Plastic - Full Frame	Strongly Agree	Attractive, Comfortable
7	Pilot - Plastic - Full Frame	Agree	Beautiful, Durable, Elegant, Ergonomic, Good Quality, Light Weight, Practical, Trendy
8	CatEye - Metal - Full Frame	Strongly Agree	Attractive, Comfortable
9	CatEye - Metal - Full Frame	Agree	Beautiful, Durable, Elegant, Ergonomic, Good Quality, Light Weight, Practical, Trendy
10	Oval - Metal - Full Frame	Strongly Agree	Attractive, Comfortable, Light Weight
11	Oval - Metal - Full Frame	Agree	Attractive, Beautiful, Comfortable, Durable, Elegant, Ergonomic, Fit to Hand, Good Quality, Light Weight, Practical, Trendy
12	Rectangle - Metal - Full Frame	Agree	Durable, Fit to Hand, Good Quality, Practical
13	Round - Metal - Full Frame	Strongly Agree	Affordable, Attractive, Comfortable
14	Round - Metal - Full Frame	Agree	Aesthetic, Beautiful, Durable, Elegant, Ergonomic, Good Quality, Light Weight, Modern, Practical, Trendy
15	Pilot - Metal - Full Frame	Strongly Agree	Attractive, Comfortable
16	Pilot - Metal - Full Frame	Agree	Beautiful, Durable, Elegant, Ergonomic, Good Quality, Light Weight, Practical, Trendy
17	Titanium - Full Frame - Medium Color	Strongly Agree	Comfortable
18	Titanium - Full Frame - Medium Color	Agree	Durable, Ergonomic, Good Quality, Practical
19	Titanium - Full Frame - Dark Color	Agree	Comfortable, Ergonomic, Fit to Hand, Good Quality, Practical, Strong
20	CatEye - Titanium - Full Frame - Bright Color	Strongly Agree	Comfortable
21	CatEye - Titanium - Full Frame - Bright Color	Agree	Durable, Ergonomic, Good Quality, Practical
22	Oval - Titanium - Full Frame - Bright Color	Strongly Agree	Comfortable
23	Oval - Titanium - Full Frame - Bright Color	Agree	Durable, Ergonomic, Good Quality, Practical
24	Rectangle - Titanium - Full Frame - Bright Color	Strongly Agree	Comfortable
25	Rectangle - Titanium - Full Frame - Bright Color	Agree	Aesthetic, Durable, Ergonomic, Good Quality, Practical

26	Round - Titanium - Full Frame - Bright Color	Strongly Agree	Modern
27	Round - Titanium - Full Frame - Bright Color	Agree	Affordable, Attractive, Beautiful, Casual, Comfortable, Elegant, Ergonomic, Fit to Hand, Good Quality, Light Weight, Practical, Trendy
28	Pilot - Titanium - Full Frame - Bright Color	Agree	Durable, Ergonomic, Fit to Hand, Good Quality, Practical
29	Stainless - Full Frame	Agree	Attractive, Beautiful, Comfortable, Durable, Ergonomic, Fit to Hand, Good Quality, Practical, Strong, Trendy
30	Cat Eye - Titanium - Full Frame	Strongly Agree	Attractive
31	Cat Eye - Titanium - Full Frame	Agree	Beautiful, Elegant, Light Weight, Trendy
32	Oval - Titanium - Full Frame	Strongly Agree	Attractive
33	Oval - Titanium - Full Frame	Agree	Beautiful, Elegant, Light Weight, Trendy
34	Rectangle - Titanium - Full Frame	Strongly Agree	Attractive
35	Rectangle - Titanium - Full Frame	Agree	Aesthetic, Beautiful, Elegant, Light Weight, Trendy
36	Pilot - Titanium - Full Frame	Strongly Agree	Beautiful, Elegant
37	Pilot - Titanium - Full Frame	Agree	Attractive, Light Weight, Trendy
38	Round - Titanium - Full Frame - Medium Color	Strongly Agree	Affordable, Attractive
39	Round - Titanium - Full Frame - Medium Color	Agree	Aesthetic, Beautiful, Elegant, Light Weight, Modern, Trendy
40	Round - Titanium - Full Frame - Dark Color	Strongly Agree	Modern, Trendy
41	Round - Titanium - Full Frame - Dark Color	Agree	Aesthetic, Affordable, Attractive, Beautiful, Casual, Elegant, Light Weight
42	Rectangle - Stainless - Full Frame	Agree	Aesthetic
43	Round - Stainless - Full Frame	Agree	Aesthetic, Modern
44	Pilot - Full Frame	Strongly Agree	Modern
45	Pilot - Full Frame	Agree	Aesthetic, Affordable, Casual
46	Oval - Full Frame	Agree	Aesthetic, Affordable, Casual, Modern
47	Cat Eye - Full Frame	Agree	Affordable, Casual
48	Rectangle - Full Frame - Medium Color	Strongly Agree	Affordable
49	Rectangle - Full Frame - Medium Color	Agree	Modern
50	Rectangle - Full Frame - Dark Color	Agree	Affordable

Table 6. Association rules

No	Rules	Support	Confidence	Kansei Word
1	Material =Titanium Aesthetic =Agree 134 ==> Surfaces =Plain 134	0,134	1	Aesthetic
2	Color =Bright Aesthetic =Agree 115 ==> Surfaces =Plain 115	0,115	1	Aesthetic
3	Material =Titanium Aesthetic =StronglyAgree 110 ==> Surfaces =Plain 110	0,11	1	Aesthetic
4	Color =Medium Affordable =Agree 100 ==> Surfaces =Gradient 100	0,1	1	Affordable
5	Material =Titanium Attractive =Agree 140 ==> Surfaces =Plain 140	0,14	1	Attractive
6	Color =Bright Attractive =Agree 106 ==> Surfaces =Plain 106	0,106	1	Attractive
7	Frame =Round Surfaces =Plain Attractive =Agree 102 ==> Material =Titanium 102	0,102	1	Attractive
8	Frame =Round Material =Titanium Attractive =Agree 102 ==> Surfaces =Plain 102	0,102	1	Attractive
9	Material =Titanium Beautiful=Agree 125 ==> Surfaces =Plain 125	0,125	1	Beautiful
10	Material =Titanium Beautiful=StronglyAgree 104 ==> Surfaces =Plain 104	0,104	1	Beautiful
11	Color =Medium Casual =Agree 103 ==> Surfaces =Gradient 103	0,103	1	Casual
12	Material =Titanium Casual =Agree 101 ==> Surfaces =Plain 101	0,101	1	Casual
13	Material =Titanium Comfortable =Agree 139 ==> Surfaces =Plain 139	0,139	1	Comfortable
14	Color =Medium Comfortable =Agree 115 ==> Surfaces =Gradient 115	0,115	1	Comfortable
15	Frame =Round Surfaces =Plain Comfortable =Agree 107 ==> Material =Titanium 107	0,107	1	Comfortable
16	Frame =Round Material =Titanium Comfortable =Agree 107 ==> Surfaces =Plain 107	0,107	1	Comfortable
17	Color =Medium Durable =Agree 119 ==> Surfaces =Gradient 119	0,119	1	Durable
18	Material =Titanium Elegant =Agree 122 ==> Surfaces =Plain 122	0,122	1	Elegant
19	Material =Titanium Elegant =StronglyAgree 111 ==> Surfaces =Plain 111	0,111	1	Elegant
20	Color =Bright Elegant =Agree 102 ==> Surfaces =Plain 102	0,102	1	Elegant
21	Color =Medium Elegant =Disagree 101 ==> Surfaces =Gradient 101	0,101	1	Elegant
22	Material =Titanium Ergonomic=Agree 118 ==> Surfaces =Plain 118	0,118	1	Ergonomic
23	Color =Medium Ergonomic=Agree 115 ==> Surfaces =Gradient 115	0,115	1	Ergonomic
24	Color =Medium Fit to Hand=Agree 114 ==> Surfaces =Gradient 114	0,114	1	Fit to Hand
25	Material =Titanium Fit to Hand=Agree 104 ==> Surfaces =Plain 104	0,104	1	Fit to Hand
26	Color =Bright Good Quality =Agree 139 ==> Surfaces =Plain 139	0,139	1	Good Quality
27	Material =Titanium Good Quality =Agree 138 ==> Surfaces =Plain 138	0,138	1	Good Quality
28	Color =Medium Good Quality =Agree 119 ==> Surfaces =Gradient 119	0,119	1	Good Quality
29	Material =Titanium Light Weight =Agree 108 ==> Surfaces =Plain 108	0,108	1	Light Weight
30	Material =Titanium Modern =StronglyAgree 124 ==> Surfaces =Plain 124	0,124	1	Modern
31	Material =Titanium Pratical =Agree 139 ==> Surfaces =Plain 139	0,139	1	Practical
32	Color =Bright Pratical =Agree 122 ==> Surfaces =Plain 122	0,122	1	Practical
33	Color =Medium Pratical =Agree 116 ==> Surfaces =Gradient 116	0,116	1	Practical
34	Color =Medium Strong=Agree 114 ==> Surfaces =Gradient 114	0,114	1	Strong
35	Material =Titanium Trendy =StronglyAgree 136 ==> Surfaces =Plain 136	0,136	1	Trendy

References

- [1] Foster PA, Jiang Y. Epidemiology of myopia. *Eye*. 2014, 28(2):202-8.
- [2] Dolgin E. The myopia boom. *Nature News*. 2015, 519(7543):276.
- [3] Holden BA, Fricke TR, Wilson DA, Jong M, Naidoo KS, Sankaridurg P, Wong TY, Naduvilath TJ, Resnikoff S. Global prevalence of myopia and high myopia and temporal trends from 2000 through 2050. *Ophthalmology*. 2016, 123(5):1036-42.
- [4] Morgan IG, He M, Saw SM, Krueger RR, Lam DS. Myopia: From research to practice. *The Asia-Pacific Journal of Ophthalmology*. 2016, 5(6):383-5.
- [5] Pan CW, Dirani M, Cheng CY, Wong TY, Saw SM. The age-specific prevalence of myopia in Asia: a meta-analysis. *Optometry and vision science*. 2015, 92(3):258-66.
- [6] Saw SM, Gazzard G, Koh D, Farook M, Widjaja D, Lee J, Tan DT. Prevalence rates of refractive errors in Sumatra, Indonesia. *Investigative ophthalmology & visual science*. 2002, 43(10):3174-80.

- [7] Lu B, Congdon N, Liu X, Choi K, Lam DS, Zhang M, Zheng M, Zhou Z, Li L, Liu X, Sharma A. Associations between near work, outdoor activity, and myopia among adolescent students in rural China: the Xichang Pediatric Refractive Error Study report no. 2. *Archives of ophthalmology*. 2009, 127(6):769-75.
- [8] Czepita M, Czepita D, Safranow K. Role of gender in the prevalence of myopia among polish schoolchildren. *Journal of ophthalmology*. 2019, 2019.
- [9] Kibria M, Rafiquzzaman M. Ergonomic computer workstation design for university teachers in Bangladesh. *Jordan Journal of Mechanical & Industrial Engineering*. 2019,13(2):91-103.
- [10] Daws KM, Ahmed ZA, Moosa AA. An Intelligent Quality Function Deployment (IQFD) for manufacturing process environment. *Jordan Journal of Mechanical & Industrial Engineering*. 2009, 3(1):23-30.
- [11] Nagamachi M, Lokman AM. *Kansei innovation: Practical design applications for product and service development*. CRC Press, 2015.
- [12] Nagamachi M, Lokman AM. *Innovations of Kansei engineering*. CRC Press, 2016.
- [13] Zabotto CN, Amaral DC, Hornos CJ, Benze BG. Automatic digital mood boards to connect users and designers with kansei engineering. *International Journal of Industrial Ergonomics*. 2019, 74:102829.
- [14] Kim W, Ko T, Rhiu I, Yun MH. Mining affective experience for a kansei design study on a recliner. *Applied ergonomics*. 2019, 74:145-53.
- [15] Kikumoto M, Kurita Y, Ishihara S. Kansei Engineering Study on Car Seat Lever Position. *International Journal of Industrial Ergonomics*. 2021, 86:103215.
- [16] Llinares C, Page AF. Kano's model in Kansei Engineering to evaluate subjective real estate consumer preferences. *International Journal of Industrial Ergonomics*. 2011, 41(3):233-46.
- [17] Sukwadi R, Sanjaya HP. Incorporating Kansei Engineering into service quality tools to improve the airline services. *International Journal for Quality Research*. 2018, 12(2):297.
- [18] Pitaktiratham J, Sinlan T, Anuntavoranich P, Sinthupinyo S. Application of Kansei engineering and association rules mining in product design. *International Journal of Economics and Management Engineering*. 2012, 6(9):2352-7.
- [19] Berry MJ, Linoff GS. *Data mining techniques: for marketing, sales, and customer relationship management*. John Wiley & Sons, 2004.
- [20] Hand DJ, Mannila H, Smyth P. *Principles of Data Mining*. MIT press, 2001.
- [21] Chou JR. A Kansei evaluation approach based on the technique of computing with words. *Advanced Engineering Informatics*. 2016, 30(1):1-5.
- [22] Guo F, Qu QX, Nagamachi M, Duffy VG. A proposal of the event-related potential method to effectively identify kansei words for assessing product design features in kansei engineering research. *International Journal of Industrial Ergonomics*. 2020, 76:102940.
- [23] Fayyad U, Piatetsky-Shapiro G, Smyth P. From data mining to knowledge discovery in databases. *AI Magazine*. 1996, 17(3): 37.
- [24] Guo F, Hu M, Duffy VG, Shao H, Ren Z. Kansei evaluation for group of users: A data-driven approach using dominance-based rough sets. *Advanced Engineering Informatics*. 2021, 47:101241.
- [25] Gorunescu F. *Data Mining: Concepts, models and techniques*. Springer Science & Business Media, 2011.
- [26] Chuan NK, Sivaji A, Shahimin MM, Saad N. Kansei engineering for e-commerce sunglasses selection in Malaysia. *Procedia-Social and Behavioral Sciences*. 2013. 97:707-14.
- [27] Agost MJ, Vergara M. Relationship between meanings, emotions, product preferences and personal values. Application to ceramic tile floorings. *Applied Ergonomics*. 2014, 45(4):1076-86.

Advanced Multi Criteria Optimal Design of Spiral Bevel Gear Pair using NSGA – II

N. Godwin Raja Ebenezer ^{a,*}, S. Ramabalan ^b, S. Navaneethasanthakumar ^c

^aDepartment of Mechanical Engineering, Loyola - ICAM College of Engineering and Technology, Chennai, 600 034, Tamil nadu, India

^bDepartment of Mechanical Engineering, EGS Pillay Engineering College, Nagapattinam-611 002, Tamil nadu, India

^cDepartment of Mechanical Engineering, Christian College of Engineering and Technology, Oddanchatram, Tamil nadu, 624619, India

Received 29 MARCH 2021

Accepted 19 JAN 2022

Abstract

In gear applications, quality of design significantly influences transmission, machine performance, size and weight of the gears. In the present work, a nonlinear optimization problem having three objective functions, five design variables and eleven constraints considering a spiral bevel gear pair is solved. The aim of this research is to optimize weight, pitch cone distance, and efficiency by formulating three cases. In Case 1, the objective functions, namely, weight and pitch cone distance are minimized, while treating efficiency as constraint. In Case 2, the objective functions weight is minimized and efficiency is maximized, keeping pitch cone distance as constraint. In Case 3, the objective functions pitch cone distance is minimized and efficiency is maximized, having weight as constraint. Pareto frontiers are generated by Non-dominated Sorting Genetic Algorithm (NSGA-II). Simulation is analysed and validated with literature. Results show that there is a considerable rise in weight, module, and efficiency and a decrease in cone distance than literature. Results also indicate that Case 2 formulation offers the best optimal design parameters.

© 2022 Jordan Journal of Mechanical and Industrial Engineering. All rights reserved

Keywords: Spiral Bevel Gear Drive; Design Optimization; Critical constraints; NSGA-II.

1. Introduction

Bevel gear drive is applied wherever change of directions is desirable in transmission. Spiral bevel gears are one of the basic mechanical units to transmit motion between concurrent axes. As they offer great concurrence and even transmission, they are extensively used in the aerospace, automotive and large mechanical transmission systems[1]. They yield smoother operation, less noise and vibration, since they have big overlapping tooth action. They also can carry more loads, as they possess evenly distributed tooth loads. A spiral bevel gear pair is shown in Figure 1.

Design optimization of gear transmission systems has been a puzzling problem to researchers for several years because of the following reasons: a) The practical gear design is characterized by many design parameters, much calculation time, and error susceptibility. b) It requires repetitive calculation, interrogation and drawings for gear design which leads to additional effort. Nevertheless, the use of latest computers through intelligent techniques, aid us to solve gear optimisation problems handily[2].

Optimization problems in gear design involve multiple objective functions. As multi criteria optimization offers pareto-optimal solutions set to the choice of a decision maker, it is suitable for gear research [3]. In such optimization, weights are also allowed to make a trade-off between criteria. It is highly important to identify a set of Pareto optimal solutions which satisfy all the objectives as better as possible.



Figure 1 A spiral bevel gear pair

The current advances in the research on design optimization of bevel gears is as follows:

Emmanuel Mermoz, et. al [4] optimized a spiral bevel gear using Finite Element Method (FEM), replacing sensitivity analysis. They used optimization algorithms to automatically compute the tooth contact flank surfaces. Tetsu Nagata, et.al [5] designed tooth contact analysis and tooth flank form measurement technique to calculate meshing condition by considering large spiral bevel gears. Faydor et. al[6] improved bearing contact to achieve a pre-designed parabolic function, so as to reduce magnitude of transmission errors. Liang and Xin [7] specified spiral gear mesh through dynamic simulation approach. They

* Corresponding author e-mail: gjeraja@gmail.com.

calculated angular speed, torque and meshing force on the curves of spiral bevel gears. Chung –Yunn et.al [8] performed dynamic simulation of the spiral bevel gears with specified mesh. They got the curves of angular speed, torque and meshing force on the spiral bevel gears through simulation in order to reveal dynamic characteristics of gear driving device. Chandrasekaran et al. [9] presented a brief review and analysis of latest advancements in bevel gears optimization research. Chandrasekaran et al [10] optimized a design of spiral bevel gear pair considering efficiency, weight and cone distance subject to mechanical constraints using NSGA-II.

Bevel gear optimisation through non-linear formulations, metaheuristics and other algorithms are as follows:

Arunachalam, et al [11] maximised power, efficiency and minimized overall weight and centre distance taking into account a combined objective function. They used LINGO and Real Coded Genetic Algorithm (RCGA), Ant Colony Optimisation (ACO) and Particle Swarm Optimisation (PSO) algorithms for solving the problem. Zhang, et al [12] used optimization design software Visual Basic (VB) for straight bevel gear design based on MATLAB, and Genetic Algorithm (GA). They used augmented penalty function and integer serial number encoding to obtain global optimal solution. Rai et al [13], minimized the volume of straight bevel gear considering scoring failure in straight bevel gear by advanced particle swarm optimization and RCGA. Li Tiejung [14] solved a variable helix angle bevel gear problem through a mathematical model based on GAs. They compared the same with traditional optimization methods of literature, and showed that Gas are reasonable to solve gear application problems with many constraints and variants. Padmanabhan. et.al. [15] formulated a combined objective function to optimize bevel gear pair design based on RCGA and LINGO. Ebenezer et al [16] proposed nature inspired algorithms, namely, Simulated Annealing (SA), Fire fly Algorithm (FA) and Cuckoo Search (CS) to optimize volume of a straight bevel gear. Zolfagari et al. [17] optimized volume of straight bevel gear based on the American Gear Manufacturers Association (AGMA) stipulations using SA and GA.

Bevel gear optimisation taking into account power losses are as follows:

Graham Johnson et al [18]. optimized design of shrouded meshing gears pair that run at representative speeds and oil flow in a rig with speed and torque measurement. They quantified three main windage power loss contributors, namely, air alone, recirculation of oil under the shroud and acceleration of the feed oil. Oil and bearing churning losses, seal and windage losses are hooked on the speed of the gear pair. Bearing sliding friction and rolling friction losses are reliant on the load on the gear pair. To measure air losses (windage losses) researchers in the past conducted experiments on test rigs. Diab et. al [19] conducted a set of experiments in a test rig and obtained an empirical equation for determining windage power loss. They considered dimensional and fluid flow analysis.

The cited literature reveals a clear gap as follows:

1. Certain essential constraints, namely, contact ratio, line of action, load carrying capacity and power loss due to meshing loss in bearings and seals were not considered. Contact ratio is the main factor in the load carrying capacity and dynamic performance of the gears. Greater contact ratio lowers the vibration and noise of

the transmission system. But in this research, all these are considered.

2. The researchers dealt with only two design variables, namely, number of teeth of pinion and module of the gear. In this paper, three more additional design variables viz. shaft diameter, power and face width are included.
3. Some researchers considered only combined objective functions. In such cases, the decision maker does not know how to choose the weighing factors, when functions of optimization problem are not familiar to him [20]. In this research, multiple objectives are formulated as three cases, and in each case, two objectives are taken for optimization with the third one as a constraint along with additional constraints, which does not demand weighting factors.
4. Only heuristic algorithms or conventional techniques were generally used by the researchers in the literature. As these algorithms partition the whole problem into sub problems, they are appropriate only for solving single criteria gear design problems. As multi-criteria problems are computationally intensive, it is fair to use multi-objective optimization algorithms, such as NSGA-II, which gives greater performance and does not require any weight functions.

Taking cognizance of the above observation, to bridge the gap besides normal constraints, certain other additional critical constraints and design variables are also considered. This work is based on Chandrasekhar et al. [10] and Arunachalam, et al [11], but in this work, three more design variables, six other additional constraints are incorporated for optimization in three separate cases to augment performance, design and power transmission.

2. Design optimization formulation of the Spiral bevel gear problem

In this research, a spiral bevel gear pair is considered. The design data for the problem are given in Table 1.

2.1. Design example

A spiral bevel gear pair presented in [10] is considered. Certain additional design variables and critical constraints are also taken into account.

2.1.1. Objective Functions

The aim is to optimize objective functions, namely, weight, pitch cone distance and efficiency of the spiral bevel gear pair. To decide optimum solutions, three cases based on the problem's objectives are formulated separately and optimized along with additional constraints.

In Case 1, the objective functions weight and pitch cone distance are minimized, with efficiency as constraint, in Case 2, the objective functions weight is minimized and efficiency is maximized, keeping pitch cone distance as constraint and in Case 3, the objective functions pitch cone distance is minimized and efficiency is maximized, having weight as constraint. The limiting values of the objective functions, which are treated as constraint in each case are selected from literature [10].

Table 1 Design data for the bevel gear drive optimization

Parameters	Value	Parameters	Value
Transferred power, (P)	37.285kW	Working temperature (deg C)	50
Material for pinion and gear	Steel 20 Mn 5 Cr 5 IS: :4432-1988	Pinion / gear tooth shape	Properly crowned
gear ratio, i_{tot}	4.778	Gear teeth form	Full depth, conifex
Input pinion speed, n (rpm)	500	Reliability	0.99
Coefficient of friction, f	0.08	Load on driven machine	Medium shock
Pressure angle, ϕ (deg)	20	Shafts material	SAE 1060
Young's Modulus, E	$2.15 \times 10^5 \text{ N/mm}^2$	Pinion/gear tooth hardness (HB)	350
Ratio between cone distance and face width ψ_y	$0.357Z_1$	Life (no of cycles)	10^8
Ratio between average module and face width ψ_m	8	Safety factor –shaft design, S_{FS}	1.5
Density of the material	$7.86 \times 10^{-6} \text{ kg/mm}^2$	Safety factor for bending, S_F	1.2
Design bending stress, $[\sigma_b]$	430 N/mm^2	Safety factor for pitting, S_H	1.2
Design crushing stress, $[\sigma_c]$	1100 N/mm^2		

The objective functions equations (1), (2) and (3), are adopted from [10] as follows:

Total weight of the spiral bevel gear pair

$$f_1 = W = W_1 + W_2, \tag{1}$$

where weight of the pinion,

$$W_1 = 42.438 \rho m_t^3 z_1 \tag{2}$$

and weight of gear,

$$W_2 = 68.52 \rho m_t^3 z_2 \tag{3}$$

Efficiency of the gear,

$$f_2 = \eta = 100 - P_L \tag{4}$$

where

$$P_L \text{ is Power loss} = 50f \left\{ \frac{\cos\theta + \cos\gamma}{\cos\phi_n} \right\} \cos^2\beta \frac{(H_s^2 + H_t^2)}{(H_s + H_t)} \tag{5}$$

and

$$H_s = (i + 1) \left\{ \left[\sqrt{\left(\frac{R_0}{R}\right)^2 - \cos^2\phi_n} \right] - \sin\phi_n \right\} \tag{6}$$

$$H_t = \left(\frac{i+1}{1}\right) \left\{ \left[\sqrt{\left(\frac{r_0}{r}\right)^2 - \cos^2\phi_n} \right] - \sin\phi_n \right\} \tag{7}$$

where $R_0 = R + \text{one addendum}$. One addendum for 20° full depth involute system = One average Module = m_{av} ,

where $m_{av} = m_t \left(\frac{\psi_y - 0.5}{\psi_y} \right)$, $r_0 = r + m_{av}$; $R_0 = R + m_{av}$; $r = d_1/2$; $R = d_1/2$, $d_1 = m_t z_1$ and $d_2 = m_t z_2$, d_1 , d_2 are pitch diameter of the large end of the bevel pinion and gear in mm, W_1 , W_2 are weight of the pinion and gear.

3. Pitch cone distance of the gear pair,

$$f_3 = R_c = 0.5m_t z_1 \sqrt{i^2 + 1} \tag{8}$$

2.2. Design variables

The design variable function of the bevel gear pair is formulated as follows:

$$F(x) = F(m, z_1, b, d_s, P) = F(x_1, x_2, x_3, x_4, x_5) \tag{9}$$

where m is module, z_1 is number of teeth on pinion, b is face width and d_s is diameter of the shaft and P is input power.

Upper and lower design bound are continuous variables as follows:

$$5 \leq m \leq 10, 5 \leq z_1 \leq 12; 20 \leq b \leq 60, 15 \leq d_s \leq 40 \text{ and}$$

$P = 29.828 \text{ kW}, 37.285 \text{ kW}$ and 52.199 kW . Here the design variable power is considered as a discrete variable.

2.3. Constraints

Crucial mechanical constraints along with certain added critical constraints are considered.

2.3.1. Bending stress of the gears

As per design requirements, bending strength and contact stress must be lower than allowable bending stress and contact stress. The equations (10 - 13) are reported in [10].

$$\left[\frac{0.7R\sqrt{(i^2+1)}[M_t]}{(R-0.5b)^2 b m_n Y_p} \right] \leq [\sigma_b] \tag{10}$$

where,

R is cone distance (mm) and $[M_t]$ is design twisting torque (Nmm),

$[\sigma_b]$ is allowable bending stress number (N/mm²), b is face width of gear (mm), m_n is normal module (mm), and Y_p is form factor of gear.

2.3.2. Crushing stress of the gears

The contact stress constraint is devised as:

$$\frac{0.72}{(R-0.5b)} \sqrt{\frac{(i^2+1)^3}{ib}} E [M_t] \leq [\sigma_c] \tag{11}$$

where i is gear ratio, E is Young's Module (N/mm²), $[\sigma_c]$ is allowable contact stress number (N/mm²), $[M_t]$ is design twisting torque (Nmm), and b is face width (mm).

2.3.3. Pitch cone distance

This constraint is developed as:

$$\frac{41.4885}{(0.357Z_1 - 0.5)^3} \leq R \tag{12}$$

where Z_1 is number of gear teeth and R is cone distance (mm).

2.3.4. Average module

This constraint is established as:

$$1.15 \cos \beta_{av} \sqrt[3]{\frac{[M_t]}{y_v [\sigma_b] \psi_m Z_1}} \leq m_{av} \quad (13)$$

m_{av} is average module (mm), β_{av} , ψ_y are mean spiral angles, y_v is form factor.

2.3.5. Shaft diameter

The equations (14 - 20) are stated in [16].

The shaft diameter constraint is as follows:

$$\left[\frac{32 S_{FS}}{\pi} \sqrt{\left(\frac{T}{S_y}\right)^2 + \left(\frac{M}{S_e}\right)^2} \right]^{\frac{1}{3}} - d_s \leq 0 \quad (14)$$

where S_y, S_e are yield strength and endurance limit of the shaft material (N/mm²), T is torque transmitted by the shaft, (Nmm) and M is maximum bending moment on the shaft (Nmm), d_s is shaft diameter (mm) and S_{FS} is safety factor for pitting.

2.3.6. Gear face width

The constraint is laid in equation (15) as follows:

$$b \leq \{0.3R, 10m_t\} \quad (15)$$

where b is gear face width (mm), and m_t is transverse module of gears (mm).

2.3.7. Power loss in the gear

It is an important constraint, as efficiency depends on the power loss of the gear pair.

The range of power loss percentage should be between 1.2 and 2.2% of input power.

It is given by,

$$P_{loss} - 1.2 \% (P) \leq 0, \quad (16)$$

Where

$$P_{loss} = P \mu_{mz} H_v + \mu F v + 7.69 \times 10^{-6} d_s^2 n, \quad (17)$$

where P_{loss} is the loss of power (W), F is bearing load (N), v is peripheral speed (m/s), μ_{mz} is average coefficient of friction, H_v is gear power loss factor, μ is coefficient of friction in the bearing, n is rotational speed (rpm), d_s is shaft diameter (mm).

2.3.8. Contact Ratio (CR)

As spiral bevel gears have curved oblique teeth, they mesh with a rolling contact similar to helical gears. So, the action of a spiral gear is same as the helical gear. For such a model bevel gear pair, contact ratio should be between 1.4 and 2. It is given by,

$$1.4 \leq CR \leq 2 \quad (18)$$

where

$$CR = \frac{(\sqrt{(r_1+a)^2 - r_{b1}^2} + \sqrt{(r_2+a)^2 - r_{b2}^2} - (r_1+r_2) \sin \phi)}{\pi m \cos \phi} \quad (19)$$

where suffix 1 for pinion and 2 for gear, r_b is base circle radius (mm), a is addendum (mm), m is module of the gear (mm) and ϕ is transverse pressure angle.

2.3.9. No involute interference

If the pinion tooth makes contact with the gear tooth or the involute of the pinion comes in that range, this occurs.

To obtain no involute interference the following constraint is used.

$$\sqrt{(r_1+a)^2 - r_{b1}^2} - C \sin \phi \leq 0 \quad (20)$$

where C is centre distance between the gears and ϕ is transverse pressure angle of the gear.

2.3.10. Load carrying capacity

Load carrying capacity F_1 should be more than minimum load carrying capacity F_{min} of the gears reported in [23]. It is given by,

$$F_{min} - F_1 \leq 0 \quad (21)$$

where

$$F_1 = F_t + \frac{[21(Cb+F_t)]}{21v + \sqrt{(Cb+F_t)}} [25] \quad (22)$$

where F_t is transmitted load (N), C is deformation factor depending on machining error, ($C = 228 e Nmm$), e is expected error, ($e = 0.02$ mm), v is the velocity of the gear in /sec and $b =$ face width or base width of gear (mm).

2.3.11. Line of action

To achieve even and constant rotation, arc of action should be more than line of action [1]. Accordingly, this constraint is expressed.

$$\frac{2\pi}{\tan \phi} \leq Z_1 + Z_2 \quad (23)$$

where Z_1, Z_2 are number of teeth of pinion and gear.

3. Optimization Algorithms

3.1. Multi objective optimization algorithms

Engineering optimization problems can be of single-objective optimization (SOO) or multi-objective optimization (MOO). The SOO is a formulation of a combined function that characterises the overall effect. But the MOO is a construction of multi criteria, which are diverse and conflicting with wide-ranging solution methods. Multi criteria optimization problems along with modelling have been handled by Moneim [26], Benatallah et al [27], Kazem et al [28] in motion planning and wind systems.

3.1.1. NSGA-II

The NSGA-II algorithm is a modest and direct method as elaborated in [21]. It uses an elitist principle, so that only elites can be carried forward to the next generation. It also employs a clear diversity preserving mechanism known as crowding distance. In NSGA-II, the emphasis is on producing non-dominated solutions. It is possible to realise this by using crowded comparison criterion in the tournament selection as well as in the phase of population reduction. In this research, optimization is performed in MATLAB environment using code [22].

4. Results and discussion

Simulation by NSGA-II for (Case I, Case 2 and Case 3) respectively are presented in Table 2. Optimal design parameters by the algorithm of this work and the literature [10] are compared.

From Table 2, certain interesting observations are made. The weight of gear has significantly increased from 19.923 kg (for $z_1=10$) to 22.81 kg (Case 1). It is the same with module also, which has increased from 8.729 mm (for $z_1=10$) to 9.853mm (Case 2). But positively, there is a decrease in the value of Cone pitch diameter (186.904 mm) compared to 213.625 mm (for $z_1=10$) of the literature. In the same way, there is an

increase in efficiency from 97.546% (for $z_1=10$) to 98.406% (Case 2). The pinion teeth value has also slightly decreased from 10 (for $z_1=10$) to 9.192. A careful observation shows that Case 2 yields better optimal parameters than other cases. The best optimum design parameters (Case 2) are as follows: $m=9.853$ mm, $z_1=9.192$, $b=27.064$ mm, $d_s=23.84$ mm, and $W=26.319$ kg, $R_c=213.625$ mm, and $\eta=98.535$ % .

Table 2 Optimal values (Case 1, Case 2 and Case 3) by NSGA-II of the present research and literature [10]

Power 37.285kW						
Parameters	Presented paper			Literature [10]		Percentage change in values (between Case 2 and Literature for, $z_1=10$)
	Case 1	Case 2	Case 3			
Module (mm), m	9.846	9.853	9.356	8.719	8.241	-13.00
Pinion teeth, z_1	7.788	9.192	8.566	10	11	+0.88
Face width (mm) b	46.335	27.064	24.301	Not considered	Not considered	-
Diameter of the shaft (mm), d_s	35.952	26.783	30.753	Not considered	Not considered	-
Weight of gear (kg), W	22.181	26.319	19.923	19.923	18.411	-32.10
Cone pitch distance (mm), R_c	186.904	213.625	195.553	213.625	220.978	0.00
Efficiency of the gear (%), η	97.546	98.535	98.406	97.546	97.745	1.01

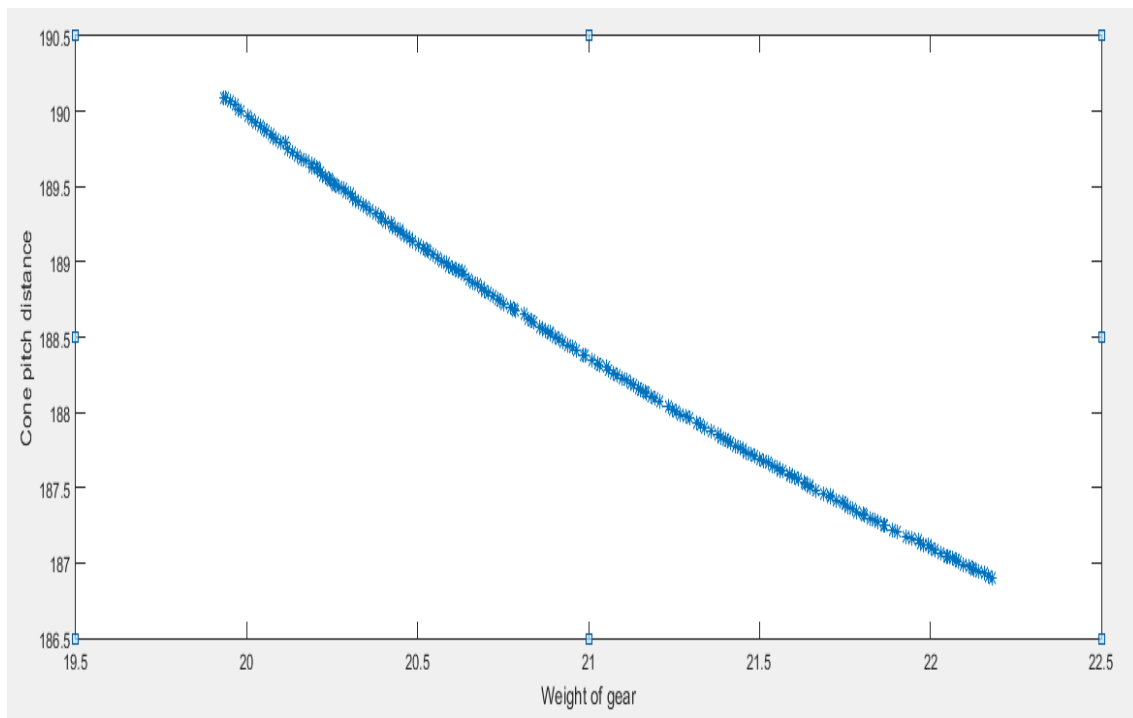


Figure 2. Optimized results (Weight of Gear and Cone distance) by NSGA-II (Case 1)

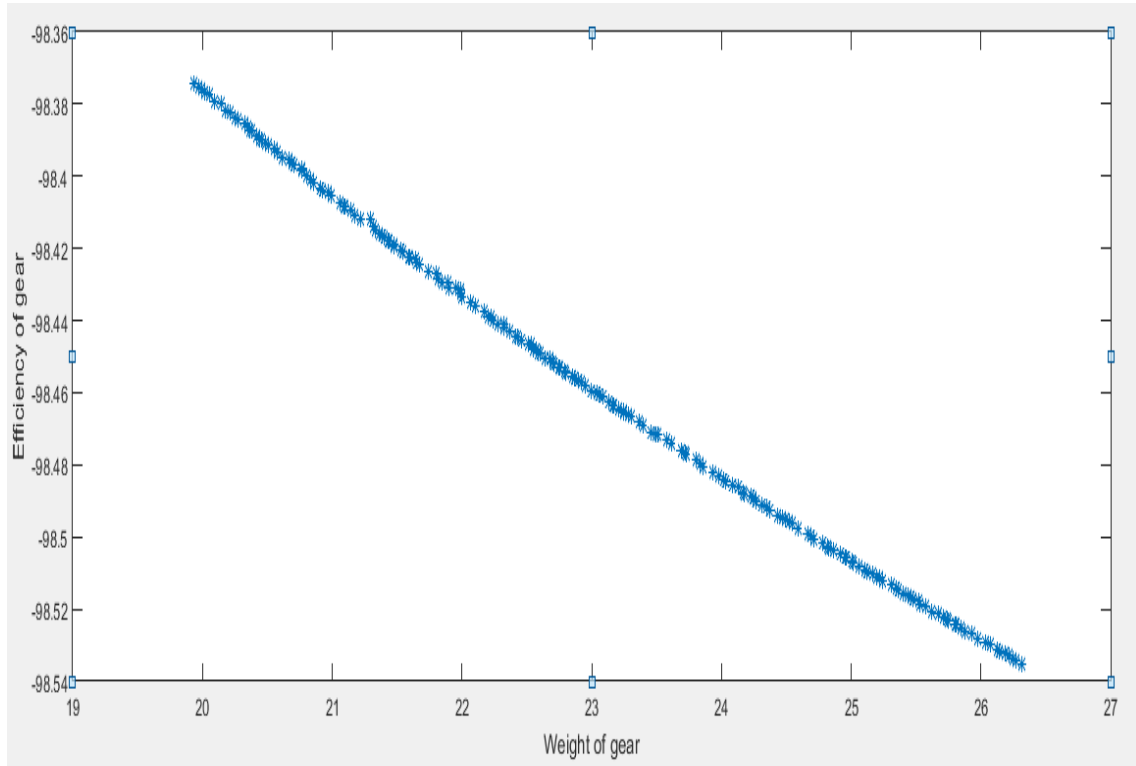


Figure 3. Optimized results (Weight of gear and Efficiency of gear) by NSGA-II (Case 2)

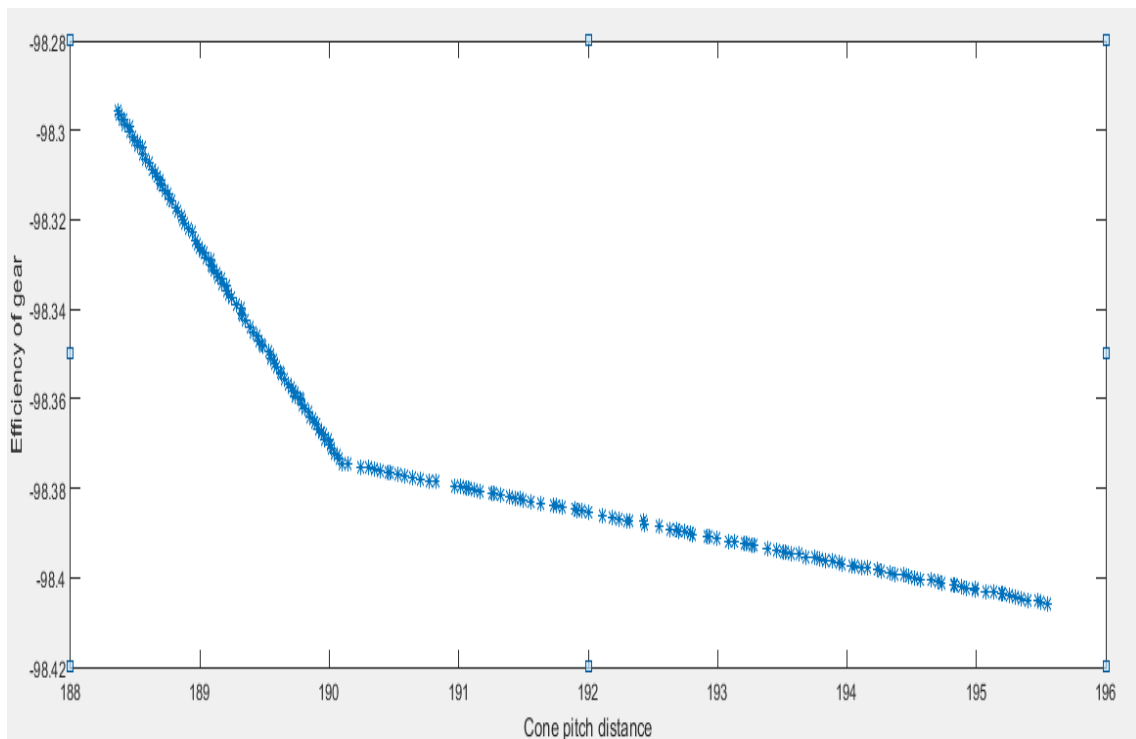


Figure 4. Optimized results (Cone pitch distance and Efficiency of gear) by NSGA-II (Case 3)

In Table 2, the third objective function that was kept as a constraint in each case is shown in bold values. It is also noted that, there is an increase of 32.10 % in weight with the additional constraints and design variables as compared to literature. But an increase in efficiency 1.01% is realised than literature results. As cone distance is made as a constraint in Case 2 (the limiting value of the same is the cone distance value of the literature), there is no percentage change. The plots of optimization

results are presented Figure 2, Figure 3, Figure 4 and comparison of the same are given in Figure 5.

From Table 3, and Figure 6, it is also noted that design variables, viz. shaft diameter and face width of the gears alone have responded with respect to the different power inputs. But surprisingly there is no such response seen in any of the other design variables irrespective of change in input power.

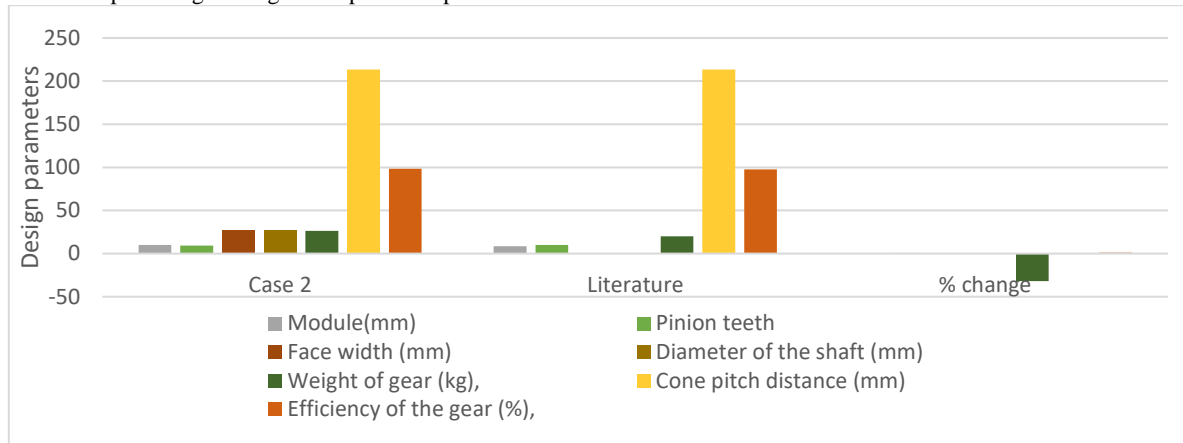


Figure 5. Comparison of results of this work (Case 2) and literature [10]

Table 3. Optimal values (Case 1, Case 2 and Case 3) by NSGA-II of the present research for various power inputs

Parameters	Power 29.828kW			Power 52.199kW		
	Case 1	Case 2	Case 3	Case 1	Case 2	Case 3
Module (mm), m	9.838	9.853	9.356	9.837	9.853	9.356
Pinion teeth, z_1	7.785	9.192	8.565	7.785	9.192	8.565
Face width (mm) b	36.594	33.625	42.398	48.283	33.737	50.174
Diameter of the shaft (mm), d_s	23.608	36.341	27.370	35.768	35.173	36.597
Weight of gear (kg), W	22.189	26.318	19.923	22.188	26.319	19.923
Cone pitch distance (mm), R_c	186.890	213.625	195.552	186.891	213.625	195.548
Efficiency of the gear (%), η	97.546	98.535	98.405	97.546	98.535	98.405

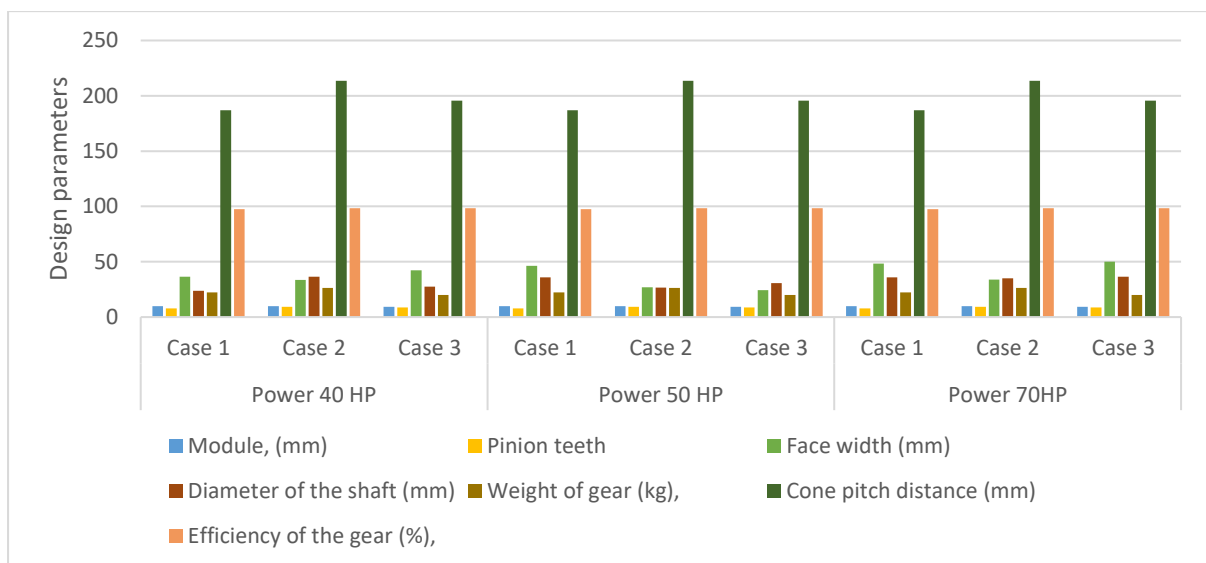


Figure 6. Comparison of results of this work for various power inputs

5. Conclusion and future scope

In this research, optimum parameters for a spiral bevel gear pair with three objective functions along with added design variables and critical mechanical constraints are obtained. The main findings of the research are as follows:

1. The weight of gear has considerably increased from 19.923 kg (for $z_1=10$) to 22.81 kg (Case 1). It is the same thing in module also, that has increased from 8.729 mm (for $z_1=10$) to 9.853mm (Case 2) in comparison to literature. It is tolerable as this value has been realised with added critical constraints and design variables.
2. The finest optimum design parameters (Case 2) are as follows:
 $a = 9.853\text{mm}$, $z_1 = 9.192$, $b = 27.064\text{mm}$, $d_s = 23.84\text{ mm}$, and $W = 26.319\text{ kg}$, $R_c = 213.625\text{ mm}$, and $\eta = 98.535\%$.
3. A decrease in cone pitch diameter (186.904 mm) is noted (213.625 mm) for $z_1=10$ than that of literature. In the same way, there is also an increase in efficiency from 97.546% (for $z_1=10$) to 98.406% (Case 2). It is noteworthy, as these have been accomplished, with added critical constraints and design variables.
4. There is a considerable rise of 32.10 % weight with additional constraints and design variables than that of the literature. But a surge in efficiency of 1.01% is also observed than that of the literature results.
5. The change in input power had caused design variables, viz. shaft diameter and face width of the gears to respond well. But remarkably there is no such reaction in any of the other design variables. This work is readily applicable and appropriate for optimization of related gear drives used in industries. Certain additional constraints such as profile shift constraint discussed in [24] and tribological constraints can also be considered for future work.

Conflict of interest

On behalf of all authors, the corresponding author states that there is no conflict of interest.

References

- [1] Shigley, J.E. (2011), Shigley's Mechanical Engineering Design, Tata McGraw-Hill
- [2] Deb, K. (2005), Multi-Objective Optimization Using Evolutionary Algorithms, Wiley. Deb, K. and Deb,
- [3] Srinivas N, Deb K., Multi-objective function optimization using non-dominated sorting genetic algorithms. IEEE Trans on Evolutionary Computation 1995; 2(3): 221-248.
- [4] Emmanuel Mermoz, Julien Astoul, Marc Sartor, Jean-Marc Linares, Alain Bernard. A new methodology to optimize spiral bevel gear topography. CIRP Annals - Manufacturing Technology, Elsevier, 2013, 62, pp.119 - 122.
- [5] Tetsu Nagata, Hayato Shichino, Yukio Tamura, Hitoshi Kawai, Yoriko Ohta, Masaharu Komori, Development of optimal tooth flank in spiral bevel gears by contact analysis and measurement, Komatsu Technical report, Vol 59 No. 166, 2013
- [6] Faydor L. Litvin, Alfonso Fuentes, Kenichi Hayasaka, Design, manufacture, stress analysis, and experimental tests of low-noise high endurance spiral bevel gears, Mechanism and Machine Theory, Volume 41, Issue 1, January 2006, Pages 831-118.
- [7] Jihui Liang, Lili Xin, Dynamic simulation of spiral bevel gear based on Solidworks and Adams- Journal of Theoretical and Applied Information Technology 20th January 2013. Vol. 47 No.2.
- [8] Chung Yunn Lin, Chung Biau Tsay, Zhang Hua Fong, "Computer aided manufacturing of spiral bevel and hypoid gears by applying optimization techniques", Journal of Materials and Processing Technology 114, 7 June 1999, 22-35.
- [9] G.Chandrasekaran, Advances in the design optimization and manufacturing optimization of bevel gears-A Review, International Journal of Engineering Research & Technology (IJERT)-NCRAIME-2015 Conference Proceedings, pp. 129-133
- [10] G. Chandrasekaran, V.S. Sreebalaji, R. Saravanan, J. Maniraj, Multiobjective Optimisation of Bevel Gear Pair design using NSGA-II, Materials Today: Proceedings, Volume 16, Part 2, 2019, Pages 351-360
- [11] S.Arunachalam, S. Padmanabhan; V. Srinivasa Raman; P. Asokan; Subramaniam Arunachalam; Tom Page, Design optimisation of bevel gear pair, International Journal of Design Engineering, 2011 Vol.No.4, pp364-393.
- [12] Xiaoqin Zhang, Yu Rong, Jingjing Yu, Liling Zhang and Lina Cui, Development of Optimization Design Software for Bevel Gear Based on Integer Serial Number Encoding Genetic Algorithm, JOURNAL OF SOFTWARE, VOL. 6, NO. 5, MAY 2011.
- [13] Rai, P. and Barman, A.G. (2020), "Optimizing the design of straight bevel gear with reduced scoring effect", Engineering Computations, Vol. 37 No. 7, pp. 2391-2409.
- [14] Li Tiejun, Zhu Chengshi, Ye Long, Optimal Design of Variable Helix Angle Bevel Gear based on Genetic Algorithms, Journal of Mechanical Transmission, 2007-027
- [15] Padmanabhan.S; Chandrasekaran.M, Srinivasa Raman V, Multiobjective optimisation of bevel gear design using real coded genetic algorithm, National Journal on advances in building sciences and mechanics, Vol 2 No 2, October 2011.
- [16] Ebenezer, G.R.N., Ramabalan, S. and Navaneethasanthakumar, S. (2019), "Advanced design optimization on straight bevel gears pair based on nature-inspired algorithms", SN Applied Sciences, Vol. 1 No. 10, p. 1155
- [17] Zolfaghari, A., Goharimanesh, M. and Akbari, A.A. (2017), "Optimum design of straight bevel gears pair using evolutionary algorithms", Journal of the Brazilian Society of Mechanical Sciences and Engineering, Vol. 39 No. 6, pp. 2121-2129.
- [18] Graham Johnson, Budi Chandra, Colin Foord and Kathy Simmons, Windage Power Losses From Spiral Bevel Gears With Varying Oil Flows and Shroud Configurations, Journal of Turbomach. 131(4), 041019 (Jul 13, 2009).
- [19] Y.Diab, F.Ville, P.Velex, Windage losses in high speed gears-Preliminary experimental and theoretical results, Journal of Mechanical design, September 2004, Vol. 126, pp. 903-908
- [20] Arora JS (2012) Introduction to optimum design, 3rd edn. Academic Press, New York
- [21] K. Deb and A. Pratap and S. Agarwal and T. Meyarivan, "A Fast and Elitist Multiobjective Genetic Algorithm: NSGA-II", IEEE Transactions on Evolutionary Computation, Vol 6, No.2, April 2002, pp. 182-197.
- [22] Tamilselvi Selvaraj (2021). MATLAB code for Constrained NSGA II - Dr.S.Baskar, S. Tamilselvi and P.R.Varshini (<https://www.mathworks.com/matlabcentral/fileexchange/49806-matlab-code-for-constrained-nsga-ii-dr-s-baskar-s-tamilselvi-and-p-r-varshini>), MATLAB Central File Exchange. Retrieved January 8, 2021.
- [23] R. C. Sanghvi, A. S. Vashi, H. P. Patolia, R. G. Jivani, "Multi-Objective Optimization of Two-Stage Helical Gear

- Train Using NSGA-II", Journal of Optimization, vol. 2014, Article ID 670297, 8 pages, 2014.
<https://doi.org/10.1155/2014/670297>
- [24] N. Godwin Raja Ebenezer, S. Ramabalan & S. Navaneethasanthakumar (2020) Design optimisation of mating helical gears with profile shift using nature inspired algorithms, Australian Journal of Mechanical Engineering, DOI: 10.1080/14484846.2020.1761007
- [25] S.Md. Jalaludeen, Machine design vol-2 (Design of transmission Systems), Anuradha Publications, 2017, India.
- [26] Bahaa Ibraheem Kazem *, Ali Ibrahim Mahdi, Ali Talib Oudah, " Motion Planning for a Robot Arm by Using Genetic Algorithm ", Jordan Journal of Mechanical and Industrial Engineering, Volume 2, Number 3, ISSN 1995-6665 Pages 131 – 136, Sep. 2008
- [27] Ahmed Farouk Abdul Moneim, " Fuzzy Genetic Prioritization in Multi-Criteria Decision Problems ", Jordan Journal of Mechanical and Industrial Engineering, Volume 2, Number 4, ISSN 1995-6665 Pages 175 – 182, December. 2008.
- [28] A. Benatallah, L.Kadi a,* , B. Dakyo b a, " Modelling and Optimisation of Wind Energy Systems ", Jordan Journal of Mechanical and Industrial Engineering, Volume 4, Number 1, ISSN 1995-6665 Pages 143 – 150, Jan.. 2010

An Experimental Investigation of Double Pipe Heat Exchanger Performance and Exergy Analysis Using Air Bubble Injection Technique

Farhan Lafta Rashid¹, Shaheed Mahdi Talib², Ahmed Kadhim Hussein³,
Obai Younis^{4,*}

¹Department of Petroleum Engineering, University of Kerbala, Kerbala, Iraq.

²General Directorate of Education in Kerbala, Ministry of Education, Kerbala, Iraq.

³Mechanical Engineering Department, College of Engineering, University of Babylon - Babylon City, Iraq.

⁴Department of Mechanical Engineering, College of Engineering at WadiAddwaser, Prince Sattam Bin Abdulaziz University, WadiAddwaser, KSA

Received 31 OCT 2021

Accepted 20 JAN 2022

Abstract

To ensure the transfer of thermal energy in high efficiency, a heat exchanger which has the ability to transfer thermal energy in the least time and cost, is used. There are many drawbacks to traditional surface-type heat exchangers, such as the problem of fouling, high resistance to heat transfer to the surface, and increased cost. The technique of air bubble injection is inexpensive, hopeful, and rarely used for improving the heat exchangers' thermal performance. The present article covers heat transfer and exergy analysis even without injecting an air bubble (3 mm in diameter) at the intake of a tube, shell, and tube and shell heat exchanger. The obtained findings indicate that those heat exchangers that injected air bubbles had a higher Nusselt number than heat exchangers that did not inject air bubbles. The technique of bubble injecting through both shell and tube raises the Nusselt number by a factor of between 2.13%-25.18%. The maximum NTU was achieved by injecting an air bubble into both the shell and tube intakes at a $Re=15000$. Estimated heat transfer improvements associated with injecting air bubbles into the intake of a tube, shell, or both tube and shell are 8.31% and 13.50%, respectively. Compared to the absence of an injected air bubble, the performance increases by 31.8%, 45.1%, and 54.2%, respectively, when the tube, shell, or both the tube and shell are injected with air bubbles.

© 2022 Jordan Journal of Mechanical and Industrial Engineering. All rights reserved

Keywords: Injection of the air bubble, heat transfer enhancement, bubbly heat exchanger, two-phase flow.

Abbreviation

HE	heat exchanger
HEs	heat exchangers
STHE	shell and tube heat exchanger
STHEs	shell and tube heat exchangers
ICE's	internal combustion engines

Nomenclature

Q	heat transfer rate (kW)
m	mass flow rate (kg/s)
C_p	specific heat (kJ/kg.°C)
T	temperature (°C)
U	overall heat transfer coefficient (kW/m ² .°C)
A	area (m ²)
LMTD	logarithmic mean temperature difference (°C)
E	exergy loss (Joules)
e	non-dimensional exergy loss (---)
h	heat transfer coefficient (W/m ² .°C)
k	thermal conductivity (W/m.°C)
L	length (m)
u	velocity (m/s)
Re	Reynolds number (---)
NTU	number of transfer units (---)
Nu	nusselt number (---)

D	diameter (m)
Pr	Prandtl number (---)

Greek

ϵ	effectiveness (---)
Δ	forward difference
ν	kinematic viscosity (m ² /s)

Subscripts

h	hot
c	cold
in	inlet
out	outlet
e	exit
i	inside
o	outside

1. Introduction

During the last decades, many researchers were searching to optimize energy systems or conserve energy because of the limited fossil fuel resources and enormous ecological issues generated by the excellent direction of

* Corresponding author e-mail: oubeytaha@hotmail.com.

energy attrition. This route of work spreads through large areas, from energy transmutation in tiny scales like domestic appliances and internal combustion engines, to energy transformation systems in considerable scale industries. The HE can be considered as the one among the most popular customarily applied in transfer phenomena of thermal energy, which is applied in small and large applications, such as petrochemical industries, medical, food, power plants, ventilation, air conditioning systems, wastewater treatment, and heating. Improving the HE efficiency by enhancing the heat transfer rate was addressed by numerous researchers. There are two kinds of methods for increasing the heat transfer rate named passive and active methods. In the case of the passive method, it is not required to have an outer power to keep the strength of heat transfer augmentation mechanism such as additives for fluids and swirl flow devices. The active methods demand outer power like vibrating the surface or stirring the fluid [1]. Heat transfer plays an important part in the energy world because higher heat transfer efficiency means more heat is recovered from the process under examination, and higher heat recovery efficiency means more energy savings. As a result, a HE is a device that may save energy by recovering heat by the heat transfer process, and the stored heat may be used for many applications [2]. Out of all HEs, STHE is the most common type of HEs used in industrial applications. This might be owing to a variety of reasons, including the working fluid's ability to tolerate extreme temperatures ranging (-250-800 °C) and ultimate pressures (6000psi), as well as ease of maintenance and manufacture. The main applications of this HE are found in industries, such as food processing industries, power plants, manufacturing industries, chemical and petrochemical industries, etc. To upgrade the double pipe HE performance, several heat transfer enhancement techniques were used. The air bubble injection technique may be thought of as a low-cost and promising method of improving the thermal properties of an STHE. In this technique, air bubbles are injected into the flowing fluids which move along the fluid leaving behind the void which is occupied by the ambient fluid causing turbulence in the animated fluid which results in augmenting the heat transfer rate. Moreover, the injection of air bubbles can reduce the skin friction drag near the wall which also causes turbulence in the moving fluid. This technique can be applied for heat transfer enhancement [3]. Over the latest few years, injection of air-gas bubbles into the STHes has been specified as an active method for creating turbulence in the fluid flow [4, 5]. Gabillet et al. [5] wrote an increment in the velocity and turbulence of flowing fluid when injection of air bubbles in the flowing fluid stream. The innovative work adopted by Zavaragh et al. [6], who injected air bubbles through an ICE's cooling arrangement to minimize emission and specify fuel consumption of the engine, and to obtain higher heat transfer rates.

Celeta et al. [7] presented a heat transfer enhancement by 10 times on studying the impact of injection of AB (air bubbles) at the entry of a heated canal. Dizaji and Jafar [8] discussed the effect of injection of air bubbles on effectiveness and Nusselt in STHes. Researchers found 6-35% augmentation in the Nusselt number and 10-40% enhancement in the effectiveness. Jiagai et al. [9] studied

the phenomena behind the reduction of skin friction drag in boundary layers due to the injection of air bubbles.

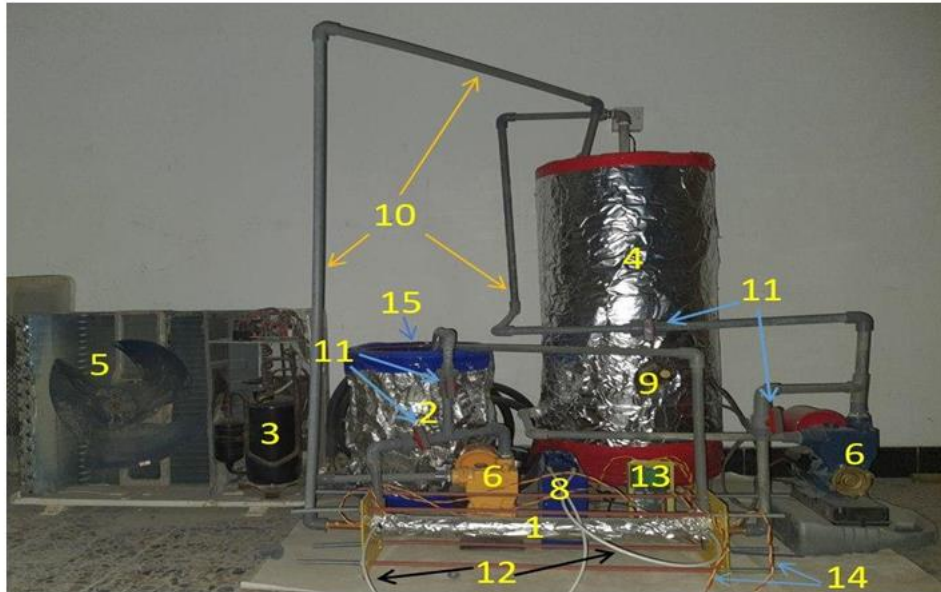
Mattson and Mahesh [10] revealed the bubble sizing effect on the fluid flow turbulence and found that the bubbles of smaller size just affect the flow close to the wall or the generation point while bubbles of larger size are easily able to penetrate to further space in a turbulent flow regime.

Delauré et al. [11] investigated the impact of an ellipsoidal air bubbling in sluggish water on heat flow and discovered that heat flux was increased. Jacob et al. [12] performed a comparison of the near-wall shear stress and Reynolds stress of two-phase flow (air bubble-water mixture) to single-phase flow and found that these stresses are more important in two-phase flow than in liquid phase flow only. Nandan and Singh [13] used air bubbles in double pipe HEs where they succeeded in obtaining a remarkable increase in the HE performance. Celeta et al. [14] investigated the impact of injection of the air bubble at the inflow of a heated canal and found that it increased heat transmission by tenfold. Shaheed et al. [15] used a double pipe HE to investigate the heat transfer performance and exergy analysis of air injection in various places. They reported that injecting air bubbles through the exchanger increased the Nusselt number by 2.41-25.5% in comparison to the exchanger with no air injection. Marzouk et al. [16] used a simple approach to explore the impact of air bubble injection in tube sidewalls. The flow rate was increased from 14 to 18 LPM, while the wet shell-side flow rate remained constant at 18 LPM. Emad et al. [17] developed techniques for predicting the influence of air injection into STHes on thermal performance using supervised machine-learning algorithms. This procedure was carried out by introducing air bubbles into the shell at various flow rates in order to get the HE's best thermal performance. Nazaruddin et al. [18] investigated the thermal performance of a twin-pipe HE when an air bubble was injected into the inner tube's water stream. The heat transfer coefficient and the number of transfer units both were enhanced by 33% and 38%, respectively. Sajida et al. [19] researched the influence of injecting air bubbles on the augmentation of heat transfer pressure drop for turbulent flow in 2-helical coil HEs. The exergy loss and NTU can be intensified by injecting air bubbles because of the bubbles' mobility (buoyancy force) and increasing the turbulence level and mixing the boundary layer of the fluid flow.

The major goal of this research is to explore the effects of injecting different air bubbles flow rates on the thermal properties of a horizontal double pipe HE. The injection of air bubbles was performed at several locations, including the shell inlet, tube inlet, and combined shell and tube inlets. A comparison was performed between the results obtained in this study and those obtained by Naphon et al. [20], it is apparent that the current study's findings corresponded to the aforementioned equation.

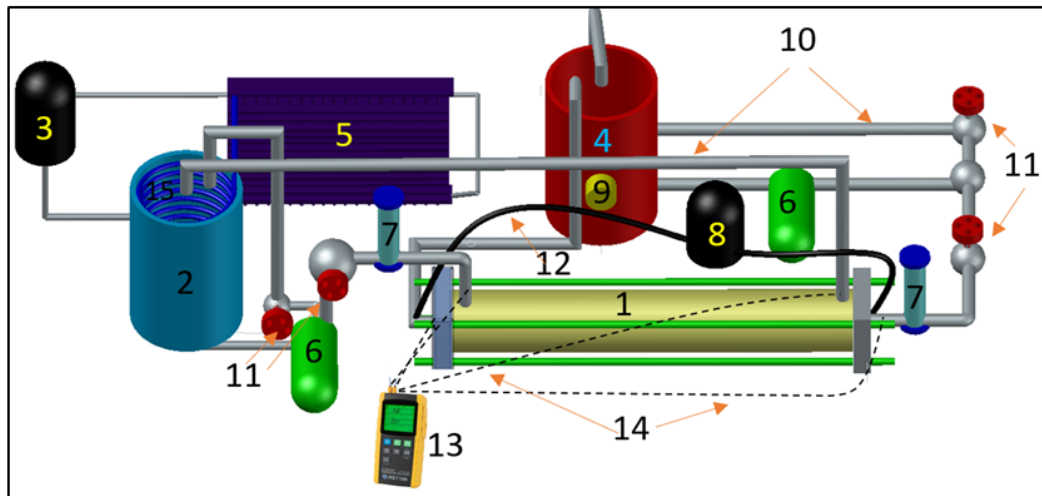
2. Experimental Setup

Figure (1) presents a schematic representation of the experimental rig. The air injection system, cold water loop, hot water loop, and test section make up the experimental setup. The test section instances are shown in Figure (3).



1. test section , 2. cold-water storage , 3. air-compressor , 4. hot-water storage, 5. condenser, 6. water pump, 7. water-rotameter, 8. air pump, 9. thermostat and dimmer, 10. connecting pipes, 11. valves, 12. air transmission tubes, 13. data-logger, 14. thermocouple wire, 15. evaporator

Figure 1. The experimental rig



1. test section , 2. cold-water storage , 3. air-compressor , 4. hot-water storage, 5. condenser, 6. water pump, 7. water-rotameter, 8. air pump, 9. thermostat and dimmer, 10. connecting pipes, 11. valves, 12. air transmission tubes, 13. data-logger, 14. thermocouple wire, 15. evaporator

Figure 2. Graphical representation of the experimental setup

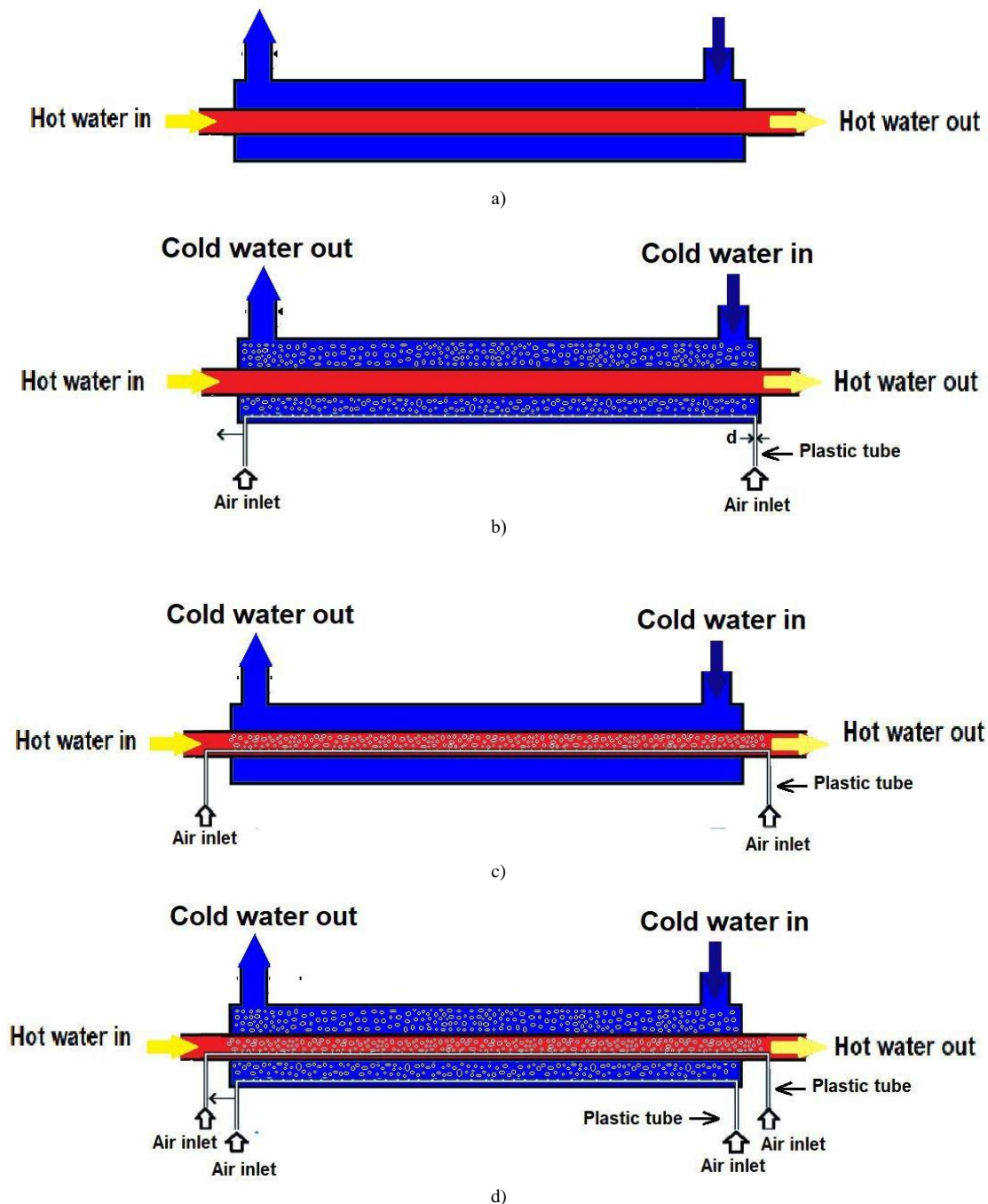


Figure 3. Test section

a) no air bubble injection, b) injecting air bubble through the shell, c) injecting air bubble through the tube, d) injecting air bubble into both tube and shell

The specifics of each test part are provided in table (1). To acquire the wall temperature, thermocouples of K-type with a reliability of 0.1°C were placed at the entrance and outflow of the tube and shell, as well as on its wall boundary.

The needed water is warmed up in hot water storage of 50-liter capacity. A controller of proportional-integral-derivative (PID) has been applied to adjust the hot water temperature. At a temperature of 50°C , several flow rates of hot water (4, 5.25, 6.5, 7.65, 8.9, 10.1, 11.3, 12.5 LPM) were investigated at the shell side. The cold water is

pumped at room temperature and 4 LPM (constant flow rate). To adjust the fluid flow on the tube and shell sides, two flow devices with an accuracy of around 1% each were fitted. Air was injected at a flow rate of 0.06 LPM using an aquarium pump.

Before the test, the instruments were calibrated. Tests have been carried out in a variety of circumstances (four). The first was performed with hot water (distilled) in the tube and cold water (distilled) in the shell. Different readings were obtained during five minutes, and the average of the data was used for analysis.

Table 1. Details of the test section

Item	Value
Length	610 mm
Diameter of shell	57 mm
External tube diameter	29 mm
Internal tube diameter	26 mm

The uncertainty and accuracy of the tests are recorded in the table below (2).

Table 2. The uncertainty and accuracy of the tests

Instruments	Accuracy (%)	Uncertainty
Thermocouple type K	0.1	± 0.10
Rotameter (kg/s)	0.2	± 0.01
Data Logger ($^{\circ}\text{C}$)	0.1	---

3. Data reduction

For the counter flow of multi-coil HE, the experimental heat transfer rate is obtained by [21]:

$$Q_h = m_h C_{ph} (T_{in,h} - T_{out,h}) \quad (1)$$

$$Q_c = m_c C_{pc} (T_{out,c} - T_{in,c}) \quad (2)$$

Q_{ave} (the averaged heat transfer) can be estimated by using equation (3):

$$Q_{ave} = \frac{Q_h + Q_c}{2} \quad (3)$$

U_h (the overall heat transfer coefficient) is predicted using Eqn. (4):

$$U_h = \frac{Q_{ave}}{A_h LMTD} \quad (4)$$

Where

LMTD: defined as logarithmic mean temperature difference, which may be predicted using equation (5):

$$LMTD = \frac{\Delta T_1 + \Delta T_2}{\ln \frac{\Delta T_1}{\Delta T_2}} \quad (5)$$

$$\Delta T_1 = T_{in,h} - T_{out,c} \quad (6)$$

$$\Delta T_2 = T_{out,h} - T_{in,c} \quad (7)$$

Where, $T_{in,h}$, and $T_{out,h}$, are the temperature of hot water inlet and outlet, respectively and, $T_{in,c}$, and $T_{out,c}$ indicates the inlet cold water and outlet cold water temperature, respectively.

The exergy loss and the non-dimensional exergy loss are predicted by using the methods of Akpinar and Bicer with aids of equations (8-12) [22].

$$E_h = T_e \left\{ m_h \times C_{ph} \times \ln \frac{T_{ho}}{T_{hi}} \right\} \quad (8)$$

$$E_c = T_e \left\{ m_c \times C_{pc} \times \ln \frac{T_{co}}{T_{ci}} \right\} \quad (9)$$

$$E = E_h + E_c \quad (10)$$

$$e = \frac{E}{T_e \times C_{min}} \quad (11)$$

$$C_{min} = \text{Min}\{C_h \text{ and } C_c\} \quad (12)$$

h_i (heat transfer coefficients) are calculated using the Wilson plots method with aids of equations (13-15) [23-29].

$$\frac{1}{U_i} = \frac{1}{h_i} + \frac{A_i \ln \left(\frac{d_o}{d_i} \right)}{2KL\pi} + \frac{A_i}{A_o h_o} \quad (13)$$

$$\frac{1}{U_i} = \frac{1}{h_i} + M \quad (14)$$

$$h_i = B Re^m \quad (15)$$

B, M, and m may be calculated using curve fitting.

$$\frac{1}{U_i} = \frac{1}{B Re^m} + M \quad (16)$$

NTU (the number of heat transfer units) is calculated by using equation (17):

$$NTU = \frac{AU}{C_{min}} \quad (17)$$

C_{min} (minimum heat capacity) can be predicted using equation (18):

$$C_h = m_h C_{ph}, C_c = m_c C_{pc}, C_{min} = \text{Min}\{C_h \text{ and } C_c\} \quad (18)$$

The effectiveness of the double pipe HE is predicted by equation (19):

$$\varepsilon = \frac{\text{heat transfer (actual)}}{\text{maximum heat transfer}} \quad (19)$$

The maximum heat transfer value is calculated by using equation (20):

$$Q_{max} = (m \cdot c)_{min} (T_{inlet,h} - T_{inlet,c}) \quad (20)$$

The experimental value of the Nusselt number is predicted by equation (21):

$$Nu = \frac{h_i D}{K} \quad (21)$$

4. Results and Discussion

Before injecting air in the HE, Nusselt number was validated with Naphon et al. correlation [21], which is written as:

$$Nu = 1.84(Re - 1500)^{0.32} \quad 5000 \leq Re \leq 25000, Pr = 0.7 \quad (22)$$

Figure (4) shows the validation with Naphon et al. [20] correlation. It is clear that the results obtained by the current study agreed well with the aforementioned equation with a maximum difference for the Nusselt number of 7.2%.

Results of the Nusselt number are shown in Figs. (4, 5, and 6). Figure (5) reveals the variation of Nusselt number with Reynolds number for air bubbles injection in the inlet of the shell. Figure (6) presents the variation of Nusselt number with Reynolds number for injection of air bubble in the tube inlet. Figure (7) illustrates the variation of Nusselt number with Reynolds number for air bubbles injection in the inlet of both tube and shell.

In figures (5-7), injecting air bubbles in the HE produced a higher Nusselt number than the exchanger without injecting air bubbles. The effect of air bubble injection into the inner tube is less than that of air bubble injection into the outer tube in terms of the heat transfer rate. This could be because the air bubbles increase the turbulence level of the water flow, and the air bubbles may collect near the inner wall of the inner tube and thus act as an insulator. As for the Reynolds number, it ranged between 5000 and 16000, so changing this number (increasing the flow rate) will lead to an increase in the heat transfer rate and thus the Nusselt number will increase. Depending on the condition of injection of the air bubble in the HE and Reynolds number, the increment in Nusselt number ranged from 2.13% to 25.18%.

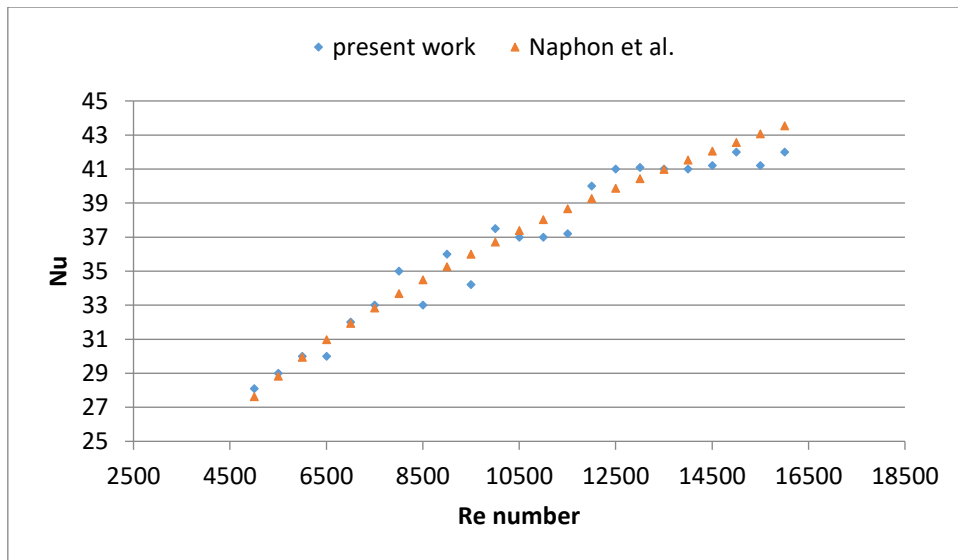


Figure 4. Verification of the present work results with reference [20] for the case of no air bubble injection

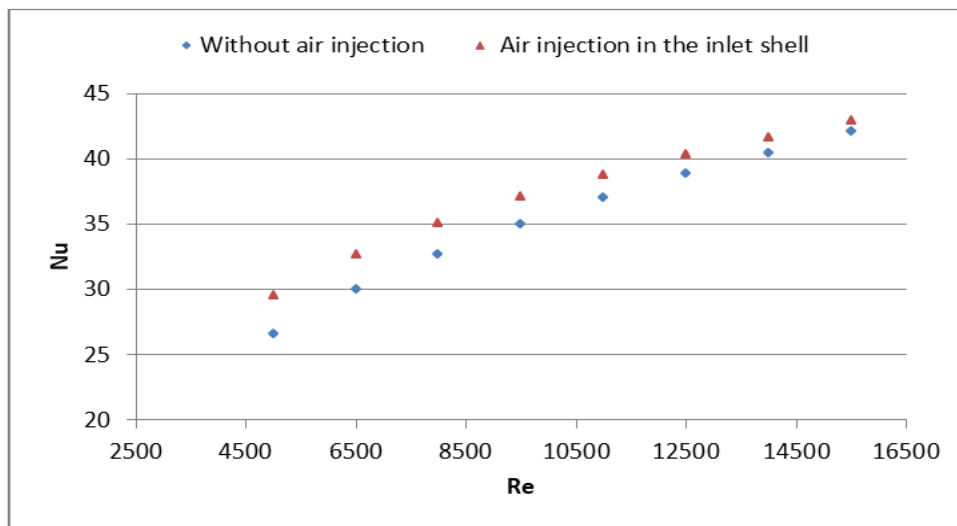


Figure 5. Nusselt number against Reynolds number with/without air bubbles injection through the inlet of the shell

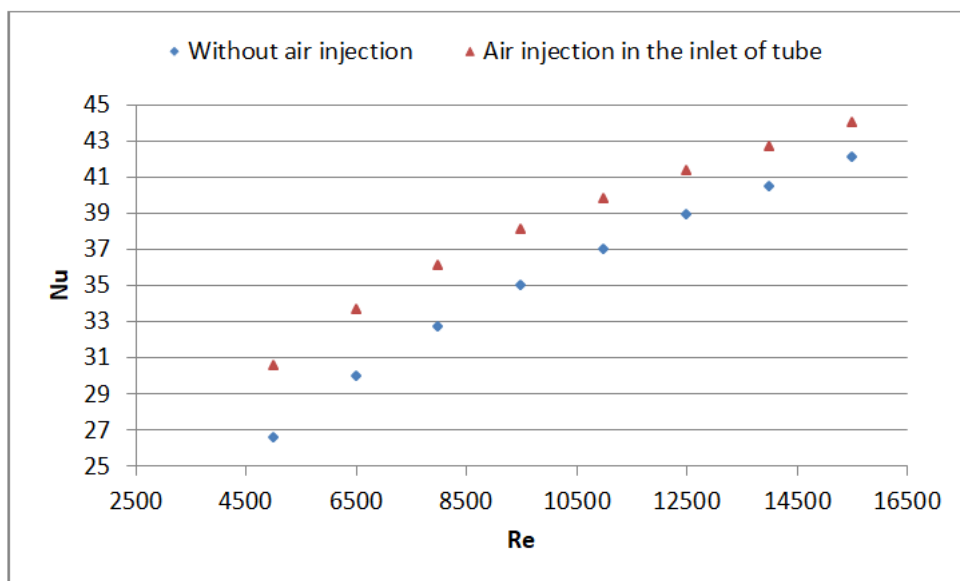


Figure 6. Nusselt number vs. Reynolds number without and with injecting air bubble in the tube inlet

Figure (8) manifest that the highest augmentation in Nusselt number was done for injecting air bubble in the tube and shell inlet at the minimum value of Reynolds number (5000). The lowest augmentation in Nusselt number took place for injection of air bubble in the inlet of the shell at the maximum value of Reynolds number (15000). For all cases, increasing Reynolds number enhances the ratio of augmented Nusselt number/ non-augmented Nusselt number. The air bubbles increase the water flow turbulence level, and the air bubbles may collect near the inner wall of the inner tube and thus act as an insulator. Increasing the Reynolds number, which means increasing the flow rate, will lead to an increase in the heat transfer rate and thus the ratio of augmented

Nusselt number/ non-augmented Nusselt number will increases.

Fig. (9) Shows a variation of NTU with Reynolds number. It has been shown that the increment in Reynolds number directly enhances the amount of NTU. This may be due to the formation of a vacuum through the rising air bubbles during the flow along the water causing turbulence in the flowing fluid which leads to more heat transfer from the surfaces by the running water. Depending on the injection of air bubble situation, minimum NTU was occurred for injecting air bubble in the inlet of the shell at the minimum value of Reynolds number (Re=5000), and highest NTU value was achieved for injecting air bubble in the tube and shell inlet at the maximum value of Reynolds number (Re=15000).

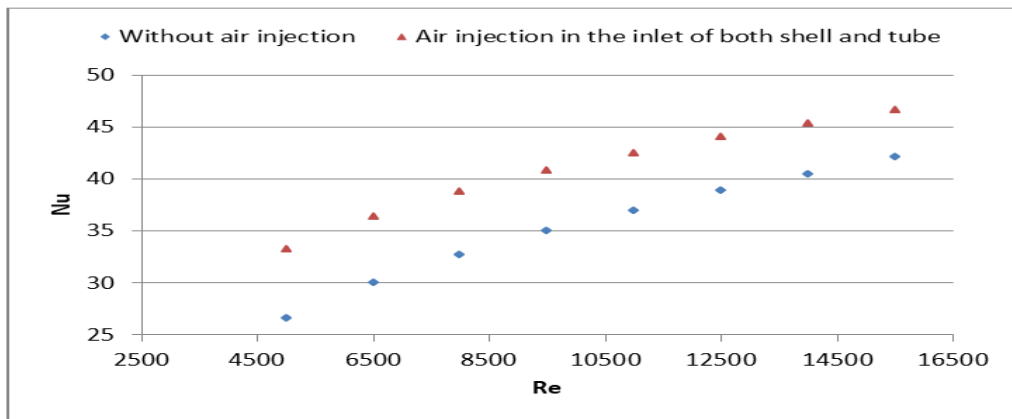


Figure 7. Nusselt number against Reynolds number without and with injecting air bubble through the inlet of both shell and tube

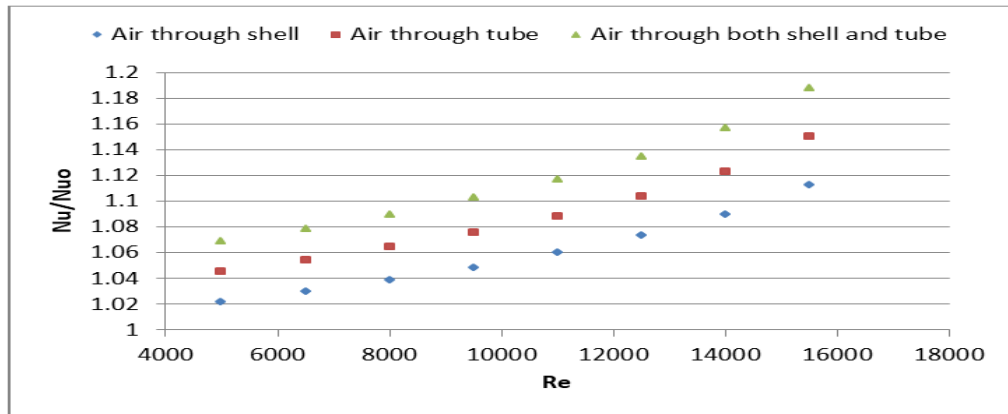


Figure 8. Enhanced Nusselt number against Reynolds number

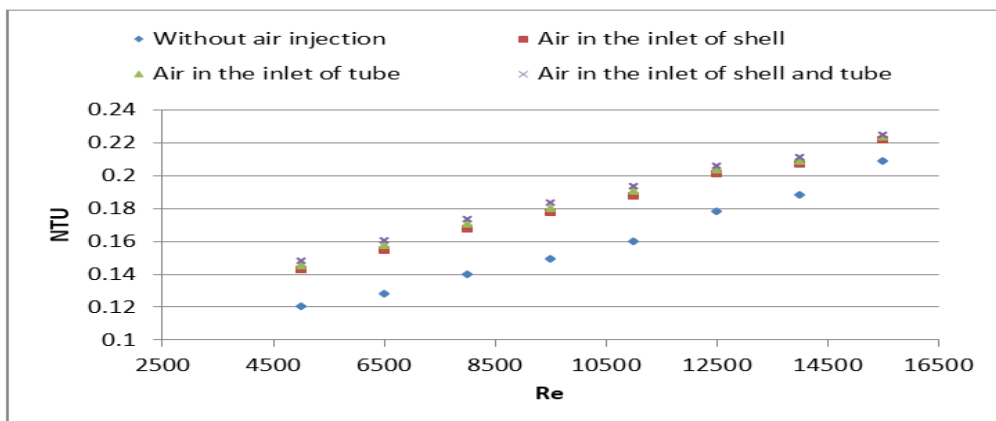


Figure 9. Enhanced NTU vs. Reynolds number

The analysis of exergy loss is a substantial factor in the design of the HE. Exergy is the ultimate beneficial work gained from any thermal system. Attaining higher performance of the HE means attaining maximum work from the system. One of the primary sources of exergy loss in HEs is the difference in temperature between hot and cold fluids. When increasing the dimensionless exergy loss, the system will extract the maximum amount of energy possible. The injection of an air bubble in the inlet of a shell has the lowest dimensionless exergy, whereas the injection of an air bubble in the inlet of both tube and shell has the highest dimensionless exergy. The air bubbles injection produces greater dimensionless exergy, in comparison to that produced in the case of no air bubble injection.

Figure (11) suggests that the heat transfer rate is in direct proportion to the Reynolds number. In other words, the rate of heat transfer is directly proportional to the mass flow rate. If the flow rate increases, the rate of heat transfer will increase. Furthermore, figure (11) indicates that injecting air bubbles through the inlet of both the tube and shell produced the highest rate of heat transfer, followed by air bubbles injection into the tube's inlet, then the

injection of the air bubble into the shell's inlet, and finally the case of no air bubble injection. In comparison to the case of no air bubbles injection, the heat transfer augmentation for injection of air bubbles in the intake of the tube, shell inlet, and both tube and shell inlets is 4.41%, 8.31%, and 13.50%, respectively. This increase occurs at various Reynolds numbers, depending on how the experiment was conducted.

The HE effectiveness is the ratio of verifiable to the maximum heat transfer achievable. As a result, a high heat transfer rate denotes a high HE efficiency. The effectiveness is directly proportional to the Reynolds number, as seen in figure (12). Figure (12) also presents that injecting air bubbles in the inlet of both tube and shell resulted in the greatest effectiveness, followed by air bubble injection into the inlet of tube, air bubbles injection into the shell inlet, and finally without injecting air bubbles. In comparison to the situation of no injecting air bubbles, the augmentation in the effectiveness for air injecting in the intake of shell, tube, and both tube and shell is 31.8%, 45.1%, and 54.2%, respectively. It is worth noting that these improvements happened at various Reynolds numbers when the experiment was carried out.

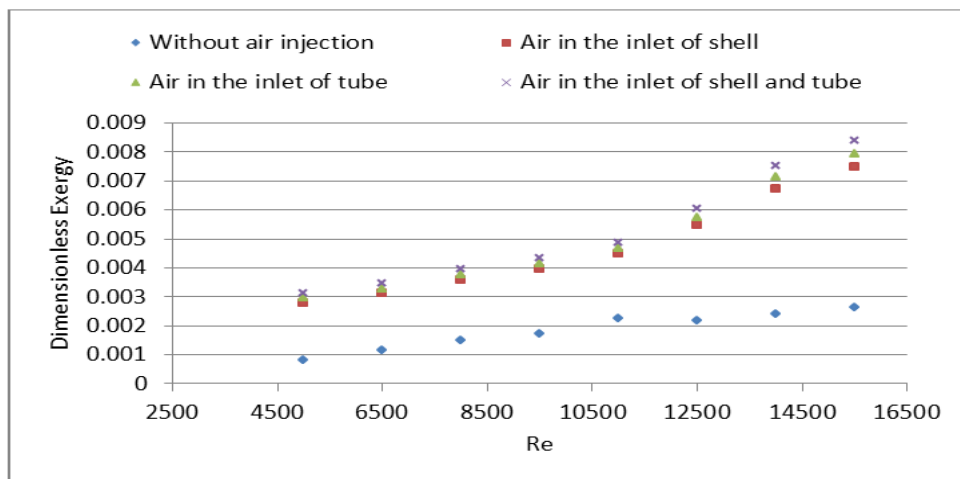


Figure 10. Dimensionless exergy vs. Reynolds number

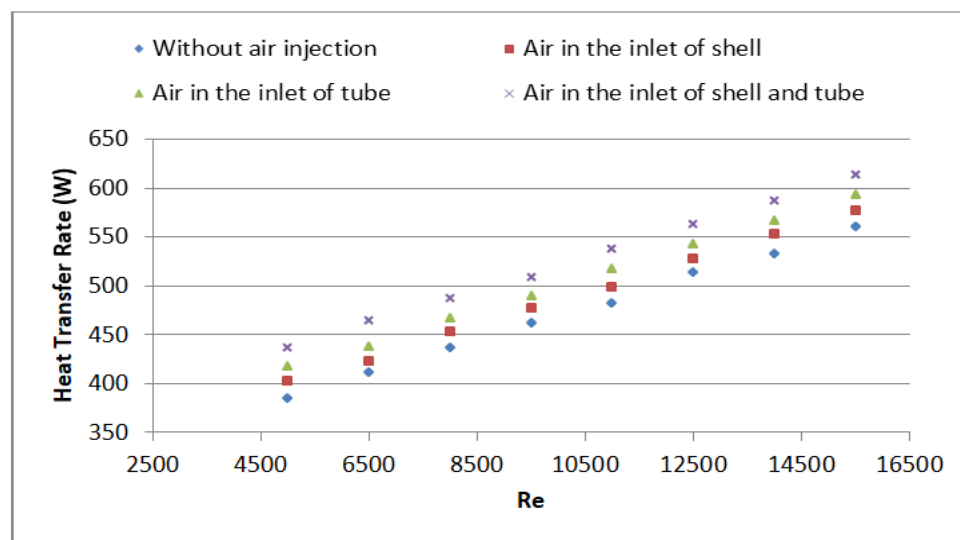


Figure 11. Average heat transfer vs. Reynolds number

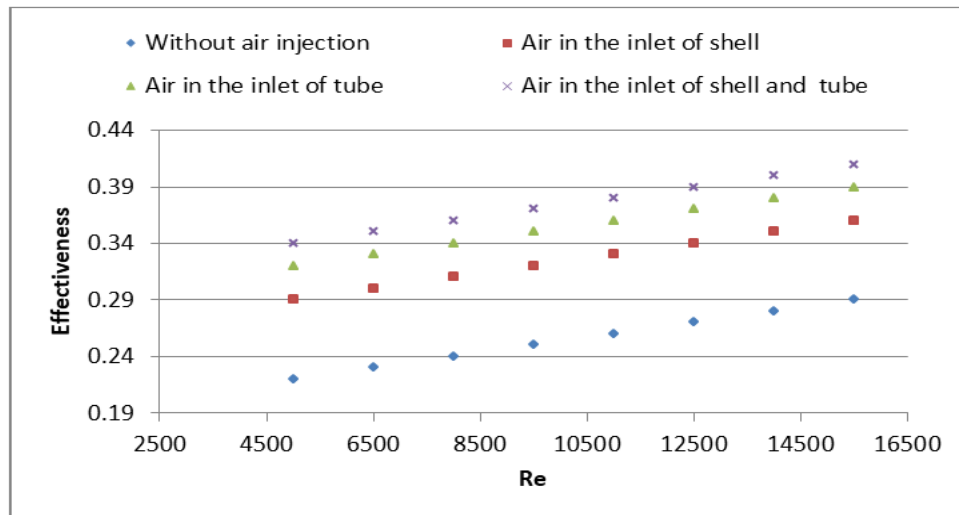


Figure 12. Effectiveness vs. Reynolds number

5. Conclusions

In this work, the counter-current flow performance in a horizontally mounted double-pipe HE under the impact of air bubbles injection was presented. The following key findings were concluded:

1. Injection of air bubbles is one of the hopeful ways in augmenting the heat transfer rates.
2. Generally, the injection of air bubbles through the HE resulted in a higher Nusselt number in comparison with the HE with no air bubbles injection.
3. The Nusselt number was increased by 2.13% to 25.18% when injecting air bubbles into the HE. The maximum enhancement in Nusselt number occurred for air bubbles injection in the inlet of both tube and shell at the minimum value of Reynolds number. Minimum enhancement in Nusselt number occurred for injecting air bubbles in the inlet of the shell at the maximum value of Reynolds number. Increasing Reynolds number (flow rate) decreases the ratio of enhanced Nusselt number/ non-enhanced Nusselt number.
4. As the Reynolds number rises, the value of NTU rises as well. At low minimum Reynolds numbers, the lowest NTU was seen for injecting air bubbles through the shell inlet, while maximum NTU was observed for injecting air bubbles in the inlet of both the shell and the tube at maximum Reynolds numbers.
5. Generally, injecting air bubbles through the HE resulted in higher values of dimensionless exergy when compared to the case of no air bubbles injection. Air bubbles injection in the shell inlet has the lowest dimensionless exergy, whereas air bubbles injection in the inlet of both tube and shell has the highest.
6. In comparison to the situation of no air bubbles injection, the enhancement in heat transfer rate for injecting air bubbles in the intake of shell, tube, and both shell and tube is 4.41%, 8.31%, and 13.50%, respectively.
7. In comparison with the case of no air bubbles injection, the efficacy increase for air bubble injection in the intake of shell, tube inlet, and both shell and tube inlets is 31.8%, 45.1%, and 54.2%, respectively. This

increase occurs at various Reynolds numbers, depending on how the experiment was conducted.

Acknowledgment

The Deanship of Scientific Research of Prince Sattam bin Abdulaziz University in Alharj, Saudi Arabia, funded this publication.

References

- [1] Mohammad Mahdi Heyhat, Adel Abdi, Ali Jafarad, "Performance evaluation and exergy analysis of a double pipe heat exchanger under air bubble injection", *Applied Thermal Engineering*, 143 (2018), 582–593.
- [2] Cancan, Z., Yafei et al. "Review heat exchanger: Research development of self-rotating inserts in heat exchanger tubes", *International Journal of Engineering-Transactions A: Basics*, Vol. 27, No. 10, (2014), 15-26.
- [3] Saleh Khorasani, Abdolrahman Dadvand, "Effect of air bubble injection on the performance of a horizontal helical shell and coiled tube heat exchanger", *Applied Thermal Engineering*, Volume 111, 25 January 2017, Pages 676–683.
- [4] Itaru Michiyoshi, Akimi Serizawa, "Turbulence in two-phase bubbly flow", *Nucl. Eng. Des.* 95 (1986) 253–267.
- [5] C. Gabillet, C. Colin, J. Fabre, "Experimental study of bubble injection in a turbulent boundary layer", *Int. J. Multiph. Flow* 28 (4) (2002) 553–578.
- [6] Hadi Ghasemi Zavaragh, Aliriza Kaleli, Faraz Afshari, "Ali Amini, Optimization of heat transfer and efficiency of engine via air bubble injection inside engine cooling system", *Appl. Therm. Eng.* 123 (2017) 390–402.
- [7] G. P. Celata et al., "Heat Transfer Enhancement by Air Injection in Upward Heated Mixed Convection Flow of Water", *International Journal of Multiphase Flow*, 25, 1999, pp 1033-1052.
- [8] H.S. Dizaji and S. Jafarmadar, "Heat Transfer Enhancement due to air Bubble Injection into a Horizontal Double Pipe Heat Exchanger", *International Journal of Automotive Research*, 4 (4), 2014, pp 902-910.
- [9] Jiaccai Lu et al., "The Effect of Bubbles on the Wall Drag in Turbulent Flow", *Physics of Fluids*, 17, 2005.
- [10] M. Mattson, K. Mahesh, "Simulation of Bubble Injection in a Turbulent Boundary Layer", *Physics of Fluid*, 23, 2011.
- [11] Delauré, Y., Chan, V. and Murray, D., "A simultaneous IV and heat transfer study of bubble interaction with free

- convection flow", *Experimental Thermal and Fluid Science*, Vol. 27, No. 8, (2003), 911-926.
- [12] Jacob, B., Olivieri, A., Miozzi, M., Campana, E.F. and Piva, R., "Drag reduction by microbubbles in a turbulent boundary layer", *Physics of Fluids*, Vol. 22, No. 11, (2010), 115104.
- [13] Nandan, A. and Singh, G., "Experimental study of heat transfer rate in a shell and tube heat exchanger with air bubble injection", *International Journal of Engineering Transaction B: Applications*, Vol. 29, No. 8, (2016), 1160-1166.
- [14] Celata, G., Chiaradia, A., Cumo, M. and D'annibale, F., "Heat transfer enhancement by air injection in upward heated mixed convection flow of water", *International Journal of Multiphase Flow*, Vol. 25, No. 6, (1999), 1033-1052.
- [15] Shaheed Mahdi Talib, Farhan Lafta Rashid, and Muhammad AsmailEleiwi, "The Effect of Air Injection in a Shell and Tube Heat Exchanger", *Journal of Mechanical Engineering Research and Developments*, 47(2021), 305-317.
- [16] S.A.Marzouk, M.M.Abou Al-Sood, Magda K.El-Fakharany, Emad M.S.El-Said, "Thermo-hydraulic study in a shell and tube heat exchanger using rod inserts consisting of wire-nails with air injection: Experimental study", *International Journal of Thermal Sciences*, Vol. 161, 2021, 106742.
- [17] Emad M.S.El-Said, Mohamed Abd Elaziz, Ammar H.Elsheikh, "Machine learning algorithms for improving the prediction of air injection effect on the thermohydraulic performance of shell and tube heat exchanger", *Applied Thermal Engineering*, Vol. 185, 2021, 116471.
- [18] Nazaruddin Sinaga, Saleh khorasani, Kottak karan Soopy Nisar, Amr Kaood, "Second law efficiency analysis of air injection into inner tube of double tube heat exchanger", *Alexandria Engineering Journal*, Vol. 60, Iss. 1, 2021, pp. 1465-1476.
- [19] Sajida LaftaGhashim, AyserMuneerFlayh, "Experimental investigation of heat transfer enhancement in heat exchanger due to air bubbles injection", *Journal of King Saud University - Engineering Sciences*, Vol. 33, Iss. 7, 2021, pp. 517-524.
- [20] P. Naphon, M. Nuchjapo, J. Kurujareon, "Tube side heat transfer coefficient and friction factor characteristics of horizontal tubes with helical rib", *Energy Conversion and Management*, 47 (2006), 3031-3044.
- [21] Holman JP (1986) *Heat transfer*. McGraw-Hill Inc - New York.
- [22] Akpınar, E.K. and Bicer, Y., "Investigation of heat transfer and exergy loss in a concentric double pipe exchanger equipped with swirl generators", *International Journal of Thermal Sciences*, Vol. 44, No. 6, (2005), 598-607.
- [23] J. Rose, Heat-transfer coefficients, Wilson plots and accuracy of thermal measurements, *Experimental Thermal and Fluid Science*, 28, 77-86, 2004.
- [24] K. Wongcharee, S. Eiamsa-ard, Heat transfer enhancement by using CuO/water nanofluid in corrugated tube equipped with twisted tape, *Int. Comm. Heat Mass Transfer* 39(2012) 251-257.
- [25] S. Pethkool, S. Eiamsa-ard, S. Kwankaomeng, P. Promvonge, Turbulent heat transfer enhancement in a heat exchanger using helically corrugated tube, *Int. Comm. Heat Mass Transfer* 38 (2011) 340-347.
- [26] N. Jamshidi, M. Farhadi, D.D. Ganji, K. Sedighi, Experimental analysis of heat transfer enhancement in shell and helical tube heat exchangers, *Applied Thermal Eng.* 51, 644-652, 2013.
- [27] H. Shokouhmand, M.R. Salimpour, M.A. Akhavan-Behabadi, Experimental investigation of shell and coiled tube heat exchangers using Wilson plots, *International Communications in Heat and Mass Transfer* 35 (2008) 84-92.
- [28] Ahmad Al-Qaisia , Jamil Al Asfar, Nabeel Abu Shaban, AreejEniezat, Experimental Investigation of the Performance of a Vortex Tube with Conical Control Valve, *Jordan Journal of Mechanical and Industrial Engineering* 14 (2020) 195-204.
- [29] Oyewola, O.M, Ismail, O. S, Abu, K., Numerical Simulation of Forced Convection Flows over a Pair of Circular Cylinders in Tandem Arrangement, *Jordan Journal of Mechanical and Industrial Engineering* 13 (2019) 221-230.

A Review of the Recent Development in Machining Parameter Optimization

Mohsen Soori^{*}, Mohammed Asmael

Department of Mechanical Engineering, Eastern Mediterranean University, Famagusta, North Cyprus, Via Mersin 10, Turkey.

Received 9 NOV 2021

Accepted 15 JAN 2022

Abstract

The optimization process is applied to the machining operations in order to provide continual improvement in accuracy and quality of produced parts. The effects of machining parameters in milling operations, such as spindle speed, depth of cut and feed rate are investigated in order to minimize the surface roughness as well as the time of machining process. The effective machining parameters, such as depth of cut, feed rate and spindle speed in turning operations are investigated to minimize the surface roughness as well as the time of machining process. Also, machining parameters, such as peak current, gap voltage, duty cycle and pulse on time in Electro Discharge Machining (EDM) operations can be optimized in order to obtain the optimized material removal rate, tool wear, and surface roughness in part production process. To improve material removal rate, surface roughness, and spark gap in part production process using the wire EDM operations, machining parameters, such as spark on time, spark off time, input current are studied and optimized. To calculate optimized machining parameters, different optimization methods, such as Taguchi method, fuzzy logic algorithm, artificial intelligence, genetic algorithm, artificial neural networks, artificial bee colony algorithm, ant colony optimization and harmony search algorithm are used. As a result, time and cost of accurate production can be reduced to increase productivity in part production process using machining operations. In this paper, a review of machining parameter optimization is presented and future research works are also suggested. The main aim of the study is to review the challenges and limitations of the optimization techniques used in optimizing machining parameters. It has been observed that the research field can be moved forward by reviewing and analyzing recent achievements in the published papers.

© 2022 Jordan Journal of Mechanical and Industrial Engineering. All rights reserved

Keywords: Machining Parameters, Optimization, Efficiency of part production.

1. Introduction

To remain in competitive environment of marketing, time and cost of part production should be analyzed and minimized in terms of efficiency enhancement in part production process. Machining time and surface roughness can be minimized in order to increase efficacy in part production process. Also, cutting tool life as well as tool wear can be maximized in order to decrease the cost of part production using machining operations. The optimized machining parameters can be calculated using different optimization methods to increase efficiency in process of part production. To calculate optimized machining parameters, different optimization methods, such as Taguchi method, fuzzy logic algorithm, artificial intelligence, genetic algorithm, artificial neural networks, artificial bee colony algorithm, ant colony optimization and harmony search algorithm are used. As a result, machining cost and production time of machined components can be decreased and the quality of the final products can be increased in terms of productivity enhancement of part production using optimized machining parameters.

Electrical discharge machining (EDM) is a non-traditional processing technique that involves cutting materials from a component by a series of repetitive

electrical discharges over electrodes and the part being manufactured in the existence of a dielectric fluid [1]. The machining parameters optimization of the EDM is reviewed by Nahak and Gupta [1] in order to increase efficiency during the machining operations. To increase efficiency in part production process, Optimization process of machining parameters is reviewed by Mukherjee and Ray [2]. A review in optimizing machining parameters is presented by Yusup et al. [3] to analyze and classify the previous research works in order to increase productivity in part production process.

Predicting surface roughness in machining is reviewed by Benardos and Vosniakos [4] to analyze the applications of different optimization methodology in terms of efficiency enhancement of part production. Advanced optimization techniques in machining parameters of electric discharge machining, abrasive jet machining, ultrasonic machining is reviewed by Rao and Kalyankar [5] to increase productivity in part production process using machining operations. Literature review of optimization technique for chatter suppression in machining is presented by Razlan Yusoff et al. [6] to decrease the chatter in machining operations using optimized machining parameters, such as spindle design, tool path, cutting process, and variable pitch. To increase productivity in part production process using turning

^{*} Corresponding author e-mail: mohsen.soori@gmail.com.

operations, optimization process of machining parameters is reviewed by Aggarwal and Singh [7].

A review in recent development of mechanical behavior of materials during machining operations is presented by Soori and Asmael [8] in order to increase accuracy as well as efficiency in machining operations. Applications of the Computer Aided Process Planning (CAPP) in manufacturing systems is reviewed by Soori and Asmael [9] to analyze and expand the computer applications in production engineering. Recent development in friction stir welding process is studied by Soori et al. [10] in order to develop the part manufacturing process using welding operations. To study and minimize the cutting temperature during milling operations, through which it is difficult to cut materials, advanced virtual machining system is presented by Soori and Asmael [11]. To minimize the residual stress and deflection error in five axis milling operations of turbine blades, advanced virtual machining system is proposed by Soori and Asmael [12].

To minimize the deflection error in five axis milling operations of impeller blades, Soori and Asmael [13] developed virtual machining systems. To analyze and modify the applications of the Virtual manufacturing systems in development process of part production, virtual product development is studied by Soori [14]. To develop the decision support systems in the data warehouse management, advances in web-based decision support systems is studied by Dastres and Soori [15]. To develop the applications of the artificial neural networks in different areas, such as risk analysis systems, drone control, welding quality analysis and computer quality analysis, a review in recent development and applications of the systems is presented by Dastres and Soori [16].

Applications of the information communication technology in the environmental protection is presented by Dastres and Soori [17] in order to decrease the effects of technology development to the natural disaster. To increase surface quality during five-axis milling operations of turbine blades, Soori et al. [18] presented advanced virtual machining system. To analyze and modify the machining operations in virtual environments, virtual machining systems and applications are presented by Soori et al. [19-23].

In the present research work, different issues of research related to machining parameter optimization are categorized to provide a useful study for the researchers in the interesting field. As a result, new ideas in machining parameter optimization process and gaps in the existing literature are obtained and future research works are also suggested in order to push forward this interesting research field.

Section 2 presents a review of research works related to machining parameter optimization. In section 3, research works are classified according to the different topics in research to the machining parameter optimization, and future research works in the interesting field are also suggested.

2. Review of research works in machining parameter optimization

The research works in the field of machining parameter optimization is recently developed in different topics of machining operations to increase quality as well as efficiency in the part production. Several approaches are recently developed in the optimization process of machining parameters. The different topics of research works are classified in this section in order to review their achievements in the research field.

2.1. Taguchi method

The optimization technique of Taguchi method is developed by Professor Genichi Taguchi of Telegraph Company of Japan in order to increase productivity in production process of robust products. According to Taguchi method, total loss generated by a product to the society after shipping is the quality of the manufactured product. In order to increase the product quality in minimizing the effects of noise factors in part production process, the experimental design as an optimization technique is investigated by Taguchi. Review on optimization of cutting parameters in machining using Taguchi method is presented by Chandel and Giri [24] to increase surface quality of produced parts using machining operations. To increase surface quality of produced parts using the abrasive flow machining technology, study of machining parameter optimization based on Taguchi method is investigated by Li et al. [25]. The optimized machining parameters in end milling operations of Inconel 718 super alloy is obtained by Maiyar et al. [26] in order to increase surface quality of produced parts using machining operations.

To improve material removal rate, surface roughness, and spark gap in part production process using wire cut electrical discharge machining operations, the Taguchi grey relational analysis is investigated by Rajyalakshmi and Ramaiah [27]. To obtain the optimized tool wear, surface roughness and cutting forces in machining operations, optimization of machining parameters, such as spindle speed, feed rate and depth of cut during micro-milling of Ti6Al4V titanium alloy and Inconel 718 materials using Taguchi method is presented by Kuram and Ozcelik [28]. Optimized machining parameters, such as peak current, gap voltage, duty cycle and pulse on time in Electro Discharge Machining (EDM) of AISI D3 steel materials using Taguchi method is investigated by Nipanikar [29] to increase efficiency of part production process. WEDM Parameter Optimization for Silicon/Magnesium Composite Using Taguchi Based method is studied by Kavimani et al. [30] to calculate the maximum material removal rate with minimal surface roughness in part production process. The optimization cycle of machining parameters, such as spark on time, spark off time, input current and wire feed rate in wire EDM on aluminum and mild steel using Taguchi method to reduce surface roughness in component production processes is investigated by Tilekar et al. [31]. To increase productivity in part production processes, the effect of CNC milling machining parameters on surface finish using Taguchi method is investigated by Joshi and Kothiyal [32].

The application of the Taguchi method in the optimization phase of machining parameters, such as speed, cut depth and feed rate, in order to reduce the surface roughness in part production process in the milling operation of glass fiber reinforced plastic is studied by Ghalme et al. [33].

2.2. Fuzzy logic algorithm

The optimization method of fuzzy logic is an alternative search mechanisms optimization technique to find optimal solutions for complex optimization problems. There are different steps for the optimization algorithm of the fuzzy logic. In the first step, in order to evaluate the selection criteria, the matrix of the membership degree of the existing bids is constructed. Then, in order to calculate the optimized member of the population by obtaining maximum of the global membership degree as an inference operator, the vector of the global membership degree of the bids to the selection criteria is created. Finally, the optimized member is selected and validated according to the selection criteria of the optimization method. To increase material removal rate in part production processes using EDM of AISI 316 LN stainless steel, optimization of process parameters such as pulse current, pulse on-time, and pulse off-time using fuzzy-based multi-objective PSO is investigated by Majumder [34]. To increase efficiency in part manufacturing process, application of the Fuzzy logic algorithm in obtaining the optimized machining parameters is reviewed by Adnan et al. [35].

Optimization process of machining parameters, such as the depth of cut, cutting speed, feed rate, and tool nose runoff for CNC machining operations using fuzzy and game theory methods is investigated by Chuang et al. [36] to increase cutting tool life in machining operations by obtaining the optimized condition of the tool wear and cutting noise. To increase efficiency in part production process, the optimization algorithm of fuzzy theory in optimization process of electrical discharge machining process is applied by Lin and Lin [37]. To calculate optimized machining parameters, such as cutting speed, feed rate, depth of cut, nose radius and cutting environment in terms efficiency enhancement of part production process, application of the fuzzy theory method in optimization process in high speed CNC turning of AISI P-20 tool steel is investigated by Gupta et al. [38]. To increase efficiency in die casting process of magnesium alloy, application of the fuzzy logic algorithm in optimization process of machining parameter, such as the pressure of injection, the plunger velocity and the filling time is investigated by Chiang et al. [39].

The effective parameters of turning of Al-SiC-Gr for hybrid metal matrix composites using the using grey-fuzzy algorithm is investigated by Suresh et al. [40] to obtain the optimal level of machining parameters in turning operations. Optimization process of multiple characteristics of EDM parameters based on desirability approach and fuzzy logic in machining process of super alloy Inconel 718 is presented by Sengottuvel et al. [41] to maximize the material removal rate, tool wear and minimize surface roughness in EDM production process. Optimization of electro discharge machining process

parameters with fuzzy logic for stainless steel 304 is studied by Ubaid et al. [42] to obtain the optimized pulse off time and current parameters in EDM machining operations. Optimization of material removal rate in Wire EDM using fuzzy logic and artificial neural network is investigated by Ashok et al. [43] to calculate the optimized Pulse-on, Pulse- off, current and servo voltage parameters in terms of efficiency enhancement of part production. Multi-objective optimization of wire electro discharge machining process parameters using grey-fuzzy approach is investigated by Das et al. [44] to improve productivity in part production process using machining operations.

2.3. Artificial intelligence

The artificial intelligence optimization algorithm is population based optimization technique in which the best member of the population is selected within the specified range. The behaviour of natural entities for each member of population is a solution for the optimization problem. As a result, the optimized member of the considered population is obtained using the artificial intelligence method. To calculate optimized machining parameters in terms of efficiency enhancement of part manufacturing process, applications of the artificial intelligence to calculate optimized machining parameters is reviewed by Park and Kim [45].

To increase productivity in part production process using turning operations, applications of the artificial intelligence in optimization process of part production is investigated by Aggour et al. [46]. Automatic prediction of required surface roughness by monitoring wear on face mill teeth using artificial intelligence is presented by Pimenov et al. [47] to monitor the main drive power in terms of productivity enhancement of part production process. Parameters forecasting and optimizing of laser welding operations using the artificial intelligence techniques is investigated by Nikolić et al. [48] to increase efficiency in part production process using laser welding operations. Application of the artificial intelligence in parameter optimization process of a multi-pass milling process is investigated by Rao and Pawar [49] to minimize production time in terms of productivity enhancement of part production. Artificial intelligence applications for fault diagnosis of rotating machinery is reviewed by Liu et al. [50] to increase accuracy and efficiency in part production process using rotating machinery systems. To obtain the desired surface quality in machined parts using optimized feed rate and spindle speed, supervision controller for real-time surface quality assurance in CNC machining using artificial intelligence is developed by Moreira et al. [51]. To minimize the surface roughness of produced parts in turning operations of medical stainless steel, modeling and optimization of surface roughness parameters using artificial intelligence methods is investigated by Kovač et al. [52]. An optimization algorithm is developed by Wang et al. [53] to provide better efficiency and lower power consumption for a milling process. Flowchart of the developed optimization method in the study is shown in the figure 1[53].

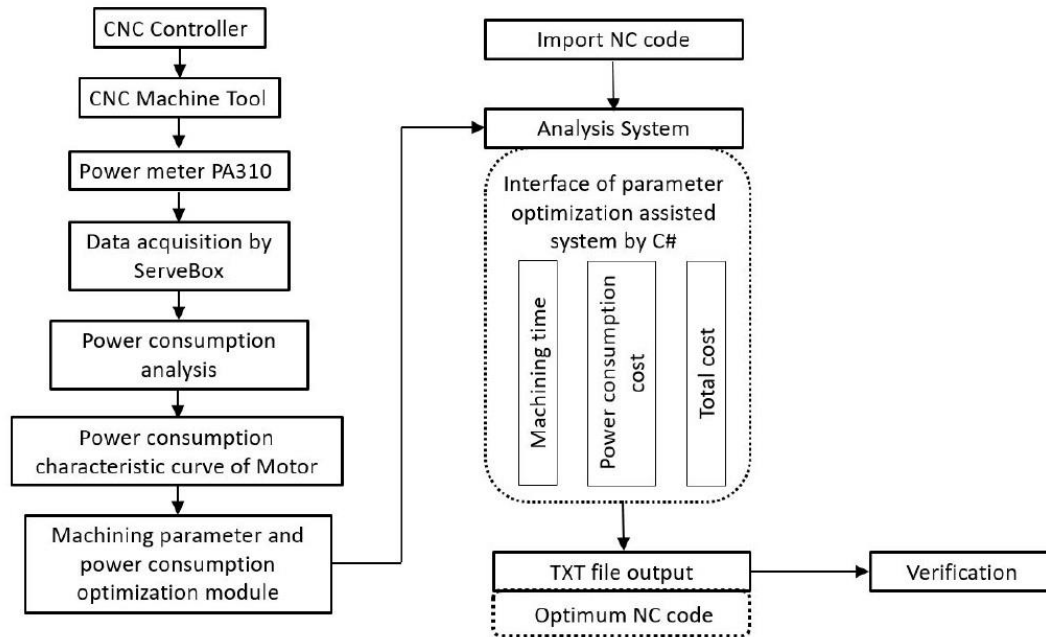


Figure 1. Optimization flowchart machining and power consumption [53]

2.4. Genetic algorithm

To obtain the optimized member in a population, the genetic optimization algorithm is presented which can solve the linear and nonlinear problems. To implement the optimization method, a set of chromosomes or strings with an infinite length is considered for each bit which is called a gene. A population is a selected number of chromosomes, and a generation is the population at a given time. Reproduction, crossover, and mutation are main operators of the algorithms. The Reproduction is the first operator of the algorithm which copies individual strings into a separate string according to their fitness values. The crossover is the second genetic operator which exchanges some part of two or more chromosomes to reproduce new offspring with the hope of collecting all good features of previous ones. Finally, to keep diversity in the population in order to get a quicker convergence, mutation is applied after crossover to provide a small randomness into the new chromosome.

To increase accuracy in part production process using optimized fitness value in machine tools, application of the genetic algorithm in obtaining the optimized parameters of support vector machine is investigated by Zhu et al. [54]. In order to increase performances of machining operations using the optimized machining parameters, Chandrasekaran et al. [55] presented a review in application of the neural networks, fuzzy sets and genetic algorithms in machining parameter optimization process.

The optimization process of cutting parameters, such as cutting speed, feed rate, cutting depth, and the number of passes for multi-pass milling operations using genetic algorithms to improve efficiency in part production processes is studied by An et al. [56]. Machining parameter optimization of the milling process based on

genetic algorithms to increase efficiency and decrease the cost of component production processes is presented by Yang et al. [57].

Zhang et al. [58] investigated the application of the genetic algorithm to obtain optimized machining parameters, such as processing time and electrode wear in micro-EDM machining operations, to improve efficiency in component production processes. Selvam et al. [59] presented optimization of machining parameters for face friction operation in a vertical CNC milling machine using genetic algorithm to minimize surface roughness in mild steel milling operations using three zinc-coated carbide devices. Ahmad et al. [60] presented optimization of cutting parameters for end milling operation by soap-based genetic algorithm to improve productivity in part production processes.

Sardiñas et al. [61] presented multi-objective optimization of cutting parameters, such as cut size, feed rate, and spindle speed in turning processes using the genetic algorithm in order to improve profitability in part production processes. Genetic algorithm-based optimization of the cutting parameters in turning processes to reduce machining time in component production processes is presented by D'addona and Teti [62]. The optimization process of drilling parameters, such as cutting speed, feed rate, and cutting environment in AISI 1045 drilling using surface response technique and genetic algorithm to reduce surface roughness in part production process is investigated by Kilickap et al. [63]. Optimized machining parameters, such as feed rate and spindle speed using the genetic algorithm to decrease the tool deflection error in the milling operations is presented by Soori et al. [23]. Flowchart and strategy of machining parameters optimization by genetic algorithm is shown in Fig. 2 [23].

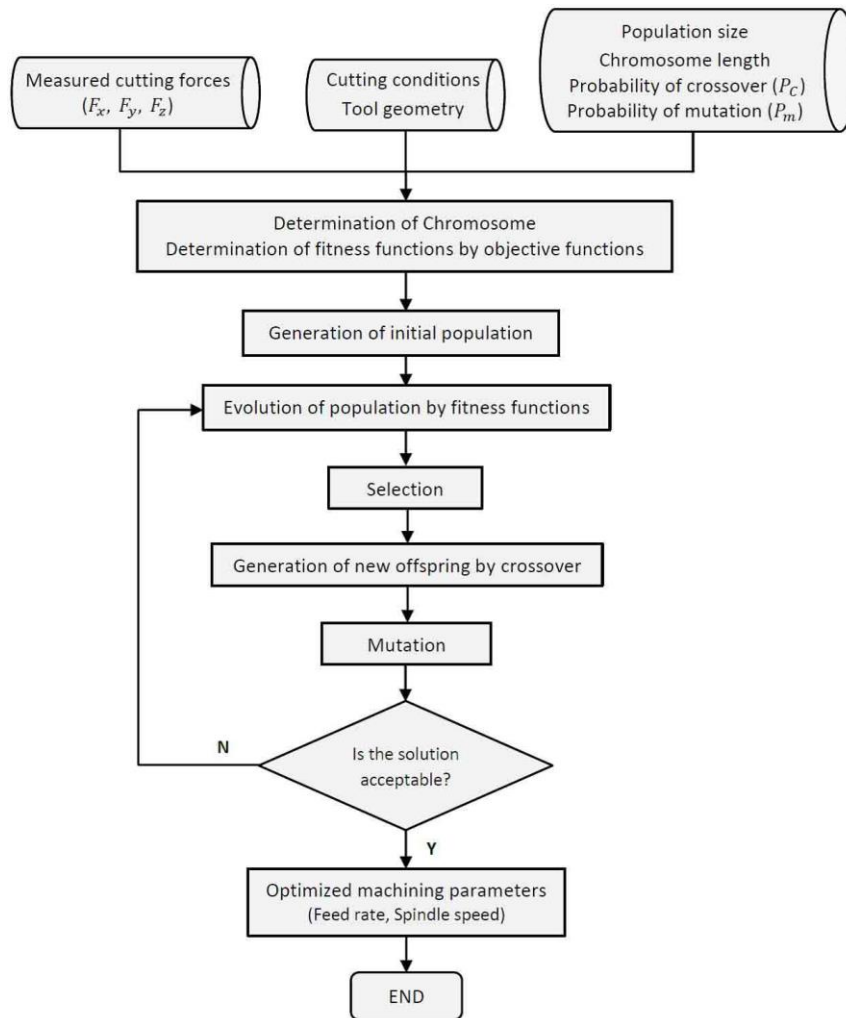


Figure 2. Flowchart and strategy of machining parameters optimization by genetic algorithm[23].

2.5. Artificial Neural networks

The Artificial neural network (ANN) optimization method is nonlinear mapping systems in the field of artificial intelligence to calculate the optimized parameters by using a non-linear regression. To calculate the optimized parameters, the new objective function should be polynomial. As a result, the optimum setting of different parameters till date remains a troublesome assignment can be calculated as optimized parameter of the problem.

The production of an artificial neural network for surface roughness and system prediction to reduce surface roughness of generated parts is investigated by Iriaye et al. [64].

To improve efficiency in the component development process, the application of the artificial neural networks and the genetic algorithm to obtain the selection of cutting inserts and the optimization of cutting parameters for turning operations is proposed by Pardo [65]. Optimization of surface roughness parameter in milling operations using fuzzy logic and artificial neural network methods is investigated by Vignesh et al. [66] to increase surface quality of produced parts using milling operations. In order to increase profit rate, and the quality of the final products in part production process, parameter optimization of

milling operation using teaching-learning-based optimization and artificial neural network is studied by Warghat and Deshmukh [67]. To minimize the surface roughness of produced parts in the end milling machining operations, application of the artificial neural network in prediction of the surface roughness is presented by Zain et al. [68]. To enhance the productivity in part manufacturing process, optimization of neural network using taguchi-grey relational analysis with signal-to-noise ratio approach for 2.5D end milling process is presented by Kumar et al. [69]. Optimum machining parameters in face milling operations of X20Cr13 stainless steel by using neural network and harmony search algorithm is investigated by Razfar et al. [70] to minimize the surface roughness in part production process.

2.6. Artificial bee colony algorithm

The Artificial Bee Colony algorithm is a stochastic algorithm based on population that simulates the foraging behavior of honey bee colonies to determine the optimal parameter in the problems. Inside the algorithm three classes of bees are known as working bees, onlookers, and scouts. The algorithm only contains one artificial bee used for each supply of food. Working bees go to their food source and back to hive and dance in this area. The

onlookers observe the dances of working bees and choose food sources according to dances to pick the best type of food. As a result, the best source of food is chosen as optimized member of the population.

To obtain optimized metal removal rate and surface roughness in component production processes, the parametric optimization method of electrochemical machining, electrochemical discharge machining and electrochemical micromachining processes using artificial bee colony algorithm is presented by Samanta and Chakraborty [71]. To enhance efficiency in part production processes, a modified artificial bee colony algorithm for real-parameter optimization process in machining operations is investigated by Akay and Karaboga [72].

Optimization of cutting parameters in multi-pass turning using artificial bee colony is investigated by Yildiz [73] to increase productivity in part production process using turning operations. Application of the artificial bee colony algorithm in parameter optimization of support vector machine is studied by Ming and Yue-qiao [74] to increase accuracy in part production process using optimized fitness value in machine tools. To minimize the surface roughness of produced parts, optimal machining control parameters using artificial bee colony is investigated by Yusup et al. [75]. Das et al. [76] investigated the application of artificial bee colony algorithm in the component development process to optimize the material removal rate and surface roughness in EDM of EN31 tool steel.

To enhance the productivity in part manufacturing process using laser beam machining operations, optimized process parameters of the production method using artificial bee colony algorithm is studied by Mukherjee et al. [77]. Multi-objective optimization of process parameters for the electrochemical machining of SIC composite using a hybrid fuzzy-artificial bee colony algorithm to optimize material removal speeds, to reduce surface roughness and to over-cut in component output using electrochemical machining is presented by Solaiyappan et al. [78]. Das et al. [79] presented a research work on electrochemical machining of EN31 steel for optimizing the rate of material removal and surface roughness using artificial bee colony algorithm.

2.7. Simulated annealing

To calculate the optimized parameter in the problem, the simulation of annealing process of heated solids is considered. In the annealing process, the temperatures of heated solids are increased to convert it to the liquid phase. Then, it will slowly cool through lowering the temperature of the heat bath. The minimum energy state with the greatest probability at the lowest temperature of the part in an annealing process will be selected as the optimized parameter of the problem. To present applications of the simulation methodologies in machining parameter optimizations, integration of process simulation in machining parameter optimization is investigated by Stori et al. [80]. A technique for optimizing Non-linear programming is used in the analysis to select process parameters based on closed-form analytical constraint equations. The application of the genetic algorithm and simulated annealing in order to optimize machining

parameters, such as cutting distance, cutting speed and feed rate for turning cylindrical stock operations to improve the surface quality of the component output is presented by Thompson and Fidler [81]. To optimize the machining parameters during CNC turning operations of AL alloys, advanced optimization methodology based on simulated annealing technique is presented by Aghdeab et al. [82].

Machining condition optimization by genetic algorithms and simulated annealing to improve performance in component development processes using machining operations is presented by Khan et al. [83]. The optimization of electric discharge machining using simulated annealing to simultaneously increase the rate of material removal as well as minimize surface roughness is investigated by Yang et al. [84]. Optimization of multi-pass milling using parallel genetic algorithm and parallel genetic simulation annealing to improve efficiency in machining operations using optimized machining parameters is presented by Wang et al. [85].

To achieve the global optimization of product development and manufacturing in part production using machining operations, a simulated annealing-based optimization approach for integrated process planning and scheduling is investigated by Li and McMahon [86]. To estimate optimal process parameters of the abrasive waterjet machining operations, applications of the genetic algorithm and simulated annealing is investigated by Zain et al. [87]. The optimization cycle of turning process parameters for cylindrical parts using the simulated annealing approach to increase performance in product manufacturing utilizing turning operations is investigated by Kolahan and Abachizadeh [88]. Multi-objective optimization of high-speed milling operations with simultaneous genetic computational annealing to increase performance in machining operations utilizing tailored machining parameters is presented by Wang et al. [89]. To minimize the surface roughness in end milling Ti-6Al-4V, applications of the simulated annealing method in obtaining the optimized machining parameters, such as radial rake angle is investigated by Zian et al. [90]. The developed flowchart in the study for optimization process of machining parameters is shown in the figure 3 [90].

2.8. Ant colony optimization

The ant colony optimization algorithm is inspired by the foraging actions of the ants in discovering short paths between their nests and sources of food. Growing ant in this algorithm represents a complete solution to find the shortest route between their nest and food sources. After all the ants create solutions, local search is then applied to determine the optimal response to the question. The flowchart of the ant colony optimization is presented by Karaboga and Akay [91] as shown in the figure 4.

Optimization of multi-pass turning operations using ant colony system is investigated by Vijayakumar et al. [92] to minimize the surface roughness of produced parts. Optimization of operations sequence in computer aided process planning of part production using an ant colony algorithm is studied by Krishna and Rao [93] to increase efficiency in part manufacturing using optimized production parameters. To decrease the cost for machining

operations, application of ant colony optimization algorithm in process planning optimization is investigated by Liu et al. [94]. Optimized process design for a hybrid punch and laser cutting system using ant colony optimization to achieve the best cutting tool paths in terms of quality enhancement of the component manufacturing cycle is presented by Wang and Xie [95]. Parameter optimization of support vector machine by improved ant colony optimization is presented by Rongali and Yalavarthi [96] to optimize the parameters of machining operations in terms of productivity enhancement of part production. Multi objective optimization in drilling operations of carbon fiber reinforced composites using ant colony algorithm is presented by Sankar and Umamaheswarrao [97] to increase material removal rate in terms of efficiency enhancement of part manufacturing process. To minimize machining time in improving the

efficiency of component production processes, tool path length optimization of contour parallel milling operations based on modified ant colony is investigated by Abdullah et al. [98]. To minimize cutting tool failure in terms of increased productivity of the component production process, delamination factor and optimization of cutting force in the finishing of carbon fiber reinforced polymer composites using back propagation neural network-ant colony optimization is presented by Soepangkat et al. [99]. The use of the ant colony optimization for machining parameters in final milling operations to eliminate surface roughness in component development processes is studied by Kadirgama et al. [100]. Optimization of cutting parameters in multipass turning operation using ant colony algorithm method is studied by Pansare et al. [101] to enhance efficiency in part production process.

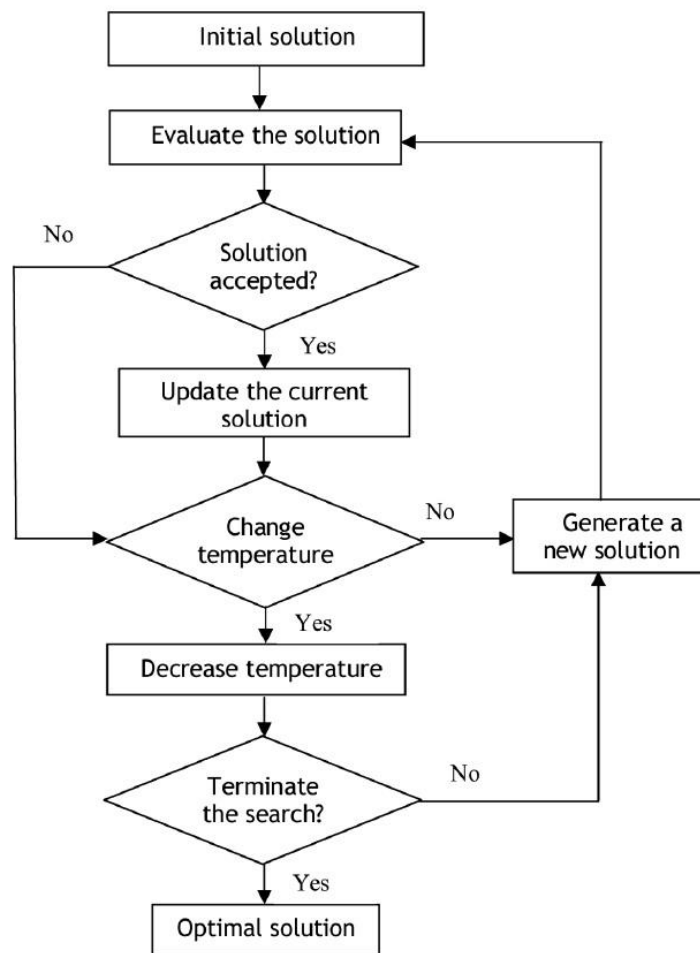


Figure 3. The developed flowchart for optimization process of machining parameters by using the simulated annealing method [90].

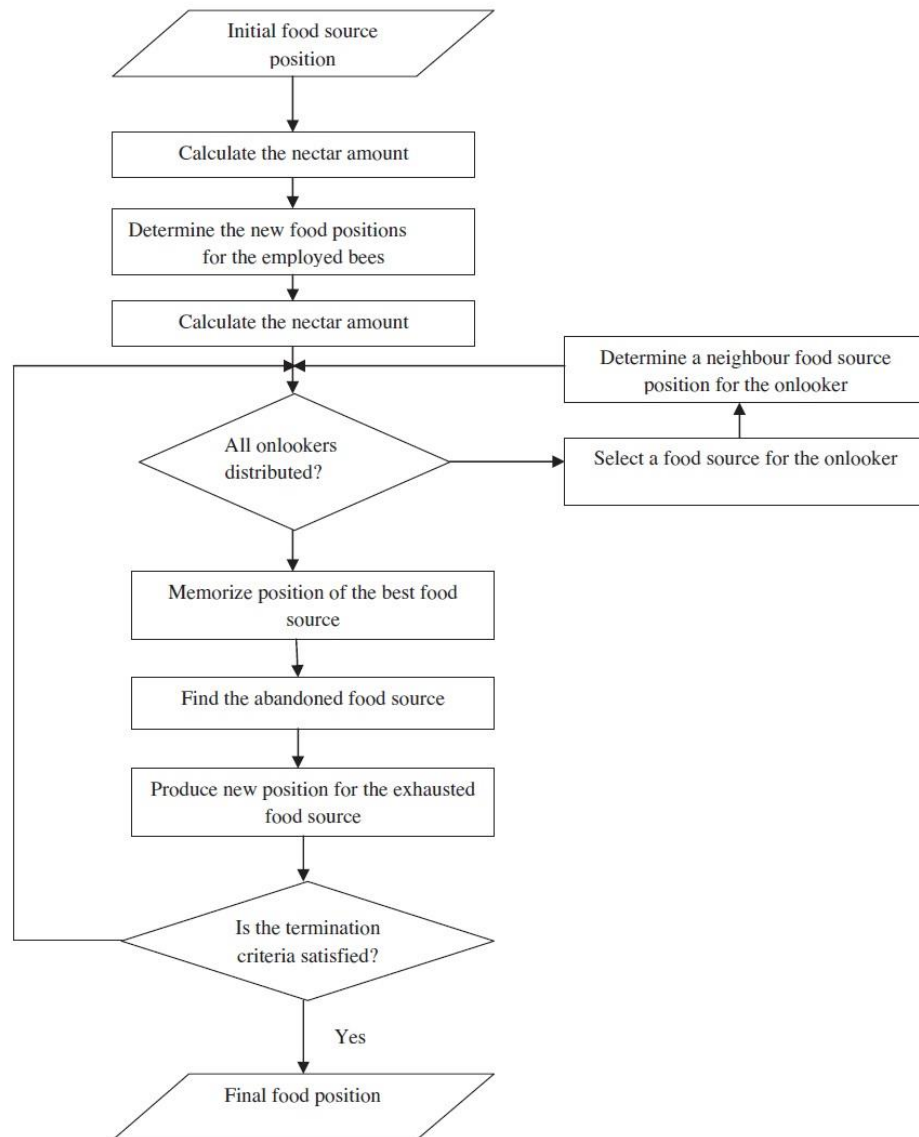


Figure 4. The flowchart of the ant colony optimization [91].

2.9. Particle swarm optimization

The optimization of the population-based particle swarm is developed using the technique of artificial intelligence to calculate the optimal parameter. In this algorithm, a population of simple agents is created, interacting locally with each other and with their environment to get the optimized member as a point or surface in an n-dimensional space. Particles then move through solution space, and are evaluated in compliance with those success requirements at each time period. The orientation of each particle is determined by its best-known local location, and it is also directed towards the best-known search-space locations. As a consequence, the swarm may be estimated as the optimal community participant for the right solutions. Application of the particle swarm optimization method in obtaining the optimized machining parameters such as time for machining, the material removal rate, and the feed rate is investigated by Vergara-Villegas [102] in order to increase efficiency in part production process. To obtain the

maximum material removal rate and good surface roughness in electrochemical machining operations, application of the particle swarm optimization method in the part production process is investigated by Chenthil and Ravindran [103]. In order to obtain the minimum quantity lubrication environment in machining operations of the Titanium Alloy, application of the surface methodology and particle swarm optimization is investigated by Gupta et al. [104]. To increase efficiency in machining operations of hard to cut materials such as Inconel 718 super alloy, application of the particle swarm optimization method in optimization process of electrical discharge machining parameters, such as material removal rate, electrode wear ratio, surface roughness and radial overcut are studied by Mohanty et al. [105]. The optimization process of machining parameters, such as spindle speed, feed rate, and cut depth in machining operations of AA6061 materials using surface reaction methodology and particle swarm optimization to reduce surface roughness and power consumption in terms of productivity enhancement of component output is investigated by Lmalghan et al.

[106]. Implementation of particle swarm optimization and surface reaction technique for machining parameters optimization of aluminum matrix composites in milling process is presented by Malghan et al. [107]. Surface roughness modeling and optimization in keyway milling using ANN, genetic algorithm, and particle swarm optimization to minimize surface roughness in part production processes is investigated by Ghosh et al. [108]. The use of the genetic algorithm and particle swarm optimization in order to obtain standardized parameters of laser beam micro machining operations such as current (A), pulse frequency (Hz), and scanning speed (mm / sec) to improve surface quality in generated pieces is investigated by Kalita et al. [109]. In order to reduce surface roughness in the component manufacturing process utilizing milling operations, an efficient cellular particle swarm optimization for parameter optimization of a multi-pass milling method is investigated by Gao et al. [110]. Optimization of characteristic parameters in milling by using particle swarm optimization is presented by Župerl et al. [111] to minimize the surface roughness by using optimized cutting speed and feed rates in machining operations. The developed optimization algorithm to obtain the optimized cutting conditions in the study is shown in the figure 5 [111].

2.10. Scatter search technique

The Scatter search optimization technique is a method based on combining decision rules and constraints in order to obtain the best solution based on the original elements. As a result, joining solutions based on generalized path are calculated and evaluated in order to select the best solution as optimized solution of the population. To increase efficiency in part production process, optimization of machining parameters, such as depth of cut, feed and cutting speed using scatter search algorithm is investigated by Siva and Balachithra [112]. To obtain the maximum machine power, required surface finish and maximum cutting speed in milling operations, optimization of machining parameters using the scatter search approach method is presented by Krishna and Rao [113]. To improve production efficiency and output levels in component manufacturing processes, multi-objective optimization of surface grinding operations for machining operations, such as wheel speed, job piece size, dressing depth and dressing lead using scatter check approach is investigated by Krishna and Rao [114]. An optimum parallel set of design and manufacturing tolerances for specific stack-up conditions using scatter search approach to reduce the overall cost of manufacturing in component production cycle is presented by Krishna and Rao [115]. Determination of optimal machining conditions using scatter search is studied by Chen and Chen [116] to improve the machining economics, machining quality and machining safety in part manufacturing process using machining operations. Application of the scatter search optimization for multi node machining operations with fixture layout is presented by Prabu [117] to minimize geometric error and deformation in workpiece during machining operations. Flowchart representing scatter search in fixture layout optimization is shown in the figure 6 [117].

2.11. Response surface methodology

In the response surface optimization methodology, sequence of designed experiments is used in order to obtain an optimal solution for the problems. In this method, statistical approaches can be employed to maximize the speed of optimization calculation in order to find the optimal answer within less computational works. Parameter optimization in forming operations of the AA5052 Aluminum using response surface methodology is presented by Mugendiran et al. [118] to optimize the surface roughness as well as wall thickness condition in part production process. The optimization mechanism of the abrasive water jet machining parameters, such as pumping system, stand-off distance and nozzle speed in green composite parts using reaction surface technique to reduce surface roughness and cycle time in component production processes is studied by Bhowmik and Ray [119]. Prediction and optimization of machining parameters for minimizing power consumption and surface roughness in machining operations using response surface methodology is investigated by Kant and Sangwan [120]. The developed optimization algorithm in the study is shown in the figure 7 [120]. To obtain the optimized machining parameters during electrochemical machining operations, application of the response surface methodology is presented by Kalaimathi et al. [121]. The response surface method is applied by Vinayagamoorthy et al. [122] to obtain the optimized thrust force and torque during drilling operations of composite structures.

To reduce surface roughness in developed parts using turning operations, the optimization of machining parameters for turning operations based on surface reaction methodology is studied by Makadia and Nanavati [123]. Process parameter optimization for fused deposition modeling using surface response technique combined with fuzzy inference framework to increase accuracy and efficiency in the production process of the component is investigated by Peng et al. [124]. To minimize the surface roughness in machining operations of glass fiber reinforced plastics with a polycrystalline diamond tool, application of Taguchi and response surface methodologies is investigated by Palanikumar [125]. Parametric optimization of powder mixed electrical discharge machining by response surface methodology to maximize the rate of material removal and minimize surface roughness in part production processes is presented by Kansal et al. [126]. The optimization of device geometry parameters for turning AISI 1040 steel operations based on the reaction surface technique to reduce surface roughness in component development processes is studied by Neşeli et al. [127]. Multi-process parameter optimization in face milling of Ti6Al4V alloy using response surface methodology is investigated by Saini et al. [128] to obtain the optimized surface roughness, tool wear and tool vibration conditions in part production process. To minimize surface roughness in part production process using electric discharge machining operations, optimization of the machining parameters, such as pulse current, pulse on-time and pulse off-time for Al/ZrO₂ composite workpiece through response surface methodology is presented by Alagarsamy et al. [129]. To investigate effects of machining parameters, such as

machining voltage and machining on time, on the recast material layer and micro-hardness of the machined sample, optimization of Micro-electro Discharge Drilling Parameters of Ti6Al4V Using Response Surface Methodology and Genetic Algorithm is presented by Kumar and Hussain [130]. Optimization of machining parameters, such as cutting speed, feed rate and approach

angle and cutting fluids based on response surface methodology in turning operations of titanium alloy is investigated by Kumar Gupta et al. [131] to minimize quantity lubrication and surface roughness in turning operations. The developed methodology in the study is shown in the figure 8[131].

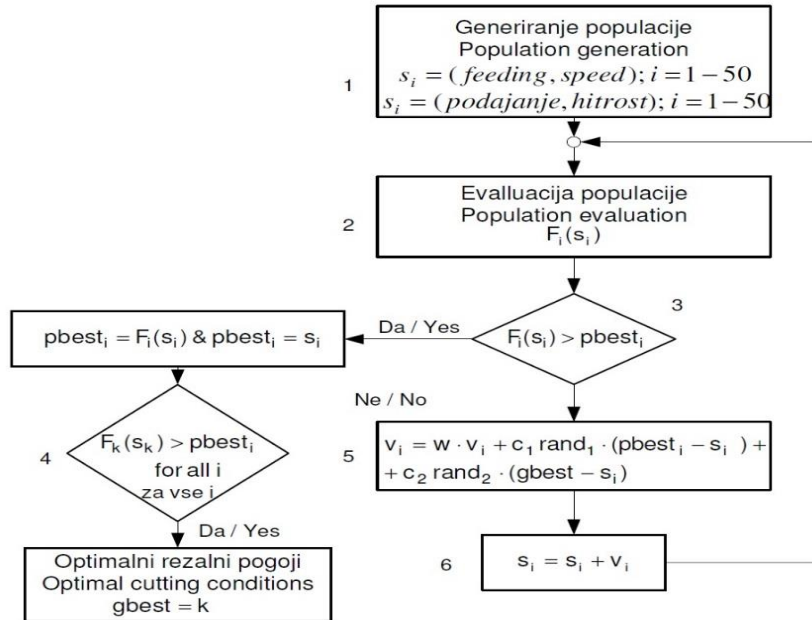


Figure 5. The developed optimization algorithm using particle swarm optimization to obtain the optimized cutting conditions [111].

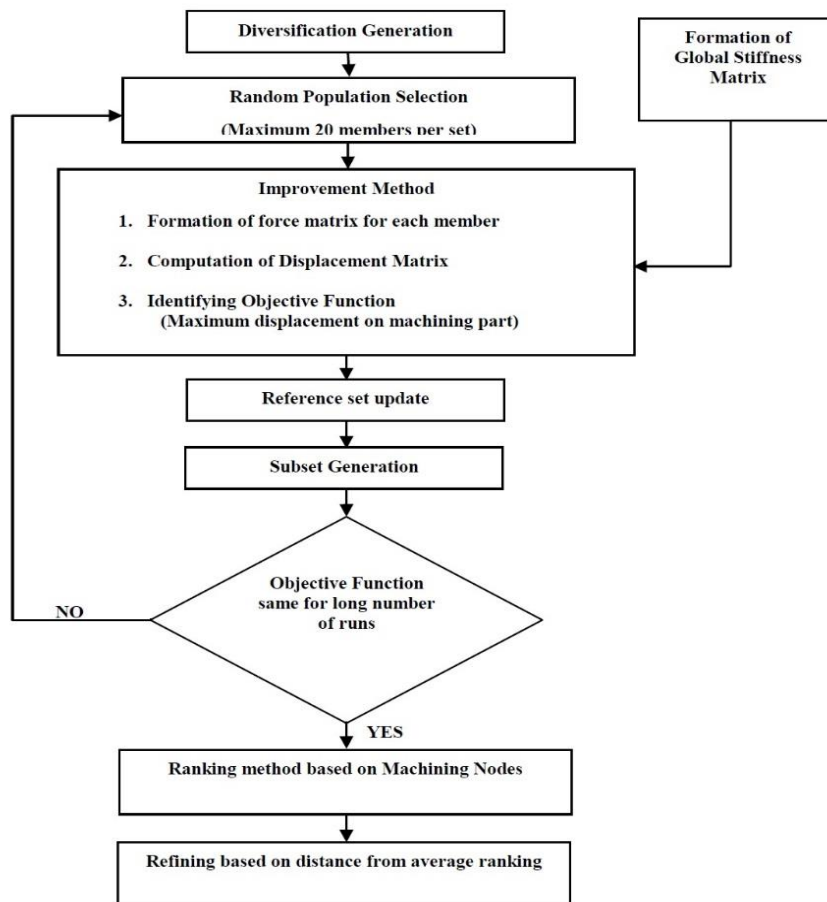


Figure 6. Flowchart representing scatter search in fixture layout optimization [117].

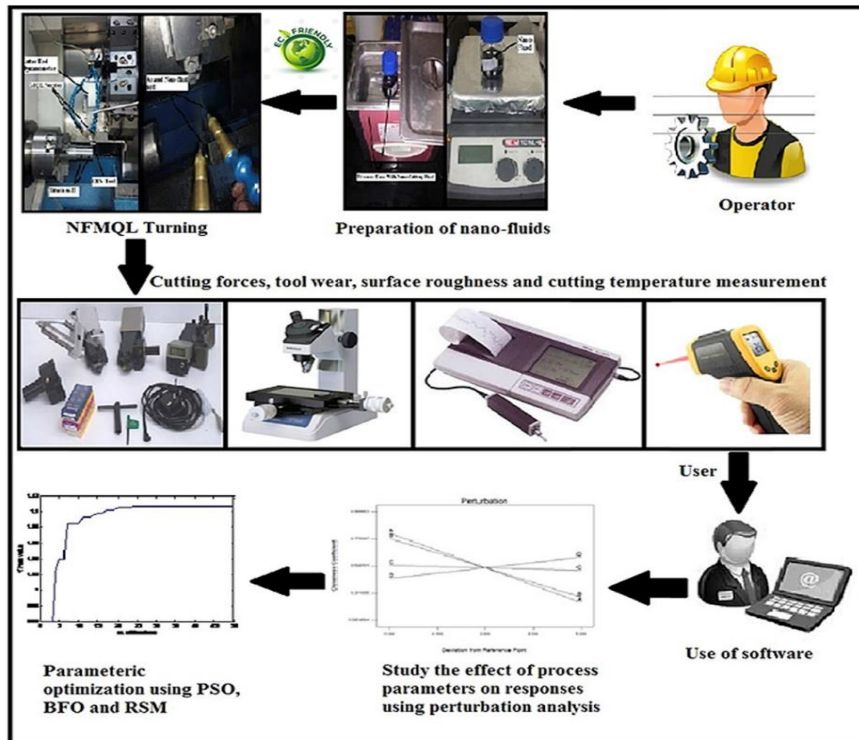


Figure 7. The developed optimization methodology to minimize quantity lubrication and surface roughness in turning operations [131].

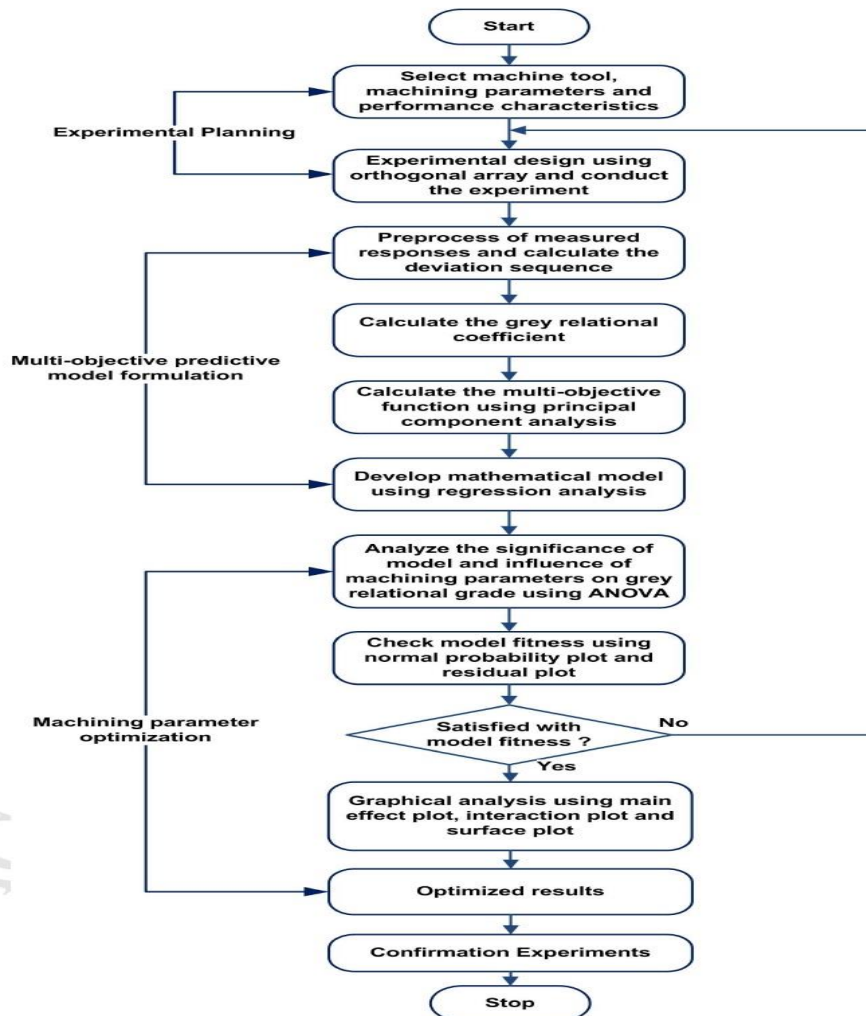


Figure 8. The developed optimization algorithm to minimize power consumption and surface roughness in machining operations [120].

2.12. Harmony search algorithm

In the harmony search optimization algorithm, the behavior of the musicians in finding a pleasing harmony is simulated in order to obtain the optimized member of population. The process of search for the perfect harmony is based on the optimization method in calculating the optimal solutions in engineering problems. Optimization process of electric discharge machining parameters such as pulse on time, peak current, servo voltage and servo speed using harmony search algorithm is investigated by Deris et al. [132] to minimize surface roughness in part production process. To obtain the optimum cutting parameters such as number of passes, depth of cut in each pass, cutting speed and feed rate for multi-pass face-milling operations, application of the harmony search algorithm in minimizing the total cost of produced parts is presented by Zarei et al. [133]. Optimization of drilling process parameters using harmony search algorithm to improve productivity in component production processes is presented by Chatterjee et al. [134]. The application of a Fuzzy Embedded Harmony Search Algorithm to obtain optimized machining parameters such as drill speed, feed and drill diameter in drilling operations of CFRP (polyester) composites to obtain optimized thrust power, torque, surface roughness and delamination factor conditions in component

production processes is presented by Abhishek et al. [135]. Optimization approach to determine the optimal process parameters such as part thickness, taper angle, pulse duration, discharge current, wire speed and wire tension in wire electrical discharge machining process during taper cutting operation using the harmony search algorithm is investigated by Nayak et al. [136] to optimize the angular error, surface roughness, and cutting speed conditions in part production process. In order to minimize surface roughness in the component development cycle using milling operations, parametric optimization of face friction using harmony search algorithm is proposed by Nagarchi and Patel [137]. Application of the harmony search optimization in obtaining the EDM machining process parameters, such as pulse on time, peak current, servo voltage and servo speed in die sinking operations of SS316L stainless steel is studied by Deris et al. [138] to increase dimensional accuracy of produced parts using EDM machining operations. Optimization process of machining parameters such as spindle speed, feed rate and depth of cut in turning operations of AISI D2 Steel using the Grey Relation Analysis integrated with Harmony Search method is investigated by Kumari et al. [139] to maximize the material removal rate and minimize the surface roughness in part production process.

Recent development of the machining parameter optimization is shown in the table 1.

Table 1. Recent development of machining parameter optimization

Topic of research work	Papers	Finding/ Discoveries
Taguchi method	[26]	The machining parameters are designed to improve the surface strength of the manufactured parts in Inconel 718 super alloy's end milling operations.
	[28]	Parameters of machining such as spindle rpm, feed rate and cut depth during micro-milling of Ti6Al4V titanium alloy and materials from Inconel 718 are optimized.
	[32]	The effect of CNC milling machining parameters on surface finish using Taguchi method is investigated to increase productivity in component production process.
Fuzzy logic algorithm	[36]	The process of optimizing machining parameters such as the cutting depth, cutting speed, feed rate, and tool nose runoff for CNC machining operations are studied using fuzzy and game theory techniques.
	[40]	The optimization of machining parameters is explored when transforming Al-SiC-Gr hybrid metal matrix composites using grey-fuzzy algorithm.
	[44]	Multi-objective optimization of process parameters for wire electro discharge machining using grey-fuzzy methodology is investigated to improve component output efficiency.
Artificial intelligence	[46]	Applications of the artificial intelligence in the optimization process of part production are investigated to increase productivity in part production process using turning operations.
	[49]	Application of artificial intelligence in the parameter optimization method of a multi-pass milling method is studied in order to reduce the machining time.
	[51]	To improve surface quality in machined components, supervisory controller is developed using artificial intelligence for real-time surface quality assurance in CNC machining.
Genetic algorithm	[56]	To maximize performance, the optimization process of cutting parameters such as cutting speed, feed rate, cutting depth and number of passes is studied using genetic algorithms for multi-pass milling operations.
	[59]	Optimization of machining parameters for face friction operation in a vertical CNC milling machine is introduced using genetic algorithm to minimize surface roughness.
	[62]	Genetic algorithm-based optimization of cutting parameters in turning processes is introduced to reduce machining time.
Artificial Neural networks	[65]	The implementation of artificial neural networks and genetic algorithm to obtain the cutting-insert selection and cutting-parameter optimization is investigated in order to improve the output in turning operation.
	[67]	Parameter optimization of milling operation is researched using teaching-learning-based optimization and artificial neural network.
	[69]	Optimum machining parameters in X20Cr13 stainless steel face milling operations are investigated through the use of neural network and harmony search algorithm.
Artificial bee colony algorithm	[71]	To optimize material removal efficiency, parametric optimization processes of electrochemical machining, electrochemical discharge machining and electrochemical micromachining processes using artificial bee colony algorithm are provided.
	[75]	Optimal machining control parameters using artificial bee colony are investigated to reduce the surface roughness of the generated parts.
	[78]	Multi-objective optimization of process parameters for SiC composite electrochemical machining is introduced using hybrid fuzzy-artificial bee colony algorithm.
Simulated annealing	[80]	Integration of process simulation into machining parameter optimization is explored in order to present implementations of the simulation methodologies of machining parameter optimization.
	[83]	Made state optimization by genetic algorithms and virtual annealing is proposed to increase performance in component manufacturing processes using machining operations.
	[87]	Versions of genetic algorithm and computational annealing are explored to approximate optimum process parameters of the abrasive water jet machining operations.
Ant colony optimization	[93]	Optimization of operations sequence using an ant colony algorithm is studied in computer-aided process planning of component output.
	[96]	Optimization of support vector machine parameters is provided by improved optimization of ant colony to maximize the machining performances.
	[100]	To minimize the surface roughness of the manufactured parts, the modification of the optimization of the ant colony is studied for machining parameters in end milling operations.
Particle swarm optimization	[102]	For maximize performance, the use of the particle swarm optimization approach is investigated in obtaining the optimized parameters of machining such as machining time, material removal rate and feed rate.
	[105]	To improve efficiency in the electrical discharge machining, the use of the particle swarm optimization approach in the optimization process of parameters such as material removal rate, electrode wear ratio, surface roughness, and radial overcut is studied.
	[108]	Modeling and optimization of surface roughness in keyway milling using ANN, genetic algorithm, and particle swarm optimization is studied to minimize surface roughness of generated sections.
Scatter search technique	[113]	To achieve full machine tool power, necessary surface finish and full cutting speed in milling operations, optimization of the machining parameters is provided using the scatter quest technique.
	[115]	To minimize the machining costs, optimum design range and manufacturing tolerances are provided simultaneously with specific stack-up conditions using scatter search process.
	[117]	To reduce the geometric error, implementation of scatter search optimization with a fixture architecture is introduced for multi-node machining operations.
Response surface methodology	[119]	To minimize surface roughness, the process of optimizing abrasive water jet machining parameters such as pumping mechanism, stand-off width, and nozzle speed in sections of green composites is studied using reaction surface methodology.
	[126]	Parametric optimization of powder blended electrical discharge machining by reaction surface technique is provided to optimize the rate of material removal.
	[128]	Multi-process parameter optimization in face friction of Ti6Al4V alloy using reaction surface methodology is investigated to reduce the surface roughness.
Harmony search algorithm	[132]	The method of optimizing electric discharge machining parameters such as pulse on time, peak speed, servo voltage and servo velocity is investigated using harmony search algorithm to minimize surface roughness.
	[135]	The implementation of a Fuzzy embedded harmony search algorithm to obtain optimized machining parameters such as drill rpm, feed and drill diameter in CFRP (polyester) composite drilling operations is introduced.
	[138]	In order to improve dimensional precision, the application of harmony search optimization is studied in obtaining the parameters of the EDM machining cycle such as pulse on time, peak current, servo voltage and servo speed in the SS316L stainless steel die sinking operations.

3. Conclusion and future research works

In the present research work, a review in recent development of machining parameter optimization is presented. In order to provide a review in optimization procedures of machining parameters, applications of the different optimization methods, such as Taguchi method, fuzzy logic algorithm, artificial intelligence, genetic algorithm, artificial neural networks and artificial bee colony algorithm, simulated annealing, ant colony optimization, particle swarm optimization, scatter search technique, response surface methodology and harmony search algorithm in optimization process of machining parameters is investigated. The results of machining parameters such as spindle speed, cut distance, and feed rate are studied to reduce the surface roughness as well as machining time in milling operations. The efficient machining parameters such as cut width, feed rate, and spindle speed are investigated to reduce the surface roughness as well as time of machining cycle in turning operations. In the Electro Discharge Machining (EDM) operations, the machining parameters such as peak speed, gap voltage, service cycle and pulse on time are optimized to achieve the optimal material removal efficiency, tool wear and surface roughness in component development method. Using the wire EDM operations, machining parameters such as spark on time, spark off time, input current are analyzed and optimized to increase material removal efficiency, surface roughness and spark gap in component production cycle. To maximize the material removal rate, minimize the surface roughness and over-cut in part production process using electrochemical machining operations, effective machining parameters such as current, voltage, electrolyte concentration and feed rate are analyzed and optimized. In the abrasive water jet machining operations, machining parameters such as jet transverse speed, stand-off distance and abrasive flow are optimized in order to minimize the surface roughness and maximize the material removal rate in part production process. The effective machining parameters such as laser power, cutting speed, pressure of the gas and pulse width in the laser beam machining operations are optimized in order to minimize the surface roughness and maximize the material removal rate in part production process.

Machining operations of hard to cut materials such as super alloys and Inconel materials and composite materials can be analyzed and optimized to increase efficiency in part production process. Application of optimization process in increasing the cutting tool life can be developed by considering the different materials of cutting tools, cutting tool wear and generated heat in the cutting zone. The automated tool changing systems in machine tool centers can be analyzed in order to be optimized. Also, parameters of cutting tool geometries as shape and different angles can be analyzed and optimized in order to decrease cutting forces in terms of cutting tool life enhancement in machining operations. Moreover, cutting inserts and tool holders can be optimized in order to improve efficiency in part production process using machining operations. Energy consumption of machine tools can be analyzed in order to be decreased using optimization methods in order to decrease cost of part production. Quantity lubrication parameters during

machining operations can be considered to be optimized in order to be minimized. Form tolerance and orientation tolerance in EDM machining operations can be considered in order to obtain the optimized machining parameters. Parameters of micro-and nano-machining operations can be analyzed in order to be optimized in terms of productivity enhancement of part manufacturing.

Waste materials in part production process using machining operations can be decreased by applying the optimized machining parameters to the process of part production. Applications of virtual machining systems in optimization process of machining operations can be developed in order to increase the effects of optimization techniques in terms of productivity enhancement of part production. Application of the Computer Aided Process Planning (CAPP) in the optimization process of machining operations can be investigated in order to increase added values in process of part production. Application of mathematical modeling in increasing the surface roughness of produced part can be developed by using optimized machining parameters in order to increase quality as well as efficiency in part manufacturing process. The process of workpiece clamping and machining fixtures can be analyzed and optimized in order to increase accuracy in process of part production using machining operations. Moreover, machining fixture layout for tolerance requirements can be optimized in machining operations in order to increase accuracy in part production process.

The optimization process can be applied to the grinding as well as polishing operations in terms of productivity enhancement of part production using optimized machining parameters. Applications of mathematical modelling as well as computational methods in optimization process of machining operations can be developed in order to enhance the efficiency of machining operations. Machining parameters in multi-passes of roughing as well as finishing operations can be optimized in order to decrease the machining time as well as productivity of part production using machining operations. Applications of optimization methods in the intelligent machining systems can be investigated in order to provide intelligent machining parameter selection and intelligent process management during machining operations. Machining parameters optimization of ultrasonic assisted turning and milling operations can be investigated in order to minimize the residual stress as well as vibration during chip formation process. Surface quality during milling operations of matrix composite structures can be analyzed in order to be enhanced by using the optimized machining parameters. Application of online monitoring systems in machining parameters optimization can be studied in order to decrease the cutting tool failure and energy consumption during machining operations. Optimization process of sustainable manufacturing process can be studied to reduce negative environmental consequences while preserving energy and natural resources in part production process using machining operations.

The residual stress due to machining operations in produced parts can be decreased using optimized machining parameters in order to increase performances of machined parts in the hard-working conditions. Multi-pass machining operations can be analyzed and optimized in order to decrease time and cost of part production.

Effective machining parameters in chatter and vibration can be analyzed in order to increase accuracy in machined parts by using the optimized machining parameters. The machining operations in the fourth generation of developed industries as industry 4.0 can be analyzed and optimized in order to modify the process of part production.

These are suggestions for the future research works in the research filed of machining parameters optimization to increase efficiency in part manufacturing process using machining operations. So, high quality products regarding to the minimization of machining time and cost of part production can be presented in terms part production development using optimized machining operations.

References

- [1] Nahak, B.; Gupta, A. A review on optimization of machining performances and recent developments in electro discharge machining. *Manufacturing Review*, 2019, 6: 2.
- [2] Mukherjee, I.; Ray, P.K. A review of optimization techniques in metal cutting processes. *Computers & Industrial Engineering*, 2006, 50(1-2): 15-34.
- [3] Yusup, N.; Zain, A.M.; Hashim, S.Z.M. Evolutionary techniques in optimizing machining parameters: Review and recent applications (2007–2011). *Expert Systems with Applications*, 2012, 39(10): 9909-9927.
- [4] Benardos, P.; Vosniakos, G.-C. Predicting surface roughness in machining: a review. *International journal of machine tools and manufacture*, 2003, 43(8): 833-844.
- [5] Rao, R.V.; Kalyankar, V. Optimization of modern machining processes using advanced optimization techniques: a review. *The International Journal of Advanced Manufacturing Technology*, 2014, 73(5-8): 1159-1188.
- [6] RazlanYusoff, A.; Suffian, M.; Taib, M.Y. Literature review of optimization technique for chatter suppression in machining. *Journal of Mechanical Engineering and Sciences (JMES)*, 2011, 1: 47-61.
- [7] Aggarwal, A.; Singh, H. Optimization of machining techniques—a retrospective and literature review. *Sadhana*, 2005, 30(6): 699-711.
- [8] Soori, M.; Asamel, M. Mechanical Behavior of Materials in Metal Cutting Operations, A Review. *Journal of New Technology and Materials*, 2020, 10(2).
- [9] Soori, M.; Asmael, M. CLASSIFICATION OF RESEARCH AND APPLICATIONS OF THE COMPUTER AIDED PROCESS PLANNING IN MANUFACTURING SYSTEMS. *Independent Journal of Management & Production*, 2021, 12(5): 1250-1281.
- [10] Soori, M.; Asamel, M.; Solyali, D. Recent Development in Friction Stir Welding Process: A Review. *SAE International Journal of Materials and Manufacturing*, 2020, 14(1): 18.
- [11] Soori, M.; Asmael, M. Cutting temperatures in milling operations of difficult-to-cut materials. *Journal of New Technology and Materials*, 2021, 11(1): 47-56.
- [12] Soori, M.; Asmael, M. Virtual Minimization of Residual Stress and Deflection Error in the Five-Axis Milling of Turbine Blades. *Strojniški vestnik/Journal of Mechanical Engineering*, 2021, 67(5): 235-244.
- [13] Soori, M.; Asmael, M. MINIMIZATION OF DEFLECTION ERROR IN FIVE AXIS MILLING OF IMPELLER BLADES. *Facta Universitatis, series: Mechanical Engineering*, 2021. DOI: 10.22190/FUME210822069S
- [14] Soori, M. *Virtual product development*. 2019: GRIN Verlag.
- [15] Dastres, R.; Soori, M. Advances in Web-Based Decision Support Systems. *International Journal of Engineering and Future Technology*, 2021, 19(1): 1-15.
- [16] Dastres, R.; Soori, M. Artificial Neural Network Systems. *International Journal of Imaging and Robotics (IJIR)*, 2021, 21(2): 13-25.
- [17] Dastres, R.; Soori, M. The Role of Information and Communication Technology (ICT) in Environmental Protection. *International Journal of Tomography and Simulation*, 2021, 35(1): 24-37.
- [18] Soori, M.; Asmael, M.; Khan, A.; Farouk, N. Minimization of surface roughness in 5-axis milling of turbine blades. *Mechanics Based Design of Structures and Machines*, 2021: 1-18. DOI: 10.1080/15397734.2021.1992779
- [19] Soori, M.; Arezoo, B.; Habibi, M. Accuracy analysis of tool deflection error modelling in prediction of milled surfaces by a virtual machining system. *International Journal of Computer Applications in Technology*, 2017, 55(4): 308-321.
- [20] Soori, M.; Arezoo, B.; Habibi, M. Virtual machining considering dimensional, geometrical and tool deflection errors in three-axis CNC milling machines. *Journal of Manufacturing Systems*, 2014, 33(4): 498-507.
- [21] Soori, M.; Arezoo, B.; Habibi, M. Dimensional and geometrical errors of three-axis CNC milling machines in a virtual machining system. *Computer-Aided Design*, 2013, 45(11): 1306-1313.
- [22] Soori, M.; Arezoo, B. Virtual Machining Systems for CNC Milling and Turning Machine Tools: A Review. *International Journal of Engineering and Future Technology*, 2021, 1(18): 56-104.
- [23] Soori, M.; Arezoo, B.; Habibi, M. Tool deflection error of three-axis computer numerical control milling machines, monitoring and minimizing by a virtual machining system. *Journal of Manufacturing Science and Engineering*, 2016, 138(8).
- [24] Chandel, D.K.; Giri, P.K. A Review on Optimization of Cutting Parameters in Machining using Taguchi Method. 2019.
- [25] Li, J.; Liu, W.; Yang, L.; Sun, F. Study of abrasive flow machining parameter optimization based on Taguchi method. *Journal of Computational and Theoretical Nanoscience*, 2013, 10(12): 2949-2954.
- [26] Maiyar, L.M.; Ramanujam, R.; Venkatesan, K.; Jerald, J. Optimization of machining parameters for end milling of Inconel 718 super alloy using Taguchi based grey relational analysis. *Procedia engineering*, 2013, 64: 1276-1282.
- [27] Rajyalakshmi, G.; Ramaiah, P.V. Multiple process parameter optimization of wire electrical discharge machining on Inconel 825 using Taguchi grey relational analysis. *The International Journal of Advanced Manufacturing Technology*, 2013, 69(5-8): 1249-1262.
- [28] Kuram, E.; Ozcelik, B. Optimization of machining parameters during micro-milling of Ti6Al4V titanium alloy and Inconel 718 materials using Taguchi method. *Proceedings of the Institution of Mechanical Engineers, Part B: Journal of Engineering Manufacture*, 2017, 231(2): 228-242.
- [29] Nipanikar, S. Parameter optimization of electro discharge machining of AISI D3 steel material by using Taguchi method. *Journal of Engineering research and studies*, 2012, 3(3): 7-10.
- [30] Kavimani, V.; Prakash, K.S.; Thankachan, T.; Nagaraja, S.; Jeevanantham, A.; Jhon, J.P. WEDM Parameter Optimization for Silicon@ r-GO/Magnesium Composite Using Taguchi Based GRA Coupled PCA. *Silicon*, 2019: 1-15.
- [31] Tilekar, S.; Das, S.S.; Patowari, P. Process parameter optimization of wire EDM on Aluminum and mild steel by using taguchi method. *Procedia Materials Science*, 2014, 5: 2577-2584.
- [32] Joshi, A.; Kothiyal, P. Investigating effect of machining parameters of CNC milling on surface finish by taguchi

- method. *International Journal on Theoretical and Applied Research in Mechanical Engineering*, 2013, 2(2): 113-119.
- [33] Ghalme, S.; Mankar, A.; Bhalerao, Y. Parameter optimization in milling of glass fiber reinforced plastic (GFRP) using DOE-Taguchi method. *SpringerPlus*, 2016, 5(1): 1376.
- [34] Majumder, A. Process parameter optimization during EDM of AISI 316 LN stainless steel by using fuzzy based multi-objective PSO. *Journal of Mechanical Science and Technology*, 2013, 27(7): 2143-2151.
- [35] Adnan, M.M.; Sarkheyli, A.; Zain, A.M.; Haron, H. Fuzzy logic for modeling machining process: a review. *Artificial Intelligence Review*, 2015, 43(3): 345-379.
- [36] Chuang, K.-C.; Lan, T.-S.; Zhang, L.-P.; Chen, Y.-M.; Dai, X.-J. Parameter Optimization for Computer Numerical Controlled Machining Using Fuzzy and Game Theory. *Symmetry*, 2019, 11(12): 1450.
- [37] Lin, C.; Lin, J.; Ko, T. Optimisation of the EDM process based on the orthogonal array with fuzzy logic and grey relational analysis method. *The International Journal of Advanced Manufacturing Technology*, 2002, 19(4): 271-277.
- [38] Gupta, A.; Singh, H.; Aggarwal, A. Taguchi-fuzzy multi output optimization (MOO) in high speed CNC turning of AISI P-20 tool steel. *Expert Systems with Applications*, 2011, 38(6): 6822-6828.
- [39] Chiang, K.-T.; Liu, N.-M.; Chou, C.-C. Machining parameters optimization on the die casting process of magnesium alloy using the grey-based fuzzy algorithm. *The International Journal of Advanced Manufacturing Technology*, 2008, 38(3-4): 229-237.
- [40] Suresh, P.; Marimuthu, K.; Ranganathan, S.; Rajmohan, T. Optimization of machining parameters in turning of Al-Si-Cr hybrid metal matrix composites using grey-fuzzy algorithm. *Transactions of Nonferrous Metals Society of China*, 2014, 24(9): 2805-2814.
- [41] Sengottuvel, P.; Satishkumar, S.; Dinakaran, D. Optimization of multiple characteristics of EDM parameters based on desirability approach and fuzzy modeling. *Procedia Engineering*, 2013, 64: 1069-1078.
- [42] Ubaid, A.M.; Dweiri, F.T.; Aghdeab, S.H.; Abdullah Al-Juboori, L. Optimization of electro discharge machining process parameters with fuzzy logic for stainless steel 304 (astm a240). *Journal of Manufacturing Science and Engineering*, 2018, 140(1).
- [43] Ashok, R.; Poovazhagan, L.; Srinath Ramkumar, S.; Vignesh Kumar, S. Optimization of Material Removal Rate in Wire-EDM Using Fuzzy Logic and Artificial Neural Network. in *Applied Mechanics and Materials*. 2017. Trans Tech Publ.
- [44] Das, P.P.; Diyaley, S.; Chakraborty, S.; Ghadai, R.K. Multi-objective optimization of wire electro discharge machining (wedm) process parameters using grey-fuzzy approach. *Periodica Polytechnica Mechanical Engineering*, 2019, 63(1): 16-25.
- [45] Park, K.S.; Kim, S.H. Artificial intelligence approaches to determination of CNC machining parameters in manufacturing: a review. *Artificial Intelligence in Engineering*, 1998, 12(1-2): 127-134.
- [46] Aggour, K.S.; Gupta, V.K.; Ruscitto, D.; Ajdelsztajn, L.; Bian, X.; Brosnan, K.H.; Kumar, N.C.; Dheeradhada, V.; Hanlon, T.; Iyer, N. Artificial intelligence/machine learning in manufacturing and inspection: A GE perspective. *MRS Bulletin*, 2019, 44(7): 545-558.
- [47] Pimenov, D.Y.; Bustillo, A.; Mikolajczyk, T. Artificial intelligence for automatic prediction of required surface roughness by monitoring wear on face mill teeth. *Journal of Intelligent Manufacturing*, 2018, 29(5): 1045-1061.
- [48] Nikolić, V.; Petković, D.; MiloVanČević, M.; Deneva, H.; Lazov, L.; Teirumenieka, E. Optimization of Laser Cutting Parameters Using an Adaptive Neuro-fuzzy Methodology. *Lasers in Engineering (Old City Publishing)*, 2018, 40.
- [49] Rao, R.V.; Pawar, P.J. Parameter optimization of a multi-pass milling process using non-traditional optimization algorithms. *Applied soft computing*, 2010, 10(2): 445-456.
- [50] Liu, R.; Yang, B.; Zio, E.; Chen, X. Artificial intelligence for fault diagnosis of rotating machinery: A review. *Mechanical Systems and Signal Processing*, 2018, 108: 33-47.
- [51] Moreira, L.C.; Li, W.; Lu, X.; Fitzpatrick, M.E. Supervision controller for real-time surface quality assurance in CNC machining using artificial intelligence. *Computers & Industrial Engineering*, 2019, 127: 158-168.
- [52] Kovač, P.; Savković, B.; Rodić, D.; Aleksić, A.; Gostimirović, M.; Sekulić, M.; Kulundžić, N. Modelling and Optimization of Surface Roughness Parameters of Stainless Steel by Artificial Intelligence Methods. in *Proceedings of the International Symposium for Production Research 2019*. 2019. Springer.
- [53] Wang, S.-M.; Lee, C.-Y.; Gunawan, H.; Yeh, C.-C. An Accuracy-Efficiency-Power Consumption Hybrid Optimization Method for CNC Milling Process. *Applied Sciences*, 2019, 9(7): 1495.
- [54] Zhu, N.; Feng, Z.-G.; WANG, Q. Parameter Optimization of Support Vector Machine for Classification Using Niche Genetic Algorithm [J]. *Journal of Nanjing University of Science and Technology (Natural Science)*, 2009, 1.
- [55] Chandrasekaran, M.; Muralidhar, M.; Krishna, C.M.; Dixit, U. Application of soft computing techniques in machining performance prediction and optimization: a literature review. *The International Journal of Advanced Manufacturing Technology*, 2010, 46(5-8): 445-464.
- [56] An, L.B. Optimal selection of machining parameters for multi-pass turning operations. in *Advanced Materials Research*. 2011. Trans Tech Publ.
- [57] Yang, Y.; Shen, X.-I.; Shao, H. Machining parameter optimization of milling process based on genetic algorithms. *Ji Xie She Ji Yu Yan Jiu (Machine Design and Research)(China)*, 2001, 17(2): 60-62.
- [58] Zhang, L.; Jia, Z.; Wang, F.; Liu, W. A hybrid model using supporting vector machine and multi-objective genetic algorithm for processing parameters optimization in micro-EDM. *The International Journal of Advanced Manufacturing Technology*, 2010, 51(5-8): 575-586.
- [59] Selvam, M.D.; Dawood, D.; Karuppusami, D.G. Optimization of machining parameters for face milling operation in a vertical CNC milling machine using genetic algorithm. *IRACST-Engineering Science and Technology: An International Journal (ESTIJ)*, 2012, 2(4).
- [60] Ahmad, N.; Tanaka, T.; Saito, Y. Optimization of cutting parameters for end milling operation by soap based genetic algorithm. *power*, 2005, 318(2): 5.
- [61] Sardinias, R.Q.; Reis, P.; Davim, J.P. Multi-objective optimization of cutting parameters for drilling laminate composite materials by using genetic algorithms. *Composites Science and Technology*, 2006, 66(15): 3083-3088.
- [62] D'addona, D.M.; Teti, R. Genetic algorithm-based optimization of cutting parameters in turning processes. *Procedia Cirp*, 2013, 7: 323-328.
- [63] Kilickap, E.; Huseyinoglu, M.; Yardimeden, A. Optimization of drilling parameters on surface roughness in drilling of AISI 1045 using response surface methodology and genetic algorithm. *The International Journal of Advanced Manufacturing Technology*, 2011, 52(1-4): 79-88.
- [64] Iriaye, E.; Ighravwe, D.; Alade, A.; Afolalu, S.; Adelakun, O. Development of artificial neural network for surface roughness and machine prediction. in *Journal of Physics: Conference Series*. 2019. IOP Publishing.

- [65] Pardo, B.E.S., Cutting-insert selection and cutting-parameter optimization for turning operations based on artificial neural networks and genetic algorithm. 2018.
- [66] Vignesh, M.; Sasindran, V.; Krishna, S.A.; Madusudhanan, A.; Gokulachandran, J. Predictive model development and optimization of surface roughness parameter in milling operations by means of fuzzy logic and artificial neural network approach. in IOP Conference Series: Materials Science and Engineering. 2019. IOP Publishing.
- [67] Warghat, S.T.; Deshmukh, T. Parameter optimization of milling operation using teaching-learning-based optimization and artificial neural network. MAYFEB Journal of Mechanical Engineering, 2017, 1.
- [68] Zain, A.M.; Haron, H.; Sharif, S. Prediction of surface roughness in the end milling machining using Artificial Neural Network. Expert Systems with Applications, 2010, 37(2): 1755-1768.
- [69] Kumar, D.; Chandna, P.; Pal, M. Efficient Optimization of Neural Network using Taguchi-grey Relational Analysis with Signal-to-Noise Ratio Approach for 2.5 D End Milling Process. American Journal of Mechanical Engineering and Automation, 2018, 5(2): 30.
- [70] Razfar, M.R.; Zinati, R.F.; Haghshenas, M. Optimum surface roughness prediction in face milling by using neural network and harmony search algorithm. The International Journal of Advanced Manufacturing Technology, 2011, 52(5-8): 487-495.
- [71] Samanta, S.; Chakraborty, S. Parametric optimization of some non-traditional machining processes using artificial bee colony algorithm. Engineering Applications of Artificial Intelligence, 2011, 24(6): 946-957.
- [72] Akay, B.; Karaboga, D. A modified artificial bee colony algorithm for real-parameter optimization. Information sciences, 2012, 192: 120-142.
- [73] Yildiz, A.R. Optimization of cutting parameters in multi-pass turning using artificial bee colony-based approach. Information Sciences, 2013, 220: 399-407.
- [74] Ming, Y.; Yue-qiao, A. SVM parameter optimization and application based on artificial bee colony algorithm [J]. Journal of Optoelectronics. Laser, 2012, 2.
- [75] Yusup, N.; Sarkheyli, A.; Zain, A.M.; Hashim, S.Z.M.; Ithnin, N. Estimation of optimal machining control parameters using artificial bee colony. Journal of Intelligent Manufacturing, 2014, 25(6): 1463-1472.
- [76] Das, M.K.; Kumar, K.; Barman, T.K.; Sahoo, P. Application of artificial bee colony algorithm for optimization of MRR and surface roughness in EDM of EN31 tool steel. Procedia materials science, 2014, 6: 741-751.
- [77] Mukherjee, R.; Goswami, D.; Chakraborty, S. Parametric optimization of Nd: YAG laser beam machining process using artificial bee colony algorithm. Journal of Industrial Engineering, 2013, 2013.
- [78] Solaiyappan, A.; Mani, K.; Gopalan, V. Multi-objective optimization of process parameters for electrochemical machining of 6061Al/10% Wt Al₂O₃/5% Wt SiC composite using hybrid fuzzy-artificial bee colony algorithm. JJMIE, 2014, 8(5).
- [79] Das, M.K.; Kumar, K.; Barman, T.K.; Sahoo, P. Investigation on electrochemical machining of EN31 steel for optimization of MRR and surface roughness using artificial bee colony algorithm. Procedia Engineering, 2014, 97: 1587-1596.
- [80] Stori, J.; Wright, P.; King, C. Integration of process simulation in machining parameter optimization. 1999.
- [81] Thompson, M.; Fidler, J. Application of the genetic algorithm and simulated annealing to LC filter tuning. IEE Proceedings-Circuits, Devices and Systems, 2001, 148(4): 177-182.
- [82] Aghdeab, S.H.; Mohammed, L.A.; Ubaid, A.M. Optimization of CNC Turning for Aluminum Alloy Using Simulated Annealing Method. Jordan Journal of Mechanical & Industrial Engineering, 2015, 9(1).
- [83] Khan, Z.; Prasad, B.; Singh, T. Machining condition optimization by genetic algorithms and simulated annealing. Computers & Operations Research, 1997, 24(7): 647-657.
- [84] Yang, S.-H.; Srinivas, J.; Mohan, S.; Lee, D.-M.; Balaji, S. Optimization of electric discharge machining using simulated annealing. Journal of Materials Processing Technology, 2009, 209(9): 4471-4475.
- [85] Wang, Z.; Rahman, M.; Wong, Y.; Sun, J. Optimization of multi-pass milling using parallel genetic algorithm and parallel genetic simulated annealing. International Journal of Machine Tools and Manufacture, 2005, 45(15): 1726-1734.
- [86] Li, W.; McMahon, C.A. A simulated annealing-based optimization approach for integrated process planning and scheduling. International Journal of Computer Integrated Manufacturing, 2007, 20(1): 80-95.
- [87] Zain, A.M.; Haron, H.; Sharif, S. Genetic algorithm and simulated annealing to estimate optimal process parameters of the abrasive waterjet machining. Engineering with computers, 2011, 27(3): 251-259.
- [88] Kolahan, F.; Abachizadeh, M. Optimizing turning parameters for cylindrical parts using simulated annealing method. World academy of science, Engineering and technology, 2008, 46(1): 436-439.
- [89] Wang, Z.; Wong, Y.; Rahman, M.; Sun, J. Multi-objective optimization of high-speed milling with parallel genetic simulated annealing. The International Journal of Advanced Manufacturing Technology, 2006, 31(3-4): 209-218.
- [90] Zain, A.M.; Haron, H.; Sharif, S. Simulated annealing to estimate the optimal cutting conditions for minimizing surface roughness in end milling Ti-6Al-4V. Machining Science and Technology, 2010, 14(1): 43-62.
- [91] Karaboga, D.; Akay, B. A comparative study of artificial bee colony algorithm. Applied mathematics and computation, 2009, 214(1): 108-132.
- [92] Vijayakumar, K.; Prabhakaran, G.; Asokan, P.; Saravanan, R. Optimization of multi-pass turning operations using ant colony system. International Journal of Machine Tools and Manufacture, 2003, 43(15): 1633-1639.
- [93] Krishna, A.G.; Rao, K.M. Optimisation of operations sequence in CAPP using an ant colony algorithm. The International Journal of Advanced Manufacturing Technology, 2006, 29(1-2): 159-164.
- [94] Liu, X.-J.; Yi, H.; Ni, Z.-h. Application of ant colony optimization algorithm in process planning optimization. Journal of Intelligent Manufacturing, 2013, 24(1): 1-13.
- [95] Wang*, G.; Xie, S. Optimal process planning for a combined punch-and-laser cutting machine using ant colony optimization. International Journal of Production Research, 2005, 43(11): 2195-2216.
- [96] Rongali, S.; Yalavarthi, R. Parameter optimization of support vector machine by improved ant colony optimization. in Proceedings of the second international conference on computer and communication technologies. 2016. Springer.
- [97] Sankar, B.R.; Umamaheswarrao, P. Multi objective optimization of CFRP composite drilling using ant colony algorithm. Materials Today: Proceedings, 2018, 5(2): 4855-4860.
- [98] Abdullah, H.; Ramli, R.; Wahab, D.A. Tool path length optimisation of contour parallel milling based on modified ant colony optimisation. The International Journal of Advanced Manufacturing Technology, 2017, 92(1-4): 1263-1276.
- [99] Soepangkat, B.O.P.; Effendi, M.K.; Pramujati, B.; Norcahyo, R.; Robbany, F. Delamination factor and cutting force optimizations in end-milling of carbon fiber reinforced

- polymer composites using backpropagation neural network-ant colony optimization. in AIP Conference Proceedings. 2019. AIP Publishing LLC.
- [100] Kadirgama, K.; Noor, M.; Rahman, M.; Sani, M.; Ariffin, A. Surface Roughness Analysis in End Milling with Response Ant Colony Optimization. in 6th International Conference on Numerical Analysis in Engineering (NAE2009). 2009.
- [101] Pansare, V.B.; Kavade, M.V. Optimization of cutting parameters in multipass turning operation using ant colony algorithm. *International Journal of Engineering Science & Advanced Technology*, 2012, 2(4): 955-960.
- [102] Vergara-Villegas, O.O.; Ramírez-Espinoza, C.F.; Cruz-Sánchez, V.G.; Nandayapa, M.; Neco-Caberta, R. A Methodology for Optimizing the Parameters in a Process of Machining a Workpiece Using Multi-objective Particle Swarm Optimization, in *New Perspectives on Applied Industrial Tools and Techniques*. 2018, Springer. p. 129-151.
- [103] Chentil Jegan, T.M.; Ravindran, D. Electrochemical machining process parameter optimization using particle swarm optimization. *Computational Intelligence*, 2017, 33(4): 1019-1037.
- [104] Gupta, M.K.; Sood, P.; Sharma, V.S. Machining parameters optimization of titanium alloy using response surface methodology and particle swarm optimization under minimum-quantity lubrication environment. *Materials and Manufacturing Processes*, 2016, 31(13): 1671-1682.
- [105] Mohanty, C.P.; Mahapatra, S.S.; Singh, M.R. A particle swarm approach for multi-objective optimization of electrical discharge machining process. *Journal of Intelligent Manufacturing*, 2016, 27(6): 1171-1190.
- [106] Lmalghan, R.; Rao, K.; ArunKumar, S.; Rao, S.S.; Herbert, M.A. Machining parameters optimization of AA6061 using response surface methodology and particle swarm optimization. *International Journal of Precision Engineering and Manufacturing*, 2018, 19(5): 695-704.
- [107] Malghan, R.L.; Rao, K.M.; Shettigar, A.K.; Rao, S.S.; D'Souza, R. Application of particle swarm optimization and response surface methodology for machining parameters optimization of aluminium matrix composites in milling operation. *Journal of the Brazilian Society of Mechanical Sciences and Engineering*, 2017, 39(9): 3541-3553.
- [108] Ghosh, G.; Mandal, P.; Mondal, S.C. Modeling and optimization of surface roughness in keyway milling using ANN, genetic algorithm, and particle swarm optimization. *The International Journal of Advanced Manufacturing Technology*, 2019, 100(5-8): 1223-1242.
- [109] Kalita, K.; Shivakoti, I.; Ghadai, R.K. Optimizing process parameters for laser beam micro-marking using genetic algorithm and particle swarm optimization. *Materials and Manufacturing Processes*, 2017, 32(10): 1101-1108.
- [110] Gao, L.; Huang, J.; Li, X. An effective cellular particle swarm optimization for parameters optimization of a multi-pass milling process. *Applied Soft Computing*, 2012, 12(11): 3490-3499.
- [111] Župerl, U.; Čuš, F.; Gečevska, V. Optimization of the characteristic parameters in milling using the pso evaluation technique. *Strojniški vestnik-Journal of Mechanical Engineering*, 2007, 53(6): 354-368.
- [112] Siva, R.S.; Balachithra, B. Optimization of Machining Parameters using Scatter Search Algorithm. *Journal of Advances in Mechanical Engineering and Science*, 2016, 2(4): 11-1.
- [113] Krishna, A.G.; Rao, K.M. Optimisation of machining parameters for milling operations using a scatter search approach. *The International Journal of Advanced Manufacturing Technology*, 2006, 31(3-4): 219-224.
- [114] Krishna, A.G.; Rao, K.M. Multi-objective optimisation of surface grinding operations using scatter search approach. *The International Journal of Advanced Manufacturing Technology*, 2006, 29(5-6): 475-480.
- [115] Krishna, A.G.; Rao, K.M. Simultaneous optimal selection of design and manufacturing tolerances with different stack-up conditions using scatter search. *The International Journal of Advanced Manufacturing Technology*, 2006, 30(3-4): 328.
- [116] Chen, M.-C.; Chen, K.-Y. Determination of optimal machining conditions using scatter search, in *New optimization techniques in engineering*. 2004, Springer. p. 681-702.
- [117] Prabu, P.M.; Rajasekar, K.; Vignesh, R.; Navaneethasanthakumar, S. Scatter search optimization for multi node machining fixture layout. *The International Journal of Engineering and Science*, 2014, 3(1): 30-37.
- [118] Mugendiran, V.; Gnanavelbabu, A.; Ramadoss, R. Parameter optimization for surface roughness and wall thickness on AA5052 Aluminium alloy by incremental forming using response surface methodology. *Procedia Engineering*, 2014, 97: 1991-2000.
- [119] Bhowmik, S.; Ray, A. Prediction and optimization of process parameters of green composites in AWJM process using response surface methodology. *The International Journal of Advanced Manufacturing Technology*, 2016, 87(5-8): 1359-1370.
- [120] Kant, G.; Sangwan, K.S. Prediction and optimization of machining parameters for minimizing power consumption and surface roughness in machining. *Journal of cleaner production*, 2014, 83: 151-164.
- [121] Kalaimathi, M.; Venkatachalam, G.; Sivakumar, M. Experimental Investigations on the Electrochemical Machining Characteristics of Monel 400 Alloys and Optimization of Process Parameters. *Jordan Journal of Mechanical & Industrial Engineering*, 2014, 8(3).
- [122] Vinayagamoorthy, R.; Rajeswari, N.; Karuppiah, B. Optimization Studies on Thrust Force and Torque during Drilling of Natural Fiber Reinforced Sandwich Composites. *Jordan Journal of Mechanical & Industrial Engineering*, 2014, 8(6).
- [123] Makadia, A.J.; Nanavati, J. Optimisation of machining parameters for turning operations based on response surface methodology. *Measurement*, 2013, 46(4): 1521-1529.
- [124] Peng, A.; Xiao, X.; Yue, R. Process parameter optimization for fused deposition modeling using response surface methodology combined with fuzzy inference system. *The International Journal of Advanced Manufacturing Technology*, 2014, 73(1-4): 87-100.
- [125] Palanikumar, K. Application of Taguchi and response surface methodologies for surface roughness in machining glass fiber reinforced plastics by PCD tooling. *The International Journal of Advanced Manufacturing Technology*, 2008, 36(1-2): 19-27.
- [126] Kansal, H.; Singh, S.; Kumar, P. Parametric optimization of powder mixed electrical discharge machining by response surface methodology. *Journal of materials processing technology*, 2005, 169(3): 427-436.
- [127] Neşeli, S.; Yaldız, S.; Türkeş, E. Optimization of tool geometry parameters for turning operations based on the response surface methodology. *Measurement*, 2011, 44(3): 580-587.
- [128] Saini, A.; Chauhan, P.; Pabla, B.; Dhama, S. Multi-process parameter optimization in face milling of Ti6Al4V alloy using response surface methodology. *Proceedings of the Institution of Mechanical Engineers, Part B: Journal of Engineering Manufacture*, 2018, 232(9): 1590-1602.
- [129] Alagarsamy, S.; Ravichandran, M.; Sakthivelu, S.; Kumar, S.D.; Chanakyan, C.; Meignanamoorthy, M. Optimization of electric discharge machining parameters on surface roughness for Al/ZrO₂ composite through response surface methodology. *Materials Today: Proceedings*, 2020.

- [130] Kumar, P.; Hussain, M. Optimization of Micro-electro Discharge Drilling Parameters of Ti6Al4V Using Response Surface Methodology and Genetic Algorithm, in Numerical Optimization in Engineering and Sciences. 2020, Springer. p. 449-456.
- [131] Gupta, M.K.; Sood, P.; Sharma, V.S. Optimization of machining parameters and cutting fluids during nano-fluid based minimum quantity lubrication turning of titanium alloy by using evolutionary techniques. Journal of Cleaner Production, 2016, 135: 1276-1288.
- [132] Deris, A.M.; Zain, A.M.; Sallehuddin, R.; Sharif, S. Modeling and Optimization of Electric Discharge Machining Performances using Harmony Search Algorithm. ELEKTRIKA-Journal of Electrical Engineering, 2019, 18(3-2): 56-61.
- [133] Zarei, O.; Fesanghary, M.; Farshi, B.; Saffar, R.J.; Razfar, M. Optimization of multi-pass face-milling via harmony search algorithm. Journal of materials processing technology, 2009, 209(5): 2386-2392.
- [134] Chatterjee, S.; Abhishek, K.; Yadav, R.K.; Mahapatra, S. Optimization of drilling process parameters by harmony search algorithm. in International Conference on Recent Advances and Innovations in Engineering (ICRAIE-2014). 2014. IEEE.
- [135] Abhishek, K.; Datta, S.; Mahapatra, S.S. Multi-objective optimization in drilling of CFRP (polyester) composites: Application of a fuzzy embedded harmony search (HS) algorithm. Measurement, 2016, 77: 222-239.
- [136] Nayak, B.B.; Mahapatra, S.S.; Chatterjee, S.; Abhishek, K. Parametric appraisal of WEDM using harmony search algorithm. Materials Today: Proceedings, 2015, 2(4-5): 2562-2568.
- [137] Nagarchi, M.B.; Patel, D. Parametric optimization of face milling using harmony search algorithm. International journal of engineering development and research, 2014, 2(2): 1722-1729.
- [138] Mat Deris, A.; Zain, A.M.; Salehuddin, R.; Sharif, S. Overview of Harmony Search (HS) algorithm for green manufacturing industries. in Applied Mechanics and Materials. 2015. Trans Tech Publ.
- [139] Kumari, S.; Kumar, A.; Yadav, R.K.; Vivekananda, K. Optimisation of machining parameters using grey relation analysis integrated with harmony search for turning of aisi d2 steel. Materials Today: Proceedings, 2018, 5(5): 12750-12756.

A New Microchannel Heat Sink Design Using Porous Media Inserts

Hamdi E. Ahmed^{a*}, Issam M. Ali Aljubury^b, Ammar A. Farhan^c, Mohammed Gh. Jehad^a

^aDepartment of Mechanical Engineering, University of Anbar, 31001 Ramadi, Iraq

^bDepartment of Mechanical Engineering, University of Baghdad, 10071 Baghdad, Iraq

^cDepartment of Energy Engineering, University of Baghdad, 10071 Baghdad, Iraq.

Received 21 NOV 2021

Accepted 31 JAN 2022

Abstract

ACFD study is carried out to enhance the turbulent convection heat transfer of a solid plate-fin micro channel heat sink (MCHS). The goal of this study is to replace the solid fins with porous fins having a constant and variable cross-sectional area with the vertical and axial direction. Convergent and divergent porous fins are also explored. The effect of doubling the size of the porous fins is tested as only the foam is proposed to be above the heat sink substrate without channels. The FVM is adopted for solving the governing equations in 3D. Temperature-dependent properties of water are considered. The results are displayed in terms of the Nusselt number (Nu), wall temperature distribution, pressure drop, friction factor, hydraulic-thermal performance (JF), temperature contours, and wall temperature uniformity (TU). The results reveal that the maximum Nuis 21.0 times associated with a friction factor increase of 3.06 times compared to the traditional design. The highest JF is 15.87 for the MCHS-5 when $a = 1.0$ mm and $b = 0.0$ mm at $Re = 3000$. The non-uniform cross-sectional area of the porous fin shows a great thermal performance compared to the standard one. A slight increase in the Nu with high pressure drop penalty is shown when the porous media volume is doubled.

© 2022 Jordan Journal of Mechanical and Industrial Engineering. All rights reserved

Keywords: Porous media, MCHS, Turbulent flow, Hydraulic-thermal performance, Temperature-dependent fluid properties.

Nomenclatures

a	width of the fin base, m
A_c	heat transfer surface area, m ²
b	width of the fin tip, m
C	Inertia coefficient
CF	Forchheimer factor
c_p	Specific heat capacity, J/kg·K
D_h	hydraulic diameter, m
d_e	Edge diameter of porous zone, m
d_p	Pore diameter, m
f	Friction factor
H	fin height, m
h	Convection heat transfer coefficient, W/m ² ·K
JF	Hydro-thermal performance factor
k	Turbulent kinetic energy, m ² /s ²
K	Permeability, m ²
L	length of the MCHS, m
N	number of the heat sink channels
Nu	Nusselt number
p	Pressure, Pa
Pr	Prandtl number
q	Heat flux, W/m ²
Re	Reynolds number
S_ϕ	source term
T	Temperature, K

TU	Temperature uniformity factor
u	fluid velocity, m/s
W	substrate width, m
x, y, z	x, y, z -coordinates
x^+, y^+, z^+	Criteria of mesh refinement

Greeks

α	Thermal diffusivity, m ² /s
T_ϕ	turbulent diffusion coefficient
ϵ	turbulent energy dissipation rate, m ² /s ³
γ	Thermal conductivity, W/m·K
ρ	Fluid density, kg/m ³
ϵ	Porosity
μ	Dynamic viscosity, Pa·s
μ_e, μ_l, μ_t	effective, laminar, turbulent viscosity, Pa·s
ϕ	transported scalar

Subscripts

eff	effective
f	fin
f	fluid
m	mean
p	porous
s	solid

* Corresponding author e-mail: hamdi.ahmed@uoanbar.edu.iq.

1. Introduction

Recently, MCHS has received much attention due to the quick progress in microelectronic technology, the power density of electronic components is increasing continuously, which restricts their performance development. To ensure the electronic components operate safely and functionally, efficient thermal management techniques are critical and urgently required. The microchannel heat sink (MCHS) was introduced first by Tuckerman and Pease [1] in the 1980s and has become a promising alternative technique for heat rejection because it can remove a heat flux as high as 790 W/cm^2 . The MCHS has attracted a great deal of attention during the last three decades due to its wide thermal applications, convenient size, reliability, operating stability, and cooling efficiency [2, 3]. It is used for cooling microelectronic components, such as electric generators, microfluidic microbial fuel cells, heat exchangers in the automotive market, concentrator photovoltaic systems, and light-emitting diodes. Therefore, the MCHS is recognized as one of the most promising cooling techniques which offers high heat absorption from the chips. In the past decades, a lot of investigations were carried out experimentally and/or numerically to reduce the thermal resistance and pumping power of MCHS as they are considered as the two key issues for evaluating the hydraulic-thermal performance. [4–8]. The performance of these devices is directly related to the substrate temperature; therefore, it is a crucial issue to maintain the electronic equipment below the critical temperature [9]. Thermal resistance, cooling uniformity (Wall temperature distribution uniformity), and pressure drop (pumping power) are all critical metrics for MCHS [2, 10].

Metal foam is a particular kind of porous medium that can absorb a significant amount of heat from the solid through conducting and rejecting it to the fluid by convection. Metal foam shows different attractive features in comparison with its solid material counterparts. It has advantages, such as low volume, low density, high thermal conductivity, high effective heat transfer surface area, high flow-mixing capability, and low manufacturing cost. It is used in several thermal systems, such as heat exchangers, heat sinks, fuel cells, and solar collectors. It was shown that the use of metal foam insertion can enhance thermal performance significantly up to 40 times. The solid/fluid thermal conductivity was observed to be an important parameter to increase the heat dissipation by coolants. Researchers observed a high-pressure drop penalty accomplished to the thermal performance enhancement with the existence of metal foam [11–14].

The MCHS with metal foam insert increases both the surface contact area-to-volume ratio and local velocity mixing of the coolant, therefore, resulting in a better convective heat transfer rate. The thermal performance of such kinds of heat sinks can be improved by designing the configurations and porosity conditions properly, thus making the heat sink with porous insertion suitable for micro-size electronics cooling [15–18].

Hung et al. [15] investigated computationally the laminar hydraulic-thermal performances of MCHS by filling the channels with porous inserts in form of

rectangular, outlet enlargement, trapezoidal, thin rectangular, block, and sandwich distributions. It was noted that the trapezoidal porous distribution had thermal superiority at low Re number, while the rectangular porous distribution had thermal superiority at high Re number among other designs. The thermal performance was increased by using the porous inserts and also increased at a high Re number. A significant increase in the pressure drop was monitored when a porous medium was added to the channel. Hung et al. [19] explored numerically the laminar hydraulic and thermal performance of MCHS by enlarging the channel outlet using a porous insertion. It was demonstrated that increasing the width or height enlargement ratio could reduce the pressure drop across the channel. An enhancement in the Nusselt number and temperature control effectiveness and a reduction in the thermal resistance was observed. They stated that improving the hydraulic and thermal performance of the MCHS might be significantly obtained. A remarkable increase in the pressure drop was displayed across the MCHS by using the porous insertion.

Li et al. [10] investigated the thermal management of high-powered electronic components by inserting a metal foam in pin-fin hybrid heat sinks numerically. Their proposed design could enhance the heat transfer more than the metal foam heat sink and the pin-fin heat sink. They attributed this improvement to the increase in heat conduction and heat convection. They found that the heat transfer of the proposed design was more influenced by the foam porosity, whilst the pressure drop was affected by the pore size. Their results demonstrated that the thermal performance ratio of the proposed design was 1.6 times more than the traditional pattern. Seyf and Layeghi [20] studied the laminar thermal performance of an elliptical pin-fin heat sink with and without metal foam inserts numerically. It was indicated that the structural properties of porous media insert could considerably affect the frictional loss and heat transfer of the heat sink. An increase in the Nusselt number by 400% in some cases could be achieved by reducing the porosity and increasing the Re number (particularly at low Re number). An increase in the pressure drop was displayed with decreasing permeability and increasing the Re number.

Chuan et al. [8] modified the design of the MCHS by utilizing porous fins instead of solid fins to reduce the pressure drop across the heat sink. They found that the pressure drop was decreased by 47.9% lower than the traditional one while only an increment of 5% was recorded in the thermal resistance. They stated that the use of porous fins could cause a non-zero velocity of coolant at the interface between the channel and porous fin in which the coolant might behave like a “slip” on the channel wall. Chen [9] analyzed the laminar forced convection heat transfer in MCHS by considering the MCHS as a fluid-saturated porous medium due to the small dimensions of the microstructures. They found that the solid temperature distribution was unaffected by the fluid inertia force and the channel aspect ratio, while the dimensionless velocity distribution and the fluid temperature distribution relied on the inertial force parameter and the aspect ratio. The Nu number was increased with increasing the aspect ratio and porosity, whereas it was decreased with increasing the effective thermal conductivity ratio. Less effect of the

inertial force on the mean fluid temperature and the Nu number was found.

Li et al. [2] proposed an improved design of double-layer MCHS having high thermal performance and low frictional loss using porous media insertion under the laminar flow regime. They compared the thermal performance of four patterns; solid-fins single layer, porous-fins single layer, solid-fins double layer, and porous-fins double-layer MCHS. Their numerical results inferred that the porous fins upper layer and solid fins lower layer showed the lowest thermal resistance and best channel wall temperature uniformity among others at the corresponding Re number. A lower pressure drop of porous fins in the double-layered MCHS played a key role in the thermal performance enhancement. Ghahremannezhad et al. [3] accomplished a numerical comparison between the thermal-hydraulic performance of solid-plate-fin and porous-plate-fin double-layered MCHS. They could obtain higher thermal-hydraulic performance. The pumping power and thermal resistance could be minimized by optimizing the porous media parameters. Changing the porous fin thickness could increase the heat transfer rate. The superiority of their proposed pattern was verified with different porosities of substrates and MCHS materials. Wang et al. [4] explored the performance of a porous-ribs double-layer MCHS numerically. The upper layer was porous media fins while the lower layer was solid fins. It was revealed that not only the cooling performance was remarkably increased, but around 14.06%, also the consumption of the pumping power was also noticeably decreased by 16.40% in comparison with the traditional one. The optimized model showed more substrate temperature uniformity and lower than the baseline pattern. Arasteh et al. [11] enhanced the hydrothermal performance of the double-layered heat sink by using a porous sinusoidal fin under the laminar flow regime. At the optimum porous thicknesses, nanofluid was employed to enhance the heat sink thermal performance. By varying the porous thickness, the optimum porous thickness was obtained. The maximum hydraulic-thermal performance was 2.12.

Feng et al. [21] implemented an experimental and numerical study on finned metal foam and metal foam heat sinks having different heights subjected under impinging air jet cooling. Their final results exhibited that for the corresponding Re number, the heat dissipation of the metal foam heat sink increased monotonously when the foam height decreased, whilst the heat transfer increased first and then slightly decreased for the finned metal foam heat sink. For the same pumping power, the heat transfer of the metal foam heat sink was unaffected by the foam height whereas it increased with increasing the foam height for the other pattern. It was reported that the heat transfer of the finned metal foam heat sink outperformed the other pattern by about 1.5–2.8 times for the corresponding having the same height. Siavashi et al. [22] studied numerically the fluid flow and heat transfer of impinging jet flow through a cylindrical porous heat sink. They have found that the decrease in the ratio of (height/diameter) of the heat sink could increase the heat transfer rate.

Deng et al. [23] carried out a comparative study between an analytical solution and 3D numerical simulation to show the effect of insertion of porous media

in a MCHS. They found that the fin-averaged temperature was lower than the channel-averaged temperature near the bottom of the channel. The maximum substrate thickness was obtained with a low convective thermal resistance.

Yerramalle et al. [24] studied numerically a flow across a channel filled partly with cylindrical porous medium under three hydro-dynamic interface conditions which were; the slip condition, the stress continuity condition, and the stress jump condition. They concluded that their numerical simulation model was better for predicting the velocity profile in the fluid zone, the velocity profile was close to the interface, and the thickness of the boundary layer was compared to the analytical solution. A rectangular channel filled with an open-cell metal foam and exposed to constant asymmetrically heat flux was studied experimentally by Arbak and Dukhan [25] to examine the forced convection heat transfer characteristics. It was shown that the channel filled with metal foam has a Colburn factor greater than that of the empty channel by 407%.

A flow through a micro-channel partly filled with a porous medium was studied analytically by Xu et al. [26] to investigate its effect on the force convective heat transfer. They obtained an exact solution for the velocity profile inside the micro-channel. Also, it was reported that the friction factor was reduced with the growth of the Darcy number. Xu et al. [27] investigated numerically the performance of convection heat transfer performance in metal-foam heat exchanger assuming local thermal equilibrium and non-equilibrium models. It was found that the Nusselt number with the local thermal equilibrium model was greater than that with the local thermal non-equilibrium model.

AL-Migdady et al [28] performed a numerical analysis on the cooling performance of phase change material-based heat sinks with Aluminum foam. While keeping the heat flux input constant, two different PCMs and three distinct coefficients of convective heat transfer values were investigated. Comparing with the non-metal foam, the aluminum foam insertion of 0.97 and 0.90 porosity resulted in a base temperature drop of 5 and 6°C, respectively. Alshare et al. [29] conducted a steady-state two-dimensional developing flow in a wavy microchannel heat sink. It was discovered that as the Knudsen number increased, the slip velocity and temperature jump raised. It has been demonstrated that raising the wave amplitude could increase the heat transfer rate associated with increasing the frictional losses.

From the review of the open literature, and based on the best knowledge of the authors, it is shown that very few numerical studies are published on using porous fins instead of solid fins in the MCHS. In addition, no paper studied the effect of using variable cross-sectional area of the porous fins on the thermal and hydraulic flow characteristics. Based on the advantages of the porous media, it is expected that the convection heat transfer surface area of the porous fin will be greater and the flow path will be longer due to the fluctuation flow through the pores of the porous media compared to the solid fin. In addition, higher pressure drop penalty is also expected, thus, it is worth asking whether the hydraulic-thermal performance will be greater than one or not. The present work aims to fill this research gap with the main objective

to investigate numerically, in three-dimensions, the impact of using porous fins having a constant or changeable cross-section with the vertical and axial direction. Different geometric parameters of porous fins are examined considering the volume of the porous media constant along the tests. The results have been displayed in terms of the Nusselt number, wall temperature, friction factor, pressure drop, hydraulic-thermal performance, temperature uniformity factor, and temperature contours and then interpreted and analyzed in detail.

2. Computational model

2.1. Model description

The domain of the computational model of an aluminum plate-fin micro-channel heat sink in which single-channel is investigated here as illustrated in Figure 1(A). The substrate width (W) and length (L) are 1 mm, and 10 mm, respectively as depicted in Figure 1(B). The height (H) of the fin is 2 mm. Thus, the height of the base of the heat sink substrate is $H/2$ and the width of the channel is $W/2$. The width of the fin is identical to the width of the flow channel. There are the channel number (N) and the number of fins ($N+1$). The hydraulic diameter is taken for the fluid zone only when the fin is solid, whilst the hydraulic diameter is doubled for the fluid and fin zones when the fin is porous media. The inlet and outlet boundary conditions are the velocity and pressure applied

at the entrance and exit of the channel, respectively. The lateral sides of the fluid domain are considered as a symmetry boundary condition. Constant heat flux is applied to the base of the substrate. The traditional MCHS is taken as a baseline case for comparing other proposed patterns to show their superiority. Therefore, the baseline pattern is denoted by MCHS-0 in this paper

2.2. Patterns and variables

Several variable parameters are investigated here for obtaining different heat sink patterns to enhance the thermal and hydraulic performance of the MCHS. The traditional pattern considered in this study is the plate-solid fin microchannel heat sink denoted by MCHS-0 and cooled by water. The first proposed design is a pattern of an aluminum porous fin with a fluid zone denoted by MCHS-1 as seen in Figure 2(A). The second pattern is using a solid fin with a porous zone (i.e., instead of the pure fluid core) denoted by MCHS-2, see Figure 2(B). The third is using a porous fin with a width of 1 mm instead of 0.5 mm while the height is 1 mm instead of 2 mm and the zone of the fluid is above the porous zone (middle porous fin with the upper fluid zone), MCHS-3, Figure 2(C). The fourth is using porous fin with porous zone, MCHS-4, Figure 2(D). The total fin volume of all the above patterns is maintained constant throughout the comparison tests.

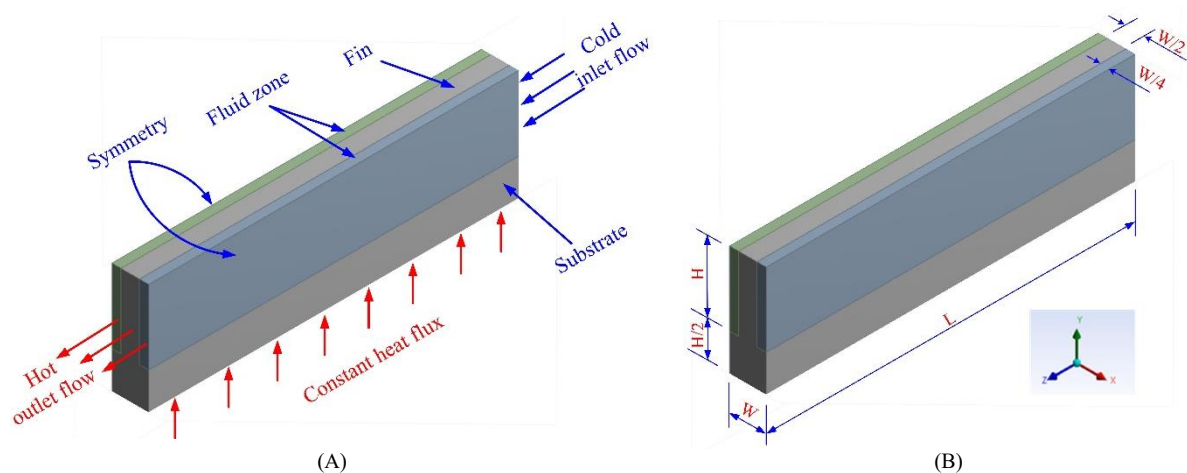


Figure 1. Schematic diagram of (A) the computational domain of the physical problem MCHS-0, and (B) geometric parameters.

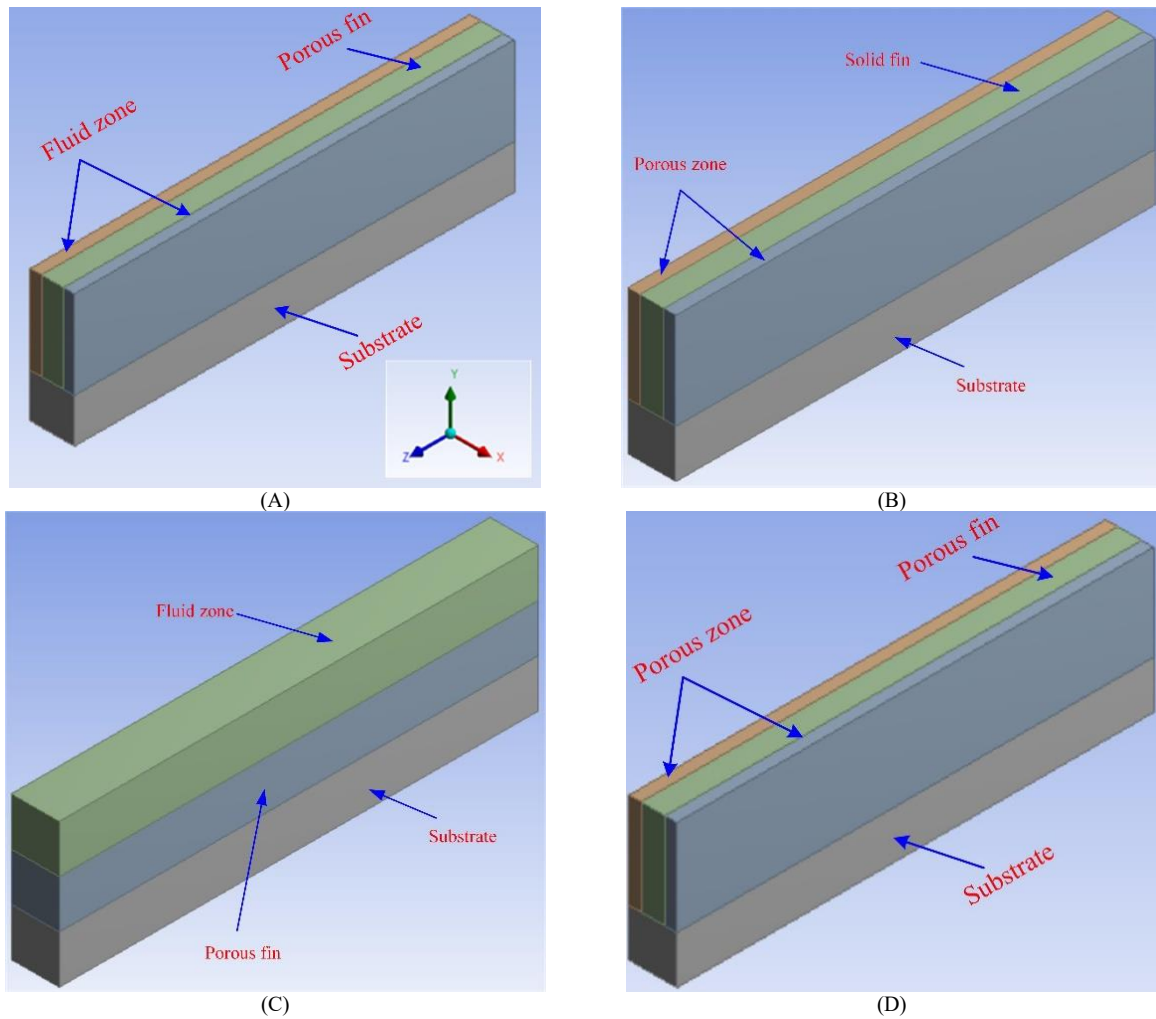


Figure 2. The patterns considered in the current study; (A) Porous fin-pure fluid zone, MCHS-1, (B) solid fin-porous zone, MCHS-2, (C) middle porous fin-upper fluid core MCHS-3, and (D) porous fin-porous zone, MCHS-4.

The pattern of MCHS-1 is further studied by varying the parameters a and b as shown in Figure 3(A). The cuboidal fin is replaced by a trapezoidal one in which the cross-sectional area of the fin is varied with the y -axis. This pattern is denoted by MCHS-5. It is worth to be mentioned that the total volume of the fins is the same. Four values for each a and b are investigated and analyzed to show their superiority in heat dissipation. These parameters are tabulated in Table 1. Further design for the porous fin is proposed here in which the cross-sectional area of the porous fin is varied with the longitudinal flow direction (z -axis). In the current situation, two patterns can be obtained; an upstream end apex-angle porous fin which is denoted by MCHS-6, and a downstream end apex-angle porous fin which is denoted by MCHS-7, as illustrated in Figure 3(B), and (C), respectively. Divergent foam fin with axial direction, MCHS-8, as seen in Figure 3(D), and convergent foam fin with axial direction, MCHS-9, as seen in Figure 3(E), are also investigated. In this style of the fin, the effect of the thermal boundary layer in the porous zone is concerned to emphasize that the uniform fin volume is not an effective and economical design. It should be

mentioned that the volume of the fin is kept constant to investigate its effect on the conductive heat transfer between the fin and substrate and the convective heat transfer between the fluid and porous media. All the above patterns are abbreviated in Table 2 for more clarification and simplification.

Table 1. Variable parameters and dimensions of the fin geometry.

No.	Variables		Fin shape
	a (mm)	b (mm)	
1.	0.5	0.5	Cuboidal cross-section normal to flow direction
2.	0.7	0.3	Trapezoidal cross-section normal to flow direction
3.	0.8	0.2	Trapezoidal cross-section normal to flow direction
4.	1.0	0.0	Triangular cross-section normal to flow direction

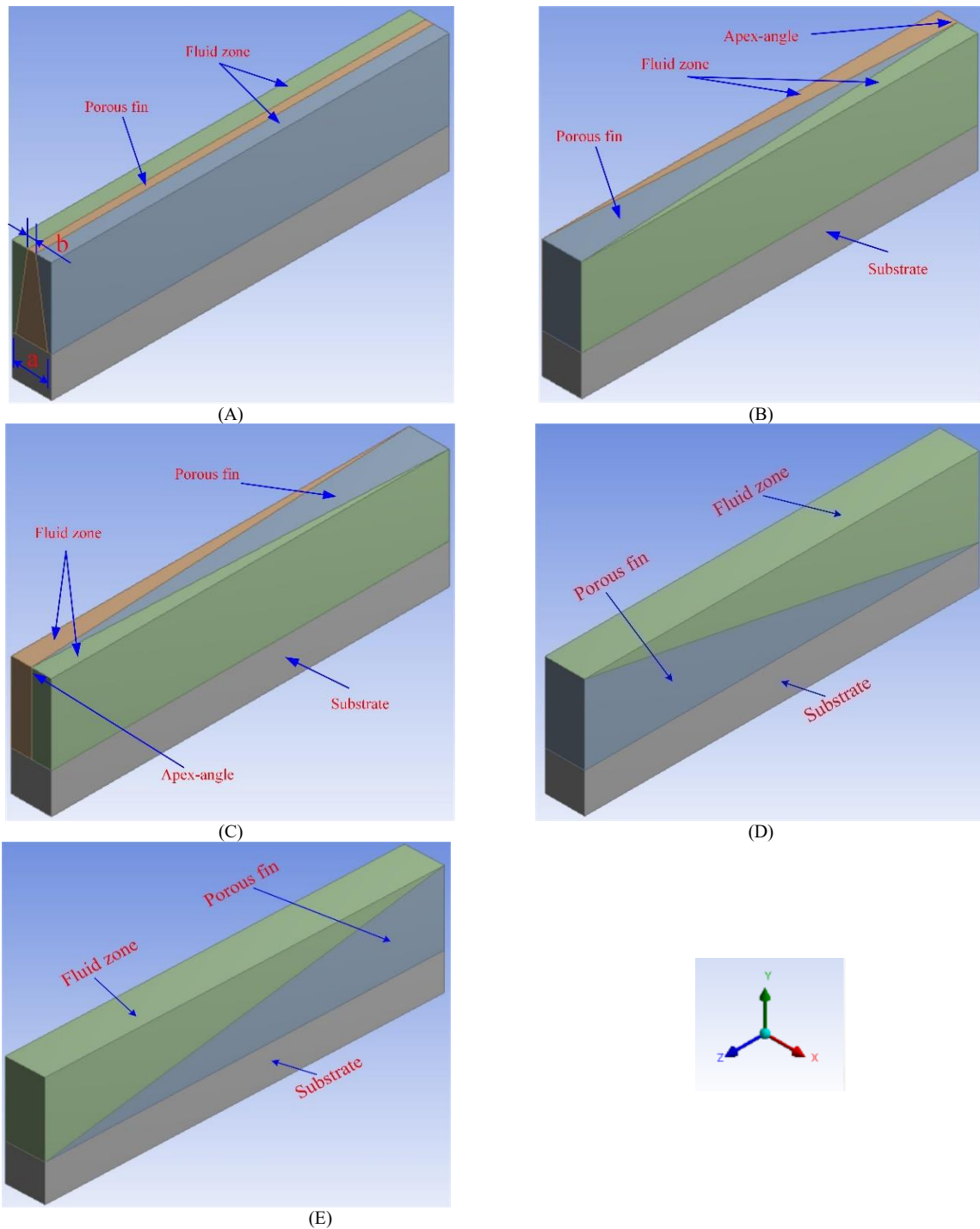


Figure 3. Schematic diagram of (A) geometric parameters of the trapezoidal porous fin- fluid zone, MCHS-5, (B) upstream apex-angle porous fin, MCHS-6, (C) downstream apex-angle porous fin, MCHS-7, (D) divergent fin with axial direction, MCHS-8, and (E) convergent fin with axial direction, MCHS-9.

Table 2. Abbreviation of all MCHS patterns proposed in this study.

No.	Patterns	Abbreviation
1	Traditional plate-fin MCHS	MCHS-0
2	Porous fin-pure fluid zone MCHS	MCHS-1
3	Solid fin-porous zone MCHS	MCHS-2
4	Middle porous fin-upper fluid zone MCHS	MCHS-3
5	Porous fin-porous zone MCHS	MCHS-4
6	Porous fin with cross-sectional area varied with y-axis MCHS	MCHS-5
7	Upstream end apex-angle porous fin MCHS	MCHS-6
8	Downstream end apex-angle porous fin MCHS	MCHS-7
9	Divergent foam fin with axial direction	MCHS-8
10	Convergent foam fin with axial direction	MCHS-9

3. Numerical approach

Computational fluid dynamics (CFD) is utilized for estimating the velocity, pressure, and temperature in the microchannel heat sink. The numerical simulation, using ANSYS-Fluent v.14, is carried out by solving the governing equations along with the boundary conditions using the finite volume method (FVM). The equations of the solid and fluid domain are solved simultaneously as a single domain conjugate problem. The flow field is solved by using the SIMPLE algorithm. The implicit method is adopted for discretizing the governing equations. Both the diffusion term and convective terms in the momentum and energy conservation equations are discretized by the second-order upwind differencing scheme. In addition, the second-order upwind differencing scheme is used for approximating the turbulent kinetic energy and turbulent dissipation rate. The solutions are considered to be converged when the normalized residuals of all variables become negligible (less than 1×10^{-6}) and the velocity components become unchangeable.

3.1. Boundary conditions

The following boundary conditions are assumed in the numerical computation. It is worth to be mentioned that owing to the symmetry, the flow through a single row of the fin is simulated.

- A heat flux of 300 kW/m^2 is applied to the bottom of the substrate base. The maximum temperature difference between the wall temperature and inlet bulk temperature does not exceed 37.7 K .
- Uniform velocity profile is assumed at the channel inlet ranged depending on the value of Reynolds number which is varied from 2000 to 6000. The inlet fluid temperature is 300 K .
- An outlet pressure condition is applied at the channel exit in which the gauge pressure equal to zero. The temperature gradient is zero ($\frac{dT}{dz} = 0$).
- No-slip boundary condition is assumed at the solid walls which are in contact with the fluid, and the heat flux is conserved ($\gamma_s \frac{dT_s}{dn} = \gamma_f \frac{dT_f}{dn}$).
- The symmetry boundary condition is applied on the right and left surfaces of the domain.
- An adiabatic and no-slip boundary conditions are applied on the other walls.

The temperature-dependent thermophysical properties of water are considered and presented in Table 3 where the temperature is in K. The values of the water properties are correlated from the data reported in [30]. The properties of the aluminum are 2702 kg/m^3 for the density, 237 W/m K for the thermal conductivity, and 903 J/kg K for the specific heat capacity. The current simulations are carried out at fixed porosity of 0.93, 10PPI, the permeability of $1.47523 \times 10^{-7} \text{ m}^2$, Forchheimer factor of 0.060, and inertia coefficient of 156.49 m^{-1} .

The permeability is estimated by the following formula[31]

$$K = d_p^2 \times 73 \times 10^5 \times (1 - \epsilon)^{-0.0224} \times \left(\frac{d_e}{d_p}\right)^{-1.11} \quad (1)$$

where d_p and d_e are the pore size and edge diameter, respectively, which are estimated from the following formulas[31]

$$d_p = 0.0254 \times (PPI)^{-1} \quad (2)$$

$$d_e = 1.18 \times \left(\frac{1}{1 - e^{-\frac{1-\epsilon}{0.04}}}\right) \times \left(\frac{1-\epsilon}{3\pi}\right)^{1/2} \quad (3)$$

The Forchheimer factor (CF) and the inertia coefficient (C) are, respectively, determined by [31]

$$CF = 29.613 \times \left[\frac{(1-\epsilon)^{1.5226}}{d_p}\right] \times \sqrt{K} \quad (4)$$

$$C = \frac{CF}{\sqrt{K}} \quad (5)$$

The effective thermal conductivity of the fluid-filled with porous media is simply estimated by[4, 31]

$$\gamma_{\text{eff}} = \epsilon \gamma_f + (1 - \epsilon) \gamma_s \quad (6)$$

3.2. Assumptions

The sintered porous media is assumed isotropic, homogeneous, and fully saturated with the working fluid. Three-dimensional, incompressible, turbulent, and steady fluid flow is considered. Temperature-dependent thermophysical fluid properties are adopted and the gravity, body forces, and radiation effects are negligible. The heat sink is insulated from the outside environment. The solid surface and the working fluid are assumed to be in local-thermal-equilibrium throughout the porous region. Forchheimer-Brinkman-Darcy equation based on a volume-averaging method is used to model the fluid flow through a porous region [32–37].

3.3. Governing equations

Based on the above assumptions, the RNG $k-\epsilon$ turbulence model is adopted, due to its high accuracy and reliability for a wide class of flows particularly for low-Reynolds number and its possibility to generate quick changes, for solving the governing equations. The continuity, momentum, and energy conservation equations can be written in a general formula:

Continuity equation:

$$\frac{\partial}{\partial x}(\rho u \phi) + \frac{\partial}{\partial y}(\rho v \phi) + \frac{\partial}{\partial z}(\rho w \phi) = \frac{\partial}{\partial x} \left[\Gamma_{\phi} \frac{\partial \phi}{\partial x} \right] + \frac{\partial}{\partial y} \left[\Gamma_{\phi} \frac{\partial \phi}{\partial y} \right] + \frac{\partial}{\partial z} \left[\Gamma_{\phi} \frac{\partial \phi}{\partial z} \right] + S_{\phi} \quad (7)$$

Table 3. Temperature-dependent thermophysical properties of water.

Quantity	Unit	Polynomial correlation
k	W/m K	$-0.8185 + 7.86 \times 10^{-3} T - 1.03 \times 10^{-5} T^2$
ρ	Kg/m ³	$754.930 + 1.8898 T - 3.62 \times 10^{-3} T^2$
μ	Pa s	$0.02466 - 1.3973 \times 10^{-4} T + 2.01 \times 10^{-7} T^2$
c_p	J/kg K	$5491.909 - 8.3940 T + 1.34 \times 10^{-2} T^2$

The equations of the flow region and the metal foam region are tabulated in Table 4 and Table 5, respectively.

Table 4. Summary of equations solved for the fluid zone (eq. 5).

Equation	ϕ	Γ_ϕ	S_ϕ
Continuity	1	0	0
x-momentum	u	μ_e	$-\frac{\partial P}{\partial x} + \frac{\partial}{\partial x} \left[\mu_e \frac{\partial u}{\partial x} \right] + \frac{\partial}{\partial y} \left[\mu_e \frac{\partial v}{\partial x} \right] + \frac{\partial}{\partial z} \left[\mu_e \frac{\partial w}{\partial x} \right]$
y-momentum	v	μ_e	$-\frac{\partial P}{\partial y} + \frac{\partial}{\partial x} \left[\mu_e \frac{\partial u}{\partial y} \right] + \frac{\partial}{\partial y} \left[\mu_e \frac{\partial v}{\partial y} \right] + \frac{\partial}{\partial z} \left[\mu_e \frac{\partial w}{\partial y} \right]$
z-momentum	w	μ_e	$-\frac{\partial P}{\partial z} + \frac{\partial}{\partial x} \left[\mu_e \frac{\partial u}{\partial z} \right] + \frac{\partial}{\partial y} \left[\mu_e \frac{\partial v}{\partial z} \right] + \frac{\partial}{\partial z} \left[\mu_e \frac{\partial w}{\partial z} \right]$
Energy	T	$\frac{\mu_e}{\sigma_T}$	0
Turbulent Kinetic energy	k	$\mu_l + \frac{\mu_t}{\sigma_k}$	$-\rho \epsilon + G$
Turbulent dissipation	ϵ	$\mu_l + \frac{\mu_t}{\sigma_\epsilon}$	$\frac{\epsilon}{k} (c_1 G - c_2 \rho) \epsilon$

$$\text{where } G = \mu_t \left\{ 2 \times \left[\left(\frac{\partial u}{\partial x} \right)^2 + \left(\frac{\partial v}{\partial y} \right)^2 + \left(\frac{\partial w}{\partial z} \right)^2 \right] + \left[\frac{\partial u}{\partial y} + \frac{\partial v}{\partial x} \right]^2 + \left[\frac{\partial v}{\partial z} + \frac{\partial w}{\partial y} \right]^2 + \left[\frac{\partial u}{\partial z} + \frac{\partial w}{\partial x} \right]^2 \right\}$$

$$\mu_e = \mu_l + \mu_t$$

Table 5. Summary of equations solved for metal foam zone (eq. 5).

Equation	ϕ	Γ_ϕ	S_ϕ
Continuity	1	0	0
x-momentum	u	μ_l	$-\epsilon^2 \frac{\partial P}{\partial x} + (\epsilon - 1) \mu_l \left[\frac{\partial^2 u}{\partial x^2} + \frac{\partial^2 u}{\partial y^2} + \frac{\partial^2 u}{\partial z^2} \right] - \rho \epsilon^2 uv \frac{\partial}{\partial y} \left[\frac{1}{\epsilon} \right] - \frac{\mu_l}{K_p} \epsilon^2 u$ $-\rho F U \epsilon^2 u$
y-momentum	v	μ_l	$-\epsilon^2 \frac{\partial P}{\partial y} + (\epsilon - 1) \mu_l \left[\frac{\partial^2 v}{\partial x^2} + \frac{\partial^2 v}{\partial y^2} + \frac{\partial^2 v}{\partial z^2} \right] - \rho \epsilon^2 vv \frac{\partial}{\partial y} \left[\frac{1}{\epsilon} \right] - \frac{\mu_l}{K_p} \epsilon^2 v$ $-\rho F U \epsilon^2 v$
z-momentum	w	μ_l	$-\epsilon^2 \frac{\partial P}{\partial z} + (\epsilon - 1) \mu_l \left[\frac{\partial^2 w}{\partial x^2} + \frac{\partial^2 w}{\partial y^2} + \frac{\partial^2 w}{\partial z^2} \right] - \rho \epsilon^2 ww \frac{\partial}{\partial y} \left[\frac{1}{\epsilon} \right] - \frac{\mu_l}{K_p} \epsilon^2 w$ $-\rho F U \epsilon^2 w$
Energy	T	$\frac{\alpha_p}{\rho}$	0

$$\text{where } |U| = (u^2 + v^2 + w^2)^{1/2}$$

4. Validation of the simulation

The present computational modeling is validated with the experimental data and numerical results reported by Feng et al. [21]. In their work, an aluminum heat sink has a base area of 68×68 mm² and a thickness of 4 mm with an aluminum metal foam having a height of 30 mm attached to the upper surface of the substrate. The heat was supplied to the base of the heat sink in which the maximum difference between the base wall temperature and inlet bulk temperature did not exceed 50 K. Air inlet impinging circular tube was attached to the upper surface of the metal foam for jetting the air and air exits from two sides of the heat sink whilst the other two sides were considered adiabatic. The airflow rate range was from 3000 to 12,000 Reynolds number. The properties of the metal foam were; 0.963 porosity, 8 PPI, 3.142×10⁻⁷ m² permeability, and 0.0492 form drag coefficient. From above, the physical domain of Feng and his group is modeled and the results of the pressure drop and Nusselt number are depicted and compared as shown in Figure 4(A) and (B), respectively. The figure shows an acceptable matching between the present predicted results and their experimental and

numerical data. Further validation is carried out with the experimental data published by Wang et al. [38]. An aluminum heat sink having 8 fins (30 mm in-height) filled with a copper metal foam inserted in heat sink channels. The porosity, permeability, and inertia coefficient of the metal foam are 0.919, 1.298×10⁻⁰⁷ m², and 0.05919, respectively, for the range of Reynolds number of 2000–8000. The k - ϵ , renormalized group turbulence model is adopted in the current simulation with the consideration of the scalable wall functions for the near-wall treatment. The mesh is refined in the fluid domain near the walls attached to the fluid taking the distance between the first cell centroid and the wall as 0.05 mm. The deviation of the pressure drop can be attributed to the fact that, in their experiments, the inlet pressure tab was positioned after the fan immediately and the outlet pressure tab was at the exit of the channel. Therefore, the pressure drop was greater in their measurements as the deviation is about 38% as shown in Figure 4(C). An acceptable agreement is observed in the Nusselt number as depicted in Figure 4(D). Thus, the present CFD modeling can be safely depended on to predict the heat transfer and fluid flow through a plate-fin heat sink having solid and/or porous media.

5. Mesh independency test

The computational domain of all patterns investigated here is meshed using hexahedral cells as shown in Figure 5(A), (B). Uniform and structural mesh are being generated and no refinement is used near the wall because the y^+ value is satisfied in the whole domain, not just near the wall. As shown in Figure 5(B), only the apex-angle of the porous fin is meshed using tetrahedral elements due to

its sharp edge. All the zones are formed as a new single part in the design modeler of ANSYS to match the mesh nodes between each two contact zones in which high-quality mesh could be obtained. The maximum, minimum, and average mesh quality obtained are 1, 0.036, and 0.987, respectively, for the pattern of MCHS-7, for instance, in which the lowest mesh quality is observed. Whereas the mesh quality of the rest patterns is, respectively, 0.9999, 0.9999, and 1.

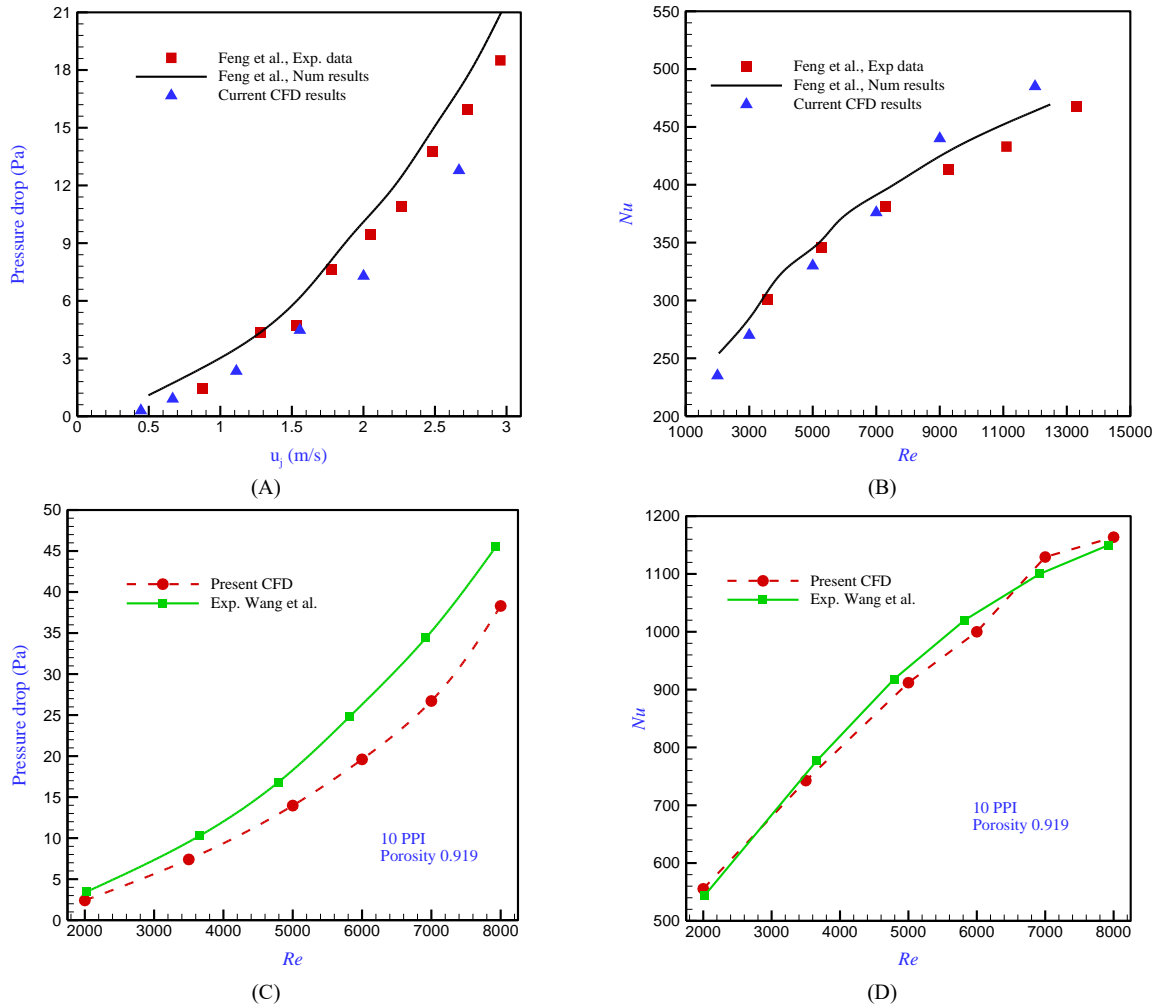


Figure 4. Validation with experimental and numerical results reported by Feng et al. [21], and Wang et al., [38]; (A) average pressure drop, (B) average Nusselt number, (C) pressure drop, and (D) average Nusselt number.

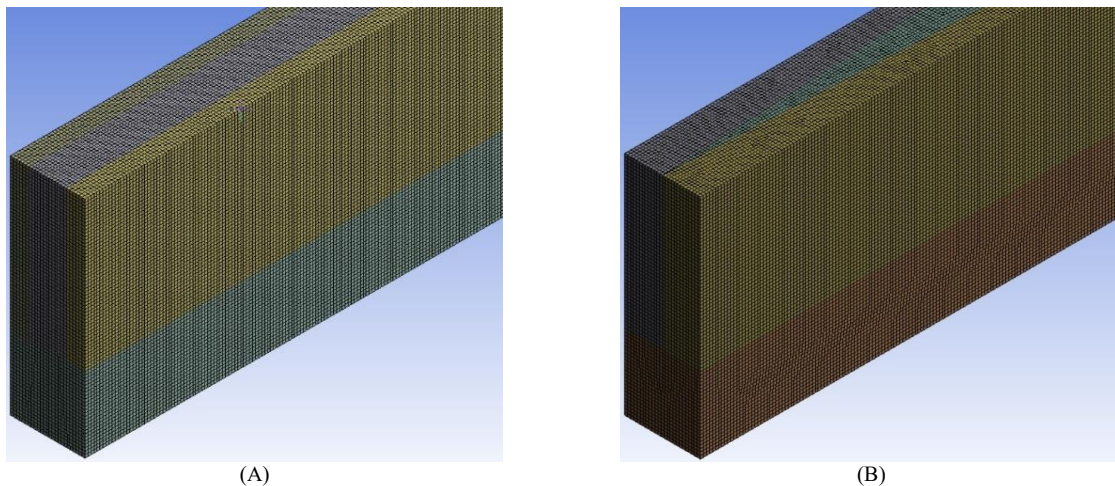


Figure 5. Meshing of the physical domain when the cross-sectional area of the fin and fluid zone is; (A) uniform, and (B) variable with the axial direction.

An extensive grid testing is carried out to guarantee grid independence. The tests are carried out at the highest value of the Reynolds number to make sure that the distance between the center of the first cell and the channel wall satisfies the value of y^+ . Different numbers of grid elements are tested as tabulated in Table 6. The axial pressure drop, outlet velocity profile, axial wall temperature distribution, and local Nusselt number are depicted with the mesh density as displayed in Figure 6(A)–(D). It is clear that the mesh density having an element size of 0.04 mm (i.e., the distance from the center of the first cell to the wall surface is 0.02 mm) is adequate and could provide accurate results in a shorter time compared to the finer one. The distance between the first cell center and the channel wall is estimated from y^+ in which the last is taken 10. This value of y^+ is fine enough due to the low turbulent Reynolds numbers covered in this

study. It should be mentioned that the domain is meshed uniformly and the x^+y^+ and z^+ are the same for any given near-wall cell.

Table 6. Nodes distribution in x -, y -, z -direction, and the total element number.

No.	Element size	node number			Total element number
	(mm)	x	y	z	
1.	0.1	10	30	100	33,000
2.	0.08	13	38	125	61,750
3.	0.06	17	50	167	141,950
4.	0.05	20	60	200	240,000
5.	0.04	25	75	250	468,750
6.	0.038	26	79	263	560,979

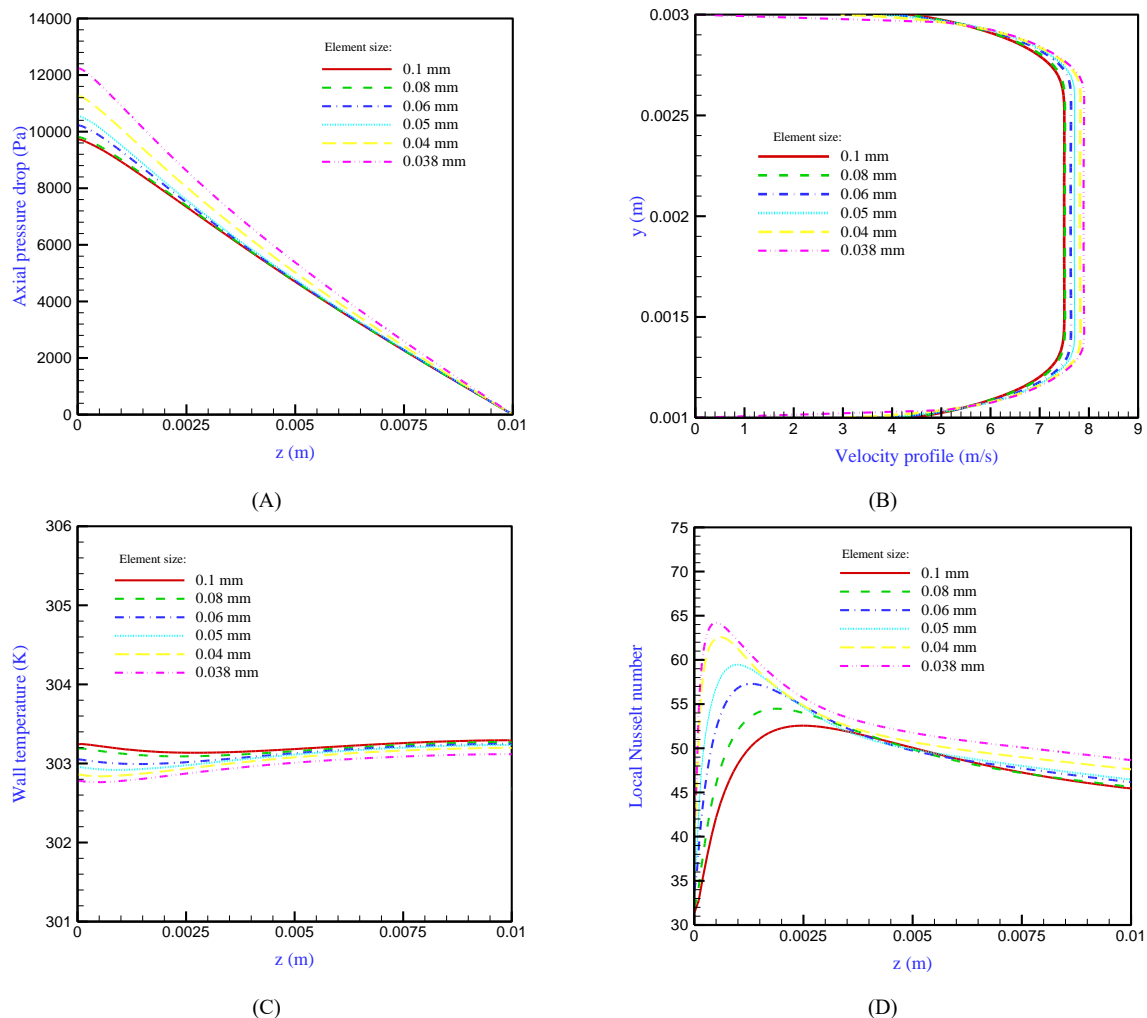


Figure 6. Quantities variation with the grid density; (A) axial pressure drop, and (B) velocity profile at the channel exit, (C) axial temperature distribution, and (D) local Nusselt number.

6. Data acquisition

The parameters estimated in the pre-processing such as the Reynolds number and post-processing, such as the Nusselt number, friction factor, and the hydraulic-thermal performance factor (JF) are interesting. The mean inlet water velocity is calculated by [30]

$$u_m = \frac{Re \mu}{\rho D_h} \quad (8)$$

where ρ , u_m , D_h , and μ represent, respectively, the fluid density, mean inlet fluid velocity, hydraulic diameter of the microchannel, and fluid kinematic viscosity. There are two hydraulic diameters estimations, one for the patterns of MCHS-0 and MCHS-2 due to the solid fin as in equation (9a), and the second for other patterns due to porous fin as in equation (9b). They are estimated according to the following formula [30]

$$D_h = 4 \frac{A}{P} = 2 \frac{H \frac{W}{2}}{(H + \frac{W}{2})} = \frac{H W}{(H + \frac{W}{2})} \quad (9a)$$

While for the patterns having porous fins

$$D_h = 2 \frac{H W}{(H + W)} \quad (9b)$$

where A and P are the cross-sectional area of the flow and wetted perimeter of the channel, respectively. The H and W are the channel height and the width of a single channel and fin, respectively. According to the last equation, the velocity of the patterns having solid fins differs from the patterns having porous fins. The turbulence intensity (I) is estimated by [39]

$$I = \frac{0.16}{\sqrt[8]{Re}} \quad (10)$$

The friction factor is estimated based on the pressure drop across the microchannel according to the velocity of the fluid is [10]

$$f = \frac{2 \Delta p D_h}{L \rho u_m^2} \quad (11)$$

The local convection heat transfer coefficient and the local Nusselt number are defined as [10]

$$h_z = \frac{q L W}{A_c [T_{z,w} - T_{z,f}]} \quad (12)$$

$$Nu_z = \frac{h_z D_h}{\gamma_f} \quad (13)$$

where q , A_c , $T_{z,w}$, $T_{z,f}$, and k_f represent, respectively, the heat flux at the substrate bottom surface, the contact surface area of water and aluminum wall for a single microchannel, the local conduction wall temperature, local bulk fluid temperature, and the thermal conductivity of the fluid. It is necessary to be mentioned that W is the width of the computational domain taken in this study.

The average Nusselt number is obtained by

$$Nu = \frac{1}{L} \int_0^L Nu_z \cdot dz \quad (14)$$

The JF factor is defined as [10, 11]

$$JF = \frac{\left(\frac{Nu}{Nu_o}\right)}{\left(\frac{f}{f_o}\right)^{1/3}} \quad (15)$$

where the subscript (o) refers to the traditional MCHS (solid fin-fluid zone).

The smaller temperature difference between the maximum and minimum temperature of the bottom of the MCHS substrate means higher temperature uniformity. Thus, the main characteristics of the temperature uniformity are the temperature difference and the

temperature distribution on the whole bottom surface of the substrate. The last is characterized by the mean square deviation of the bottom surface temperature. Therefore, a non-dimensional evaluative parameter TU is proposed to carry out a comparison between the patterns investigated here. The formula of TU is [40]

$$TU = \frac{T_{max} - T_{min}}{T_{avg}^2} \left[\frac{1}{n} \sum_{i=1}^n (T_i - T_{avg})^2 \right]^{0.5} \quad (16)$$

where T_{max} , T_{min} , and T_{avg} are the maximum, minimum, and average temperature of the substrate bottom surface, respectively. T_i is the temperature of a point on the surface, n is the number of those points which are picked uniformly. The term in the blank on the right side of the above equation represents the mean square deviation of the surface temperature. Lower TU means higher temperature uniformity.

7. Results and discussion

In the current study, the traditional flat plate-fin microchannel heat sink is developed by using metallic porous media in several forms as illustrated in the previous figures (Figure 2 and 3); porous media fins with fluid core, solid fins with porous media core, porous media attached to the substrate, and fluid core upper the porous media, porous media fins having a varied cross-sectional area with y-axis and fluid core, and porous media fins having a varied cross-sectional area with z-axis with the fluid core. The goal of this investigation is to enhance the dissipation of heat generation from the processors to the ambient keeping the size of the heat sink constant. The purpose of this study is to improve heat dissipation from the processor to the environment while keeping the size of the heat sink constant. The new and novel heat sink design proposed here achieves significant and unexpected results when compared to conventional ones, and the new design can open a wide door to the industry for modifying the speed of processors more and more while keeping the temperature of electrical components below the critical temperature. The results obtained in this study are depicted and interpreted in the following sections.

7.1. Uniform cross-sectional area of the fins heat sink

In this section, the patterns of MCHS-0, MCHS-1, MCHS-2, MCHS-3, and MCHS-4 are investigated. The volume of each zone is kept constant except the last one for showing the effect of increasing the volume of the porous media on the hydraulic and thermal performance of the MCHS.

The results of the Nusselt number of the four proposed designs of the heat sink with the traditional one over different values of Reynolds numbers are depicted in Figure 7(A). It can be seen that the thermal performance of MCHS-0 is so low and does not match the high-speed of the processors produced nowadays. The Nusselt number is significantly and unexpectedly increased in the proposed designs, and this augmentation grows with increasing Re number. The Nusselt number rises considerably in the MCHS-1 pattern. This is owing to the area of the convection heat transfer between the fluid and the solid edges of the porous media which is greater than that between the fluid and solid-fin surface. In addition, the length of the fluid path passing through the porous matrix is longer than that when the solid fin is used. A longer path means a larger time required for the coolant to reach the

outlet of the channel, and then further heat can be absorbed by the fluid. Moreover, the reattachment and redevelopment of the thermal boundary layer between the fluid and solid edges of the porous matrix could greatly enhance the heat transfer rate. The heat is absorbed from the substrate by the porous fin by conduction and then dissipated away by the coolant by convection. Therefore, further heat can be dissipated keeping the heat sink size constant. The pattern of MCHS-2 shows a greater increase in the Nusselt number. This is due to the fact that convection heat transfer occurs in two places: between the fluid and solid fins and between the fluid and porous medium domains. In addition, the area of the contact between the solid fin and porous media with the upper surface of the substrate increases in this design. An additional enhancement in the Nusselt number is obtained in the pattern of MCHS-3. As it is well-known, the porous media absorbs the heat from the substrate more than the pure fluid. Thus, in this case, the heat is transferred from the substrate by conduction, then through the porous fin by both conduction and convection, and eventually to the fluid by convection. The conduction between the porous media and the channel bottom surface is doubled. Therefore, the constant area between the porous fin base and the heat sink substrate is greater in this pattern compared to others. This design could increase the heat absorption by the porous fin. A slight enhancement in the Nusselt number is also monitored in the pattern of MCHS-4 compared to MCHS-3. From this small improvement, it can be said that no great heat dissipation can be obtained by further increases in the porous media volume, and then no more economical benefit can be received. The last design has a double volume of porous medium compared to the others in which the porous fin and porous zone are used.

The flow characteristics represented by the friction factor are depicted with Re number for the five patterns of the MCHS as shown in Figure 7(B). The traditional pattern exhibits the lowest frictional loss which is generally decreased with the increase of the Re number. This is also because the pure-fluid channel has low flow resistance compared to that using porous media. The patterns of MCHS-1 and MCHS-3 show higher frictional losses compared to the traditional one, while their friction factors are close to each other. The last two designs show the same frictional losses approximately because they have the same cross-sectional area (normal to the flow direction) for both porous fin and fluid zone. The MCHS-2 has a greater friction factor, which may be explained by the presence of the solid fin (which reduces the cross-sectional area of the fluid flow) and the flow resistance generated by the porous media. It can be said that during the flow of the fluid through the porous matrix, the solid edges of the porous media restrict the fluid flow and plays as obstacles in the flow channel. Nevertheless, the MCHS-4 provides the highest frictional losses among the other patterns due to filling the whole zone above the heat sink substrate by porous media.

The representation of the flow characteristics in terms of friction factor in the present study is not adequate unless the pressure drop along the heat sink is also highlighted for a comprehensive understanding of the flow mechanism as seen in Figure 7(C). It can be seen that the pattern of MCHS-1 and MCHS-3 exhibits the same pressure drop and their pressure drop is lower than the MCHS-0. It can be attributed to the fact that the wetted perimeter of the flow is doubled compared to the traditional one in which

the fluid velocity is lower at the corresponding Reynolds number. It can be also seen that the MCHS-4 has a pressure loss similar to that of the traditional one approximately, while a significant and tremendous increase in the pressure drop is monitored in the pattern of MCHS-2. Although the wetted perimeter of the fluid flow is small due to the use of solid fin, the pressure increases due to the flow resistance caused by the porous media zone. Thus, if the pressure drop in the MCHS is a key role, the last pattern must be avoided.

The judgment of choosing the optimal pattern cannot be made unless the hydraulic-thermal performance is illustrated in terms of the JF factor. These results are illustrated in Figure 7(D) with different values of the Re number. It is worth to be mentioned here that the hydraulic-thermal performance of the proposed patterns is compared to the traditional one. It can be seen that the maximum JF observed is for the pattern of MCHS-1, in which the JF equals 9.5 due to a high increase in the Nusselt number compared to a moderate increase in the frictional loss. More considerable enhancement in the JF is observed in the pattern of MCHS-2 owing to the conduction through the solid fin and the solid edges of the porous media and also owing to the increase in the convection heat transfer area between the fluid and the solid. The MCHS-3 shows the highest JF factor due to the great Nusselt number enhancement accomplished with a low increase in the friction factor. This enhancement in the JF reduces when the MCHS-4 is used due to remarkable improvement in the friction factor with an enhancement in Nusselt number close to that of MCHS-3.

From the above results obtained, it can be encouraged that when thermal performance is a key role in the MCHS design, MCHS-4 is recommended. If the frictional loss plays an important role, the MCHS-3 can be counseled, as the highest JF obtained in this pattern is 15.6 at $Re = 3000$. This pattern can be also advised for designers whose hydraulic-thermal performance is the target. Economically, the amount of the porous fin material requirement is lower than that of the solid fin. Based on the equation of the effective density of the porous media which can be written as[22]

$$\rho_{\text{eff}} = (1 - \epsilon)\rho_s + \epsilon\rho_f \quad (17)$$

The reduction in the mass of the fin material is 58.68% when the solid fin is replaced by the porous one. Due to higher thermal effectiveness and material saving and a lower material requirement, the designers are encouraged for implementing the metal foam fins in their new MCHS designs.

At $Re = 3000$, the contours of the temperature distribution of the MCHS-0 are illustratively shown in Figure 8(A). It is explicitly observed that this pattern exhibits a big hot spot through the whole volume of the substrate and the solid fin temperature ranged from 300 K at the beginning of the fin tip up to 352 K at the bottom of the substrate. A great temperature drop is obtained when the porous fin is used instead of the solid one as shown in Figure 8(B). The most volume of the fin is cold and its temperature ranges from 300 K to 312 K. Moreover, the beginning of the substrate is colder compared to the traditional one, while the maximum temperature of the substrate bottom is still around 352 K. A significant and unexpected temperature gradient is monitored in the pattern of MCHS-2 as illustrated in Figure 8(C). Although

the fin almost has a low temperature (300 K – 300.8 K), most of the substrate domain is green (i.e., 301 K–301.9 K). It is worth to be mentioned that the maximum temperature of the solid wall is around 302.7 K. Figure 8(D) shows that the whole volume of the fin is cold (300 K–300.9 K) and most of the half volume of the substrate is below 302.8 K. In addition, the spot of hot temperature

(i.e., 304.1 K) is only at the downstream end of the substrate (at the bottom only). The pattern of MCHS-4 is explored as shown in Figure 8(E) in which higher temperature is recorded (303.8 K) at the downstream bottom of the substrate and most of the rest of the domain is less than 302.3 K.

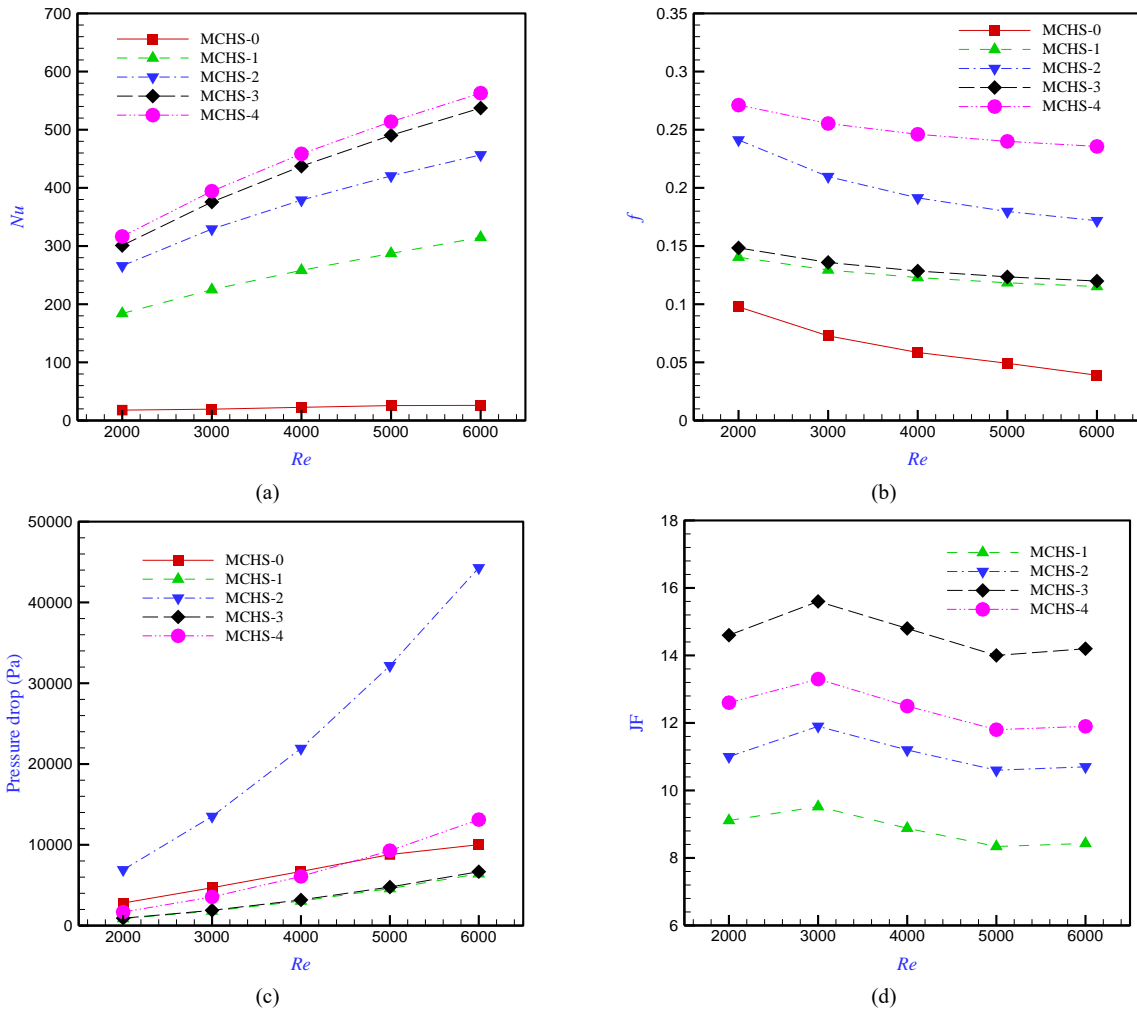


Figure 7. Comparison of the different MCHS patterns over the range of Re number; (A) Nusselt number, (B) friction factor, (C) pressure drop, and (D) JF factor.

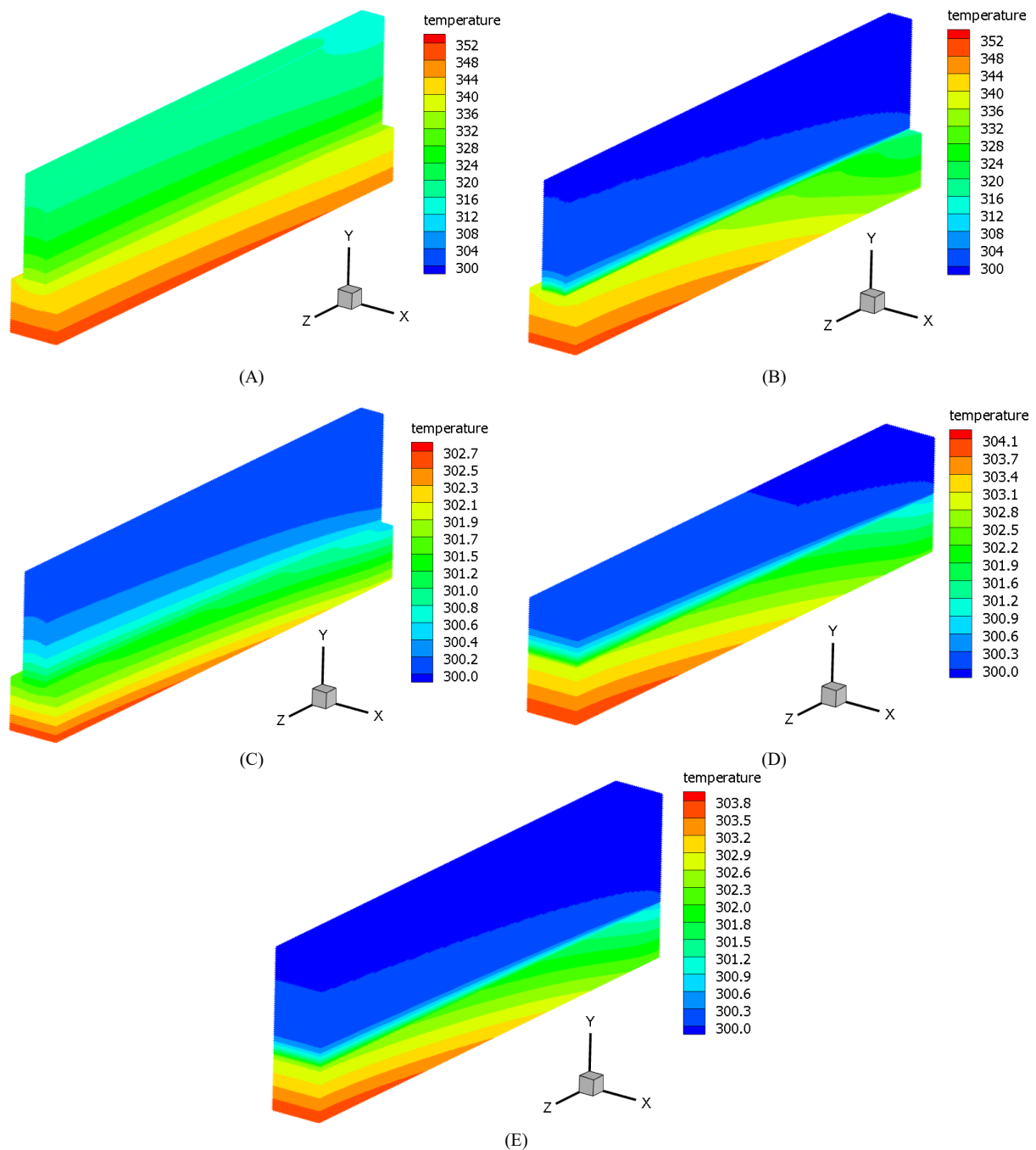


Figure 8. Contours of temperature distribution for (A) MCHS-0, (B) MCHS-1, (C) MCHS-2, (D) MCHS-3, and (E) MCHS-4.

7.2. Variable cross-sectional area of the porous fins with the y-axis

In this section, the pattern of MCHS-1 is explored here. Variable vertical cross-sectional areas of the porous fin are investigated keeping the total volume of the porous media zone constant. The length of the bottom side and topsides of the porous fin is; 0.5 mm and 0.5 mm, 0.7 mm and 0.3 mm, 0.8 mm and 0.2 mm, and finally 1.0 mm and 0.0 mm as illustratively shown in Figure 9(A)–(C), respectively.

The results of the Nusselt number with Re number for several patterns of the porous fin are displayed in Figure 9(A). The results show that the uniform cross-section porous fin provides Nu number from 184 to 314 at the lowest and highest value of Re number, respectively. This

result is the same as that shown in the previous section (7.1). When the length of the porous fin bottom is increased in the x-direction, the quantity of heat transported by conduction from the substrate to the porous fin grows, the Nusselt number is dramatically increased. This increment in the Nu number enhances with increasing the Re number. It can be said here that increasing the bottom-side length and decreasing the top-side length of the porous fin could cause higher conductive heat transfer between the fin and substrate in which the fin temperature increases due to the further heat absorbed. Thus, higher convective heat transfer occurs between the fluid and porous fin due to a large temperature difference between them. Due to the convection heat transfer between the coolant and the porous fin, the temperature of the porous fin decreases away from the wall, and this decrease in the temperature

reduces the effectiveness of the porous fin. Conclusively, the longest bottom side and zero top side porous fin (i.e., $a = 1.0$ mm and $b = 0.0$ mm) outperforms the traditional cross-sectional area of the porous fin in terms of heat transfer.

It can be also observed that the friction factor of the traditional and uniform cross-section porous fin is the lowest among all the proposed patterns as seen in Figure 9(B). However, all the other patterns provide a slight increase in the friction factor and their results are close to each other. It can be concluded that the frictional losses increase with increasing the tip angle of the cross-sectional area of the flow due to the thickening of the hydraulic boundary layer at the tip. In general, the friction factor decreases with increasing the Re number.

The results JF factor reveal that when the tip of the porous fin decreases, the JF factor increases monotonically and the results of all proposed patterns outperform the results of traditional uniform cross-sectional area porous fin as shown in Figure 9(C). The maximum JF factor obtained here is 15.9 for the last pattern shown in the figure legend. Therefore, for designing the MCHS with optimal hydraulic-thermal performance, the zero-tip length porous fin is recommended in which a wide door can be

opened for manufacturing ultra-high-speed electronic processors.

The contours of the temperature gradient of the MCHS-1 with a cross-sectional area of 0.5 mm \times 0.5 mm keeping the height constant are shown in Figure 10(A) and interpreted in the formal contours drawing. Figure 10(B) displays that when the bottom length of the fin is enlarged to be 0.7 mm and the tip length is reduced to 0.3 mm, the maximum temperature is remarkably dropped to 304.4 K. More temperature reduction is observed when the fin bottom length is enlarged to be 0.8 mm and 1.0 mm, as shown in Figure 10(C) and (D), respectively. It can be concluded that when the fin bottom width increases, the conduction area between the fin and substrate increases, and then more heat is transferred by the fin. This heat is dissipated from the fin to the fluid by convection. This convection heat transfer occurs greatly close to the bottom of the flow channel and reduces with y -direction. In that case, there is no need to keep the cross-sectional area of the fin constant with y -direction as the effectiveness of the fin reduces. These proposed patterns do not lower the quantity of fin material used, but rather change the design of the fins only when the heat transfer is significantly improved.

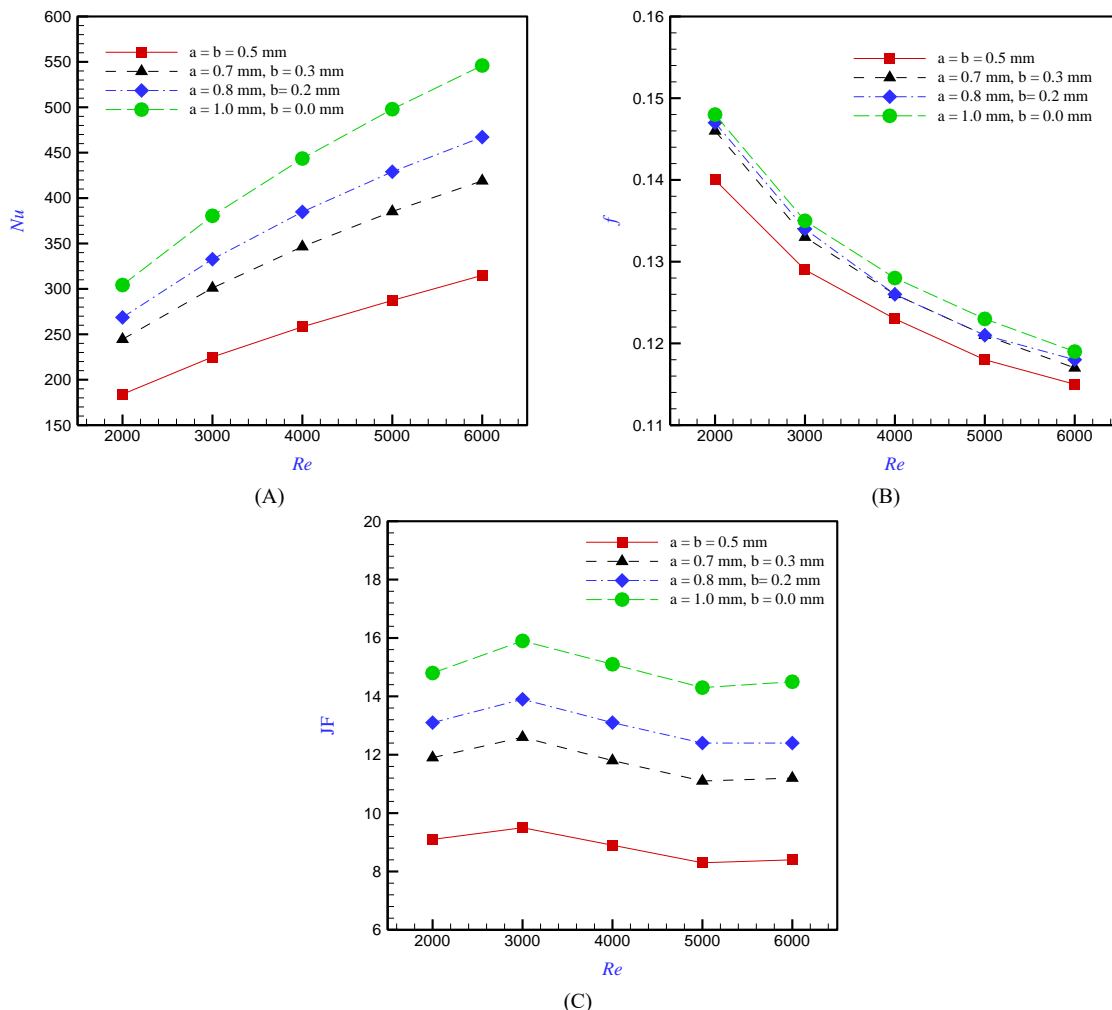


Figure 9. Effect of cross-sectional area varying with y -direction of MCHS-5 pattern on (A) the Nusselt number, (B) friction factor, and (C) JF factor.

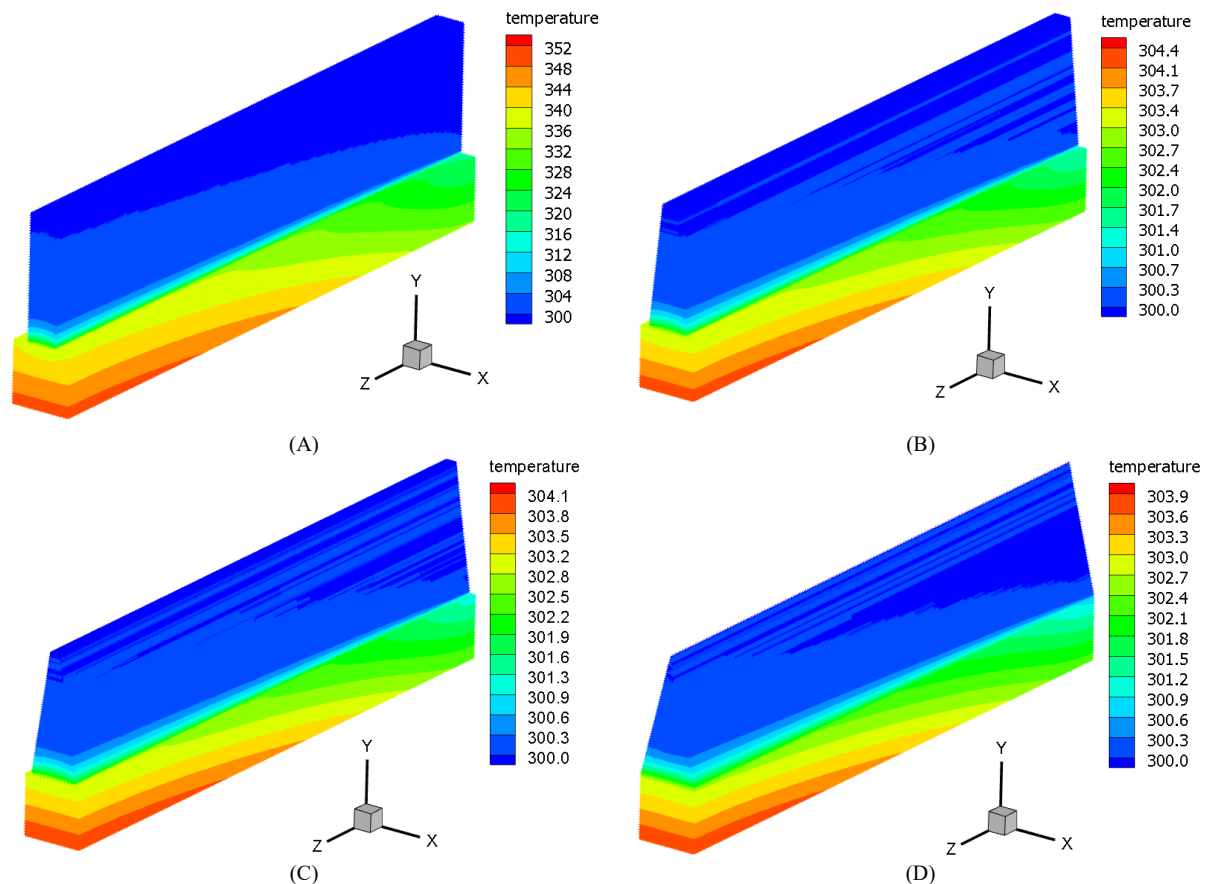


Figure 10. Contours of temperature distribution of the MCHS-5 pattern; (A) 0.5 mm, 0.5 mm, (B) 0.7 mm, 0.3 mm, (C) 0.8 mm, 0.2 mm, and (D) 1.0 mm, 0.0 mm, at $Re = 3000$.

7.3. Variable cross-sectional area of the porous fin with the z-axis

After studying the effect of varying the cross-sectional area with the y-axis, now the effect of varying the cross-sectional area with the longitudinal flow direction is investigated. It is worthy to be mentioned that the total volume of the porous fin is the same in both proposed designs and equal to the volume of the traditional porous fin volume.

The results of the Nusselt number infer that the MCHS-6 provides a lower Nusselt number than the MCHS-1 as shown in Figure 11(A). On the contrary, the MCHS-7 shows a significant increase in the Nusselt number compared to the aforementioned two patterns. It can be interpreted as the wall temperature of the upper surface of the substrate is high at the leading edge of the channel and decreases with the axial flow direction. Therefore, great heat absorption occurs at the beginning of the channel. Hence, there is no need to add more porous material downstream of the channel. Furthermore, both the MCHS-8 and MCHS-9 designs have seen a significant increase in the Nusselt number. Their heat dissipation is very similar, especially as the Reynolds number increases. Conclusively, the pattern of MCHS-8 and MCHS-9 have the optimal thermal performance compared to other patterns.

The lowest friction factor is observed for the MCHS-1 because the flow channel has a small flow resistance

along the axial flow direction (uniform cross-sectional area for the fluid zone) as shown in Figure 11(B). A higher friction factor is displayed for the MCHS-6 due to the smallest drag force at the channel inlet because of the sharp leading edge of the metal foam fin and gradually increases with the axial direction. In contrast, the friction factor of the MCHS-7 is slightly higher than the MCHS-6 because the cross-sectional area of the flow is filled with the porous media at the channel inlet in which the drag force is in its highest value. But the flow resistance decreases with the axial flow direction owing to the reduction in the cross-sectional area of the porous fin and increasing the cross-section of the fluid zone. The friction factor of pattern MCHS-8 is exactly the same as that of MCHS-7, but its Nusselt number is significantly higher. Further frictional losses are observed when the MCHS-9 is used due to the large drag force of the frontal area of the porous fin at the leading edge of the channel. In addition, the viscosity effect at the viscous sublayer in this pattern is higher than that in the MCHS-7 (as they have the same frontal area at the leading edge of the channel) and consequently greater frictional force is observed.

For a fully comprehensive picture of the hydraulic-thermal performance of these three different patterns, the JF factor is also depicted in Figure 11(C). The great value of the JF for the pattern of MCHS-6 is explicitly seen, particularly at low values of Re number, but it is lower than that of the MCHS-1. Further JF enhancement is noticed when the MCHS-7 is applied in which a huge amount of heat dissipation with a slight increase in the frictional loss

is carried out. A significant and unexpected enhancement in the JF factor is obtained in both MCHS-8 and MCHS-9. Therefore and conclusively, for the same volume of the porous fin, the engineers are encouraged to use the MCHS-8 or MCHS-9 when the Nusselt number is the vital key, and MCHS-8 when the friction plays an important role, and MCHS-8 or MCHS-9 when JF is the target, as the processor speed could be increased dramatically.

Figure 12(A) illustrates the contours of temperature distribution of the MCHS-1. This thermal behavior is explained in the formal contours figure. When the porous fin volume is kept constant, the cubic domain of the fin (MCHS-1) is replaced with a tetrahedral one having an apex-angle at the upstream end of the flow channel (MCHS-6) as seen in Figure 12(B). This design is proposed owing to its lower drag force in which the frictional loss in its lowest values. However, the temperature distribution is opposite as the highest temperature is observed at the leading edge of the substrate, and the temperature drops with the axial length.

The whole fin domain is cold and lower than 301 K. The opposite behavior is observed with the MCHS-7 as the coldest spot of the substrate is at the leading edge and the hottest is at the downstream end of the base, see Figure 12(C). It can be attributed that the hot spot substrate occurs under the low-amount material of porous fin in which the conduction is low as well. More temperature drop is observed when the pattern MCHS-8, see Figure 12(D), is used as the maximum temperature recorded is 303.8 K. Nevertheless, the maximum temperature in the MCHS-9, see Figure 12(E), is greater than the last pattern, 304.0 K, the electronic cooling by using the pattern of MCHS-9 is the optimal choice because the region of the hot spot in the last pattern is smaller and the cold region is larger. This pattern could offer better wall temperature uniformity. By looking at these contours, it can be concluded that the apex-angle of the fin can be also adjustable and investigated for obtaining uniform substrate base temperature.

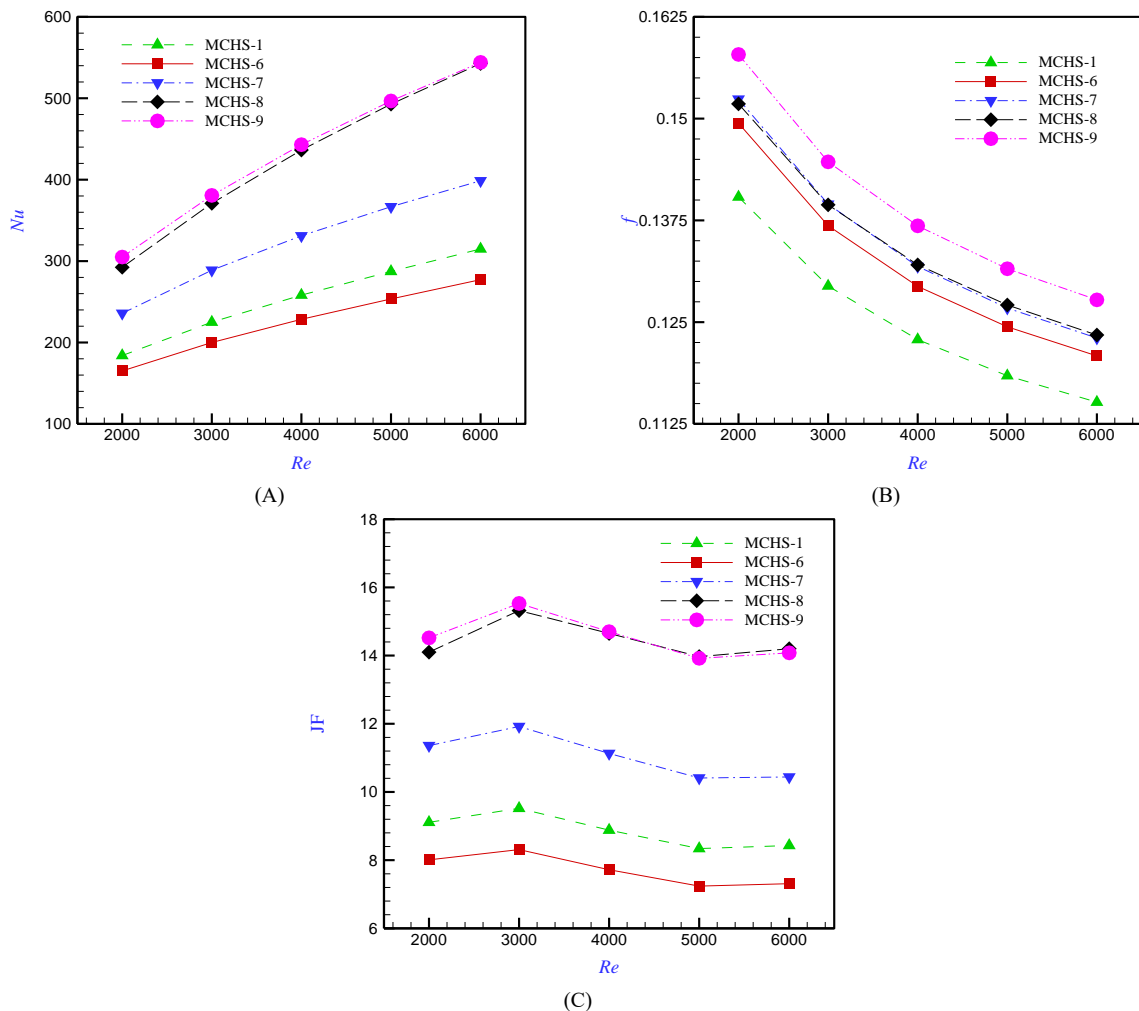


Figure 11. Comparison between the uniform and non-uniform cross-sectional area of the fin with z-direction (A) Nusselt number, (B) friction factor, and (C) JF.

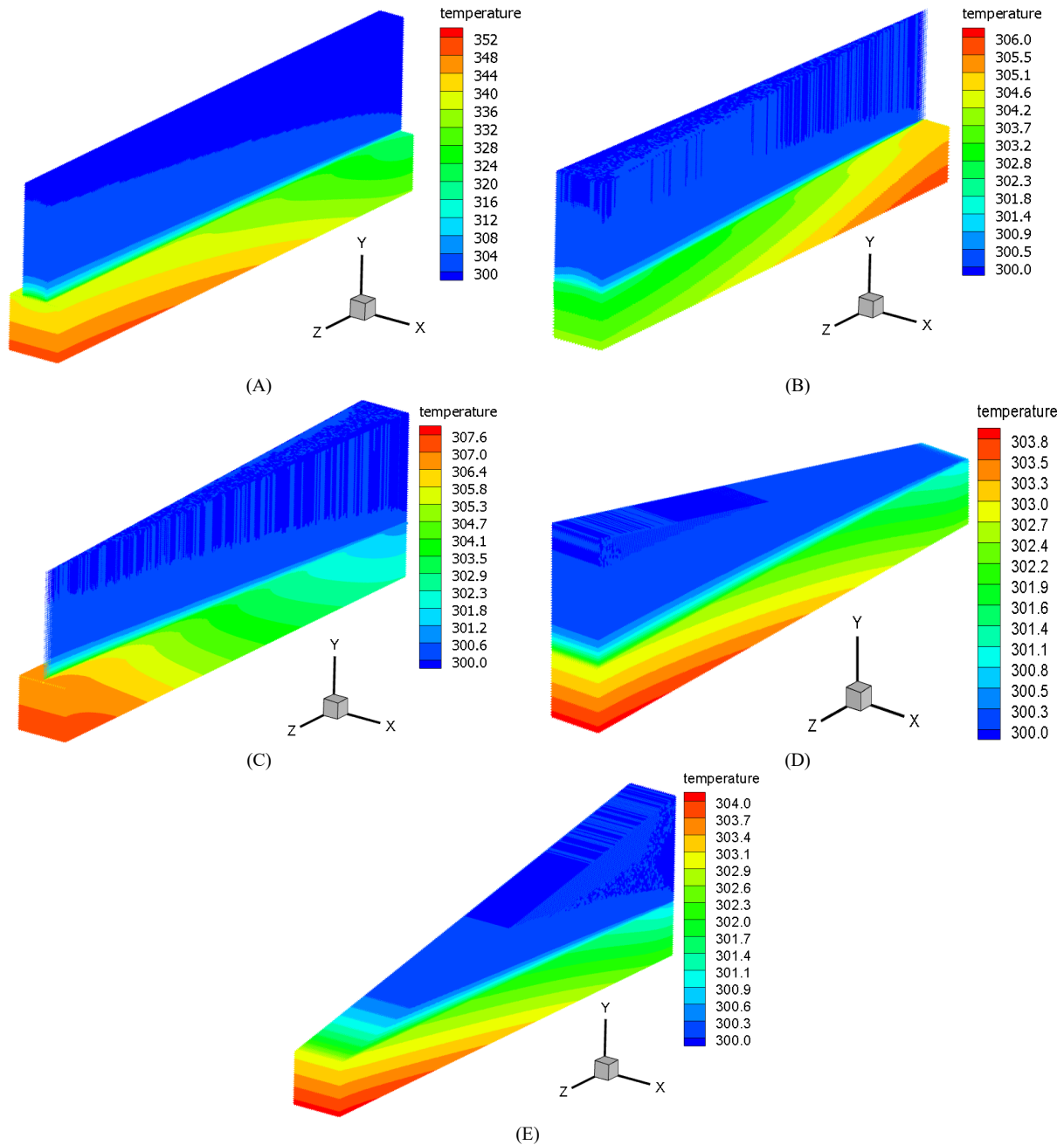


Figure 12. Contours of the temperature distribution of (A) MCHS-1, (B) MCHS-6, (C) MCHS-7, (D) MCHS-8, and (E) MCHS-9, at $Re = 3000$.

7.4. Uniformity of the wall temperature

The heat sink temperature plays an important role to protect the electronic components working below the critical temperature and increase the reliability. Therefore, the axial distribution of the temperature at the centerline of the channel bottom surface is depicted at $Re = 3000$. Figure 13(A) indicates that the MCHS-2, MCHS-3, and MCHS-4 layouts give the lowest heat sink base temperature. They also have a modest temperature variation between the upstream and downstream ends of the substrate. It is necessary to say that the MCHS-0 shows a very high wall temperature of the substrate. In addition, the pattern of MCHS-1 shows an exponential increase in the wall temperature and it shows the largest temperature difference although it provides a great heat dissipation in

comparison with the others. The pattern of MCHS-2 provides the smallest temperature difference compared to the others. When the parameters a and b are varied, all of these patterns exhibit a very small temperature difference concerning the constant cross-sectional area of the porous fin with the y-axis as shown in Figure 13(B). Precisely, the pattern of $a = 1.0$ mm and $b = 0.0$ mm shows the optimal trend. Furthermore, both the MCHS-6 and MCHS-7 display a significantly low difference in the temperature between the beginning and end of the substrate in comparison with the traditional porous fin as shown in Figure 13(C). Further study is carried out to evaluate the temperature uniformity using the non-dimensional parameter TU as shown in Figure 13(D) for three Reynolds numbers; 2000, 4000, and 6000. The smaller TU, the more temperature uniformity. It is necessary to say that the right y-axis is particular for the MCHS-1 due to its very

high TU values compared to other patterns. These high TU values can be attributed to the lower fluid velocity compared to the cases of the solid fins because the porous fin zone is included in the estimation of the hydraulic diameter at the corresponding Re number. It also emphasizes that the pattern of the MCHS-2 has the superiority of the temperature uniformity. Moreover, the TU decreases with increasing the Re number. The UT of

the patterns MCHS-6 to MCHS-9 is depicted in Figure 13(E) and also compared with the pattern of MCHS-1. As explained before, MCHS-1 has a high value of the TU and a large difference with Re . A lower value and smaller difference of TU are obtained by the pattern of MCHS-7 whilst a great TU is observed for other cases (i.e., MCHS-6, -8, and -9).

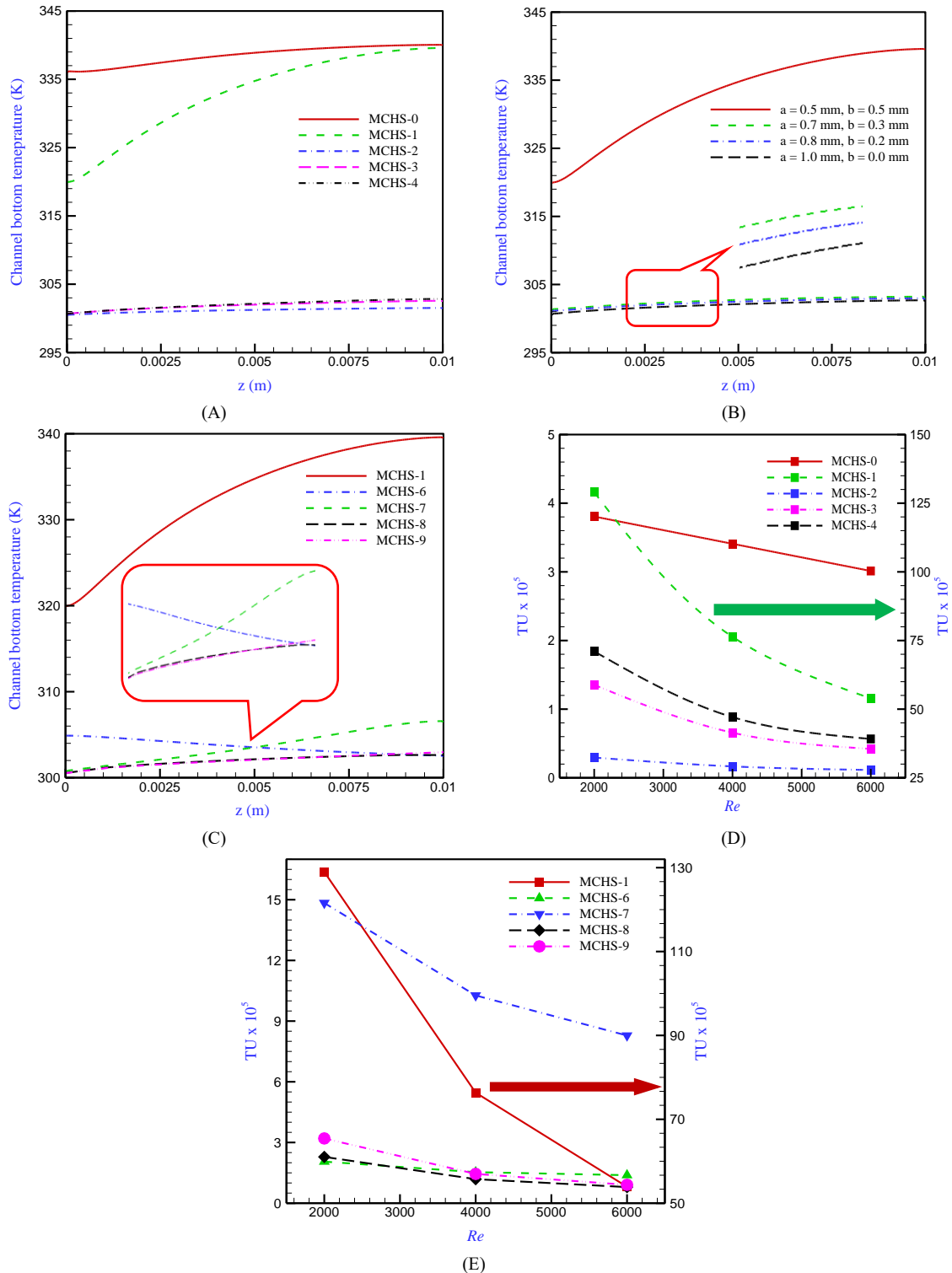


Figure 13. Temperature uniformity of the channel bottom (A) uniform cross-sectional area fin patterns, (B) MCHS-5, (C) variable cross-sectional area with z-axis at $Re = 3000$, (D) UT of MCHS-0 to -4, and (E) UT of MCHS-1 and MCHS-6 to -9.

Conclusions

In this paper, a three-dimensional computational simulation is carried out for enhancing the hydraulic and thermal performance of plate-fin MCHS using metal foam inserts over a range of Reynolds numbers from 2000 to 6000. Several new MCHS patterns are proposed considering the constant and variable cross-sectional area of the porous fin. The insert of porous media instead of the solid or fluid zone of the MCHS exhibits, in general, a significant enhancement in the Nusselt number accomplished with a moderate increase in the friction factor. The conclusions drawn from the predicted results can be summarized as follows:

1. The maximum increase in the Nusselt number and friction factor observed in the constant cross-sectional area of the porous fin is 20.66 times and 3.08 times, respectively, at $Re = 6000$ for the MCHS-3 compared to the traditional pattern. Besides, the optimal JF obtained is 15.65 at $Re = 3000$.
2. A tremendous enhancement in the Nusselt number (21.0 times) with a small increase in the friction factor (3.06 times) is observed for MCHS-5 (i.e., $a = 1.0$ mm, $b = 0.0$ mm) at $Re = 6000$, with respect to the traditional one. The maximum JF is 15.87 at $Re = 3000$ for the same pattern.
3. For the MCHS-9, a great improvement in the Nusselt number is revealed about 20.93 times at $Re = 6000$ associated with an insignificant increase in the friction factor of 3.29 times compared to the baseline one. Whilst it provides a JF of 15.53 at $Re = 3000$.
4. More enhancement in the Nusselt number (21.65 times) with additional frictional loss (6.06 times) is seen when the volume of the porous media is doubled (i.e., MCHS-4) in comparison with the traditional one, while the maximum JF factor is 11.87.
5. All proposed patterns of the MCHS exhibit a great temperature uniformity compared to the traditional fin design (MCHS-0). The optimal wall temperature uniformity (TU) observed is for the pattern of MCHS-2.

In general, all patterns that have variable cross-sectional areas of the porous fin with the vertical or axial direction provide significantly better thermal performance, hydraulic-thermal performance, and wall temperature uniformity compared to the constant cross-sectional fin area.

References

- [1] D.B. Tuckerman, R.F.W. Pease, High-performance heat sinking for VLSI, *IEEE Electron. Device Lett.* 2 (1981) 126–129.
- [2] X.-Y. Li, Sh.-L. Wang, X.-D. Wang, T.-H. Wang, Selected porous-ribs design for performance improvement in double-layered microchannel heat sinks, *International Journal of Thermal Sciences* 137 (2019) 616–626.
- [3] Ghahremannezhad, H. Xu, M.A. Nazari, M.H. Ahmadi, K. Vafai, Effect of porous substrates on thermohydraulic performance enhancement of double layer microchannel heat sinks, *International Journal of Heat and Mass Transfer* 131 (2019) 52–63.
- [4] T.-H. Wang, H.-Ch. Wu, J.-H. Meng, W.-M. Yan, Optimization of a double-layered microchannel heat sink with semi-porous-ribs by multi-objective genetic algorithm, *International Journal of Heat and Mass Transfer* 149 (2020) 119217.
- [5] S.T. Kadam, R. Kumar, Twenty first century cooling solution: microchannel heat sinks, *International Journal of Thermal Science* 85 (2014) 73–92.
- [6] S. Lu, K. Vafai, A comparative analysis of innovative microchannel heat sinks for electronic cooling, *International Communications in Heat and Mass Transfer* 76 (2016) 271–284.
- [7] N.H. Naquiuddin, L.H. Saw, M.C. Yew, F. Yusof, T.C. Ng, M.K. Yew, Overview of micro-channel design for high heat flux application, *Renewable and Sustainable Energy Review* 82 (2018) 901–914.
- [8] L. Chuan, X.-D. Wang, T.-H. Wang, W.-M. Yan, Fluid flow and heat transfer in microchannel heat sink based on porous fin design concept, *International Communications in Heat and Mass Transfer* 65 (2015) 52–57.
- [9] Ch.-H. Chen, Forced convection heat transfer in microchannel heat sinks, *International Journal of Heat and Mass Transfer* 50 (2007) 2182–2189.
- [10] Y. Li, L. Gong, M. Xu, Y. Joshi, Hydraulic and Thermal Performances of Metal Foam and Pin Fin Hybrid Heat Sink, *Applied Thermal Engineering*, 166 (2020) 114665.
- [11] H. Arasteh, R. Mashayekhi, M. Goodarzi, S.H. Motaharpour, M. Dahari, D. Toghraie, Heat and fluid flow analysis of metal foam embedded in a double-layered sinusoidal heat sink under local thermal non-equilibrium condition using nanofluid, *Journal of Thermal Analysis and Calorimetry*, <https://doi.org/10.1007/s10973-019-08168-x>.
- [12] S.Q. Hussien, A.A. Farhan, The effect of metal foam fins on the thermohydraulic performance of a solar air heater, *International Journal of Renewable Energy Research*, 9 (2) (2019) 840–847.
- [13] M.A. Nima, A.M. Ali, Numerical study of heat transfer enhancement for a flat plate solar collector by adding metal foam blocks, *Journal of Engineering*, 23(12) (2017) 13–32.
- [14] Heydari, M. Mesgarpour, M.R. Gharib, Experimental and Numerical Study of Heat Transfer and Tensile Strength of Engineered Porous Fins to Estimate the Best Porosity, *Jordan Journal of Mechanical and Industrial Engineering* 14(3) (2020) 339–348.
- [15] T.-Ch. Hung, Y.-X. Huang, W.-M. Yan, Thermal performance analysis of porous-microchannel heat sinks with different configuration designs, *International Journal of Heat and Mass Transfer* 66 (2013) 235–243.
- [16] R. Singh, A. Akbarzadeh, M. Mochizuki, Sintered porous heat sink for cooling of high-powered microprocessors for server applications, *International Journal of Heat and Mass Transfer* 52 (2009) 2289–2299.
- [17] T.C. Hung, W.M. Yan, Thermal performance enhancement of microchannel heat sinks with porous metallic medium, *Numerical Heat Transfer Part A: Application* 63 (9) (2013) 666–686.
- [18] Z.M. Wan, J. Liu, K.L. Su, X.H. Hu, S.S. M, Flow and heat transfer in porous micro heat sink for thermal management of high power LEDs, *Microelectronics Journal* 42 (2011) 632–637.
- [19] T.-Ch. Hung, Y.-X. Huang, W.-M. Yan, Thermal performance of porous microchannel heat sink: Effects of enlarging channel outlet, *International Communications in Heat and Mass Transfer* 48 (2013) 86–92.
- [20] H.R. Seyf, M. Layeghi, Numerical analysis of convective heat transfer from an elliptic pin fin heat sink with and without metal foam insert, *Journal of Heat Transfer ASME*, 132 (2010) 071401-1.

- [21] S.S. Feng, J.J. Kuang, T. Wen, T.J. Lu, K. Ichimiya, An experimental and numerical study of finned metal foam heat sinks under impinging air jet cooling, *International Journal of Heat and Mass Transfer* 77 (2014) 1063–1074.
- [22] M. Siavashi, H. Rasam, A. Izadi, Similarity solution of air and nanofluid impingement cooling of a cylindrical porous heat sink, *Journal of Thermal Analysis and Calorimetry*, <https://doi.org/10.1007/s10973-018-7540-0>.
- [23] Deng, Y. Qiu, Ch.N. Kim, An improved porous medium model for microchannel heat sinks, *Applied Thermal Engineering* 30 (2010) 2512–2517.
- [24] V. Yerramalle, B. Premachandran, P. Talukdar, Numerical investigation of the performance of interface conditions for fluid flow through a partially filled porous channel, *Thermal Science and Engineering Progress* 20 (2020) 100628.
- [25] Arbak, N. Dukhan, Performance and heat transfer measurements in asymmetrically-heated metal foam cooled by water, *Thermal Science and Engineering Progress* 20 (2020) 100688.
- [26] H.j. Xu, Ch. Zhao, K. Vafai, Analysis of double slip model for a partially filled porous microchannel—An exact solution, *European Journal of Mechanics / B Fluids* 68 (2018) 1–9.
- [27] H.J. Xu, L. Gong, C.Y. Zhao, Y.H. Yang, Z.G. Xu, Analytical considerations of local thermal non-equilibrium conditions for thermal transport in metal foams, *International Journal of Thermal Sciences* 95 (2015) 73–87.
- [28] A.K. AL-Migdady, A.M. Jawarneh, A.Kh. Ababneh, H.N. Dalgamoni, Numerical investigation of the cooling performance of PCM-based heat sinks integrated with metal foam insertion, *Jordan Journal of Mechanical and Industrial Engineering* 15(2) (2021) 191 – 197.
- [29] Alshare, W. Al-Kouz, S. Kiwan, A. Al-khalidi, M. Hader, Computational modeling of gaseous flow and heat transfer in a wavy microchannel, *Jordan Journal of Mechanical and Industrial Engineering* 10(1) (2016) 75–83.
- [30] Th.L. Bergman, A.S. Lavine, F.P. Incropera, D.P. DeWitt. *Fundamentals of Heat and Mass Transfer*. 7th edition, New York: J. Wiley, 2002.
- [31] X. Chen, F. Tavakkoli, K. Vafai, Analysis and characterization of metal foam-filled double-pipe heat exchangers, *Num. Heat Trans., Part A: App.: Int. J. Comput. Methodol.* 68 (2015) 1031–1049.
- [32] Alazmi, K. Vafai, Analysis of fluid flow and heat transfer interfacial conditions between a porous medium and a fluid layer, *International Journal of Heat and Mass Transfer* 44 (2001) 1735–1749.
- [33] Amiri, K. Vafai, T.M. Kuzay, Effect of boundary conditions on non-darcian heat transfer through porous media and experimental comparisons, *Numerical Heat Transfer J. Part A* 27 (1995) 651–664.
- [34] K. Vafai, R. Thiyagaraja, Analysis of flow and heat transfer at the interface region of a porous medium, *International Journal of Heat and Mass Transfer* 30 (1987) 1391–1405.
- [35] K. Vafai, Convective flow and heat transfer in variable porosity media, *Journal of Fluid Mechanics* 25 (1984) 233–259.
- [36] K. Vafai, C. Tien, Boundary and inertia effects on flow and heat transfer in porous media, *International Journal of Heat and Mass Transfer* 24 (1981) 195–203.
- [37] Hsu, P. Cheng, Thermal dispersion in a porous medium, *International Journal of Heat and Mass Transfer* 33 (1990) 1587–1597.
- [38] J. Wang, H. Kong, Y. Xu, J. Wu, J., Experimental investigation of heat transfer and flow characteristics in finned copper foam heat sinks subjected to jet impingement cooling, *Applied Energy* 241 (2019) 433–443.
- [39] Fluent A. 12.0 theory guide. Ansys Inc; 2009.
- [40] Z. He, Y. Yan, Sh. Feng, X. Li, Zh. Yang, Numerical study of thermal enhancement in a micro-heat sink with ribbed pin-fin arrays, *Journal of Thermal Analysis and Calorimetry* 143 (2021) 2163–2177.

Development of Water Conservation Indicators for Office Buildings Using Delphi Method

Sajad Sadi¹, Javad Gholami², Mehdi Fereydooni³, Shahab Moshari^{4*}

^{1,2} Department of mechanical engineering, Imam Hossein Comprehensive University

³ Department of Civil Engineering, Sharif University of Technology, Tehran, Iran

⁴ Department of Mechanical Engineering, Tarbiat Modares University, P.O. Box: 14115-143, Tehran, Iran

Received 2 NOV 2020

Accepted 8 FEB 2022

Abstract

One of the main concerns in source water protection and supply relates to the savings in water consumption in the building sectors. Office buildings are responsible for a considerable amount of water consumption worldwide. Thus, regulations on office buildings' water consumption would substantially reduce water consumption in the city as a whole. In order to achieve this objective, water indicators should be determined using an appropriate method. The present study focuses on the evaluation of water consumption patterns in an office building as well as the determination of the fundamental indicators for water conservation and optimization of water consumption patterns. To design and introduce the indicators using the Delphi research method, the effective parts in water consumptions for each of the building divisions have been first identified according to the consumption control improvement tools, and the index of each section also been designed. Therefore, one of the goals of this research is to identify and compile appropriate indicators of water consumption in an office building. As the first step, an office building is divided into different sections, including showers, bathrooms, kitchens, green space, and cooling/heating systems. Then, the Delphi method is utilized to prepare effective indicators of water consumption for each section. By determining each section's aforementioned factors, 38 confirmed indicators were presented for water consumption in an office building. In the end, 36 indicators which showed good validity and reliability with Cronbach's alpha values higher than 0.79 as well as Content Validity Ratios (CVR) higher than 0.53, and Content Validity Indices (CVI) higher than 0.8 are proposed as final indicators.

© 2022 Jordan Journal of Mechanical and Industrial Engineering. All rights reserved

Keywords: indicator; water policy; source water protection; water conservation; validity and reliability; Delphi method.

1. Introduction

Many cities in the arid regions of the world face a water crisis as a consequence of population growth and increased water consumption. Besides, climate change and the resulting decrease in water resources have intensified water shortage (dangers) in several parts of the world. Worldwide, urban regions are one of the primary users of water resources where people have a large share of water consumption. Thus, residential and office buildings have a considerable effect on the drinking water consumption balance. Therefore, it is necessary to accurately measure and evaluate the amount of water consumption in this building sector using proper indicators.

Any evaluation and controlling action should be equipped with accurate and proper decision-making and judgment indicators to be effective. These accurate, proper, and functional indicators are the primary step in evaluating water resources management performance. Preparation of indicators and transforming them into criteria help responsible individuals to determine the performance alignment to the goals besides the strength and weakness points of this issue and take effective steps in necessary corrections [1].

The prohibition of misusing water and energy demands a comprehensive implementation of relative standards and consumption patterns in various areas. This requires an appropriate determination of primary indicators in water consumption. By using indicators, the consumption rate and the relative effects are measured to help the planners in the water consumption field design proper water consumption patterns and prevent the unintended future consequences, making advantageous mutual results for environmental, agricultural, and urban profits [2].

The recent research showed that little knowledge is available regarding the performance efficiency of water consumption in office buildings. This lack of knowledge results in the inability of the market to respond to weak performances and to take suitable actions [3].

The unavailability of such acceptable water consumption indicators in office buildings makes it impossible to achieve the optimum water consumption pattern. Taking into account the preparation of indicators, the amount of functionality of indicators, and implementation of proper plans, positive results are achieved, including the decrease in water consumption, increase in construction quality, savings in energy consumption, and overcoming droughts.

* Corresponding author e-mail: s.moshari@modares.ac.ir.

Important water consumption areas in an office building include bathrooms, showers, kitchens, green space, and cooling-heating systems. Any area can take priority over others and have higher consumption rates depending on the building application. Generally, the average amount of water consumption in different sections of a building is demonstrated in Figure 1(a). Cunliffe et al., studied the rates of water consumption in an office building in 2008 [4]. According to their study, office buildings are responsible for a considerable amount of water consumption. Yet, there are many grounds for savings. The key goal of their research is to determine those sections in an office building where savings can be achieved in water consumption. Different subsections, including taps, leakages, plants, irrigation type, and water recycling, are considered in their study, and solutions to lower water consumption are presented in each part [4]. Zoghi Moghadam researched water consumption in the Green Building of the United States [5]. Table 1 presents the water consumption in two types of buildings according to conventional standards and the optimum (LEED) conditions.

Table 1. Water consumption (per day) in different parts of the building in standard and optimal conditions [5]

Parts	Standard (Gallons/person)	Efficient (Gallons [*] /person)
Toilets	20.1	5.12
Washer	15.1	10.6 or less
shower	12.6	5-10
Faucets	11.1	7-10.8
Dishwasher	1	0.5-1
Leaks and Others	12.7	<7.7
TOTAL	72.5	36-42

* The US gallon is used in the United States and is equal to 3.785 liters.

Achieving proper water efficiencies requires efficient Strategies such as: repairing the leaking taps, using proper showerheads, installation of flow switches in bathrooms, and using low consumption washing machines. One of the essential and efficient subjects for saving in water consumption in buildings is recycling used water for appropriate applications, e.g., irrigation and bathroom flush tanks. Therefore, the maximization of sewage efficiency in buildings is one of the key goals of water consumption decrease. More than two-thirds of the consumed water in buildings relate to the bathrooms and showers, leaving these two sections among the most necessary sections for saving strategies [5].

Schuetze et al. studied different coefficients of water consumption in buildings in 2013 [6]. The potential for saving of water consumption was discussed using environmentally sound technologies (ESTs) and the relative measurements using the Wise Water software. Required studies, were determined in buildings, for which

a considerable water consumption saving was possibly obtained with relatively small efforts and no limitations. Also, different methods of estimating the recycled water, rainwater, and the potential for using it as drinkable water-in-access were evaluated. According to their study, using proper taps and shower heads with low flow rate (low-consumption), can result in considerable water consumption savings, since more than 50 percent of the total water consumption occurs at these units. The actual amount of saving in this section depends on various factors, e.g., water pressure, types of taps and showerheads, flow distribution in taps, and the type of application in water consumption. A decrease in flow rate in valves from 14 to 7 lit/min results in an approximate saving value of 29 percent. More than 50 percent of the residential water consumption occurs using these connectors, for washing (kitchen) and bathrooms (which account for at least 46 percent of the total consumption) and toilets. Eventually, when the attitude regarding the washing level and taps is changed, saving between 23 to 43 percent is achievable. In this research, other strategies were introduced for savings, in water consumption [6].

Chebaane and Hoffman researched water consumption in office buildings in 2017 [7]. Any saving in water consumption relating to decreasing the amount of greywater and sewage led to a decrease in demand for energy used to heat or cool the water, resulting in a lower consumption as well as energy expenses. Their study showed that the office buildings are one of the main consumer sections of drinkable water in countries, and as it is shown in Figure 1(b), they are responsible for 38 percent of the total drinkable water consumption [8]. Based on their study, the most extensive consumer sections of water in an office building include bathrooms, toilets, and kitchens. Figure 1(c) indicates this division [7].

Chebaane and Hoffman described the gardens of office buildings as the largest consumer section outside the building area and presented strategies, including appropriate selection of plants for each climate, and proper selection of irrigation methods, using proper fertilizers, to achieve savings in water consumption. The next part of their research is related to the soil type in regions, which indicated a strong influence on the water consumption rate in green spaces [7].

Das et al. studied the optimization of water in the United States Green Building in 2015, describing the required water for irrigation purposes as the most extensive consumer section in an office building. They presented operational strategies to decrease water consumption in different consumer sections, including bathrooms, showers, green spaces, kitchens, and rainwater collectors. Using greywater and rainwater was shown to be an effective method for improving water consumption patterns to acceptable extents. Therefore, based on Das's research, the green space is considered as one of the largest water consumer sections in an office building for the preparation of indicators in the present study [8]. Table 2 shows a number of articles used to identify and introduce the indicators in this study.

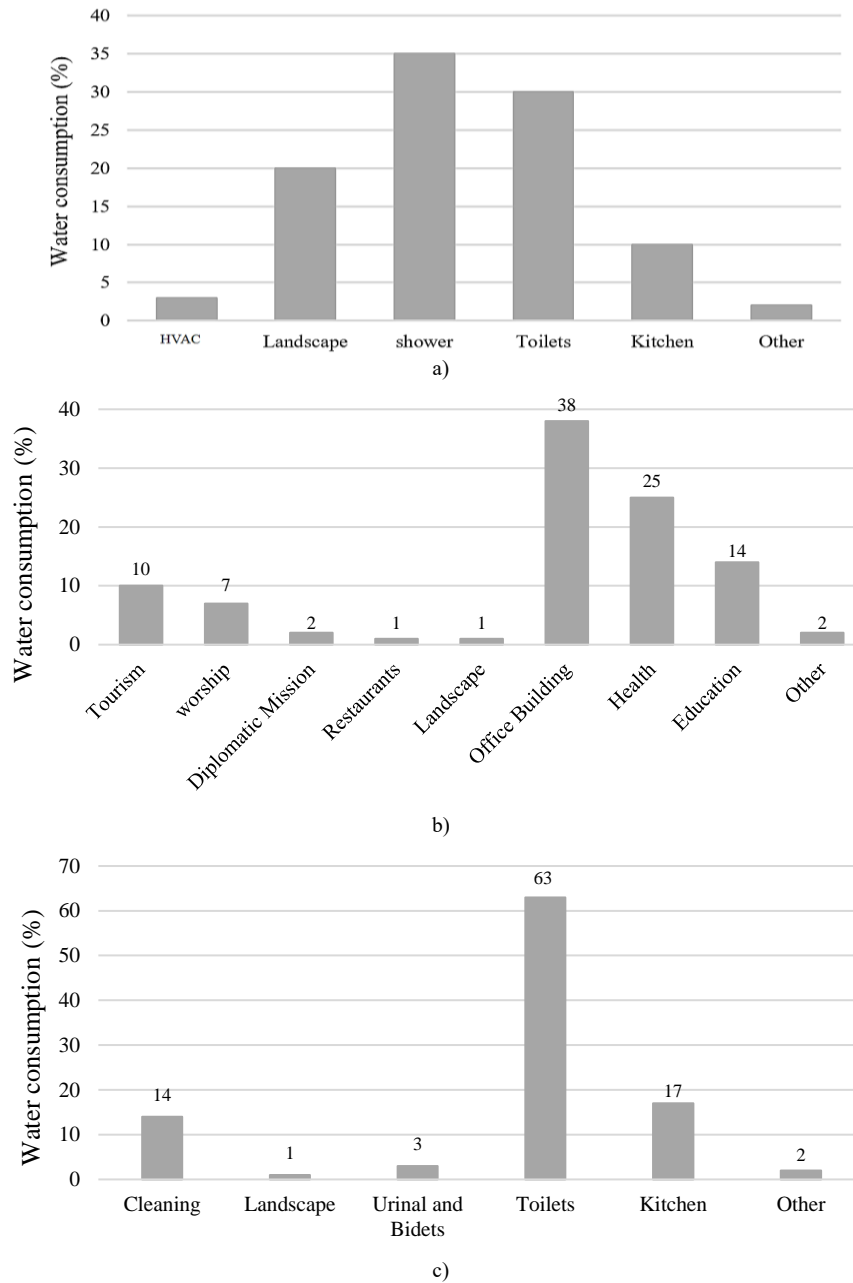


Figure 1. Percentage of water consumption, a) in different parts of an office building (HVAC: Heating, ventilation, and Air conditioning), b) in different consumer sectors of a country [8], c) in different parts of an office building [7].

Table 2. Reviewed articles to identify practical indicators for saving and protecting water consumption in buildings

Reference	Author (.et al)	Year	Conservation agent in the building	Measurement criteria (ideas for defining indicators)
[25]	Proença	2010	Toilets, faucets	Flow rate, drain tanks
[26]	Ghisi	2014	Rainwater, gray water, equipment, toilets	Amount of water recycling, equipment consumption rate
[27]	Soares	2021	Plumbing equipment, fittings, toilets	Flow rate, tank drain, equipment consumption rate
[28]	Praveena	2021	Rainwater, toilets, plumbing	Amount of water recycling, flow rate, emptying of tanks, equipment consumption rate
[29]	Marinoski	2018	Rainwater, gray water, equipment	Amount of water recycling, equipment consumption rate
[30]	Bennett	2015	Vegetation	Consumption in different climates
[31]	Shikuku	2021	Rain water, gray water	The amount of water recycled
[32]	Şahin	2019	Rainwater, toilet, bath	Amount of water recycling, flow rate, emptying of tanks, equipment consumption rate
[33]	Gultekin	2018	Equipment, rainwater, gray water, bathroom, kitchen, toilet	Amount of water recycling, equipment consumption rate, flow rate, emptying of tanks
[34]	Chu	2021	Rain water, gray water	The amount of water recycled
[35]	Beithou	2011	Gray water	The amount of water recycled

1.1. Comparison of the present work with previous studies

According to the literature, as mentioned above, many researchers in this field seek strategies for savings in water consumption in buildings. However, none of them has focused on indicators or criteria to control the (total) amount of water consumption in the office buildings.

The present study can be argued to be the first comprehensive one in this field.

Previous researchers have categorized different parts of a building in respect of different methods. In the present study, similar schemes are selected for an office building.

This study focuses on the determination and preparation of appropriate indicators for the correction of water consumption patterns in office buildings.

Since, many of the indicators presented in this research are new because of their design, the Delphi research method has been used as an effective way to provide innovative research.

It aims at investigating the determination and preparation of existing indicators in different countries to correct water consumption patterns.

This study is composed of two main parts. The first section, determining Indicators, consists of three parts, including identifying water consumption sectors (spaces) in office buildings, identifying water consumption terms in consuming sectors (spaces), and development of the indicators for each water-consuming term. In the first section, a comprehensive study has been conducted on factors affecting water consumption.

The study, using the Delphi method, has resulted in the determination of 30 new indicators in the field of office building water consumption, which had not been investigated in the previous research works.

In the second section, the determined indicators (including 30 new indicators and six existing ones) were analyzed using CVR, CVI, and Cronbach's alpha methods for the first time, which ascertained the validity and reliability of the indicators (Table 3). By using this method, the validity of the proposed indicators in terms of water consumption control in an office building has been determined.

2. Research Methodology

The Delphi method is used in the present study. This method is mainly used to seek novel and reliable ideas or to gather appropriate data for decision-making [9]. The Delphi method is a structured process to gather and categorize the knowledge of a group of experts [10]. The experts answer questionnaires; then a facilitator provides an anonymized summary of the experts' forecasts as well as the reasons they provided for their judgments. Perez

emphasizes the importance of the Delphi method and describes it as one for a "single-variable research" to forecast the future of technologies. On the other hand, the Delphi method is used in futures studies. The Delphi method is a structured process for collecting and classifying the knowledge available to a group of experts,, which is done by distributing questionnaires among these people and controlled feedback on the answers and comments received. On the other hand, one of the purposes of this article is to introduce indicators by which all effective factors in saving and conserving water can be identified. Therefore, the purpose of using the Delphi method is, firstly, to confirm the extracted indicators according to the opinion of experts, and secondly, according to their opinions and ideas, the number of indicators is completed and in a way all possible indicators can be covered.

The most important point in this process is understanding the objectives of using the Delphi method by experts. Answers must have enough knowledge in the relative field and be familiar with the literature of the subject [11]. The diagram of the research process (research methodology) is shown in Figure 2.

Table 3. Different parts, methods, and innovations of the current work.

Part	Method	Innovation	
Indicator determination	Identifying water consumption sectors (spaces) in office buildings	Library research	
	Identifying water consumption terms in consuming sectors (spaces)	Library research and Delphi method	The comprehensive conclusion of factors affecting water consumption in each section
	Determining Indicators for each water consuming term	Library research and Delphi method	Determining 30 new Indicators
Indicator analysis	Examining the Validity and reliability of the determined indicators	CVR, CVI, and Cronbach's alpha methods-	Validity and reliability analysis of the determined water consumption indicators

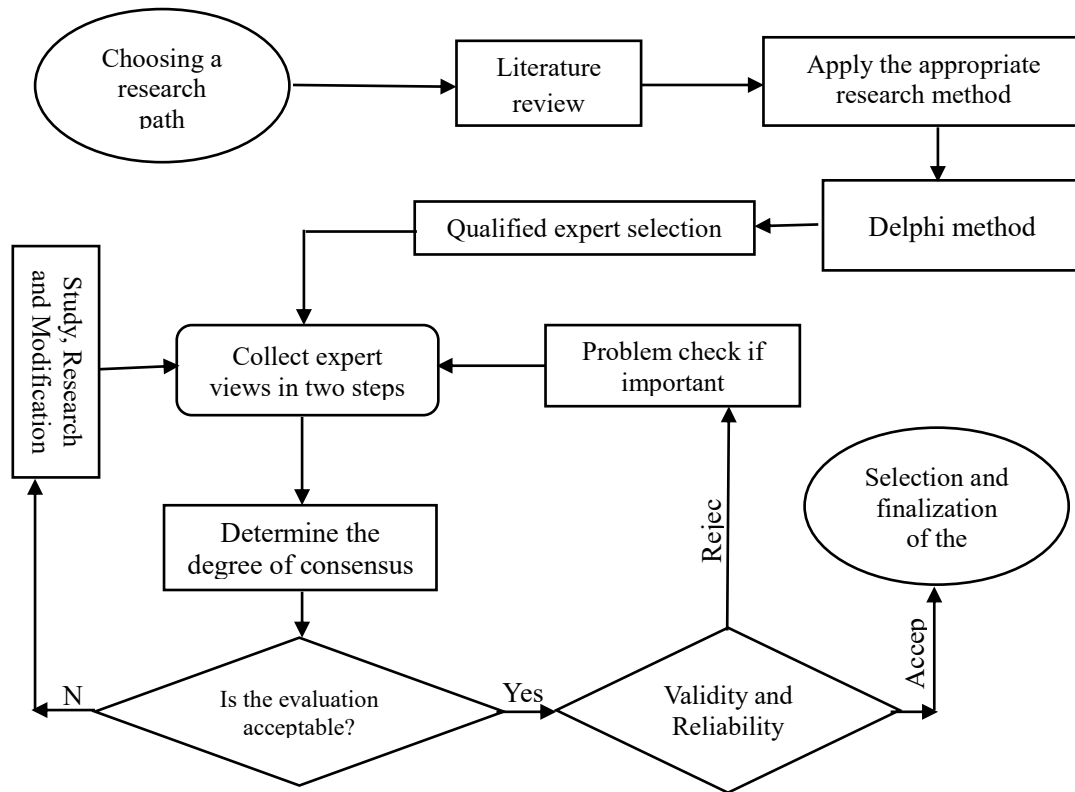


Figure 2. Diagram of research steps

2.1. Data collecting

The requirement of every research project is the proper gathering of the relative data to the research subject in terms of accurate and updated data. Therefore, two methods are used in the present study for collecting data: library studies and field studies. Libraries are the first suitable place to gather necessary data on every research subject. Thus, to have a literature survey of previous works on proposing patterns for optimization of water consumption in an office building, the required information was gathered. On the other hand, for field studies, the researcher has to go to the respective environment or desired group of users, communicate directly with the analysis units, including users, organizations, and institutes, to gather the required data. Two types of questionnaires are used in the present study for the field study [12]. Using questionnaires is preferred over other methods of data gathering methods such as interview and observation, for this method involves fewer errors due to orientations, lack of attention to considerations while answering the questions, simpler execution, the similarity of words and clauses and less consumed time [13].

After the extraction of criteria and indicators from documents, instructions, regulations, and consultations of the authors with experts in this subject, at the first stage, the first questionnaire was released between the knowledgeable and experts. A new questionnaire was prepared after the collection of the previously answered questionnaire from the experts and further studies. In this

research, a semi-structured questionnaire has been used, which means that before delivering the questionnaire to each of the experts, first the model presented in the questionnaire was explained to them and then the questionnaire was completed by the experts. The research questionnaire is a researcher-made questionnaire that consists of 8 parts: examining the validity of the question, examining the ability to measure indicators, assessing the impact on water consumption and in fact the importance of the index in an office building, examining the application of the index in different climates, Examining the existence and non-existence of index improvement strategies to reduce water consumption in an office building, examining the characteristics of an appropriate and acceptable index in the developed indicators, examining the scalability and coefficient for the developed indicators and examining the possibility of calculation. Indicators are formed in different seasons of the year (Table 4). In the second stage, the questionnaire was sent to the experts and knowledgeable about finalizing the mentioned criteria and evaluations. The final version of the questionnaire was designed after the evaluation of the selected indicators. This final questionnaire was approved by the experts and given to 30 by the experts in this field.

To quantify the opinions of the answerers, the five options Likert scales were used. The Likert scales consist of five qualitative clauses that the answerer decides one, based on their mental judgment over the importance of each criterion. Five qualitative clauses for the mentioned scale and their score equivalence and quantitative values are 1 (very low), 2 (low), 3 (average), 4 (high), and 5 (very high). [14].

2.2. Statistical Population

A statistical population is a group of users or units with at least one common indicator [15]. The sampling scheme in the present study is based on the improbable snowball methodology. In the improbable snowball method, sample units are selected by the researcher as a representative of the population. The benefits of this method include the possibility of using the researcher’s skills and knowledge in the selection of answerers and gathering the required information until the subjects are saturated [16].

In order to design proper indicators for water consumption in an office building, noting the technicality

of the subject, it was necessary to refer to a statistical population, consisting of 30 experts, including individuals such as the authorities and experts in the fields of water, agriculture, aerology, geography, environment and management and operation of water resources with academic backgrounds, professional and managerial experience.

In the present study, efforts were made to select experts from different regions to differentiate between regional and universal indicators as one of the most important indicators of every reliable index. Figure 3 shows the frequency percentage of the statistical population used in this study based on the type of activity and expertise.

Table 4. An example of a questionnaire designed to evaluate indicators (for CVR)

Indicator	Category	Questions	Evaluation				
		Measurability?	very low	low	average	high	Very high
1	Ex: discharge per minute Ex: valves	Effectiveness on water consumption?	very low	low	average	high	Very high
		Usability in different climates?	very low	low	average	high	Very high
		Is there a tool or solution to improve this indicator?	very low	low	average	high	Very high

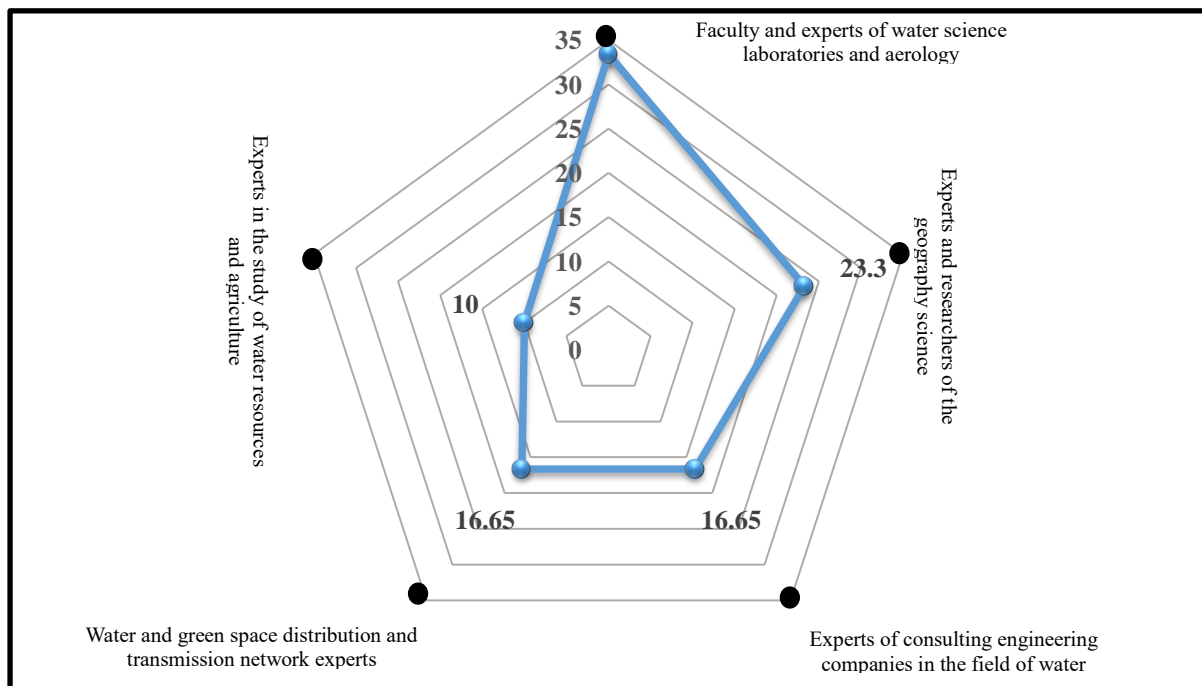


Figure 3. Graph of frequency percentage of statistical population by type of activity and specialty

2.3. Data Analysis

Gathered data are analyzed with descriptive and illative statistic methods. Descriptive and illative statistics are used for population and collected data analysis of the present study, respectively. Moreover, the commercial software MATLAB and SPSS are used for the analysis of data. To analyze the quality of indicators, illative statistical methods, e.g., the weighted average method, are used. The mean score of each factor, regarding its effectiveness, was calculated and categorized using the arithmetic mean, according to the description of scorings, 1 for: very few, 2 for: few, 3 for: average, 4 for: high, and 5 for: very high. Therefore, factors with a mean equal to or above three were selected as effective factors, and the remaining were deleted.

2.4. Validity and Reliability of Evaluation Tools (CVR & CVI)

The validity concept clarifies how well the measurement tool evaluated the desired indicator. One of the applicable methods in the determination of the validity of evaluation tools is the utilization of the content credit evaluation, proposed by Lawshe in 1975 [18]. This method measures the rate of the agreements of the knowledgeable and evaluators in "suitability or essentiality" of a criterion or the content of a model or a specific question [17]. The Lawshe coefficient needs to be calculated for each indicator and criterion according to equation 1 for illative evaluating. The content validity ratio (CVR) is calculated as follows:

$$CVR = \frac{ne - \frac{N}{2}}{\frac{N}{2}} \quad (1)$$

In the above relation, CVR indicates the Lawshe coefficient, N and ne represent the total number of experts and the number of users who had a positive view of the model or each of its evaluation criteria, respectively. The minimum value of CVR in the unilateral examinations of Lawshe was 0.33 for a statistical population of 30 users (Table 5) [18].

Table 5. The minimum values of CVR of Lawshe for suitability of content illation.

Minimum value of content illation ratio							
N of examiners	10	15	20	25	30	35	40
CVR	0.62	0.49	0.42	0.37	0.33	0.31	0.29

After the determination and calculation of CVR, the CVI index can be calculated. In order to calculate this index, examiners should state their opinion regarding three criteria of relativity or specificity, simplicity or fluency, and transparency or clearness, based on the 4-option Lickert scales for each item on the used instrument. As an example, for the criterion of measurement, options of not measurable=1, slightly measurable=2, measurable=3, and absolutely measurable=4, are used and then, using the equation 2, the content validity index (CVI) is calculated [19].

$$CVI = \frac{\text{(the number of examiners who gave a score of "very high; high; yes and approved" to an indicator)}}{\text{(total number of examiners)}} \quad (2)$$

The minimum value of the CVI index is 0.79. Hence an index with a CVI value of less than 0.79 must be omitted [20]. Reliability is defined as the capability of each tool to produce compatible results. Thus, it relates to the precision and accuracy of the measurement tools. Besides, reliability is the necessary condition for stability; therefore, reliability is a means of measurement on how close, accurate and reliable will the results of (a) measurement be, if the same questionnaire is repeated on the measured indicator [21].

The main purpose of using Cronbach's Alpha examination is to evaluate the internal similarity of the variables of a scale that is provided through introducing indicators process. This test is a way to examine the similarity of the individual's response to a variable in comparison with each of the other variables of the scale (the variable's correlation with the variable). Therefore, the reliability of the whole scale is evaluated. In fact, to measure the reliability of variables using the Cronbach's Alpha examination, the internal similarity or reliability of variables is measured [22]. Cronbach's alpha is calculated using Equation 3 for all indicators.

$$\alpha = \frac{k}{k-1} \left(1 - \frac{\sum_{i=1}^k s_i^2}{s^2} \right) \quad (3)$$

Where, k, s_i^2 , and s^2 indicate the number of questions, the variance of each question, and the variance of all questions, respectively. The closer the resulting coefficient is 1, the more reliable the questionnaire is. Note that an Alpha of less than 0.6 is generally considered to be weak. A value between 0.7 and 0.8 is considered acceptable, and values above 0.8 are appropriate. Closer values to 1 indicate better conditions.

3. Results and Discussion

An office building can be divided into different sections regarding previous studies. Division of water consumption of an office building includes bathroom, toilet, kitchen, green space, cooling/heating, and others. According to studies [7], it can be stated that the kitchen, shower, and green space are responsible for more than 97 percent of the consumed water in an office building. These sections take 35 and 30 percent of the total water consumption in an office building, respectively. This issue indicates the importance of these sections in preparing the indicators.

To fully divide sections of an office building, one must determine the influential factors on water consumption in any section, and then prepare the appropriate indicators. In showers, units, and parameters such as taps, showerheads, area, and the number of showers are among the key affecting items on water consumption. On the other hand, the flushing cistern, flush valves, taps, area, and the number of toilets are among effective items in bathrooms. Green space is one of the most important water consumption sections in an office building. Factors including the type of plants, irrigation method, water requirement of the plants, precipitation rate, irrigation with wastewater, depth of plant roots, evaporation and transpiration, soil moisture, area, and water supply are among the effective items on water consumption in green space.

When dividing a kitchen into different sections, most of the consumption relates to sanitary taps and kitchen floor area. Cooling-Heating is another part of water consumption in an office building. It has different consumption rates in respect of the type of the system. In this section, the rate of usage, exposure of cooling systems

to sunlight, and insulation of pipelines can have a strong influence on the respective water consumption.

In addition to the aforementioned items, other factors exist that can affect the rate of water consumption in an office building. Among the most important of these are the technology used in the building, water pressure, greywater, storage tanks, the total amount of consumption, climate,

and equipment. Figure 4 denotes the final division of an office building into different consumption sections.

Prior to the design and introduction of indicators, the various significant factors in water consumption, concerning the means of consumption control or optimization tools need to be determined for each section of the building. Table 6 shows the indicators developed in each section.

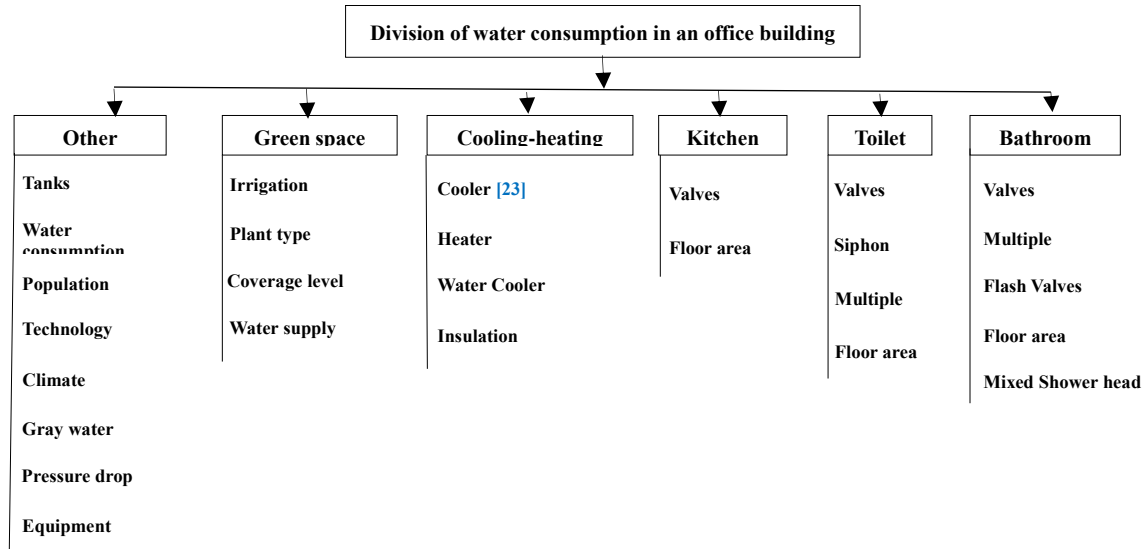


Figure 4. A final schematic diagram for categorizing water consumption in an office building

Table 6. Designed indicators in an office building.

Section	coding	Indicator No.	Categories	Indicator name	Indicator type	Calculation requirements
Bathroom (1)	$I_{1,1}$	1	Valves	Bathroom valves Discharge per minute	absolute	pipe diameter nozzle diameter nozzle type discharge outlet/discharge
	$I_{1,2}$	2	mixed Shower head	Air to Water ratio in the air and water mixed Shower head in bathroom	relative	pipe diameter nozzle diameter nozzle type discharge outlet air discharge
	$I_{1,3}$	3	Bathroom area	Maximum area of the bathroom floor	absolute	Bath floor area Building area
	$I_{1,4}$	4	Population	The ratio of the number of bathrooms to the average number of personnel in the office building per month	relative	number of bathrooms number of users per month
Toilet (2)	$I_{2,1}$	5	Valves	Toilet valves Discharge per minutes	absolute	Diameter of pipe nozzle diameter discharge outlet/discharge
	$I_{2,2}$	6	Siphon tank	Capacity of Toilet Siphon tank at each discharge	absolute	Siphon tank volume tank Dimensions
Kitchen (3)	$I_{3,1}$	7	Toilet area	Maximum area of the Toilet floor	absolute	The floor area of the toilet The total floor area of the building
	$I_{3,2}$	8	Population	The ratio of the number of Toilets to the average number of users per month	relative	number of toilets number of users per month
	$I_{3,3}$	9	Flush Valve	The volume of discharged water from the flush valve at each discharge	absolute	Discharge and volume of Discharged water pipe diameter water pressure
	$I_{3,4}$	10	Flush Valve and Siphon Tank	The supplied water ratio for the flush valve and the Siphon tank from recycled water (rain and gray) to the total water consumption for these two parts	relative	Precipitation gray water amount tank volume valve flash water volume
	$I_{3,5}$	11	Valves	Kitchen valves Discharge per minute	absolute	Diameter of pipe nozzle diameter nozzle type discharge outlet/discharge
	$I_{3,6}$	12	Kitchen area	Maximum area of the kitchen floor	absolute	Kitchen floor area Building area

Green space (4)	$I_{4,1}$	13	Irrigation	Difference in the amount of irrigation, evaporation and evapotranspiration divided by the plant's water demand	relative	amount of irrigation location of evaporation and evapotranspiration plant type plant water requirement soil moisture - root depth and ...
	$I_{4,2}$	14	Plant type	plant's Water requirement divide on available water	relative	area Water balance Plant type Plant water requirement Precipitation Runoff Humidity Penetration Evaporation and transpiration
	$I_{4,3}$	15	Coverage surface	green space to total space area (maximum area of green space)	relative	total area- green space area floor area
	$I_{4,4}$	16	Irrigation	ratio of amount of green space irrigation water to available water in the area	relative	area Water balance Plant type Plant water requirement Precipitation Runoff Humidity Evaporation and transpiration amount of Irrigation
	$I_{4,5}$	17	Water consumption	The amount of supplied irrigation water from gray water to the plant's water requirement per month	relative	Volume of gray water tank evaluation of purification system- plant type plant water requirement amount of precipitation
	$I_{4,6}$	18	Coverage surface	The ratio of the lawn area to the total area of green space	relative	measuring the green space area measuring the lawn area
	$I_{4,7}$	19	Recycled Water-Irrigation	The ratio of green space irrigated water from recycled water (rain, gray water) to the total water used for irrigation	relative	Precipitation amount of gray water water used for irrigation
Cooling – Heating (5)	$I_{5,1}$	20	cooler	ratio of the water required for cooling systems to the amount of water used for the best available cooler	relative	required water for building cooling system and base cooler
	$I_{5,2}$	21	heater	ratio of the water required for heating systems to the amount of water used for the best available heater	relative	required water for building heating system and base heater
	$I_{5,3}$	22	water cooler	the ratio of the duration in which the cooler is exposed to sunlight to the duration of sunshine in that climate	relative	Climatic Sun Length Per Day the duration in which the cooler is exposed to sun
	$I_{5,4}$	23	insulation	the ratio of length of insulated pipes to the length of total building pipes	relative	length of total building pipes and insulated pipes
Other section (6)	$I_{6,1}$	24	storage tanks	ratio of total water storage tanks to the number of people	relative	number of tanks number of people volume of each tank volume of total tanks
	$I_{6,2}$	25	total building consumption	ratio of total consuming water to the number of people per month	Relative	number of people Water meter numbers per month number of people
	$I_{6,3}$	26	population	ratio of total annual consuming water to number of available people	Relative	Water meter numbers per month for Related buildings and similar buildings
	$I_{6,4}$	27	Technology	ratio of number of modern valves to the total number of valves	Relative	Total number of valves number of modern valves
	$I_{6,5}$	28	climate-population	ratio of amount of annual total water consumption to the number of users divided by the amount of renewable water in the same year of the region	Relative	Water balance number of users Water meter numbers per month Precipitation evaporation and transpiration runoff river Lake Dam Groundwater Well Spring
	$I_{6,6}$	29	population	ratio of total consuming water to the number of users per month divided by Average of several similar buildings	Relative	Census Water meter number
	$I_{6,7}$	30	climate	ratio of water provided by modern rain management	Relative	Precipitation volume of annual or monthly storage water annual Water meter number

$I_{6,8}$	31	facilities	pressure drop in pipes to pipeline system length	Relative	Pipeline Map Pipeline Length and Number of Connections
$I_{6,9}$	32	valves	discharge of building pipes per minute	absolute	pipe diameter nozzle diameter nozzle type discharge outlet
$I_{6,10}$	33	pressure drop	pressure drop in pipes and counters to total provided pressure	Relative	pipeline map Pipeline Length and Number of Connections counter drop total pressure
$I_{6,11}$	34	pressure drop	ratio of adjacent street water pressure to pressure drop in mentioned building	Relative	Pipeline Map Pipeline Length and Number of Connections
$I_{6,12}$	35	water consumption	ratio of air to water volume in under pressure tank	Relative	tank volume water volume air volume ...
$I_{6,13}$	36	water consumption	under pressure tank capacity to amount of water consumption per day	Relative	tank volume counter number
$I_{6,14}$	37	water pressure	the longest sanitary instrument distance to gravity tank	absolute	Volume of water and volume of air and volume of reservoir
$I_{6,15}$	38	water pressure	ratio of the number of stories using gravity water to total stories	relative	Water meter number volume of reservoir
$I_{6,16}$	27	Technology	ratio of number of modern valves to the total number of valves	Relative	total number of valves number of modern valves
$I_{6,17}$	28	climate- population	ratio of amount of annual total water consumption to the number of users divided by the amount of renewable water in the same year of the region	Relative	Water balance number of users Water meter numbers per month- precipitation evaporation and transpiration runoff river Lake Dam Groundwater – Well Spring
$I_{6,17}$	29	population	ratio of total consuming water to the number of users per month divided by Average of several similar buildings	Relative	Census Water meter number
$I_{6,18}$	30	climate	ratio of water provided by modern rain management	Relative	Precipitation volume of annual or monthly storage water annual Water meter number
$I_{6,19}$	31	facilities	pressure drop in pipes to pipeline system length	Relative	Pipeline Map Pipeline Length and Number of Connections
$I_{6,20}$	32	valves	discharge of building pipes per minute	absolute	pipe diameter nozzle diameter nozzle type discharge outlet
$I_{6,21}$	33	pressure drop	pressure drop in pipes and counters to total provided pressure	Relative	pipeline map Pipeline Length and Number of Connections counter drop total pressure
$I_{6,22}$	34	pressure drop	ratio of adjacent street water pressure to pressure drop in mentioned building	Relative	Pipeline Map Pipeline Length and Number of Connections
$I_{6,23}$	35	water consumption	ratio of air to water volume in under pressure tank	Relative	tank volume water volume air volume ...
$I_{6,24}$	36	water consumption	under pressure tank capacity to amount of water consumption per day	Relative	tank volume counter number
$I_{6,25}$	37	water pressure	the longest sanitary instrument distance to gravity tank	absolute	Volume of water and volume of air and volume of reservoir
$I_{6,26}$	38	water pressure	ratio of the number of stories using gravity water to total stories	relative	Water meter number volume of reservoir

The weighted average of response to each indicator is its state of being illative and stable for its final design. As the accepted indicators are required to have an average of higher than 3 to be considered in the validity and reliability examinations, the presented indicators in Table 7 and Figure 5(a) with an average of less than 3 are omitted, and their reliability and validity will not be evaluated.

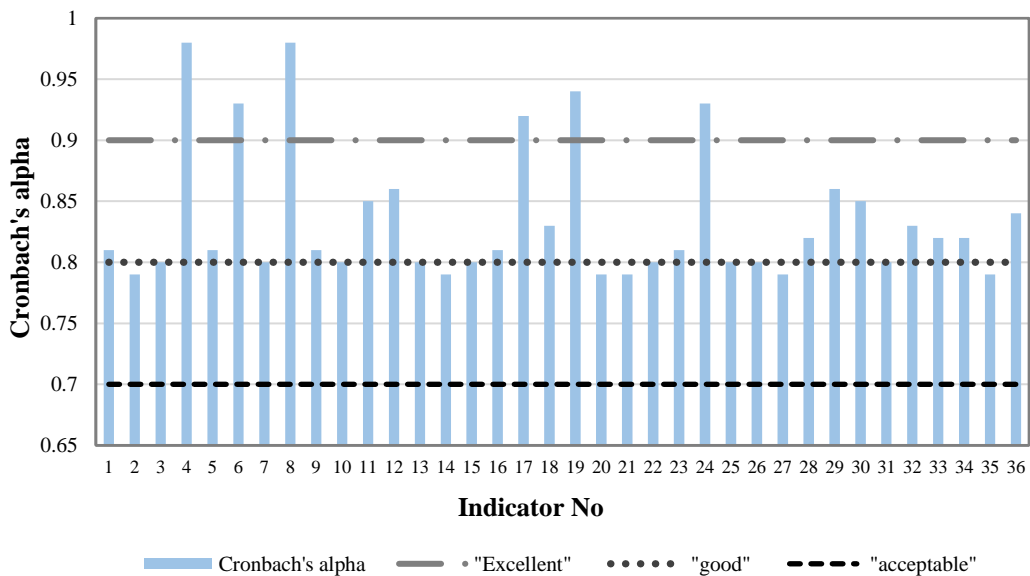
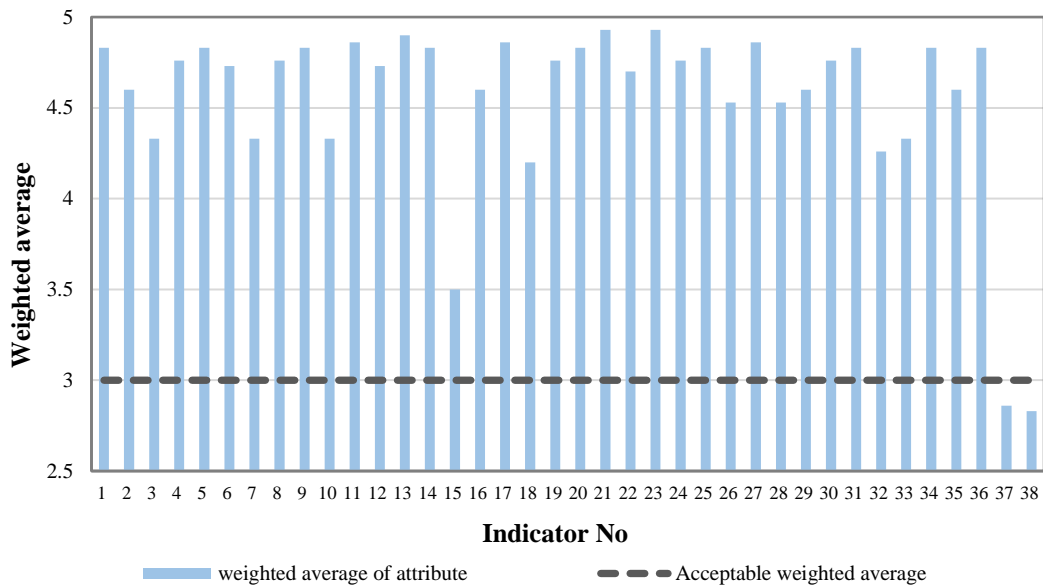
Table 7. Deleted indicators with a weighted average of less than 3

Indicator No.	Indicators with a weighted average of less than 3	Weighted average
37	highest sanitary instrument distance to gravity tank	2.86
38	ratio of number of stories using gravity water to total stories	2.83

Reaching a Cronbach's Alpha value of greater than 0.79 indicates that indicators with four designed questions have acceptable reliability (Figure 5(b)). As it was stated, reliability is the necessary condition for the evaluation of index validity. Therefore, the validity can be evaluated.

The content validity can be qualitatively calculated regarding the opinions of technicians and according to the content validity, CVR, and its index, CVI. The minimum value of CVR in unilateral examinations of Lawshe is 0.33 for a statistical population of 30 users. The validity ratio of the content is higher than 0.33 (above 0.53) for all indicators, meeting the conditions of content validity (Figure 5(c)).

The validity indicator of the content is calculated for the final confirmation. CVI index can be calculated after the calculation of CVR. The minimum acceptable value of the CVI index is 0.79, and lower values must be dismissed. Results show that all indicators have a CVI value above 0.8, being in the acceptable range with a confirmed validity (Figure 5(d)). According to examinations (weighted average, validity, and reliability), eventually, 36 indicators with high credit results are selected with respect to water consumption in an office building among the total number of 38 prepared indicators.



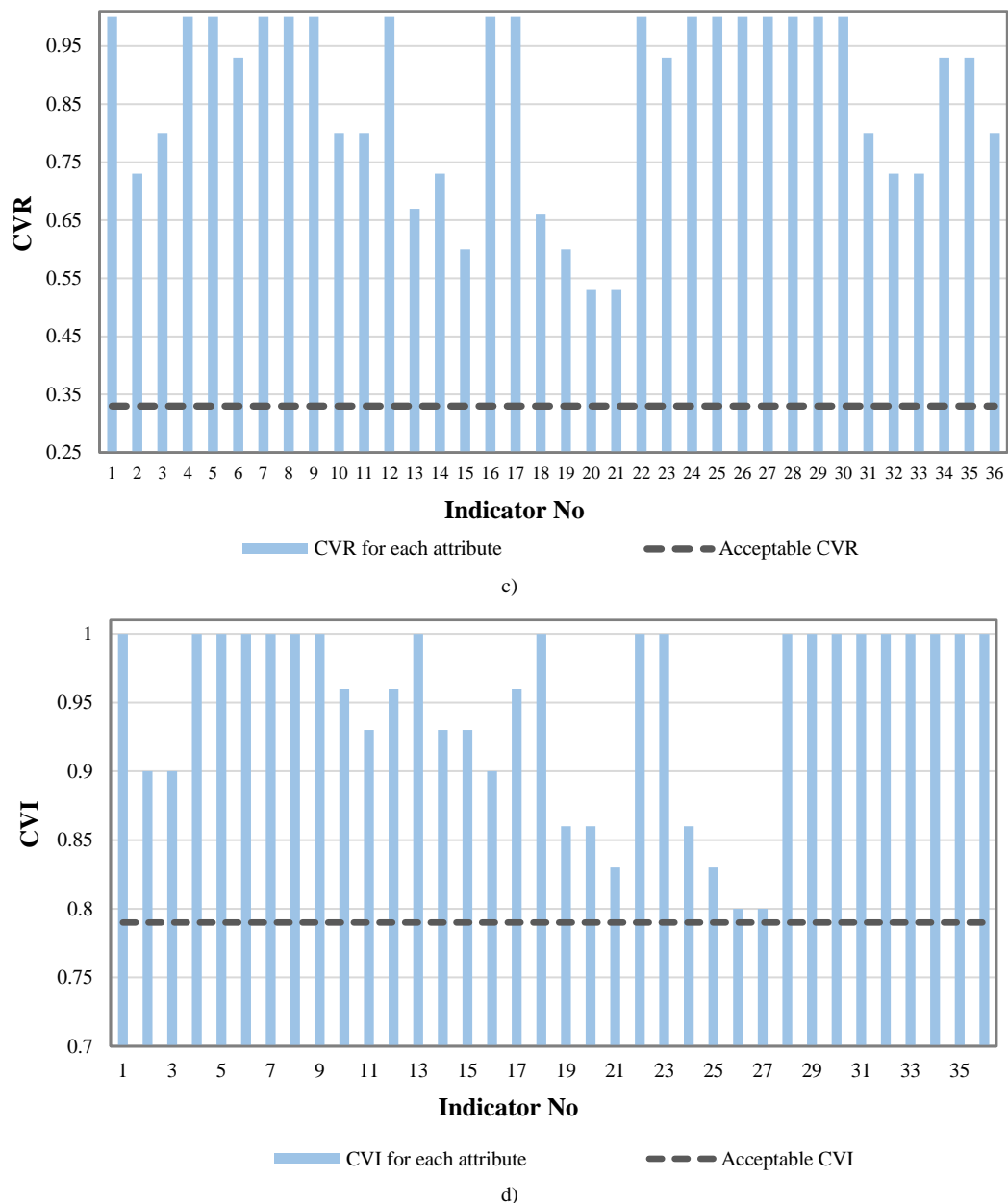


Figure 5. validity and reliability of the indicators, a) indicators for evaluating, b) Calculation of the Cronbach's alpha, c) Calculation of the CVR, d) Calculation of the CVI.

As a practical- scientific conclusion of this article, we can mention the application of this article in arid regions of the world. For example, in Iran, in the top 5 largest cities (in terms of population), all of them (Tehran, Mashhad, Karaj, Isfahan, Shiraz) are in dry regions, and considering the indicators mentioned in this study, it is possible to reduce the needs for water consumption in those cities [24].

4. Conclusion

Introduction and control of indicators are of the proper methods for energy saving. Water consumption is not an exception, and by the preparation and design of proper indicators, not only can the consumption rate be controlled, but also it can be optimized. Previous studies indicate that the office buildings are among the most important water-consuming sections in a country. In this study, an office building is divided into different sections including units such as showers, bathrooms, kitchens, green space, and cooling/heating systems. The Delphi method is used to prepare effective indicators of water

consumption for each section. In order to evaluate water consumption in an office building, 36 high credit indicators are presented as the results of this research. The main results of the present study include:

1. Due to the expert's opinions, four questions (which are mentioned in Table 3), are archived during the second stage of the Delphi method.
2. According to examinations (weighted average, validity, and reliability), eventually, 36 indicators with high credit results are selected among the total number of 38 prepared indicators (consist of 30 novel indicators).
3. Regarding to Cronbach's Alpha, $I_{1,4}$, $I_{2,2}$, $I_{3,2}$, $I_{4,5}$, $I_{4,7}$ and $I_{6,1}$ are the excellent accepted indicators.
4. Regarding to weighted average, $I_{1,3}$, $I_{3,1}$, $I_{3,4}$, $I_{4,3}$, $I_{4,6}$, $I_{6,9}$ and $I_{6,10}$ are the least important indicators in an office building.
5. For kitchens, taps and floor area have a large role in water consumption.
6. Factors, such as the amount of water consumption for each system, exposure of the cooling devices to sunlight, and insulation of pipelines strongly influence the water consumption in the cooling-heating systems.

References

- [1] Bint, L., R. Vale, and N. Isaacs. 2013. "Water Efficiency in Office Buildings." In: *Water Efficiency in Buildings*, edited by Kemi Adeyeye, Theory and Practice. 241-251.
- [2] Kendy, E., B. Aylward, et al. 2018. "Water Transactions for Streamflow Restoration, Water Supply Reliability, and Rural Economic Vitality in the Western United States." *JAWRA Journal of the American Water Resources Association* 54(2): 487-504.
- [3] Bannister, P., M. Munzinger. and C. Bloomfield. 2005. "Water Benchmarks for Offices and Public Buildings." Australia: Exergy Australia. 19 September 2005, Belconnen Australia.
- [4] Cunliffe, D., J. Bartram, E. Briand, Y. Chartier, J. Colbourne, D. Drury, J. Lee, B. Schaefer and S. Surman-Lee. 2011. "Water safety in buildings." World Health Organization supporting document that provide guidance on implementing the World Health Organization (WHO) Guidelines for drinking-water quality (GDWQ) 2008.
- [5] Zoghi Moghadam, B., 2009. "Introducing Water Efficiency of US Green Building Council's LEED Program to the freshmen of the Technology College." Architecture and Construction Management Department of the Farmingdale State College.P1.
- [6] Schuetze, T. and V. Santiago-Fandiño. 2013. "Quantitative assessment of water use efficiency in urban and Domestic Buildings." *Water* 5(3): 1172-1193.
- [7] Chebaane, M and B. Hoffman. 2017. "Office Buildings Water Efficiency Guide" USAID water demand management program.
- [8] Das, O., P. Bera and S. Moulick. 2015. "Water conservation aspects of green buildings." *International Journal of Research in Engineering and Technology (IJRET)* 13(4): 75-79.
- [9] Taylor, J.G. and S.D. Ryder. 2003. "use of the delphi method in resolving complex water resources issues." *Jawra Journal of the American Water Resources Association* 39(1): 183-189.
- [10] Edwards, D., T. Griffin and B. Hayllar. 2008. "Urban tourism research: developing an agenda." *Annals of Tourism Research* 35(4):1032-1052.
- [11] Pérez, V.L. and R. Schüler. 1982. "The Delphi method as a tool for information requirements specification." *Information & Management* 5(3): 157-167
- [12] Griffiths, S. and A.M. Yohannes. 2014. "Surgical referral criteria for degenerative rotator cuff tears: a delphi questionnaire study." *Musculoskeletal Care* 12(2):82-91.
- [13] Eigenmann, C.A., T. Skinner and R. Colagiuri. 2011. "Development and validation of a diabetes knowledge questionnaire." *Practical Diabetes International* 28(4):166-170.
- [14] Norman, G. 2010. "Likert scales, levels of measurement and the "laws" of statistics." *Advances in health sciences education* 15(5): 625-632.
- [15] Stamhuis, I.H. 2007. "A Nineteenth-Century Statistical Society that Abandoned Statistics." *Centaurus* 49(4): 307-336.
- [16] Sheu, S.J., I.L. Wei, C.H. Chen, S. Yu and F.I. Tang. 2009. "Using snowball sampling method with nurses to understand medication administration errors." *Journal of clinical nursing*, 18(4): 559-569.
- [17] Wilson, F.R., W. Pan and D.A. Schumsky. 2012. "Recalculation of the critical values for Lawshe's content validity ratio." *Measurement and Evaluation in Counseling and Development*, 45(3): 197-210.
- [18] Lawshe, C.H.1975. "A quantitative approach to content validity." *Personnel psychology* 28(4): 563-575.
- [19] Wynd, C.A., B. Schmidt and M.A. Schaefer. 2003. "Two quantitative approaches for estimating content validity." *Western Journal of Nursing Research* 25(5): 508-518.
- [20] Polit, D.F., C.T. Beck and S.V. Owen. 2007. "Is the CVI an acceptable indicator of content validity? Appraisal and recommendations." *Research in nursing & health* 30(4): 459-467.
- [21] Sonnemans, P.J.M. and W.H.J.M. Geudens. 1999. "Product reliability and the reliability of its emanating operational processes." *Quality and Reliability Engineering International* 15(6): 449-456.
- [22] Bonett, D.G. and T.A. Wright. 2015. "Cronbach's alpha reliability: Interval estimation, hypothesis testing, and sample size planning." *Journal of Organizational Behavior* 36(1): 3-15.
- [23] Khadam, M. A. A. (1988). Factors influencing per capita water consumption in urban areas of developing countries and their implications for management, with special reference to the Khartoum metropolitan area. *Water international*, 13(4), 226-229.
- [24] Eshraghi, H., Ansari, M., Moshari, S. and Gholami, J., (2019). Climatic zoning and per capita demand forecast of Iran using degree-day method. *Advances in Building Energy Research*, pp.1-26.
- [25] Proença, L. C., & Ghisi, E. (2010). Water end-uses in Brazilian office buildings. *Resources, Conservation and Recycling*, 54(8), 489-500.
- [26] Ghisi, E., Rupp, R. F., & Triska, Y. (2014). Comparing indicators to rank strategies to save potable water in buildings. *Resources, conservation and recycling*, 87, 137-144.
- [27] Soares, A. E. P., Silva, J. K. D., Nunes, L. G. C. F., Rios Ribeiro, M. M., & Silva, S. R. D. (2021). Water conservation potential within higher education institutions: lessons from a Brazilian university. *Urban Water Journal*, 1-9.
- [28] Praveena, S. M., & Themudu, S. (2021). Water Conservation Initiative in a Public School from Tropical Country: Performance and Sustainability Assessments.
- [29] Marinoski, A. K., Rupp, R. F., & Ghisi, E. (2018). Environmental benefit analysis of strategies for potable water savings in residential buildings. *Journal of environmental management*, 206, 28-39.
- [30] Bennett, B., & Kruger, F. (2015). *Forestry and water conservation in South Africa*. ANU Press.
- [31] Shikuku, J., Munala, G., Njuguna, M., Muhoro, T., Gremley, A., Nyakundi, V., & Ali, M. (2021). Cost-benefit analysis of water conservation systems installed in household buildings in Nairobi County. *Development in Practice*, 1-16.
- [32] Şahin, N. İ., & Manioğlu, G. (2019). Water conservation through rainwater harvesting using different building forms in different climatic regions. *Sustainable Cities and Society*, 44, 367-377.
- [33] GÜLTEKİN, A. B., KAPLAN, G., DEMİRCAN, R. K., & Yılmaz, H. (2018). A Study on the Water Conservation Measures in Green Buildings. *UEMK 2018 BİLDİRİ ÖZETLERİ KİTABI* 18-19 Ekim 2018 Hukuk Fakültesi, 121.
- [34] Chu, S. Study on Comprehensive Utilization of Water Resource Environment in Water-saving Design of Buildings. *Academic Journal of Environment & Earth Science*, 3(3), 47-50.
- [35] Beithou, N., Hilal, M. A., & Abu-Alshaikh, I. (2011). Thermal Analysis of Discrete Water supply in Domestic Hot Water Storage Tank. *Jordan Journal of Mechanical and Industrial Engineering*, Volume5, Number1, 29-32.

Analysis of Elastic Stress Wave Propagation in Stepped Bars, Transmission, Reflection, and Interaction: Experimental Investigation

F.Y. Fraige^{1,2*}, M.H. Es-Saheb²

¹ College of Engineering, Al-Hussein Bin Talal University, P.O. Box 25, Ma'an 71111, Jordan

² Applied Mechanical Engineering Department, College of Applied Engineering, King Saud University, Muzahimiyah Campus, P.O. Box 800, Riyadh 11421; Kingdom of Saudi Arabia

Received 27 OCT 2020

Accepted 31 JAN 2022

Abstract

The behaviour of stepped bars of different materials when impacted longitudinally by mild sphere of different radii was investigated. The passage (or propagation) of the longitudinal stress wave, created from the impact, from one end to another was recorded by strain gauges positioned at various stations along each bar. Different bar combinations with Lagrangian (material) and Eulerian (geometrical) discontinuities were investigated both experimentally and theoretically. Space – time diagrams which demonstrate the stress wave traversals across the discontinuity were constructed. The theoretical analysis of stress wave propagation in solids using the well-established Rayleigh acoustic equations assuming plane sections remain plane, was discussed, and the results were compared well with the experiments.

It was noted that a pulse travelling along a bar with a discontinuity, either in cross sectional area or material difference, will be subjected to amplification or attenuation as it passed through this discontinuity. The amount of change in amplitude was governed by the impedance ratio of the input to output bars. However, the reflected part of the pulse from the discontinuity was always attenuated, with the pulse sign governed by the impedance ratio.

© 2022 Jordan Journal of Mechanical and Industrial Engineering. All rights reserved

Keywords: stress wave; impedance; propagation; bar composites; acoustic impedance.

1. Introduction

Different types of materials and composites are used in systems and structures designed to sustain both static and dynamic load environments. The assessment and prediction of the response of those systems to complex loading conditions are crucial. The study of waves in solids aids in estimating the magnitude of stress created by impact or collision of bodies. Hence, a sound knowledge of elastic stress wave propagation in solids is important for a clear understanding of the impact phenomena and some types of fractures, such as 'spallation' and 'scabbing'. In elastic region, once a material is loaded, it deforms in a completely reversible manner. The behaviour of the material is defined by linear elastic constitutive laws, Hooke's law. This facilitates solving most dynamic problems in the elastic regime analytically. Therefore, the theories on elastic wave propagation in solids are mostly fully developed [1,2].

Stresses caused from intermediate and dynamic loading rates with strain rates in the range of $10 - 10^4$ /s) are transmitted in solids by elastic stress waves [3]. Two types of these waves exist either longitudinal or torsional. The longitudinal stress waves transmit tensile and compressive stresses with speed $C_L = (E/\rho_0)^{1/2}$, which equals the acoustic speed, whereas the torsional waves transmit shear

stresses with speed $C_T = (G/\rho_0)^{1/2}$, where E is the modulus of elasticity, ρ_0 is the density, and G is the modulus of rigidity of the solid material. A stress wave is transmitted through a body when different parts are not in equilibrium, as the case when one solid impinges another. This instability needs finite time to be felt by other parts of the body due to material properties. This is related to characteristic speeds of wave propagation. In longitudinal waves (or sometimes called compressional waves), the individual particles of the bar are displaced or move in the same direction, in case of compression waves, or opposite direction of wave travel in case of tensile wave. While, in torsional waves (or sometimes called shear waves), the particles of the solid are displaced or oscillate entirely in a plane which is transverse to the direction of the wave travel. It is well known that the longitudinal stress waves, both the compressional and tensile are transmitted through the body, while the shear torsional stress waves, known as Love waves, are mainly transmitted on the surface. This explains why these surface shear Love waves are responsible for the most damage associated with the earthquakes and seismic activities. Thus, they attain particular interest in civil engineering, and constitute main criteria for safe engineering designs.

In this paper, an attempt is made to address some issues related to stress wave propagation in longitudinal bars with particular emphasis on the experimental measurements and

* Corresponding author e-mail: Dr.feras@ahu.edu.jo.

analysis of the well-established problem of stress wave propagation in bars with geometrical and materials discontinuities. Thus, the problem of stress wave propagation in solids, particularly in long 'composite' bars, is theoretically and experimentally investigated. This includes the measurement of transmission, reflection, and interaction of the stress waves. The well-established Rayleigh acoustic equations are also given and discussed. The amplification of the stress level during its transmission and reflection in bars with different materials and geometrical discontinuities are also given and discussed. Thus, the behaviour of stepped bars of different materials when impacted longitudinally by mild steel sphere of different radii is particularly investigated. The useful applications of these waves are presented and discussed. Finally, the impact contact times for the various steel spheres and different bars are both experimentally and theoretically investigated. The structure of this work is organized as follows: relevant literature review is outlined in Section 2. The theoretical formulations and analysis of elastic stress wave propagation in long bars is outlined in Section 3 and the Appendix. Section 4 illustrates the apparatus and experimental techniques used, while Section 5 summaries the results and discussion. Finally, Conclusions and future prospects are summarized in Section 6.

2. Literature Review

The existence of sound waves and stress waves which are governed by similar equations and speeds as acoustic waves was recognized early by Rayleigh [4] and introduced after that by Sears[5], who determined the sonic velocity of the bar material using the reflection of stress wave of two ballistically axial impacted bars. Also, Hopkinson who worked on the interaction of incident and reflected waves in collided solids has described a simple technique that enables him to measure both the duration and the maximum pressure developed by an impact [6–8]. Then, his apparatus was further developed and used to establish the general form of an incident compressive pulse caused by impact of a high-speed projectile of different geometrical shapes and materials or from an explosive charge to investigate the behaviour of materials under high strain rates [9–10], and ever since was known as Hopkinson pressure bar and employed by a huge number of investigators. Amongst the large recent research deploying such a device the notable work published by Shin et al [11], who investigated numerically the characteristics of the stress pulse generated by impact of a hollow striker on the flange of a split Hopkinson tension bar. Also, stress transfer mechanism is highlighted by different flange lengths using explicit finite element analysis [12]. Furthermore, particle velocity and stress in the striker and bar generated by the striker impact on a bar with different general impedance based on one-dimensional assumptions is formulated [13].

However, after the early published detailed work by Kolsky [14] and Rinehart and Pearson [15] on waves propagation and analysis, the utilization of stress waves in engineering applications began in the early 1960s by the development of high energy rate forming processes and the uprising of space vehicles and later for determining the

mechanical properties of materials under intermediate and high strain rate loading [1,16–24].

The propagation of a longitudinal compressive stress pulse has been considered early by [9] who employed Hopkinson bar to measure the pressure produced by detonation of the explosive at its end and deduced a mathematical expression for determining the momentum associated with the pulse. Then, several attempts were made to investigate the effects associated with stress waves in rods of varying cross section [10,14,15,18], and in multi-layered plates [20,25,26]. Meanwhile, Zaid investigated the effect of stress waves in a conical bar and developed a computer program to calculate the transmitted and reflected pulses together with their interaction at any section along the bar[18]. Hascoët et al solved numerically the propagation of a shock wave in a chain of elastic beads without restoring forces under traction[27]. Later, Boaratti and Ting employed stress waves propagation sensors along pressurized tubes to detect leakage [28]. Then, Sharma studied the effect of initial stresses on the reflection of stress waves at the free surface of the medium [29]. He observed that the effect of the initial stress on the reflected waves varies with the direction of the incident wave, the elastic properties, and the anisotropy present in the material.

Recently, many new industries, such as communication, energy, automobile, aircraft, and space are expanding rapidly and striving to use increasing new materials including composites, metal matrix composites, piezoelectric materials, functionally graded material (FGM), powder compacts and superplastic materials, ceramics, and nano powders. The adoption of such newly developed materials and fast manufacturing techniques and protection against shock loadings initiated huge interest and research work on dynamic properties of these materials and structures, and further research on these newly produced materials to be shaped and formed into their final shape as to become traditionally used [30–32].

Stresses and strains developed in FGM subjected to quasi-static loading were estimated by Suresh et al [33,34]. They highlighted that by optimizing the structure and geometry of the graded interface between the two dissimilar layers, the stress levels are significantly reduced. Li et al investigated the response of plates made of metallic ceramic in two dimensions [35]. While Han et al extended the problem to three dimensions and the effect of impact was numerically investigated [36]. The FGM investigated is approximated to a multi-layered structure with uniform material properties of each layer. Then, the propagation of stress waves in FGMs using a composite wave propagation algorithm was numerically studied by Berezovski et al [37,38]. They observed that the size, shape, clustering, and in homogeneities in the random distribution of embedded reinforcement particles may affect the results of simulation of the model they proposed. Earlier, Twofighi et al examined the elastic wave propagation in the circumferential direction of anisotropic cylindrical curved plates [39]. They used Fourier series expansion technique to facilitate solving the wave propagation problem. Tasedemirics et al used split-Hopkinson pressure bar to investigate the high strain rate compression on multilayer materials [40]. The viability of modelling stress wave propagation in complex multilayer

materials has been demonstrated. They have shown that the effects of lateral confinement of a normally low-modulus interlayer material can affect the response wave propagation significantly. Xu and Rosaki assessed the generation and subsequent evolution of impact damage in heterogeneous two layered materials: one is a polymer layer which bonded to a second metallic layer when subjected to impact loading. High speed photography and dynamic photo elasticity were utilized to visualize the nature and sequence of dynamic failure modes [41]. Meanwhile, Gebbeken and Greulich developed a three-dimensional dynamic model to investigate the stress wave propagation in a reinforced concrete bar. As expected, the mechanical behaviour was characterized by cracking of the concrete [42]. However, using modified smoothed particle hydrodynamics (MSPH) method, Zhange and Batra investigated the elastic wave propagation in FGMs [43]. They showed that for the same placement of particles, the MSPH method gave better results comparing with the finite element method. But, in a later work, Perez and Al-Haik employed a one-dimensional impact problem for a layered system that comprises heterogeneous materials with different geometrical configurations [44]. They tracked the stress wave propagation using analytical model. The results showed that layered systems suffered stress amplification with inherent acoustic impedance mismatch between layers. The effect of discontinuities on the wave propagation characteristics of structures is investigated by Rafiee-Dehkharghani et al [21]. They proposed new architectures for attenuating stress waves. Due to the highly nonlinear nature of the optimization problem combined with lack of gradient information about the objective function with respect to design variables, a genetic algorithm optimization procedure was used for the optimal design of the newly defined attenuating systems.

Working on materials modelling, Ogden and Singh derived the general constitutive equation for a transversely isotropic hyper-elastic solid in the presence of initial stress based on the theory of invariants [45]. They claimed that the speed of homogeneous plane waves and surface waves depend nonlinearly on the initial stress, in contrast to the situation of the more specialized isotropic and orthotropic theories of Biot. The speeds of homogeneous plane shear waves and Rayleigh waves in an incompressible material were obtained and they noticed that significant differences from Biot's results for both isotropic and transversely isotropic materials with calculations based on a specific form of strain-energy function. Also, Barzkar and Adibi proposed a generalized Kelvin-Voigt model of viscoelasticity with the aim of bridging the gap between solids and fluids leading to a new concept of viscoelasticity which unifies the Navier-Lame and the Navier-Stokes equations [46]. On solving this equation in one dimension, propagation of stress disturbance in the so-called "Kelvin-Voigt materials" was studied. The model of these materials enabled them to investigate all the elastic and viscoelastic solids, as well as fluids and soft materials. Also, Walley and Field summarized the difference between ideal and real elastic materials [22]. They showed the dissipation mechanisms which cause attenuation of elastic waves with distance travelled. This rate of attenuation usually depends on frequency.

Recently, Ebrahimi et al reviewed mechanical, thermal, and electrical properties of nanostructures that exhibit piezoelectric behaviour including wave propagation [47]. Later, the bending of magneto-electric-elastic nanobeams and its relationship with nonlocal elasticity theory is studied [48]. Furthermore, Singhal et al investigated analytically Love-type wave vibrations in a distinct piezoelectric material thin film with a highly and weakly dielectric interface with an elastic pre-stressed plate [49]. Also, in a recent publication, Singhal and co-investigators examined Love-type wave transmission through compressive stressed orthotropic substrate welded on couple stress half-space with imperfect interface [50]. Meanwhile, Saroj et al studied the Love-type wave propagation in irregular functionally graded piezoelectric material resting over elastic half-space with irregular boundary [51].

It is important to state that despite the vast amount of work and published research, over the last few decades, in impact mechanics and stress wave propagation in materials and structures; the main efforts were clearly concentrated on the theoretical studies, simulation, numerical and modelling approaches. Hence, relatively little of this important research effort is directed to experimental investigation of this problem. This is clearly reflected in the scant experimental research works found and published.

Therefore, in this work an attempt is made to address some of these issues with particular emphasis on the experimental measurements and analysis of the well-established problem of stress wave propagation in bars with geometrical and materials discontinuities. Thus, the problem of stress wave propagation in solids, particularly in long 'composite' bars, is theoretically and experimentally investigated.

3. The Theoretical Formulations and Analysis

As stated above, the theoretical analysis of elastic stress wave propagation in long bars is very well known and established in literature. However, for convenience and benefit completion a brief summary of the most related theoretical analysis of this problem is presented [3,18]. The main equations and relations concerned are addressed and documented in the Appendix.

4. Apparatus and Experimental Techniques

The experimental setup, shown in Fig.1-a, consists of a frame(1), pendulum sphere with various radii (2), bar specimen (3), strain gauges, oscilloscope (4), amplifier, power source (5), and camera (6). The frame which is made up of two horizontal beams supported on four stands, was used to hang the test specimens in a free horizontal position. Strain pulse was produced by impacting a steel sphere supported from one end of the frame as a simple pendulum against the plane surface of the test bars. Fine adjustments for the height of the sphere were provided by two screws attached to the two beams of the frame as shown in Fig.1-b. These adjustments were necessary to ensure that the sphere impacts the test bar at the centre of its cross-sectional area.

The pulses, thus produced, were recorded using strain gauges connected at a predefined station on both the input and output bars as shown in Fig.1-c (block diagram). The strain gauges were attached diametrically opposite to the bars and connected as the active arms of the measuring Whitestone bridge. This arrangement of strain gauges eliminates bending strains and gives twice the sensitivity of that signal obtained using a single active gauge. The output of the bridge is displayed on a dual beam Tektronix

oscilloscope and then photographed using a Polaroid camera, for later processing, analysis and calculation.

The complete specifications and details of the three steel spheres used in this investigation together with the bar's combination specimens of different geometries and materials (i.e. Steel, Brass and Aluminium) are shown in Table 1, and Table 2-a, b and c respectively. Typical tapered bar specimens are shown in Fig.2-a and stepped bars specimens in Fig.2- b.

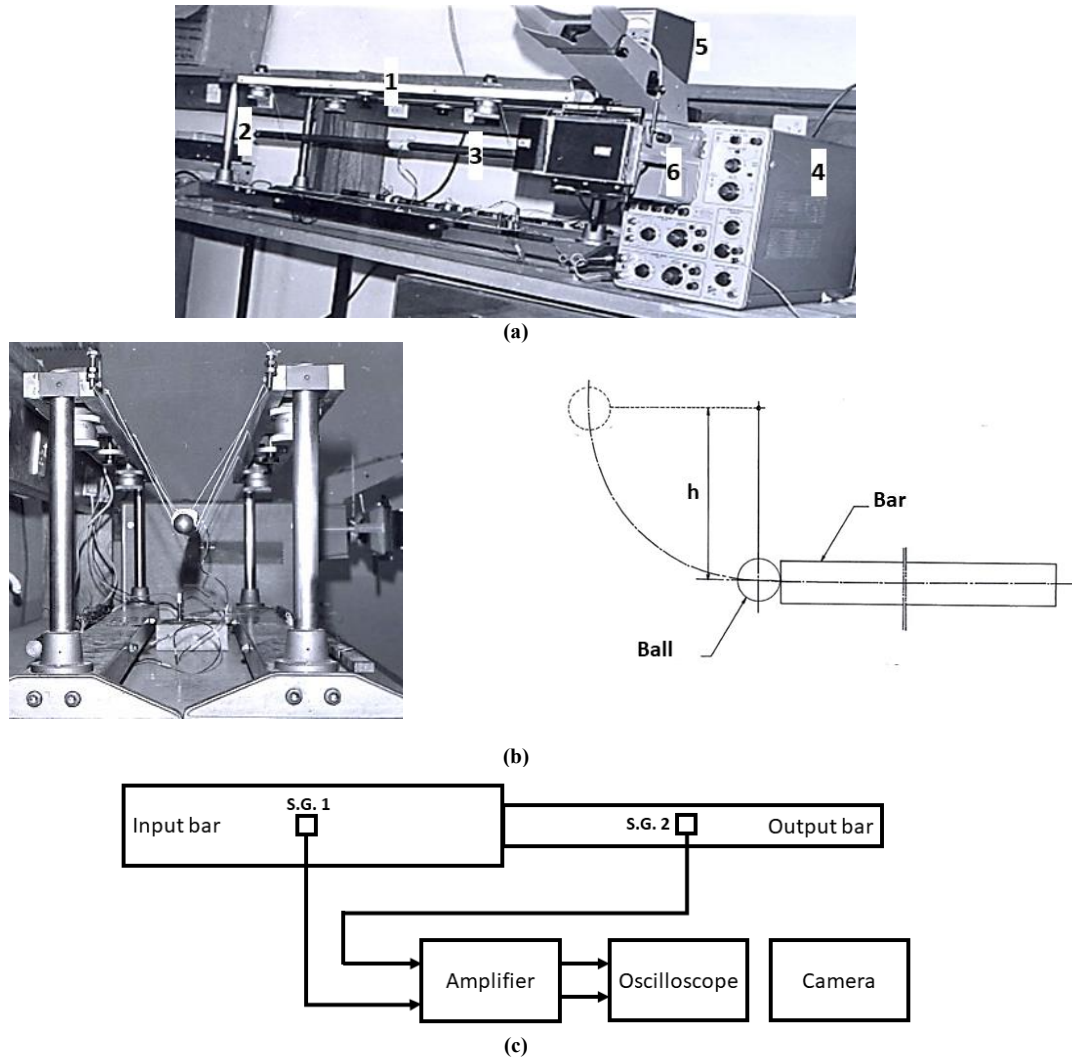


Figure 1. Experimental setup (a) Picture; shows: (1) Frame, (2)Steel sphere, (3)Rod specimen, (4) Oscilloscope, (5) DC power supply and (6) Camera; (b) Pendulum arrangement; and (c) A schematic block diagram.

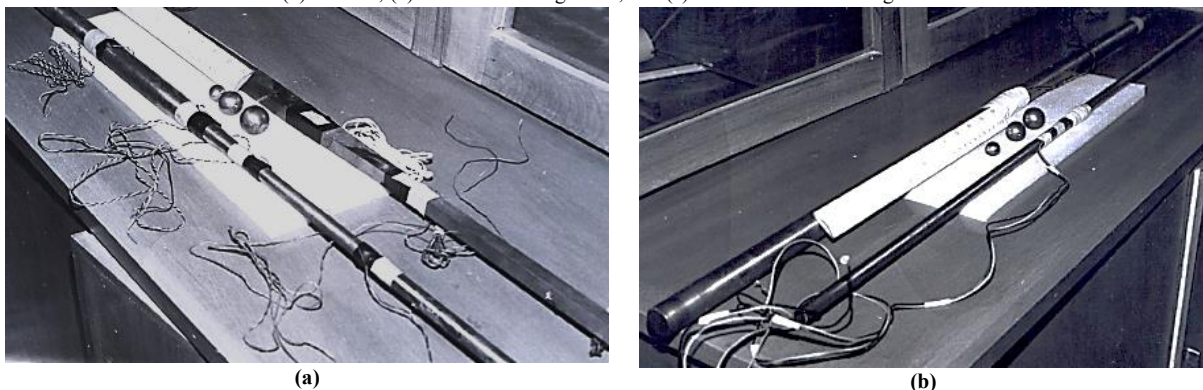


Figure 2. Tapered steel specimen; (a) Linear (rectangular and circular cross sections) and (b) Typical circular stepped steel bar specimen (circular cross sections).

Table 1. The complete details and specifications of the steel spheres used.

Sphere No.	Sphere diameter d ₂ , mm (in)	Sphere Mass m ₂ , gram (lb)
1	25.4 (1)	67.74 (0.1492)
2	22.23 (0.875)	45.49 (0.1002)
3	15.88 (0.625)	17.16 (0.0378)

Table 2. The complete details and specifications of the experimental bar specimens used.

Table 2-a. Bars combinations specimen number 1 - 10.

Sp. No.	Material	Steps No.	Diameter mm (in)	Length mm (in)	Mass kg (lb)	Remarks
1	Steel	0	25.4 (1.000)	1000 (39.37)	3.980 (8.767)	See Fig. 2-b ρ _o = 7805.73 kg/m ³ (0.282 lb/in ³)
2	Steel	0	12.7 (0.500)	1000 (39.37)	1.005 (2.214)	See Fig. 2-b
3	Brass	0	12.07 (0.475)	971.55 (38.25)	0.935 (2.059)	ρ _o = 8553.1 kg/m ³ (0.309 lb/in ³)
4	Brass	0	20.01 (0.788)	1249.93 (49.21)	3.310 (7.291)	-
5	Brass	0	28.68 (1.129)	1258.82 (49.56)	6.770 (14.912)	-
6	Aluminium	0	20.01 (0.788)	1257.3 (49.5)	1.085 (2.390)	ρ _o = 2643.43 kg/m ³ (0.0955 lb/in ³)
7	Aluminium	0	25.02 (0.985)	1244.6 (49)	1.652 (3.639)	-
8	Steel + Steel	1	25.4 (1.000)	-	-	Single stepped bar
			12.7 (0.500)	-	-	ρ _o = 7805.73 kg/m ³ (0.282 lb/in ³)
9	Brass + Brass	1	28.68 (1.129)	-	-	Single stepped bar
			12.07 (0.475)	-	-	-
10	Aluminium + Brass	0	20.01 (0.788)	-	-	Composite bar
			20.01 (0.788)	-	-	-

Table 2-b. Steel circular tapered bar specimen number 11.

Sp. No.	Material	Large diameter d ₁ mm (in)	Small diameter d ₂ mm (in)	Length mm (in)	Remarks
11	Steel	24.13 (0.95)	12.19 (0.48)	1244.6 (49.0)	See Fig. 2-a

Table 2-c. Steel rectangular tapered bar specimen number 12.

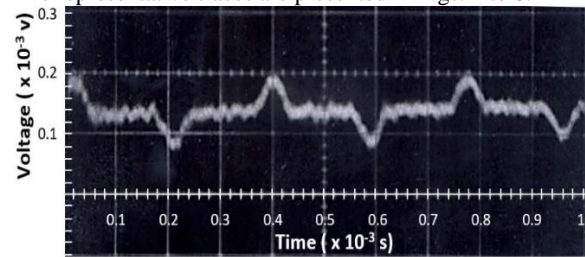
Sp. No.	Material	Thickness mm (in)	Larger width w ₁ mm (in)	Smaller width w ₂ mm (in)	Length mm (in)	Remarks
12	Steel	12.95(0.51)	25.91 (1.02)	12.95 (0.51)	1283.2 (50.52)	See Fig. 2-a

4.1. Specimen joining Method

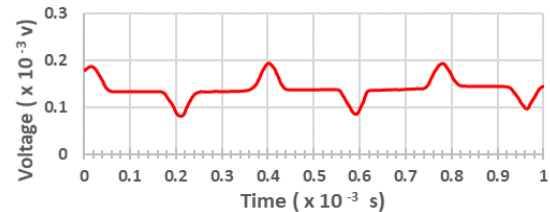
Stepped and composite bars combinations specimen numbers 8,9 and 10 (see Table 2-b), were fabricated by cementing the two bar elements together using Araldite cement. Tensile tests were carried out to determine the strength of bonds thus obtained. To separate a test specimen composed of two 25mm (1.0 in) dia. steel bars a force of 6.00 KN (1350 lb) was needed. This corresponds to a stress of 11.75N/mm² (1700psi), which is much higher than those anticipated stresses induced in the specimen during actual test conditions. The method of joining the specimens in this manner proved satisfactory and was used throughout the work.

5. Results and Discussion

Many oscilloscope traces were photographed showing stress wave propagation in the various test bars. A photograph illustrates a typical strain signal, obtained for a 25mm dia. steel bar impacted with 21.875mm (7/8 inch) dia. steel sphere is displayed in Fig. 3-a. However, all tests signals were retraced and manipulated with a digitizing signal software, and transformed to digital signal forms for further processing and calculations. Of these, five representative traces are presented in Figs. 4 to 8.



(a)



(b)

Figure 3. A typical strain signal obtained for a 25.4mm (1-inch) diameter steel bar of 984.25mm (39.37 in) length impacted with a 21.875mm (7/8 inch) diameter steel sphere; (a) A photograph; and (b) Digital signal form.

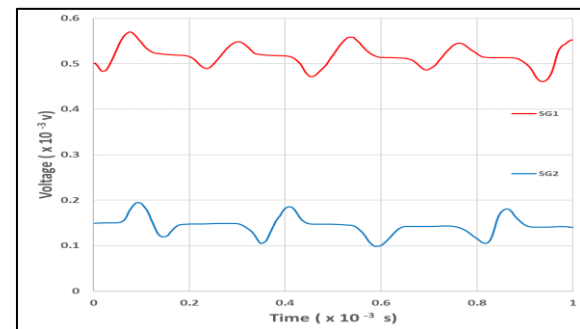


Figure 4. Strain-Time trace, for a one -step Steel bar, with area ratio A₁/A₂ = 4.

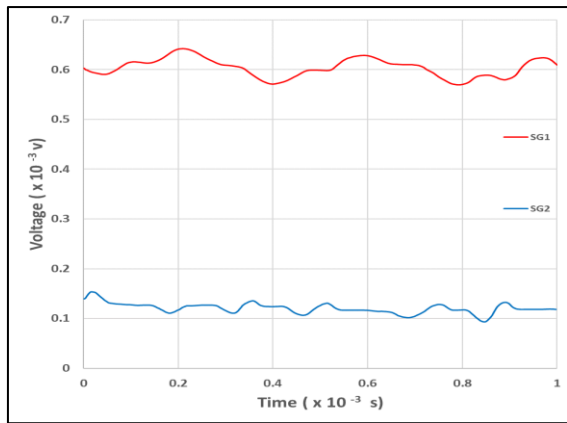


Figure 5. Strain-Time trace, for a one -step Brass bar, with area ratio $A_1/A_2 = 5.649$.

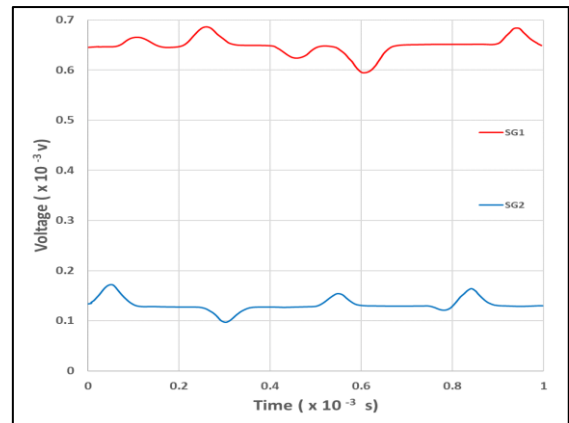


Figure 6. Strain-Time trace, for a composite bar of Aluminium and Brass, with area ratio $A_1/A_2 = 1$.

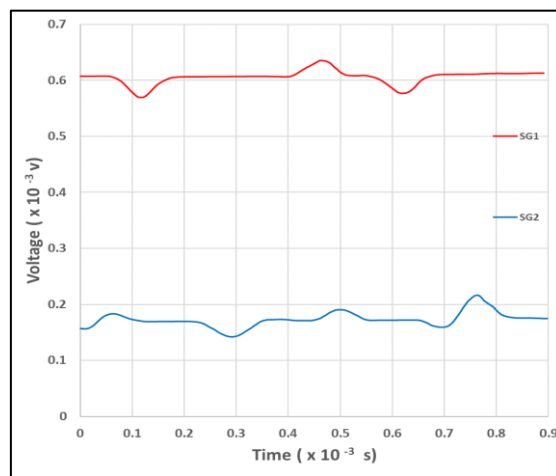


Figure 7. Strain-Time trace, for a composite bar of Brass and Aluminium, with area ratio $A_1/A_2 = 1$.

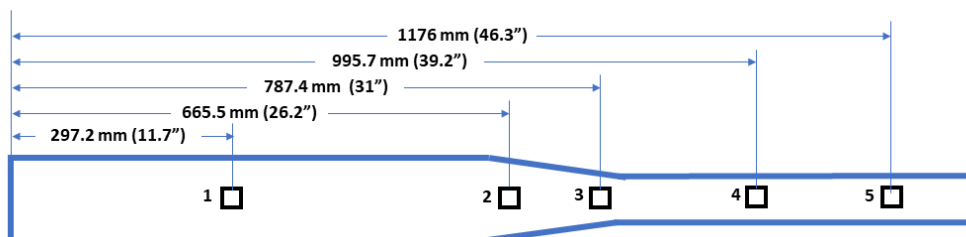
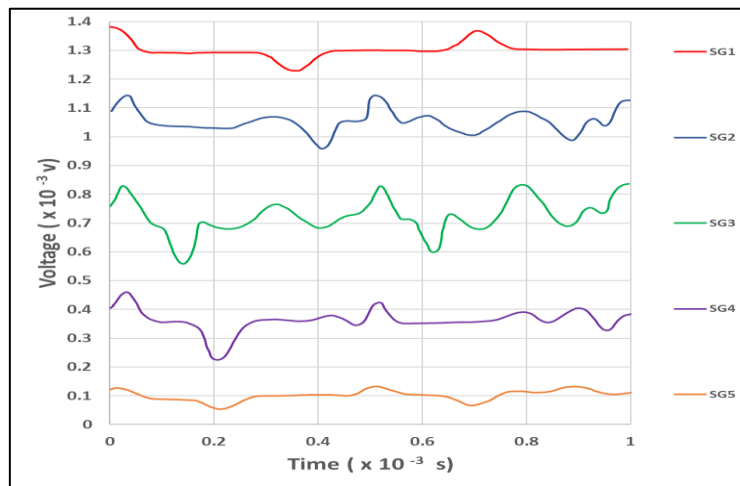


Figure 8. Strain-Time trace, for Steel tapered bar shown.

The theoretical and experimental values of the longitudinal wave speeds C_L and the Young's modulus E are calculated for the different bar materials specimens and displayed in Tables 3. The absolute relative error is less than 1.5% and 2.2% for wave speed and Young's modulus, respectively.

Table 3. The theoretical and experimental values of the longitudinal wave speed and Young's modulus for Steel, Brass and Aluminium specimens.

Sp. No.	Material	Theoretical Stress wave speed, C_L at 0° C, m/s (ft/sec.)	Experimental Stress wave speed, C_L at 25° C, m/s (ft/sec.)	Youngs Modulus, E, GPa (psi)	Experimental Youngs Modulus, E, GPa (psi)
1&2	Steel	5151 (16900)	5128 (16824)	203.4 (29.5x10 ⁶)	205.5 (29.8x10 ⁶)
3,4 &5	Brass	3352 (11000)	3401 (11160)	93.08 (13.5x10 ⁶)	95.15 (13.8x10 ⁶)
6&7	Aluminium	5090 (16700)	5102 (16740)	68.95 (10x10 ⁶)	69.64 (10.1x10 ⁶)

Also, the experimental values of the transmitted and reflected stress are calculated and displayed in Table 4 for the stepped steel, brass and composite (Aluminium and brass) bars. Meanwhile, the secondary transmitted stress (σ^T , σ^{T^2} , and σ^{T^3}) and reflected stress (σ^R , σ^{R^2} and σ^{R^3}) values for the steel and brass stepped specimens are shown in Table 5.

σ^{R^2} , σ^{R^3}) values for the steel and brass stepped specimens are shown in Table 5.

Table 4. The transmitted and reflected stress values in the stepped steel, brass and composite (Aluminium and brass) bars.

Sp. No.	Step Ratio A_1/A_2	Transmitted stress wave, σ_T	Reflected stress wave, σ_R	Remarks
8	4	1.6 σ_1	-0.6 σ_1	See Fig. 4
9	5.649	1.7 σ_1	-0.7 σ_1	See Fig. 5
10	1	1.36 σ_1	0.36 σ_1	See Fig. 6
		0.639 σ_1	-0.361 σ_1	See Fig. 7

Table 5. The secondary transmitted and reflected stress values in the steel and brass stepped bars.

Sp.No.	σ^T	σ^R	σ^{R^2}	σ^{T^2}	σ^{R^3}	σ^{T^3}	Remarks
8	1.6 σ_1	0.6 σ_1	-0.96 σ_1	-0.64 σ_1	0.58 σ_1	0.38 σ_1	See Fig. 8
9	1.7 σ_1	-0.7 σ_1	-1.2 σ_1	-0.5 σ_1	0.84 σ_1	0.38 σ_1	

Also, the results of the typical theoretical and experimental stress values of the transmitted and reflected stress wave passage (i.e. with time history), as well as the experimental detection times of the stress signals for stepped and composite bars, are calculated and shown in Tables 6 and 7 respectively.

Table 6. Typical theoretical and experimental stress values of the transmitted and reflected stress wave passage (i.e with time history) in stepped Steel, brass and composite (aluminium and brass) bars.

Theoretical Results			Experimental Results		
Time at reflection x 10 ⁻³ sec.	σ_R / σ_I	Detective time x 10 ⁻³ sec.	Time at reflection x 10 ⁻³ sec.	σ_R / σ_I	Detective time x 10 ⁻³ sec.
Steel Bar (Sp. No. 1)					
0.189	-1	0.0945	0.190	-1.00	0.09
0.378	+1	0.2835	0.380	+1.00	0.28
0.567	-1	0.4725	0.540	-1.10	0.47
0.756	+1	0.6615	0.760	+1.10	0.64
0.945	-1	0.8505	0.950	-0.96	0.85
Brass Bar (Sp. No. 4)					
0.373	-1	0.1865	0.340	-0.964	0.12
0.746	+1	0.3917	0.670	+0.923	0.43
1.119	-1	0.7647	1.100	-0.980	0.78
Aluminium Bar (Sp. No. 6)					
0.247	-1	0.1235	0.260	-1.00	0.12
0.494	+1	0.3705	0.460	+0.91	0.36
0.741	-1	0.6175	0.720	-1.12	0.63
0.988	+1	0.8645	0.940	+0.98	0.84

Table 7. Typical experimental detection times of the stress signals for stepped and composite bars.

Experimental Reflecting Time x 10 ⁻³ sec.		Experimental Detective Time x 10 ⁻³ sec.	
t	t''	T ₁	T ₂
a) Steel Stepped Bar (Sp. No. 8)			
0.16	0.24	0.00	0.06
0.38	0.50	0.20	0.31
0.61	0.70	0.41	0.54
0.84	0.93	0.64	0.56
b) Brass Stepped Bar (Sp. No. 9)			
0.12	0.10	0.00	0.00
0.30	0.25	0.13	0.16
0.50	0.40	0.33	0.29
0.68	0.61	0.52	0.46
0.85	0.82	0.72	0.65
c) Brass and Aluminium Composite Bar (Sp. No. 10)			
0.00	0.18	0.07	0.02
0.31	0.40	0.38	0.22
0.54	0.60	0.54	0.43
0.78	0.88	0.90	0.64

Furthermore, the theoretical and experimental values of the transmitted/incident and reflected/incident stress ratios at the discontinuities are calculated at a typical selected time applying Eqs. (9 and 10) and shown in Table 8. This, also, is assessed by Fig.9, which displays a constructed typical space-time diagram for a composite bar (Brass and Aluminium).

Experimental results show that nearly all recorded signals follow much the same pattern. This is because the local velocity of the elements transmitting the wave depends on the form of the disturbing force, which is affected by the geometrical shapes of the impacted bodies and the manner of applying the impact. In our case, mild steel sphere supported as a pendulum is used to produce the impact force in all tests, hence the signals obtained are of the same form.

In general, the shape of the recorded pulses is influenced by the relative values of specimen length (l) and pulse length (λ), as shown in Fig. 10. When $\lambda < l$ as shown in Fig. 10 a, the incident pulse is registered before

the wave front of the reflected pulse arrives back at the strain gauge location. The incident and reflected pulses are recorded separately and no over-lapping occurs (see for example Fig.3). A critical case arises when $\lambda=l$. Here, the wave front of the reflected pulse arrives back at the strain gauge location when the tail of the incident pulse is just about to leave the gauge. Finally, $\lambda > l$ is when over-lapping between incident and reflected waves occurs. Thus, the recorded signal will include components of both incident and reflected pulse and the usefulness of the results could be diminished.

To avoid over-lapping, the length of the bar and the axial location of the gauges along the bar must be carefully selected. Initial tests were carried out to determine the wave length of the stress pulse. Based on this, a suitable length for the various bars was chosen. The typical experimental wave length values obtained in steel, brass and aluminium specimens are measured for the various impact conditions and displayed in Table 9.

Table 8. Typical theoretical and experimental values of the transmitted/incident and reflected/incident stress ratios at typical selected times of the stress wave passage for stepped and composite bars.

Time	t_1		t_2		t_3		t_4	
Stress Ratio	σ_R/σ_I	σ_T/σ_I	σ_{R1}/σ_I	σ_{R2}/σ_I	σ_{R3}/σ_I	σ_{R4}/σ_I	σ_{T3}/σ_I	σ_{T4}/σ_I
Case A: One step Steel bar (Sp. No. 8)								
Theoretical	-0.6	1.6	-1.6	0.6	-0.96	-0.36	-0.64	0.96
Experimental	-	-	-1.5	0.7	-0.84	-0.43	-0.57	0.84
Case B: One step Brass bar (Sp. No. 9)								
Theoretical	-0.7	1.7	-1.7	0.7	-1.19	-0.49	-0.51	1.19
Experimental	-0.67	2.0	-2.0	0.59	-1.10	-0.46	-0.60	1.07
Case C: Brass and Aluminium composite bar (Sp. No. 10)								
Theoretical	-0.36	0.640	-0.64	+0.36	-0.13	-0.23	0.23	-0.870
Experimental	-0.34	0.625	-0.62	+0.32	-0.18	-0.25	0.36	-0.875

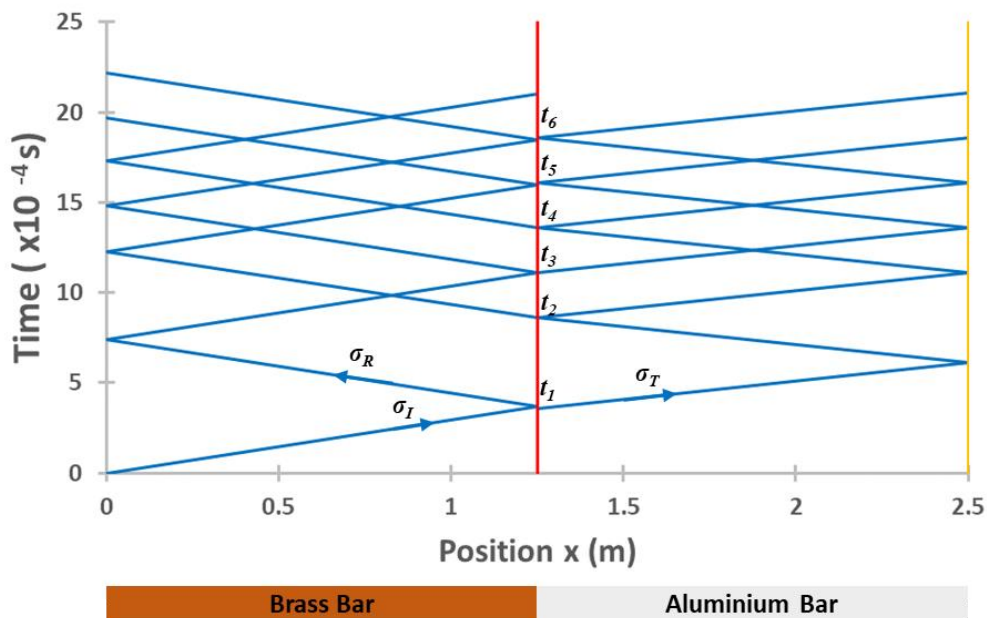


Figure 9. Space-Time diagram for composite Brass and Aluminium bar, with area ratio $A_1/A_2 = 1$.

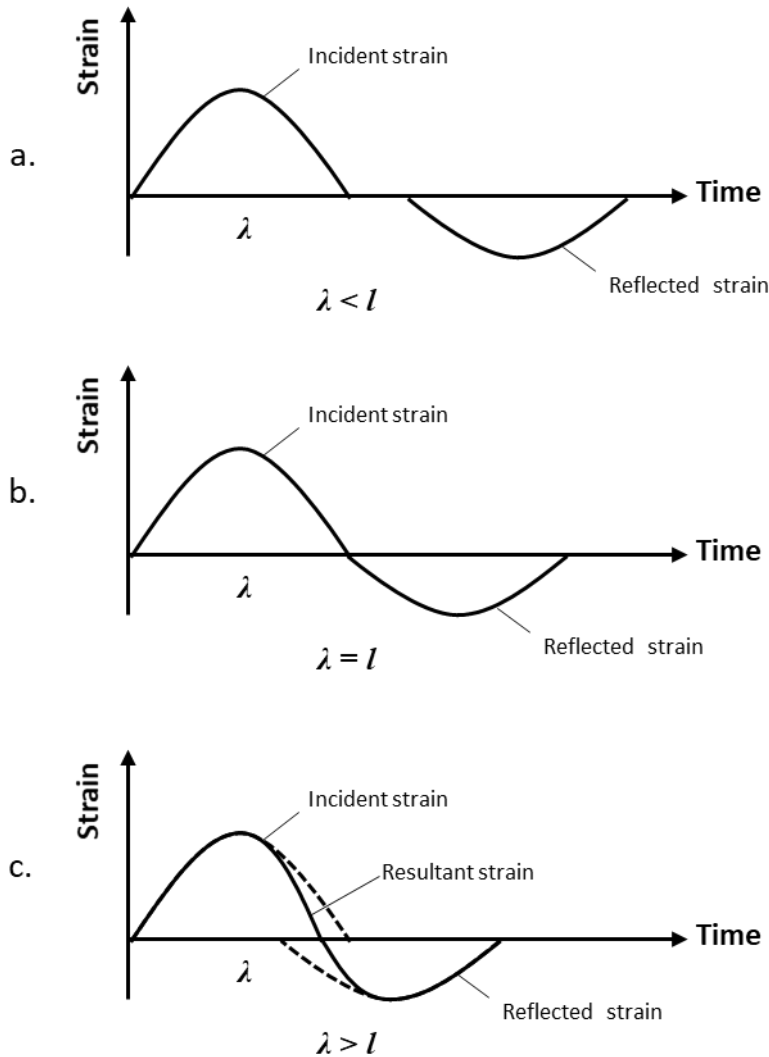


Fig. 10. Predicted wave forms in a stepped bar for different relative values of specimen length, l , and pulse length, λ .

Table 9. Typical experimental wave length values obtained in steel, brass and aluminium specimens.

Sphere Diameter, mm (in)	Wave Length, λ , m (ft)			
	Steel Bar (Sp. No. 1)	Brass Bar (Sp. No. 3)	Brass Bar (Sp. No. 4)	Aluminium Bar (Sp. No. 6)
25.4 (1)	0.732 (2.4)	0.503 (1.65)	0.469 (1.54)	0.61 (2.0)
22.23 (7/8)	0.518 (1.7)	0.402 (1.32)	0.369 (1.21)	0.457 (1.5)
15.88 (5/8)	0.411 (1.35)	0.268 (0.88)	0.274 (0.9)	0.411 (1.35)

The relative values of the incident (σ_i), reflected (σ_R) and the transmitted (σ_T) waves are governed by the mechanical impedance ratio of the input bar to that of the output bar. A very important conclusion can be drawn from this. Consider that a compressive stress wave is applied, for example, to a concrete column. Upon reflection, the wave will become tensile. As concrete is stronger in compression than tension, it is conceivable that the column would fracture in tension even though the amplitude of the initial applied pulse was less than the ultimate strength of concrete in compression. Values of σ_R/σ_i and σ_T/σ_i as measured directly from the records seem in reasonable agreement with the theoretical predictions.

In the theoretical analysis some assumptions have been made such as "plane sections remain plane"; the validity of this assumption is questionable near a discontinuity. The behaviour of the stress waves at the discontinuity is

complicated by local stress waves interactions taking place in the vicinity of the discontinuity. Also, Poisson's ratio and consequently radial inertia have been neglected. In actual situations, the radial vibrations could lead to dispersion of the applied pulse.

The significance of the space-time diagram, see Fig. 9, is that it shows the times when the stress wave passes any axial location along the bar. Values of time read from this diagram at the location of the gauges seem to tie in with the corresponding values on the recorded results. This adds weight to the accuracy of the experimental results.

When bars of different materials of the same length are impacted with the same sphere, the signals produced are almost the same in shape, but differ in amplitude and wave length, depending on the properties of the materials, and the wave speed in each, as illustrated in Figs. 3-8. It was noticed, also, that when a bar is impacted with spheres of

different diameters, the larger sphere gives longer contact time. Hence, values of the contact time between the impinging sphere and the end of the bar was calculated and found to be in good agreement with those measured from the length of the pulse. The details of the mechanics of elastic spheres impact based on the Hertz problem analysis including the main equations used for calculation of the contact times are shown in the Appendix. Thus, the theoretical and experimental contact times plotted against the radii of the three impacting spheres, are shown in Fig. 11.

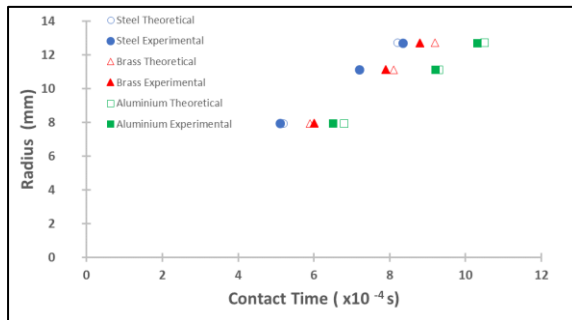


Figure 11. Theoretical and experimental variation of contact time with sphere radii for Steel, Aluminium and Brass bars.

The apparatus used was simple and could be upgraded with little effort. Some difficulties were, however, experienced in recording the signals. At first, there was a large amount of noise superimposed on the signal. This was partly solved using differential amplifiers and appropriate earthing of the system. In this manner most of the noise was suppressed and the signal/noise ratio was increased to an acceptable level. Another problem was associated with the triggering of the oscilloscope. The method adopted was to utilise the initial strain pulse to trigger the beam. This resulted in the loss of an essential part of the first pulse. These problems may be overcome with the use of more sensitive gauges (e.g. semi-conductor strain gauges) and the use of external triggering system.

Finally, the study of the impact stresses and the phenomena of stress waves in solids is of great value due to its wide applications. In fact, there are many occasions in engineering design where some components are subjected to impact loads or various impact fractures, such as spalling and scabbing (i.e. Fractures of bars and plates due to stress wave reflections), which are difficult to explain without the knowledge of the stress wave behaviour. Thus, stress wave aspects are widely used in military, machine element design and load sudden release applications. Extended studies of the different bar's configurations, materials and geometrical shapes including tapered and multi-stepped bars as well as the collinear collision of bars are essential. The design of impact momentum traps is very useful for structure safety.

6. Conclusions

In this work, the theoretical and experimental study of longitudinal stress wave propagation in solid composite bars with various geometrical and material discontinuities is successfully achieved. The stress wave propagation in simple composite bar configuration impacted longitudinally with steel spheres involving geometrical (i.e. tapered and stepped bars) and materials

(steel, aluminium, and brass i.e. composite bars) discontinuities combinations is theoretically evaluated and experimentally measured successfully. The theoretical and experimental values obtained, are found to be in excellent agreement reaching 98% accuracy. The shape of the recorded stress pulse is found to be influenced by the relative values of specimen length (l) and pulse length (λ). It is also, observed that the behaviour of the stress waves at a discontinuity is complicated by local stress waves interactions taking place in the vicinity of the discontinuity. The stress waves trapped and reverberate in the solid setting up wave interference that could produce large transient stresses were confirmed. The values obtained for the relative values of the incident reflected and transmitted waves are proven to be governed by the impedance ratio of the input bar to that of the output bar. The impedance matching condition (i.e. when the impedance ratio is unity) is also observed. Furthermore, the calculated and measured values, of the contact time between the impinging sphere and the end of the bar, based on Hertz analysis, are found to be in excellent agreement.

Finally, these promising results obtained, encourage further investigation on more complex composite structures and various damages and fractures involved in the impact process. A comprehensive theoretical and experimental investigation covering the damages caused by the stress waves and their transmission, reflection, and interaction causing scabbing and multiple scabbing fractures is discussed, recommended, and needed. Furthermore, the order of the composite materials 'cladding' process, which affects these phenomena and fracture mechanisms involved require intensive future research. The design and use of the momentum traps to avoid such fractures is also suggested.

Acknowledgement

The authors extend their appreciation to the Deanship of Scientific Research at King Saud University for funding the work through the research group project no. RGP-VPP-036.

References

- [1] Achenbach J. D., 1975, Wave Propagation in Elastic Solids, Elsevier, ISBN: 0720403251, Netherlands.
- [2] Bedford, A. & Drumheller, D.S., 1994, Introduction to Elastic Wave Propagation, John Wiley & Sons Ltd., West Sussex, England. updated version is available <https://imechanica.org/files/awave.pdf>, accessed 07/09/2019.
- [3] Zaid, A.I.O. 2016, Stress Waves in Solids, Transmission, Reflection and Interaction and Fractures Caused by Them: State of the Art, International Journal of Theoretical and Applied Mechanics, 1, pp 155-164.
- [4] Rayleigh, J.W.S., 1877, Theory of Sound, Vol 1, Macmillan, and Co. London UK.
- [5] Sears, J. S., 1907, On the longitudinal impact of metal rods with rounded ends, Transactions of the Philosophical Society, 21 (2), pp. 49 - 105. <https://www.math.fsu.edu/~agashe/junk2.pdf>.
- [6] Hopkinson B., 1914, A method of measuring the pressure produced in the detonation of high explosives or by the impact of bullets, Philosophical Transactions

- of the Royal Society A, 213, pp. 437 – 456. DOI: <https://doi.org/10.1098/rsta.1914.0010>.
- [7] Hopkinson B., 1914, The effects of the detonation of gun cotton, *Trans. North-East Coast Inst. Eng. And Shipbuilders*, 30, pp. 199.
- [8] Hopkinson B., 1921, The pressure of a blow. In *The scientific papers of Bertram Hopkinson* (eds JA Ewing, J Larmor), pp. 423–437. Cambridge, UK: Cambridge University Press.
- [9] Landon J.W. & Quinney H., 1923, Experiments with the Hopkinson pressure bar, *Proceeding of Royal Society Series A*, 103 (723), pp. 622-643. <https://doi.org/10.1098/rspa.1923.0084>.
- [10] Davies R.M., 1948, A critical study of the Hopkinson pressure bar, *Philosophical Transactions of The Royal Society of London Series A*, 240, pp. 375.
- [11] Shin H, Lee J-H, Kim J-B, & Sohn S-I., 2020, Design guidelines for the striker and transfer flange of a split Hopkinson tension bar and the origin of spurious waves. *Proceedings of the Institution of Mechanical Engineers, Part C: Journal of Mechanical Engineering Science*. 234(1), pp. 137-151. doi:10.1177/0954406219869984.
- [12] Shin H, Kim S, & Kim J-B., 2020, Stress Transfer Mechanism of Flange in Split Hopkinson Tension Bar. *Applied Sciences*, 10(21):7601. <https://doi.org/10.3390/app10217601>.
- [13] Shin H, & Kim D. 2020, One-dimensional analyses of striker impact on bar with different general impedance. *Proceedings of the Institution of Mechanical Engineers, Part C: Journal of Mechanical Engineering Science*.;234(2), pp. 589-608. doi:10.1177/0954406219877210.
- [14] Kolsky, H., 1953, *stress waves in solids*, 1st edition, Oxford University Press [at the Clarendon].
- [15] Rinehart J. S. & Pearson J. 1954, *Behavior of Metals under impulsive loads*, American Society for Metals, Cleveland, Ohio, USA.
- [16] Tsui T.Y., 1968, Wave Propagation in a Finite Length Bar with a Variable Cross Section, *Journal of Applied Mechanics-ASME*, 35(4), 824-825. <https://doi.org/10.1115/1.3601317>.
- [17] Kinslow R., 1970, *High velocity impact phenomena*, 1st edition, Academic press, 1970. <https://doi.org/10.1016/B978-0-124-08950-1.X5001-0>.
- [18] Johnson W., 1972, *Impact strength of materials*, Edward Arnold Ltd., London, UK.
- [19] Zaid, A.I.O. 1997, Effects of Stress Wave Propagation in conical Rods, in *Proceedings of the 5th International Symposium on Advanced Materials (ISAM -5)*, Khan, A.Q. (Ed.), 21st – 25th Sept 1997, pp. 576-581, Doctor AQ Khan Research Laboratories Kahuta Rawalpindi, Pakistan.
- [20] Goldsmith W. & Sackman J. L., 1992, An experimental study of energy absorption in impact on sandwich plates, *International Journal of Impact Engineering*, 12 (2), pp.241–262. [https://doi.org/10.1016/0734-743X\(92\)90447-2](https://doi.org/10.1016/0734-743X(92)90447-2).
- [21] Rafiee-Dehkharghani R., Aref A.J., & Dargush G., 2015, Stress Wave Attenuation in Solids for Mitigating Impulsive Loadings, Technical Report: MCEER-15-0003, ISSN 1520-295X. <http://www.eng.buffalo.edu/mceer-reports/15/15-0003.pdf>.
- [22] Walley S.M. & Field J.E., 2016, Elastic Wave Propagation in Materials, Module in Materials Science and Materials Engineering doi:10.1016/B978-0-12-803581-8.02945-3.
- [23] Sha Y., Dianhao C., & Jun X., 2019, Novel propagation behavior of impact stress wave in one-dimensional hollow spherical structures, *International Journal of Impact Engineering* 134, 103368, <https://doi.org/10.1016/j.ijimpeng.2019.103368>.
- [24] Damamme G., Vermunt J., Pierre Zappa D., & Klöcker H., 2019, Stress release waves in plastic solids, *Journal of the Mechanics and Physics of Solids*, 128, p 21–31. DOI: 10.1016/j.jmps.2019.03.021.
- [25] Rinehart, J.S., 1951, Some quantitative data bearing on the scabbing of metals under explosive attack, *Journal of Applied Physics*, 22, pp.555. <https://doi.org/10.1063/1.1700005>.
- [26] Jung J., 1979, Stress-Wave Grading Techniques On Veneer Sheets, General Technical Report FPL-27, US. Department of Agriculture, Forest Products Laboratory, 1979. available online <https://www.fpl.fs.fed.us/documnts/fplgtr/fplgtr27.pdf>.
- [27] Hascoët E., Herrmann H.J., & Loreto V., 1999, Shock propagation in a granular chain, *The American Physical Review E*, 59, No 3, pp 3202-3206. DOI: 10.1103/PhysRevE.59.3202.
- [28] Boaratti M.F.G. & Ting D.K.S., 2005, International Nuclear Atlantic Conference (INAC 2005), Santos, SP, Brazil, August 28 to September 2, 2005, ABEN, ISBN: 8599141015.
- [29] Sharma M. D., 2007, Effect of initial stress on reflection at the free surface of anisotropic elastic medium, *Journal of Earth System Science*, 116, pp. 537-551, DOI:10.1007/S12040-007-0049-8.
- [30] Cao Z., Liang N., Zeng S., & Gang X., 2022, Dynamic Response Analysis of the Impact Force of Steel Wheel on the Elastic Half-Space, *Jordan Journal of Mechanical and Industrial Engineering*, 16(1), pp. 53 – 62.
- [31] Yousuf L., 2019, The Effect of Temperature on the Stresses Analysis of Composites Laminate Plate, *Jordan Journal of Mechanical and Industrial Engineering*, 13(4), pp. 265 – 269.
- [32] Ali M., 2016, Synthesis and Characterization of Epoxy Matrix Composites Reinforced with Various Ratios of TiC, *Jordan Journal of Mechanical and Industrial Engineering*, 10(4), pp. 231 – 237.
- [33] Suresh S., Giannakopoulos A.E., & Alcalá J., 1997, Spherical indentation of compositionally graded materials: Theory and Experiments, *Acta Materialia*, 45 (4), pp.1307-1321. DOI: 10.1016/S1359-6454(96)00291-1.
- [34] Suresh S., 2001, Graded materials for resistance to contact deformation and damage, *Science*, 292 (5526), pp. 2447-2451. DOI: 10.1126/science.1059716.
- [35] Li Y., Ramesh K.T., & Chin E.S.C., 2001, Dynamic characterization of layered and graded structures under impulsive loading, *International Journal of Solids and Structures*, 38 (34-35), pp. 6045-6061. DOI:10.1016/S0020-7683(00)00364-4.
- [36] Han X., Liu G.R., & Lam K.Y., 2001, Transient Waves in Plates of Functionally Graded Materials, *International Journal for Numerical Methods in Engineering*, 52(8) pp 851-865. <https://doi.org/10.1002/nme.237>.
- [37] Berzovski A., Engelbrecht J., & Maugin G.A., 2003a, Numerical simulation of two-dimensional wave propagation in functionally graded materials, *European journal of mechanics-A/solid*, 22 (2), pp.257-265. [https://doi.org/10.1016/S0997-7538\(03\)00029-9](https://doi.org/10.1016/S0997-7538(03)00029-9).
- [38] Berzovski A., Engelbrecht J., Maugin G.A., 2003b, Stress wave propagation in functionally graded materials, WCU 2003, Paris, September 7-10, pp. 507-509. Corpus ID: 55589577, <http://www.conforg.fr/wcu2003/procs/cd1/articles/000101.pdf>.
- [39] Towfighi, S., Kundu, T., & Ehsani, M. (2002). Elastic wave propagation in circumferential direction in anisotropic cylindrical curved plates. *Journal of Applied Mechanics, Transactions ASME*, 69(3), 283-291. <https://doi.org/10.1115/1.1464872>.
- [40] Taşdemirci A., Hall I.W., Bazle A., Gama B.A., & Güden M., 2004, The Effects of Layer Constraint on Stress Wave Propagation in Multilayer Composite Materials, Army Research Laboratory, ARL-CR 550, available online at https://pdfs.semanticscholar.org/31ee/bc7281a310f64acfeeb6467bc9442b93a4ac.pdf?_ga=2.170619689.825782730.1574531385-1510146761.1566846515. Accessed 23/11/2019.

- [41] Xu L.R., & Rosakis A.J., 2005, Impact Damage Visualization of Heterogeneous Two Layer Materials Subjected to Low Speed Impact, *International Journal of Damage Mechanics*, 14(3), pp. 215 – 223. DOI:10.1177/1056789505048604.
- [42] Gebbeken N. & Greulich S., 2005, Effects of Stress Wave Propagation in Reinforced Concrete Bond considering Crack Opening. *EUROMECH Colloquium 460, Numerical Modelling of Concrete Cracking*, Innsbruck, Austria.
- [43] Zhang G.M., & Batra R.C., 2007, Wave Propagation In Functionally Graded Materials by Modified Smoothed Particle Hydrodynamics (MSPH) Method, *Journal of Computational Physics*, 222 (1), pp. 374- 390, DOI: 10.1016/j.jcp.2006.07.028.
- [44] Perez F. Jr. & Al-Haik M., 2009, Analysis of elastic stress wave propagation through a complex composite structure, *International Journal of Theoretical and Applied Multiscale Mechanics*, 1(2), pp.164–175. DOI:10.1504/IJTAMM.2009.029216.
- [45] Ogden R.W. & Singh B., 2011, Propagation of waves in an incompressible transversely isotropic elastic solid with initial stress: Biot revisited, *Journal of Mechanics of Materials and Structures*, 6 (1-4), pp 453-477. <https://msp.org/jomms/2011/6-1/jomms-v6-n1-p28-p.pdf>.
- [46] Barzkar A. & Adibi H. 2015, On the Propagation of Longitudinal Stress Waves in Solids and Fluids by Unifying the Navier-Lame and Navier-Stokes Equations, *Mathematical Problems in Engineering*, Volume 2015, Article ID 789238, pp. 1-9, <http://dx.doi.org/10.1155/2015/789238>.
- [47] Ebrahim F., Hosseini S. H. S., & Singhal A., 2020, A comprehensive review on the modeling of smart piezoelectric nanostructures, *Structural Engineering and Mechanics*, 74 (5), pp 611-633, DOI: <https://doi.org/10.12989/sem.2020.74.5.611>.
- [48] Ebrahimi, F., Karimiasl, M. & Singhal, A., 2021, Magneto-electro-elastic analysis of piezoelectric–flexoelectric nanobeams rested on silica aerogel foundation. *Engineering with Computers*, 37, pp 1007–1014. <https://doi.org/10.1007/s00366-019-00869-z>.
- [49] Singhal A., Sahu S. A., Nirwal S., & Chaudhary S., 2019, Anatomy of flexoelectricity in micro plates with dielectrically highly/weakly and mechanically compliant interface, *Materials Research Express*, 6, 105714, <https://doi.org/10.1088/2053-1591/ab3f52>.
- [50] Singhal A., Sahu S. A., Chaudhary S., & Baroi J., 2019, Initial and couple stress influence on the surface waves transmission in material layers with imperfect interface, *Materials Research Express*, 6, 105713, <https://doi.org/10.1088/2053-1591/ab40e2>.
- [51] Saroj P. K., Sahu S. A., Singhal A., & Abo-Dahab S. M., 2019, On the transference of Love-type waves in pre-stressed PZT-5H material stick on SiO₂ material with irregularity, *Materials Research Express*, Volume 6, Number 12, DOI: 10.1088/2053-1591/ab5544.
- [52] Timoshenko S., & Goodier J.N., 1951, *Theory of Elasticity*, McGraw-Hill, 2nd ed. New York.

Appendix

A summary of the most related theoretical analysis of the stress wave propagation problem in long bars as well as the elastic impact of spheres is presented[3,18].

The propagation of a compressive pulse in uniform long bars

In a stationary uniform isotropic bar, which is to transmit a longitudinal compressive pulse. Let u denote the displacement of a typical plane, originally distant x from a reference point O. Then $(u + \frac{\partial u}{\partial x} \partial x)$ denotes displacement of a parallel plane, initially at a distant $(x + \partial x)$ from a reference point O. The equation of motion for an element of the bar of initial cross section A_0 is

$$-\frac{\partial \sigma_0}{\partial x} \partial x A_0 = A_0 \rho_0 \partial x \frac{\partial^2 u}{\partial t^2}$$

$$\frac{\partial \sigma_0}{\partial x} = -\rho_0 \frac{\partial^2 u}{\partial t^2} \tag{1}$$

Where, ρ_0 is the density of the material in its unstrained state. The strain in an element of length ∂x is $\frac{\partial u}{\partial x}$. Thus $-\frac{\sigma_0}{\partial u / \partial x} = E$, where E is Young's Modulus.

Thus, differentiating we get,

$$\frac{\partial \sigma_0}{\partial x} = -E \frac{\partial^2 u}{\partial x^2} \tag{2}$$

And using this in Eq. (1) and after rearranging, one can find that:

$$\frac{\partial^2 u}{\partial t^2} = C_L^2 \frac{\partial^2 u}{\partial x^2} \tag{3}$$

Where, $C_L = \sqrt{E/\rho_0}$ is the Longitudinal stress wave speed.

A general solution for Eq. (3) is in the form

$$u = f(x - ct) + F(x + ct)$$

Where f and F are independent arbitrary functions. This is called the D'Alembert solution of the one-dimensional wave equation. The functions f and F describe waves that propagate in the positive and negative x directions with constant velocity or wave speed c ,[2].

The propagation of a tensile pulse in non-uniform long bars

In a stationary non-uniform isotropic rod, which is to transmit a longitudinal tensile pulse. Following the known analysis given by[3,18], we get the equation of motion for an element as:

$$\left(\sigma + \frac{\partial \sigma}{\partial x} \delta x\right) \left(A + \frac{\partial A}{\partial x} \delta x\right) - \sigma A = A \rho_0 \delta x \frac{\partial^2 u}{\partial t^2}$$

Neglecting the higher order differential term contains $(\delta x)^2$ and rearranging gives:

$$\frac{\partial \sigma}{\partial x} + \frac{\sigma}{A} \frac{\partial A}{\partial x} = \rho_0 \frac{\partial^2 u}{\partial t^2} \tag{4}$$

Recall that the strain in an element of length ∂x is $\frac{\partial u}{\partial x}$.

Thus,

$$E = \frac{\sigma}{\partial u / \partial x} \tag{5}$$

Differentiating,

$$\frac{\partial \sigma}{\partial x} = E \frac{\partial^2 u}{\partial x^2}$$

And using this in Eq. (4) and after rearrangement and manipulation, one can get:

$$\frac{\partial^2 u}{\partial x^2} + \left(\frac{1}{A} \frac{\partial A}{\partial x}\right) \frac{\partial u}{\partial x} = \frac{\rho_0}{E} \frac{\partial^2 u}{\partial t^2} \tag{6}$$

If the cross-sectional area of the bar is uniform, this equation reduces to Eq. (3) shown above.

$$\frac{\partial^2 u}{\partial t^2} = C_L^2 \frac{\partial^2 u}{\partial x^2}$$

The stress transmission in bars having a discontinuity in cross-sectional area and for bars composed of different materials

Consider an incident elastic wave of compressive stress of intensity σ_I moving through a stationary bar of material S_1 of cross-sectional area A_1 we note, this is partly reflected and partly transmitted at the surface of discontinuity, where another bar of material S_2 of cross-sectional area A_2 is perfectly attached to S_1 [3,18].

The stress wave transmitted through S_2 of intensity σ_T and that reflected back through S_1 , σ_R may be found with the aid of equations, $\sigma_0 = E \vartheta_0 / C_L$ and $\sigma_0 = \rho_0 C_L \vartheta_0$. Bearing in mind that the conditions to be satisfied at the surface of discontinuity are:

The forces on plane surface of discontinuity acting from S_1 and S_2 are always equal, and

The particle velocity in this plane, in material, for S_1 and S_2 , are equal.

If both σ_R and σ_T are taken to be compressive, then,

$$A_1(\sigma_I + \sigma_R) = A_2 \sigma_T \tag{7}$$

And noting that σ_I and σ_R are associated with waves travelling in opposite directions, therefore (b) gives,

$$V_I - V_R = V_T \quad \text{or}$$

$$\sigma_I - \sigma_R = \sigma_T \tag{8}$$

Where V denote particle speed and subscripts I, R and T refer to incident, reflected and transmitted stresses. Hence,

$$\sigma_T = \frac{2A_1 \rho_2 C_2}{A_1 \rho_1 C_1 + A_2 \rho_2 C_2} \sigma_I \tag{9}$$

And

$$\sigma_R = \frac{A_2 \rho_2 C_2 - A_1 \rho_1 C_1}{A_1 \rho_1 C_1 + A_2 \rho_2 C_2} \sigma_I \tag{10}$$

From Eq. (9) note that for simple change in cross-sectional areas, i.e. when S_1 and S_2 are of the same material and $\rho_1 = \rho_2$ and $C_1 = C_2$, the incident and reflected waves have the same or opposite signs according to the increase or decrease in size of the cross sectional area; and at the same time the intensity of the transmitted stress falls below or exceeds the intensity of the incident stress.

Eqs. (9) and (10) are approximate since the derivations are based on some simplifying assumptions; and at the discontinuity, condition (b) is true only inside the material, not at the end surfaces. Complicated local stress wave interactions occur in the vicinity of the surface of discontinuity and for a length equal to about the first diameter. Note that for $\rho_1 = \rho_2$ and $E_1 = E_2$ i.e. $C_1 = C_2$

If $A_2/A_1 \rightarrow 0$, i.e. the end of the rod is effectively free and the above equations give $\sigma_R \rightarrow -\sigma_I$ and $\sigma_T \rightarrow 2\sigma_I$, and

If $A_2/A_1 \rightarrow \infty$, i.e. the end of the rod is effectively fixed, $\sigma_R \rightarrow \sigma_I$ and $\sigma_T \rightarrow 0$.

Eqs. (9) and (10) show that a small shaft on the end of one larger in cross-sectional area can act as a wave (or momentum) trap to a pulse or blow on the far end of the larger shaft.

For no wave to be reflected from the discontinuity in the bar, it is required that $\sigma_R = 0$, and then $A_1 \rho_1 C_1 = A_2 \rho_2 C_2$, i.e. impedance matching. So that:

$$\sigma_T = \sigma_I \cdot \sqrt{\frac{E_2 \rho_2}{E_1 \rho_1}} \tag{11}$$

The central elastic impact of sphere

Following the well-known Hertz analysis of two spheres undergone simple elastic impact. The equation of motion for each sphere is given by

$$m_1 \frac{dV_1}{dt} = -P \text{ and } m_2 \frac{dV_2}{dt} = -P \quad (12)$$

Let x be the distance through which the two spheres approach by virtue of local compression.

$$\frac{dx}{dt} = V_1 + V_2 \quad (13)$$

After differentiating and using Eq. (12), one can find that:

$$\frac{\partial^2 x}{\partial t^2} = -P \left(\frac{m_1 + m_2}{m_1 \cdot m_2} \right) \quad (14)$$

Let, $\mu = \frac{m_1 + m_2}{m_1 \cdot m_2}$, then

$$\frac{\partial^2 x}{\partial t^2} = -\mu P \quad (15)$$

Timoshenko and Goodier [52] give that

$$P = Kx^{3/2} \quad (16)$$

where,

$$K = \frac{4}{3\pi \left[\frac{1-\theta_1^2}{\pi E_1} + \frac{1-\theta_2^2}{\pi E_2} \right]} \left(\frac{R_1 \cdot R_2}{R_1 + R_2} \right)^{1/2} \quad (17)$$

And θ denotes Poisson's ratio. Substituting Eq. (17) into Eq. (16) and integrating gives:

$$\frac{1}{2} (\dot{x}^2 - V_0^2) = -\frac{2}{5} K \mu x^{5/2} \quad (18)$$

Where $V_0 = V_1 + V_2$ when $t = 0$,

For maximum compression, x_0 , the velocity \dot{x} is zero; Thus

$$x_0 = \left(\frac{5V_0^2}{4K\mu} \right)^{2/5} \quad (19)$$

From Eq. (18) and after rearrangement, one can get:

$$\frac{dx}{dt} = V_0 \left[1 - \left(\frac{x}{x_0} \right)^{5/2} \right]^{1/2}$$

Hence, the time to maximum compression, T , is

$$T = 1.47 \frac{x_0}{V_0} \quad (20)$$

For spherical body impacting against a plane surface, i.e. $R_1 \rightarrow \infty$

$$K = \frac{4}{3\pi \left[\frac{1-\theta_1^2}{\pi E_1} + \frac{1-\theta_2^2}{\pi E_2} \right]} (R_2)^{1/2} \quad (21)$$

And time of contact, t , is

$$t = 2T$$

Modelling and Development of Multisectional Disk Piezoelectric Transducers for Critical Application Systems

Ibrahim M. Aladwan¹, Constantine Bazilo², Emil Faure^{2*}

¹*Al-Balqa' Applied University, Amman, Jordan*

²*Cherkasy State Technological University, Cherkasy, Ukraine*

Received 13 JUNE 2021

Accepted 30 JAN 2022

Abstract

The accuracy and reliability of computer systems largely depend on the characteristics of the transducers. The main advantage of using multisectional piezoceramic transducers is their special structure that makes it possible to implement fundamentally different circuits in such one element with a simultaneous increase in the degree of integration and hybridization of their operational properties. Diversity and variation of practical applications of piezoelectric transducers and devices on their bases naturally stimulate their theoretical research. Because of the absence of reliable and valid methods of constructing mathematical models of multisectional piezoelectric transducers, it is essential to consider the excitation of oscillations in transducers with group inclusion of sections taking into account the acoustic feedback. The paper considers the development of the mathematical model of a multisectional disk piezoelectric transducer taking into account the acoustic feedback that exists between the area under the electrode of the primary electrical circuit and all, without exception, the areas located under the electrodes of the secondary circuits. Proposed scheme maintains its logical structure in the wide range of the number of sections. The features of constructing mathematical models of multisectional transducers that arise when the sections are switched on in groups are considered. Based on the modelling, the methods for modifying disk piezoelectric transducers using a polyelectrode design, technology of additional elements, the spatial power structure of piezoelectric transducers, and physical models of transducers based on multisectional piezoelectric disks with improved characteristics, are described. The designs of a multifunctional piezoelectric transducer in the volume of one body are proposed.

© 2022 Jordan Journal of Mechanical and Industrial Engineering. All rights reserved

Keywords: piezoelectric disk, multifunctional transducer, physical processes, mathematical description, critical systems.

1. Introduction

The stable operation of computer systems, especially of critical application, largely depends on the reliability of the functioning of such computer systems. The most important part in this issue is the reliability of the functioning of both software and hardware of computer systems [1].

The integral elements of the hardware of computer systems regarding the characteristics of which the accuracy and reliability of their operation largely depend, are transducers [2].

Automatic space stations, autonomous deep-sea floating objects, and any other objects, access to which is very difficult, impossible or extremely dangerous for humans, such as (nuclear reactors, chemically hazardous objects, underground objects, orbiting satellites, etc.) are among the computer systems of critical application where high reliability, stability, autonomy, maximum uptime of such ultra-reliable transducers are required [3], [4].

The block diagram of the location of the sensors in the computer system on the example of a data collection and management system [5] is shown in Figure 1. Different material objects, such as cars, spaceships, human bodies, various liquids and gases can be the subjects of measurements. Data about the measured object is collected by sensors, some of which (2, 3 and 4) are located on the surface or inside the object. Sensor 1 has no direct

connection with the object, i.e. is contactless. Sensor 5 can perform various functions. It often serves to control conditions within the data collection system itself.

Many modern systems have to be built into rather miniature devices. Very often the geometry of the printed circuit board of a system is determined by the case of the device for which it is intended. Therefore, the miniaturization of execution is one of the problems of the developer of modern systems [6].

The main advantage of using transducers from piezoceramic materials [7], [8] with separated electrodes in computer systems is determined by their special structure. This makes it possible to implement fundamentally different circuits in one such element, with a simultaneous increase in the degree of integration and hybridization of their operational properties [9].

Diversity and variation of practical applications of piezoelectric transducers and devices on their bases naturally stimulate their theoretical research.

As some studies have shown, transducers based on multisectional disk piezoceramic elements, have a number of advantages [3]. Some principles of constructing a mathematical model of disk piezoelectric transducers are given in works [10], [11]. However, based on the analysis of literary sources [12], [13] it was determined that at present there are no methods for constructing mathematical models of multisectional piezoelectric transducers for computer systems of critical application.

* Corresponding author e-mail: fauremilr@gmail.com.

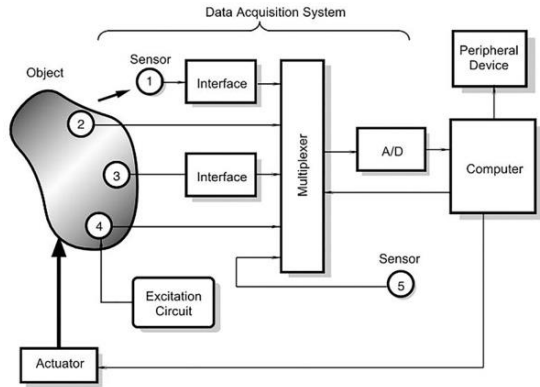


Figure 1. Location of sensors in the data collection system. Sensor 1 is non-contact, sensors 2 and 3 are passive, sensor 4 is active, and sensor 5 is built into the data collection system [5]

The aim of the paper is to construct a mathematical model of multisectional piezoceramic disk transducers and to develop examples of multisectional transducers with improved characteristics.

2. Materials and methods

Consider a piezoelectric disk transducer with separated electrodes, which has two or more secondary electrical circuits. In what follows, such transducers will be called multisectional or polyelectrode.

Figure 2 schematically depicts a disk transducer with three ring electrodes in secondary electrical circuits. The electrode of the primary electrical circuit has the shape of a circle with a radius $R_1^{(2)}$. A source of electrical potential difference $U_0 e^{i\omega t}$ is connected to it (U_0 is an amplitude of electrical potential difference; $i = \sqrt{-1}$ is an imaginary unit; ω is a circular frequency; t is a time).

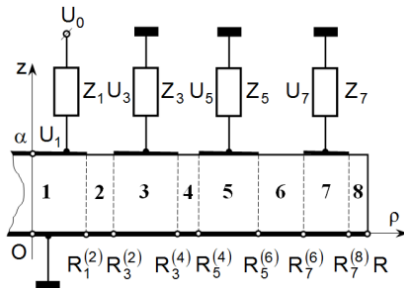


Figure 2. Design diagram of a multisectional piezoelectric transducer with three secondary electric circuits

The output impedance of the source of electrical potentials is indicated by the symbol Z_1 . The symbols Z_3, \dots, Z_7 indicate the electrical impedances of the loads in the secondary electrical circuits of the transducer. A piezoelectric disk element is made of PZT type material. The bottom surface ($z=0$) of the disk is completely electroded [14] and grounded. $R_{2n+1}^{(2n)}$ and $R_{2n+1}^{(2n+2)}$ are left and right boundaries of the circular area under the electrode of the $(2n+1)$ -th number, α is a disk thickness.

In some cases, it turns out to be advisable to group inclusion of sections of a multisectional disk piezoelectric transducer [3]. Consider the features of calculating the transformation ratios that arise in these situations (Fig. 3).

Figure 3, schematically shows four-sectional piezoelectric transducer, two electrodes of which are included in the primary electrical circuit. Such an inclusion allows, in principle, to increase the power of signals in secondary electrical circuits. The other two ring electrodes are included in two different secondary electrical circuits.

The mathematical model of the multisectional piezoelectric transducer (Fig. 3, a) can be written as follows:

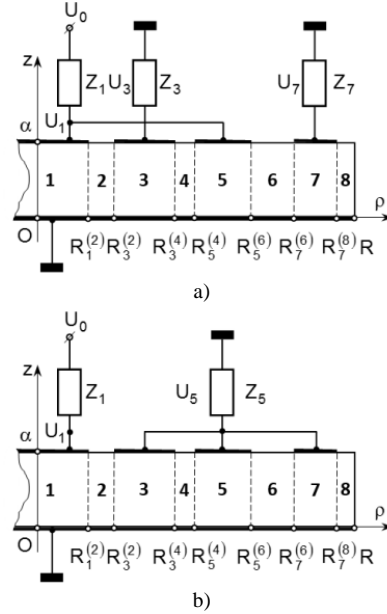


Figure 3. Design diagrams of multisectional piezoelectric transducers with group inclusions of sections

$$K_{2n+1}(\omega) = \frac{\Psi_{2n+1}(k, R)}{1 - i\omega C_1^* Z_1 \left\{ \Psi_1(k, R) - 1 + \left(\frac{C_5^*}{C_1^*} \right) [\Psi_5(k, R) - 1] \right\}}$$

($n = 1; 3$), (1)

where frequency-dependent dimensionless functions $\Psi_1(k, R)$, $\Psi_3(k, R)$, $\Psi_5(k, R)$ and $\Psi_7(k, R)$ are defined in Appendix A; C_1^* and C_5^* are the electrical capacities of the disk areas under electrodes 1 and 5, respectively; k is a wave number of radial oscillations in the $(2n+1)$ -th area under the corresponding electrode.

Figure 3, b schematically shows a disk transducer with three ring electrodes in secondary electrical circuits. The electrode of the primary electric circuit has the disk shape with radius $R_1^{(2)}$. The source of the difference of electric potentials $U_0 e^{i\omega t}$ is connected to it. The output resistance of the source of electric potentials is indicated by a symbol Z_1 . The symbol Z_5 indicates the electrical load impedance in the secondary electrical circuit of piezoelectric transducer.

The mathematical model of the multisectional piezoelectric transducer (Fig. 3, b) can be written as follows:

$$K_5(\omega) = - \frac{\Psi_5(k, R)}{1 - i\omega C_1^* U_1 [\Psi_1(k, R) - 1]}$$

(2)

where frequency-dependent dimensionless functions $\Psi_1(k, R)$ and $\Psi_5(k, R)$ are defined in Appendix B.

Expression (2) differs from all known results obtained by other authors in that it is constructed taking into account the acoustic feedback that exists between the area under the electrode of the primary electrical circuit and all, without exception, the areas located under the electrodes of the secondary circuits.

3. Modelling

It is obvious that the features of the change in the electrical impedance of the piezoelectric transducer are due to the change in the characteristics of the stress-strain state of the disk. Indeed, the electric current collected by the electroded surfaces $z = \pm a/2$ (a is a piezoelectric disk thickness) of the oscillating disk has an amplitude

$$I = -\omega \int_S D_z dS = \int_S [e_{3k1} \varepsilon_{k1} + \chi_3^e E_z] dS, \quad (3)$$

where D_z is an axial component of the electric induction vector; S and dS are area and area element of the electroded disk surface; e_{3k1} is a component of the tensor of piezoelectric constants (piezomodules); ε_{k1} is an elastic tensor component; χ_3^e is a component of the diagonal tensor of dielectric permittivity of the "clamped" sample; E_z is a component of the electric field strength vector in the volume of the deformable piezoelectric.

From the general relation (3) it clearly follows that the amplitude value of the current I and, therefore, the value $Z_{el}(\omega)$ are determined by the stress-strain state of the plate at a given frequency (values ε_{k1} and E_z) and a set of material constants (values e_{3k1} and χ_3^e). Since the deformations e_{3k1} are determined by the values of the elastic modules, it can be concluded that the analytical description of the electrical impedance of an oscillating piezoceramic disk contains the entire set of physical and mechanical parameters of piezoelectric ceramics. This

circumstance unambiguously indicates that, through the study of the features of the frequency-dependent behavior of the electrical impedance of the sample under study, one can come to the determination of the numerical values of the physical and mechanical parameters of the piezoelectric ceramics from which this sample is made.

Figure 4 shows a graph of the impedance frequency-dependent change of the disk made of PZT piezoelectric ceramics, which fluctuates in the air. The characteristic clearly shows singular points at which the modulus of electrical impedance acquires local minima and maxima. The inset in Fig. 4 shows the change in the modulus of electrical impedance near the frequency of the first local minimum. In the calculations, the following parameters were taken: the radius of piezoceramic disk $R = 33 \cdot 10^{-3}$ m; the thickness $\alpha = 3 \cdot 10^{-3}$ m; the disk material parameters [15], [16]: $c_{11}^E = 110$ GPa; $c_{12}^E = 60$ GPa; $c_{33}^E = 100$ GPa; $e_{33} = 18$ C/m²; $e_{31} = -8$ C/m² and $\chi_{33}^e = 1400 \chi_0$; $Q_M = 100$; $k = c_{12}/c_{11} = 0,324$. The ordinate shows the values of the modulus of electrical impedance in kilohms, the abscissa shows the dimensionless frequency $\Omega = \lambda R = \omega \tau_0$, where $\tau_0 = R/v$;

$v = \sqrt{c_{11}/\rho_0}$ is a speed of propagation of elastic vibrations in a thin disk. For the above parameter values $v = 3162$ m/s and $\tau_0 = 10,44 \cdot 10^{-6}$ s. The value $\Omega = \lambda R = 1$ corresponds to the frequency $f = 15,25$ kHz. The calculations were performed at the frequencies of the first two electromechanical resonances.

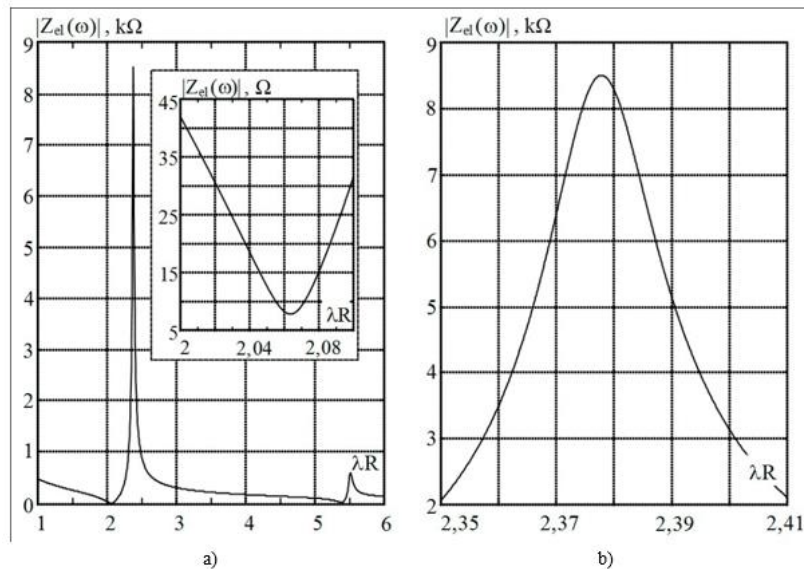


Figure 4. Disk electrical impedance modulus in mid-frequency

At the frequency of resonant energy consumption, an infinite (in amplitude) displacement current can flow through a piezoelectric disk from an ideal (lossless) piezoelectric. Infinite currents with a finite difference in electrical potentials correspond to zero values of electrical resistance. For this reason, at the frequency of electromechanical resonance (the frequency at which the resonant energy consumption of the oscillation source occurs), the electrical impedance of a disk from an ideal piezoelectric is zero. In a real piezoelectric, there are always certain losses of the energy supplied to it, and therefore, at the frequency of electromechanical resonance, the modulus $Z_{el}(\omega)$ reaches a minimum, but not zero, value. The inset in Fig. 4 shows this clearly.

At the frequency when the modulus $Z_{el}(\omega)$ reaches a local maximum, the electric current in the conductors that are connected to the electroded surfaces of the oscillating disk vanishes. Zero electric current at finite values of the electrical potential difference corresponds to an infinite electrical resistance, i.e., an open circuit. In a real piezoelectric, there are always losses (leaks), it has a finite electrical conductivity, therefore, at the frequencies of electromechanical antiresonance, $Z_{el}(\omega)$ reaches maximum, but finite, values [3].

In a real experiment, zeros and infinities are absent, since in real elastic materials there are always losses due to viscous friction. These losses can be taken into account using a parameter Q_m that makes sense to the mechanical quality factor of the material. As it is known, the quality factor is a dimensionless number, the value of which is inversely proportional to the energy losses in the oscillatory system over the period. In ideal elastic bodies, where there are no energy losses due to viscous friction, $Q_m \rightarrow \infty$. In real objects, the quality factor Q_m has a finite value.

4. Experiments

The block diagram of the laboratory model, which is used to determine the material constants of piezoelectric ceramics, is shown in Fig. 5.

A harmonic signal generator (HSG) generates an electrical potential difference $U_0 e^{i\omega t}$, the frequency of the change of sign of which is controlled by an electronic frequency meter (EFM).

Keys K1 and K2 are designed for more accurate measurement of the frequency of electromechanical resonance (key K1 is open, and key K2 is closed) and antiresonance (key K1 is closed, and key K2 is open). In the first case, the electronic voltmeter EV1 measures the voltage drop U_1 at a low impedance $|Z_{el}(\omega)|$ and therefore its sensitivity is set as high as possible. In the second case, when the key K2 is opened, the situation is repeated. The voltmeter EV2 measures the voltage drop across the resistor R_2 , the value of which is selected from the condition of the inequality $R_2 \ll |Z_{el}(\omega_a)|$, where ω_a is an electromechanical anti-resonance frequency, and the voltmeter EV2 sensitivity is set as high as possible. The frequencies of resonances and anti-resonances are reliably determined from changes in the readings of voltmeters tuned to the maximum sensitivity [16].

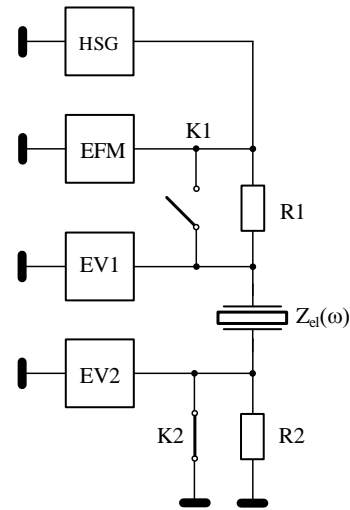


Figure 5. Circuit of experimental determination of the frequencies of electromechanical resonances and antiresonances of oscillations of a piezoceramic disk and calculation of the basic material constants of piezoelectric ceramics from their values

The electrical impedance $Z_{el}(\omega)$ of piezoceramic disk (Fig. 5), elastic vibrations in which are excited by the action of an external electric potential difference, is determined by Ohm's law for a section of the circuit,

$$Z_{el}(\omega) = \frac{U_{el}}{I}, \quad (4)$$

where I is an amplitude value of current in electric circuit.

The electrical impedance modulus of the oscillating sample $|Z_{el}(\omega)| = \frac{U_1 R_1}{(U_0 - U_1)}$ is determined from the

voltage drop U_1 across the test sample $Z_{el}(\omega)$ measured by electronic voltmeter EV1 and from the known value of U_0 . When measured with an EV2 voltmeter, the calculation formula for the modulus of electrical impedance has a

$$\text{slightly different form } |Z_{el}(\omega)| = \frac{(U_0 - U_2) R_2}{U_2}.$$

A disk piezoelectric element $\varnothing 66 \times 3$ mm made of PZT type material is used for experimental studies.

The results of measuring the electrical impedance of the piezoelectric disk in the mid-frequency area are shown in Figure 6.

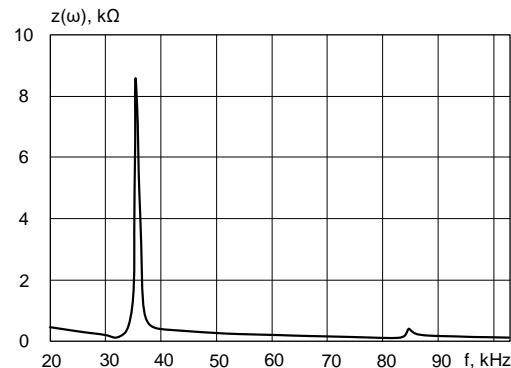


Figure 6. Electrical impedance of the piezoelectric disk in the mid-frequency area

When comparing the results of mathematical modelling of the electrical impedance of a piezoelectric disk in the region of medium frequencies (Fig. 4), and the results of experimental measurements (Fig. 6), it can be seen that the

obtained estimate is in good agreement with the true value of the electrical impedance. In this case, the frequency $f = 15,25\text{kHz}$ corresponds to the value $\Omega = \lambda R = 1$.

5. Results

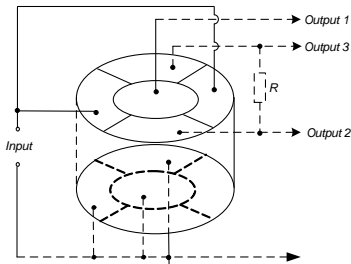
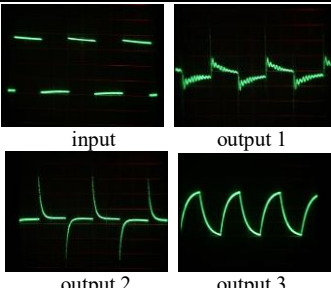
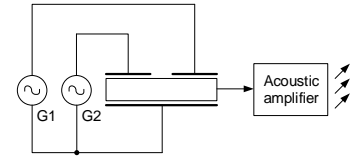
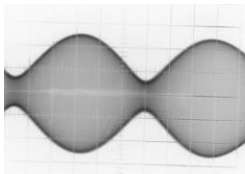
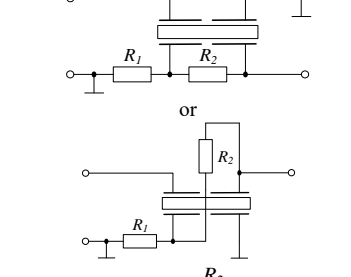
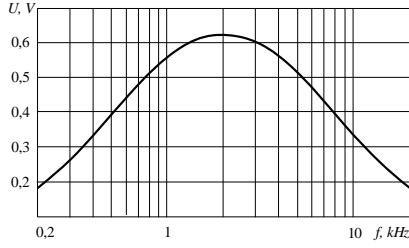
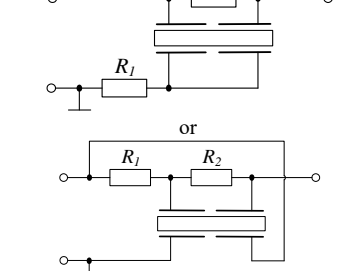
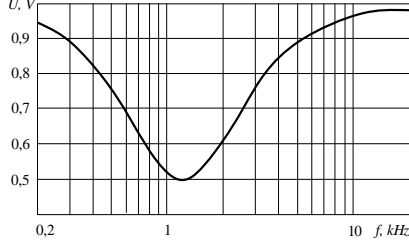
When designing piezoelectric transducers, a piezoelectric element of a certain shape and size from a certain piezoceramic material with certain electrophysical properties (characteristics) is usually used. In this case, only one transducer with certain characteristics (resonant frequency, sensitivity, etc.) can be obtained from a certain piezoelectric element. Therefore, the proposal to take into account the mutual arrangement of the vectors F , P and E when developing the designs of transducers was an extraordinary and unusual decision. Such a mutual arrangement of vectors was called the spatial power structure of piezoelectric element. For example, in order to increase the level of sound pressure created using monomorphic piezoelectric elements, it was proposed to create an electric field in the transducer so that the electric

field vector E of the excitation voltage makes an angle α with the polarization vector P , and $0 < \alpha \leq 90^\circ$ [13].

Based on modelling the authors have developed methods for modifying disk piezoelectric transducers by using a polyelectrode design, technology of additional elements and the spatial power structure of piezoelectric transducers, as well as physical models of transducers based on multisectional piezoelectric disks with improved characteristics (Table 1).

Table 1 shows a designed multifunctional piezoelectric transducer with five electrodes located on the surfaces of the piezoelectric element and oscillograms of signals at its input and outputs (position 1). The bottom electrodes are projections of the top ones. The described version of the piezoelectric transducer, which allows processing the input signal, is, of course, not the only one. Changing the size of the electrodes, their relative position allows one to influence the parameters of the output signals and opens up wide opportunities for the design of piezoelectric transducers for critical application systems.

Table 1. Designed multisectional piezoelectric transducers

No.	Transducer circuit	Output characteristic
1		
2		
3		
4		

* circuit 3 ($R_1 = 12,6\text{ k}\Omega$, $R_2 = 10,2\text{ k}\Omega$), circuit 4 ($R_1 = 9,5\text{ k}\Omega$, $R_2 = 38\text{ k}\Omega$)

The developed electroacoustic radiator based on a piezoelectric adder with two systems of electrodes and the process of interference of two oscillations are presented in Table 1 (position 2). One system of electrodes is supplied with an electric voltage from the first generator, and the frequency of oscillations of the electric voltage of this generator is set equal to or close to one of the resonant frequencies of the piezoelectric element. The second system of electrodes of the piezoelectric element is supplied with voltage from the second generator. The oscillation frequency of this generator is also set close to the same resonant frequency so that the difference between the oscillation frequencies of the first and second generators is equal to the operating frequency of the radiator. Therefore, by exciting the transducer at inaudible frequencies, one can get an audio frequency at the output.

To expand the working range, piezoelectric elements can be included in the circuits of electrical filters. One of the disadvantages of such transducers is the need to use two piezoelectric elements or a piezoelectric element and a capacitor. To eliminate this disadvantage, the piezoelectric elements with separated electrodes can be used in the transducer circuits. The developed transducer with separated electrodes in a band-pass filter circuit as well as the transducer with separated electrodes in the band-stop filter circuit and their amplitude-frequency characteristics are indicated in Table 1 (positions 3 and 4) respectively. The piezoelectric transducer based on a disk piezoelectric element $\varnothing 66 \times 3$ mm made of PZT type material was used for research.

Conclusions

Physical processes in multisectional disk piezoelectric transducer were considered. The mathematical model of a multisectional disk piezoelectric transducer was built taking into account the acoustic feedback that exists between the area under the electrode of the primary electrical circuit and all, including the areas located under the electrodes of the secondary circuits. Proposed scheme maintains its logical structure in the wide range of the number of sections. The features of constructing mathematical models of multisectional transducers that arise when the sections are switched on in groups were considered. A comparative analysis of mathematically calculated and experimentally obtained values of the electrical impedance of the oscillating piezoceramic transducer revealed high convergence between them. Based on the modeling, the methods for modifying disk piezoelectric transducers using a polyelectrode design, technology of additional elements, the spatial power structure of piezoelectric transducers, and the physical models of transducers based on multisectional piezoelectric disks with improved characteristics, were designed.

References

[1] Garsia Sespedes, N.V. Reliability of computer systems. *Mathematical machines and systems*, 2016, no. 4, pp. 146–151.

- [2] Li, J. Design of Active Vibration Control System for Piezoelectric Intelligent Structures. *International Journal of Education and Management Engineering (IJEME)*, 2012, vol. 2, no. 7, pp. 22–28. doi: 10.5815/ijeme.2012.07.04
- [3] Petrishchev, O. N., Bazilo, C. V. Principles and methods of mathematical modelling of oscillating piezoelectric elements. *Gordienko Publ., Cherkasy*, 2019.
- [4] Carazo, A.V. Piezoelectric Transformers: An Historical Review. *Actuators*, 2016, vol. 5, no. 12. doi:10.3390/act5020012
- [5] Fraden, J. *Handbook of Modern Sensors*. Springer, New York, 2010.
- [6] Barrett, S.F., Pack, D.J. *Embedded systems design and applications with the 68HC12 and HCS12*. Pearson/Prentice Hall, Upper Saddle River, NJ, 2005.
- [7] Kachapi, S. H. H. Nonlinear Vibration and Frequency Analysis of Functionally Graded- Piezoelectric Cylindrical Nano-shell with Surface Elasticity. *JJMIE*, vol. 12, no. 4, pp. 293–312.
- [8] Ebrahimi, F., Barati, M. R. Buckling Analysis of Nonlocal Embedded Shear Deformable Functionally Graded Piezoelectric Nanoscale Beams. *JJMIE*, vol. 11, no. 2, pp. 79–95.
- [9] Vavilov, V.D., Timoshenkov, S.P., Timoshenkov, A.S. *Microsystem sensors of physical quantities*. Technosfera, Moscow, 2018.
- [10] Bazilo, C. Modelling of bimorph piezoelectric elements for biomedical devices. In: Hu Z., Petoukhov S., He M. (eds) *Advances in Artificial Systems for Medicine and Education III. AIMEE 2019. Advances in Intelligent Systems and Computing*, 2020, vol. 1126. Springer, Cham, 2020, pp. 151–160. doi: 10.1007/978-3-030-39162-1_14
- [11] Bazilo, C., Usyk, L. Modelling of Piezoelectric Disk Transducers Operated on Non-axisymmetric Oscillations for Biomedical Devices. In: Hu Z., Petoukhov S., He M. (eds) *Advances in Artificial Systems for Medicine and Education IV. AIMEE 2020. Advances in Intelligent Systems and Computing*, 2021, vol. 1315. Springer, Cham, 2021, pp. 191–200. doi: https://doi.org/10.1007/978-3-030-67133-4_18
- [12] Buchacz, A., Placzek, M., Wrobel, A. Modelling of passive vibration damping using piezoelectric transducers – the mathematical model. *Maintenance and reliability*, 2014, vol. 16, no. 2, pp. 301–306.
- [13] Livingston, D., Kumar, K. P., Venugopal, N. Modelling and simulation of multiple piezoelectric transformer converters. *International Journal of Emerging Technology and Advanced Engineering*, 2013, vol. 3, no. 8, pp. 237–245.
- [14] Medianyuk, V. V., Bondarenko, Yu. Yu., Bazilo, C. V., Bondarenko M. O. Research of current-conducting electrodes of elements from piezoelectric ceramics modified by the low-energy ribbon-shaped electron stream. *Journal of Nano- and Electronic Physics*, 2017, vol. 10, issue 6, pp. 06012–1–06012–6. doi: 10.21272/jnep.10(6).06012
- [15] Bazilo, C., Zagorskis, A., Petrishchev, O., Bondarenko, Y., Zaika, V., Petrushko, Y. Modelling of Piezoelectric Transducers for Environmental Monitoring. In: *Proceedings of 10th International Conference "Environmental Engineering"*, Vilnius Gediminas Technical University, Lithuania, 2017. doi: 10.3846/enviro.2017.008
- [16] Petrishchev, O. N., Bazilo, C. V. Methodology of Determination of Physical and Mechanical Parameters of Piezoelectric Ceramics. *Journal of Nano- and Electronic Physics*, 2017, vol. 9, issue 3, pp. 03022–1–03022–6. doi: 10.21272/jnep.9(3).03022

Appendix A

$$\Psi_1(k, R) = \frac{2K_{31}^2}{kR_1^{(2)}D_0} J_1(kR_1^{(2)}) \left[M_1^{(2)} + N_1^{(8,10)} - \Psi_3(k, R)N_1^{(4,6)} - \Psi_7(k, R)N_1^{(12,14)} \right]; \quad (\text{A.1})$$

$$\begin{aligned} \Psi_5(k, R) &= \frac{2K_{31}^2}{kR_5^{(6)}D_0 \left[1 - \left(R_5^{(4)}/R_5^{(6)} \right)^2 \right]} \left\{ J_1(k, R_5^{(4)}, R_5^{(6)}) \left[-M_8^{(2)} + N_8^{(8,10)} - \right. \right. \\ &- \Psi_3(k, R)N_8^{(4,6)} - \Psi_7(k, R)N_8^{(12,14)} \left. \right] + N_1(k, R_5^{(4)}, R_5^{(6)}) \times \\ &\times \left[M_9^{(2)} + N_9^{(8,10)} - \Psi_3(k, R)N_9^{(4,6)} - \Psi_7(k, R)N_9^{(12,14)} \right] \left. \right\}; \quad (\text{A.2}) \end{aligned}$$

in which K_{31}^2 is a square of the electromechanical coupling coefficient for the radial vibration mode in a thin piezoceramic disk; $M_j^{(l)}$ is an algebraic complement that is obtained from the matrix M_0 by striking out j -th row and l -th column;

$$\begin{aligned} N_1^{(4,6)} &= -M_1^{(4)} + M_1^{(6)}; \quad N_1^{(8,10)} = -M_1^{(8)} + M_1^{(10)}; \quad N_1^{(12,14)} = -M_1^{(12)} + M_1^{(14)}; \quad N_{4n}^{(4,6)} = M_{4n}^{(4)} - M_{4n}^{(6)}; \quad N_{4n}^{(8,10)} = M_{4n}^{(8)} - M_{4n}^{(10)}; \\ N_{4n}^{(12,14)} &= M_{4n}^{(12)} - M_{4n}^{(14)}; \quad N_{4n+1}^{(4,6)} = -M_{4n+1}^{(4)} + M_{4n+1}^{(6)}; \quad N_{4n+1}^{(8,10)} = -M_{4n+1}^{(8)} + M_{4n+1}^{(10)}; \\ N_{4n+1}^{(12,14)} &= -M_{4n+1}^{(12)} + M_{4n+1}^{(14)}; \end{aligned}$$

D_0 is the determinant of the strip matrix $M_0 = \|m_j^{(l)}\|$, nonzero elements $m_j^{(k)}$ (j is a row number; l is a column number) of which are concentrated in the vicinity of the diagonal drawn from the upper left corner to the lower right corner;

$$\Psi_3(k, R) = \frac{1}{D_2} \left\{ F_1^{(3)}(k, R) \left[F_7^{(7)}(k, R) - 1 \right] - F_1^{(7)}(k, R) F_7^{(3)}(k, R) \right\}; \quad (\text{A.3})$$

$$\Psi_7(k, R) = \frac{1}{D_2} \left\{ F_1^{(7)}(k, R) \left[F_3^{(3)}(k, R) - 1 \right] - F_3^{(7)}(k, R) F_1^{(3)}(k, R) \right\}; \quad (\text{A.4})$$

$$D_2 = \left[F_3^{(3)}(k, R) - 1 \right] \left[F_7^{(7)}(k, R) - 1 \right] - F_7^{(3)}(k, R) F_3^{(7)}(k, R); \quad (\text{A.5})$$

$$F_1^{(2n+1)}(k, R) = F_0^{(2n+1)} \left[-J_1(k, R_{2n+1}^{(2n)}, R_{2n+1}^{(2n+2)}) M_{4n}^{(2)} + N_1(k, R_{2n+1}^{(2n)}, R_{2n+1}^{(2n+2)}) M_{4n+1}^{(2)} \right]; \quad (\text{A.6})$$

$$F_0^{(2n+1)} = \frac{2K_{31}^2 f_{2n+1}(\omega)}{\left\{ 1 - \left[R_{2n+1}^{(2n)}/R_{2n+1}^{(2n+2)} \right]^2 \right\} k R_{2n+1}^{(2n+2)} D_0}; \quad (\text{A.7})$$

$$F_3^{(2n+1)}(k, R) = F_0^{(2n+1)} \left[J_1(k, R_{2n+1}^{(2n)}, R_{2n+1}^{(2n+2)}) N_{4n}^{(4,6)} + N_1(k, R_{2n+1}^{(2n)}, R_{2n+1}^{(2n+2)}) N_{4n+1}^{(4,6)} \right]; \quad (\text{A.8})$$

$$F_5^{(2n+1)}(k, R) = F_0^{(2n+1)} \left[J_1(k, R_{2n+1}^{(2n)}, R_{2n+1}^{(2n+2)}) N_{4n}^{(8,10)} + N_1(k, R_{2n+1}^{(2n)}, R_{2n+1}^{(2n+2)}) N_{4n+1}^{(8,10)} \right]; \quad (\text{A.9})$$

$$F_7^{(2n+1)}(k, R) = F_0^{(2n+1)} \left[J_1(k, R_{2n+1}^{(2n)}, R_{2n+1}^{(2n+2)}) N_{4n}^{(12,14)} + N_1(k, R_{2n+1}^{(2n)}, R_{2n+1}^{(2n+2)}) N_{4n+1}^{(12,14)} \right]; \quad (\text{A.10})$$

where $J_1(k, R_{2n+1}^{(2n)}, R_{2n+1}^{(2n+2)}) = J_1(k R_{2n+1}^{(2n+2)}) - R_{2n+1}^{(2n)} J_1(k R_{2n+1}^{(2n)}) / R_{2n+1}^{(2n+2)}$ and

$N_1(k, R_{2n+1}^{(2n)}, R_{2n+1}^{(2n+2)}) = N_1(k R_{2n+1}^{(2n+2)}) - R_{2n+1}^{(2n)} N_1(k R_{2n+1}^{(2n)}) / R_{2n+1}^{(2n+2)}$ are Bessel and Neumann functions of the first order.

Appendix B

$$\Psi_1(k, R) = \frac{2K_{31}^2 J_1(kR_1^{(2)})}{kR_1^{(2)} D_0} \left[M_1^{(2)} - \Psi_3(k, R) N_1^{(4,6)} - \Psi_5(k, R) N_1^{(8,10)} - \Psi_7(k, R) N_1^{(12,14)} \right]; \quad (\text{B.1})$$

$$\Psi_5(k, R) = \frac{i\omega Z_5 C_5^* q(\omega)}{1 + i\omega Z_5 C_5^* p(\omega)}; \quad (\text{B.2})$$

$$q(\omega) = \frac{C_3^*}{C_5^*} \beta_3 + \beta_5 + \frac{C_7^*}{C_5^*} \beta_7; \quad p(\omega) = \frac{C_3^*}{C_5^*} (\lambda_3 - 1) + \lambda_5 - 1 + \frac{C_7^*}{C_5^*} (\lambda_7 - 1); \quad (\text{B.3})$$

where $C_{2n+1}^* = (\pi \chi_{33}^* / \alpha) \left[\left(R_{2n+1}^{(2n+2)} \right)^2 - \left(R_{2n+1}^{(2n)} \right)^2 \right]$ is the electrical capacity of the $(2n + 1)$ -th ring area of the disk ($n = 1, 2, 3$);

$C_1^* = \pi \left(R_1^{(2)} \right)^2 \chi_{33}^* / \alpha$; $C_5^* = \pi \left[\left(R_5^{(6)} \right)^2 - \left(R_5^{(4)} \right)^2 \right] \frac{\chi_{33}^*}{\alpha}$; χ_{33}^* is a dielectric constant for planar mode.

$$\beta_{2n+1} = \frac{2K_{31}^2}{kR_{2n+1}^{(2n+2)} \left[1 - \left(R_{2n+1}^{(2n)} / R_{2n+1}^{(2n+2)} \right)^2 \right] D_0} \left[-M_{4n}^{(2)} J_1(k, R_{2n+1}^{(2n)}, R_{2n+1}^{(2n+2)}) + M_{4n+1}^{(2)} N_1(k, R_{2n+1}^{(2n)}, R_{2n+1}^{(2n+2)}) \right]; \quad (\text{B.4})$$

$$\lambda_{2n+1} = \frac{2K_{31}^2}{kR_{2n+1}^{(2n+2)} \left[1 - \left(R_{2n+1}^{(2n)} / R_{2n+1}^{(2n+2)} \right)^2 \right] D_0} \left[S_{4n} J_1(k, R_{2n+1}^{(2n)}, R_{2n+1}^{(2n+2)}) + S_{4n+1} N_1(k, R_{2n+1}^{(2n)}, R_{2n+1}^{(2n+2)}) \right]; \quad S_{4n} = N_{4n}^{(4,6)} + N_{4n}^{(8,10)} + N_{4n}^{(12,14)}; \quad (\text{B.5})$$

$$S_{4n+1} = N_{4n+1}^{(4,6)} + N_{4n+1}^{(8,10)} + N_{4n+1}^{(12,14)}. \quad (\text{B.6})$$

3D Finite Element Method Simulations on the Influence of Tool Helix Angle in Thin-Wall Milling Process

G. Bolar*

Department of Mechanical & Manufacturing Engineering, Manipal Institute of Technology, Manipal Academy of Higher Education, 576104, Manipal, Karnataka, India

Received 15 JUNE 2021

Accepted 30 JAN 2022

Abstract

In the reported work, a three-dimensional (3D) finite element method (FEM) model was developed to assess the effect of cutter helix angle on milling forces and wall deflection considering thin-wall machining of aluminum 2024-T351 alloy. Johnson-Cook (J-C) constitutive law was employed to model the material flow, whereas the material damage was initiated using the Johnson-Cook damage criterion. Work-tool contact was established using a modified Coulombs friction model. The simulations were carried out for a fixed set of process conditions by varying the helix angle, and the predicted results were experimentally validated. Comparing the milling force and deflection values showed that numerical results augured well with the experimentally measured values. The use of an end mill with a higher helix generated lower force values. Also, a smaller magnitude of wall deflection was noted when 45° and 55° helix tools were used. The experimental investigation into the surface roughness indicated improved shearing action and surface finish when high helix tools were employed.

© 2022 Jordan Journal of Mechanical and Industrial Engineering. All rights reserved

Keywords: Thin-wall machining; helix angle; finite elementsimulation; milling force; deflection; surface roughness.

1. Introduction

The process of machining components having thin sections from a single, monolithic workpiece is known as thin-wall machining. Machining thin-wall parts pose a significant challenge as it requires the maintenance of tight dimensional tolerance, especially in the aerospace and automobile industries. Thin-wall milling is a low productivity process where approximately 90-95 % of the work material is removed during the operation. Moreover, low stiffness often deflects or deforms the thin-wall under machining forces even during CNC milling, where the tool motion is controlled precisely[1]. The in-process deflection under the action of cutting forces results in form error, thereby affecting the accuracy of the machined part.

Research reports on the development of analytical models for cutting force and deflection during thin-wall machining. Ratchev et al. [2] formulated a flexible force model for predicting the thin-wall deflection. A material removal model was included to take care of the changing work geometry and stiffness. Aijun and Zhanqiang [3] analytically predicted the static deformation in thin-wall parts with linear loads as an input. Izamshah et al. [4] developed a prediction methodology for capturing the thin-wall deflection during machining. The model combined the capabilities of statistical analysis and finite element method (FEM). Qi et al. [5] introduced a model for predicting the cutting forces for curved thin-wall milling. The model considered the wall deflection and changing workpiece curvature while predicting the cutting forces. Du et al. [6] suggested a methodology to compensate deflection error by computing milling forces and induced deformation. In the model, cutting force was developed

considering the plowing and shearing mechanisms. Later, ANSYS parametric design language (APDL) was used to predict deformation. Zhou-Long Li et al. [7] computed the surface errors by considering workpiece and tool deflections. Change in the stiffness of the thin-wall was predicted using a stiffness modification method, while the effect of the tool radial run-out was included for chip thickness calculation and hence the cutting force. Similarly, Altintas et al. [8] outlined a virtual compensation model for predicting the deflection errors in flexible blades using ball-end milling process. Arora et al. [9] put forward a mechanistic force model for in-process deflection prediction while considering the axial and radial engagement of the cutter with the workpiece during thin-wall machining. Chen et al. [10] developed a force-deformation coupling relationship for thin-wall milling process. The contact between the work-tool was defined by discretizing the cutting tool into disk elements. The modification to the instantaneous chip thickness resulted in a new force-deformation coupling relationship to obtain the changing contact conditions and material removal mechanism.

Recent literature includes many research articles on FEM-based numerical studies related to milling. Batista et al. [11] demonstrated a FE methodology for simulating the contour machining process in titanium alloy. Ji et al. [12] carried out research on the helical hole milling process. A 3D numerical model to simulate titanium alloy Ti6Al4V hole milling was developed utilizing commercial FE code ABAQUS/Explicit. The material flow was modeled using the Johnson-Cook (J-C) material model, whereas the material failure and chip formation were outlined utilizing the Johnson-Cook damage model. Coulombs friction law was applied for modeling tool-work interface contact. A

* Corresponding author e-mail: gururaj.bolar@manipal.edu.

3D FE model to simulate titanium alloy Ti6Al4V milling was developed. The workpiece was meshed finely at the cutting region to improve the efficiency of the model. The developed model was made up of 383400 C3D8RT type hexahedral elements. The total simulation time was around 180 hrs [13]. Yue et al. [14] proposed a 3D FE model with the objective of optimizing the cutting force and dimensional accuracy considering corner milling of Cr12MoV steel. The model was developed using a commercial tool DEFORM. An adaptive remeshing technique and an iterative algorithm were adopted to ensure convergence of the developed FE model. Simulated results indicated that spindle speed and feed rate influenced the machining process. An investigation into the thermal stress distribution while machining Cr12MoV mold steel of different hardness using FE analysis was conducted. Upon examination, a significant difference in thermal-stress field was noted due to the variation in material hardness in the transitional domain [15]. 3D FE analysis incorporating equivalent homogeneous material (EHM) model was developed to determine the milling forces at different speeds and feed rates for milling SiCp/Al6063/30P composite [16]. Zhang et al. [17] evaluated the machinability of a sinusoidal surface using FE simulation to determine the cutting temperature and study its influence on surface integrity while machining hardened steel. Chien et al. [18] performed FE based simulation for machining Nickel alloy using a ball end mill. Cutting forces and temperatures were measured and experimentally validated in due process. Gao et al. [19] presented a shoulder milling simulation model by coupling Eulerian-Lagrangian FE method. The simulated results were verified experimentally by machining of Al6061-T6 aluminum alloy. The developed model could accurately predict the cutting force and morphology of chips.

Few researchers have worked on FE modeling of machining processes involving thin-walls. Izamshah et al. [20] presented a transient Lagrangian FE model for simulating thin-wall in-process deflection. 3D FE model was proposed by Cui et al. [21] for simulating thin-wall milling process for machining aluminum alloy 7075-T7451. However, an interaction of single flute was considered for simulation. Huang et al. [22] examined the effect of the FE model of the material and machining induced during machining on thin-wall deformation. The material residual stress was noted to contribute to the wall deformation significantly. Lagrangian formulation-based model successfully simulated the effect of constrained thin-walls on deflection [23]. Material flow behavior and chip formation were simulated by incorporating Johnson-Cook (J-C) material and damage model. Moreover, a thermo-mechanical model was used to determine the milling forces, cutting temperature, chip morphology, and wall deflection [24].

Reviewed literature indicates that FE based investigations are focused on the bulk end milling process. Few research articles focusing on numerical simulations of the thin-wall machining process have been reported. However, a study examining the effect of cutter geometry parameters during thin-wall machining has received scant attention. Therefore, the work focuses on developing a realistic FE model to predict and analyze the impact of cutter helix angle on milling force and in-process deflection during thin-wall milling.

2. Methods and Materials

2.1. 3D Finite Element Modelling

The key to successfully simulating the machining process lies in how the model is developed. The development of the 3D FE model involves modeling of work and tool geometry, assignment of process parameters, boundary conditions, and material properties viz. material flow model, material failure model, and work-tool contact model. The temperature generated during the machining process was ignored in the model to ease computation time and memory. The Lagrangian formulation was used to analyze the transient machining problem. In order to account for large deformation and continuously changing contact, a dynamic explicit time integration scheme was adopted.

2.2. Material Constitutive Model and Material Properties

In aircraft, thin-walls are used as load-bearing structures. These are subjugated to complicated loading behavior during the operation. For fail-free functioning, the structures are desired to have proper rigidity and strength [25]. One material which satisfies the requirement is the aluminum alloys [26, 27]. Specifically, aluminum 2024-T351 is usually used since it possesses high strength and good fatigue resistance. Therefore, in the present study, the analysis is performed on commercial aerospace-grade aluminum 2024-T351 used in the construction of thin-walls. As a material, aluminum 2024-T351 is a solution-treated, cold worked and naturally aged material that is stress relieved by cold stretching [28]. The material is exclusively used in the fabrication of aircraft wings, engine baffles, and fuselage structures [29, 30].

Accurate material modeling is the key to precisely predicting the performance parameters in numerical simulations. Therefore, the material flow was denoted using the material constitutive model proposed by Johnson-Cook (J-C). It is used to model the material flow stress and accounts for the influence of plastic strain, strain rate, process temperature [31]. Accordingly, equivalent plastic flow stress is:

$$\bar{\sigma}_{jc} = \left(A + B\bar{\epsilon}^n \right) \left[1 - C \ln \left(\frac{\dot{\epsilon}}{\dot{\epsilon}_0} \right) \right] \left[1 - \left(\frac{T_c - T_{room}}{T_{melt} - T_{room}} \right)^m \right] \quad (1)$$

where $\bar{\epsilon}$ is an equivalent plastic strain, $\dot{\epsilon}$ and $\dot{\epsilon}_0$ are equivalent and reference plastic strain rates, A (MPa) the material yield strength, B (MPa) the hardening modulus, C the strain rate dependency coefficient, n is the strain hardening index, m is the thermal softening index, T_c is the temperature at the cutting zone and T_{room} and T_{melt} are room and melting temperature. According, J-C parameter values for aluminum alloy 2024-T351 and the workpiece properties are tabulated in Table 1 and Table 2, respectively. Solid carbide end mills have been considered in the study. The end mill is modeled as a rigid body since it is stiffer than the workpiece material.

Table 1.J-C material parameters for aluminum alloy 2024-T351 [32].

A (MPa)	B (MPa)	C	n	m
352	440	0.0083	0.42	1

Table 2. Physical properties of workpiece material [32].

Density of material, ρ (kg/m ³)	2700
Elastic modulus, E (GPa)	73
Poisson ratio, ν	0.33
Fracture toughness, K_{Ic} (MPa \sqrt{m})	37
Melt temperature, T_{melt} (°C)	520
Room temperature, T_{room} (°C)	25

2.3. Material Damage Criterion

The function of a cutting tool is to remove material from the work surface in the form of chips. In FE simulations, the material failure and chip separation must be modeled accordingly. The formation of chips in a numerical simulation is modeled using the damage criterion proposed by Johnson and Cook [33]. The damage model considers the influence of strain, strain rate, and temperature. The damage is initiated when equivalent plastic strain (ϵ_f) reaches a critical value and is defined by:

$$\epsilon_f = \left[D_1 + D_2 \exp \left(D_3 \frac{P}{\bar{\sigma}} \right) \right] \left[1 + D_4 \ln \left(\frac{\dot{\epsilon}}{\dot{\epsilon}_0} \right) \right] \left[1 + D_5 \left(\frac{T_c - T_{room}}{T_{melt} - T_{room}} \right) \right] \quad (2)$$

where D_1 - D_5 are damage constants, P is hydrostatic pressure and $\bar{\sigma}$ is Von Mises equivalent stress. Table 3 lists the J-C damage constants.

Table 3.J-C damage parameters for aluminum alloy 2024-T351 [32].

D_1	D_2	D_3	D_4	D_5
0.13	0.13	-1.5	0.011	0

2.4. Cutting Tool and Workpiece Contact Model

Accurate modeling of the work-tool contact is essential since the metal cutting operation is subjected to high temperature, strain, and strain rate values. Also, predicted values of milling forces, cutting temperature, and tool wear depend on the contact friction at the end milling tool and workpiece interface. Workpiece-tool contact friction is expressed using a modified Coulomb friction model in the present work. Contact between the work and the tool contact consists of two regions, namely, sticking and sliding region. Coulomb's law of friction is applicable in the sliding region, and in the sticking region, frictional stress is equated to shear stress. Relationships are expressed as:

$$\tau = k_{chip} \text{ when } \mu\sigma > k_{chip} \text{ (Sticking region)} \quad (3)$$

$$\tau = \mu\sigma \text{ when } \mu\sigma < k_{chip} \text{ (Sliding region)} \quad (4)$$

Accordingly, the value of the co-efficient of friction was considered as 0.17 [34].

2.5. Cutting Tool and Workpiece Modeling

3D geometric model of the workpiece and the cutting tool was established using commercial FE tool ABAQUS/Explicit. The work-tool assembly and initial mesh configuration are shown in Figure 1. End mills with a rake angle of 8°, a diameter of 16 mm, a clearance angle of 15°, and 4 teeth were used. Helix angle was varied, and tools with the helix of 35°, 45°, and 55° were considered in the study. The initial thickness of the wall was 1 mm. The component was meshed using element type C3D8R. The density of mesh was set higher at the work-tool interaction zone. End mills were meshed using R3D4 rigid elements. Employed cutting variables are listed in Table 4.

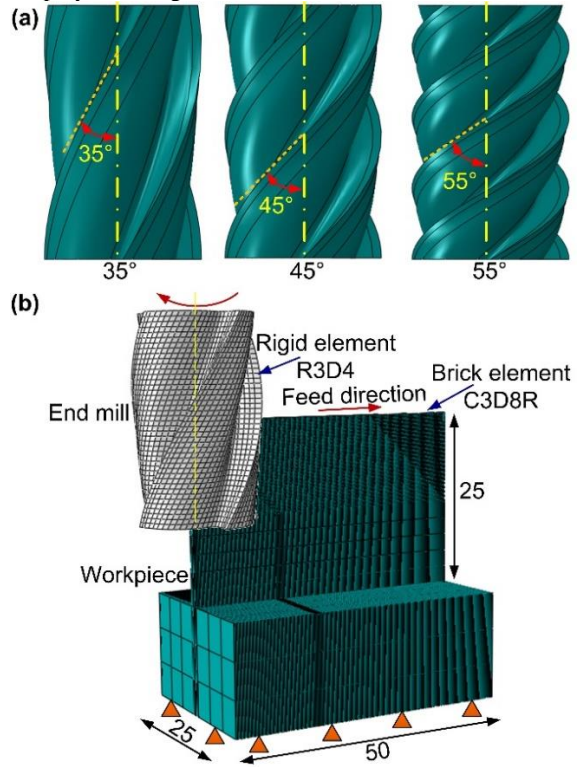


Figure 1. (a) CAD model of cutting tools with different helix angles, (b) Meshed assembly of the tool and workpiece.

Table 4. Process conditions used for simulation.

Spindle speed, n (r/min)	3500
Feed, f_i (mm/tooth)	0.1
Radial cut depth, r_d (mm)	0.3
Axial cut depth, a_d (mm)	12

2.6. Experimental Details

The aluminum workpieces were machined using a three-axis vertical machining center. The 16 mm milling cutter having different helix angles used for the experimental purpose is shown in Figure 2. The workpiece samples were machined to a pre-final dimension, with the wall thickness being 1 mm. The cutting force components were secured using a force dynamometer (Kistler 9272B).

The in-process wall deflection was acquired using a linear variable differential transformer (*Solartron: AX5/S*).

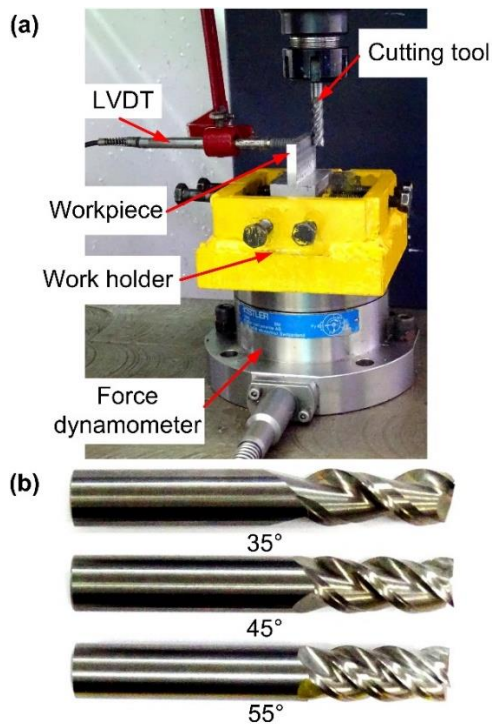


Figure 2. (a) Experimental setup, (b) Cutting tools with different helix angles.

3. Results and Discussion

3.1. Milling Force

Figure 3 shows the comparison of variation in force components F_x (normal) and F_y (feed) for different helix angles. As the values of thrust force component F_z (thrust) was comparatively small, it was neglected in this study. Also, using the experimental setup, the force components were measured and recorded. The predicted force components are represented using solid lines while dotted lines denote the experimentally measured force components. The plots show that the value of force component F_x decreased as the helix angle increased. The predicted mean force F_x when using a 35° helix tool was 82.28 N, whereas, for higher helix tools (45° and 55°), the mean force values were noted to be 66.75 N and 51.1 N, respectively. The variation in the force value is attributed to instantaneous contact points during end milling process [35]. As the number of contact points increases, the volume of work to be machined by each instantaneous cutting edge decreases. This reduces the load on each contact point, reducing the milling force value. The variation in the force component F_y acting along the feed direction was noted to be minimal for the helical angles. Moreover, the predicted and the experimental results for the forces agree well. However, forces predicted by the numerical model were marginally lower than experimental results. Variation is ascribed to assumptions made during the numerical model viz. chatter-free machining, isotropic nature of the work material, tool run-out, etc.[24].

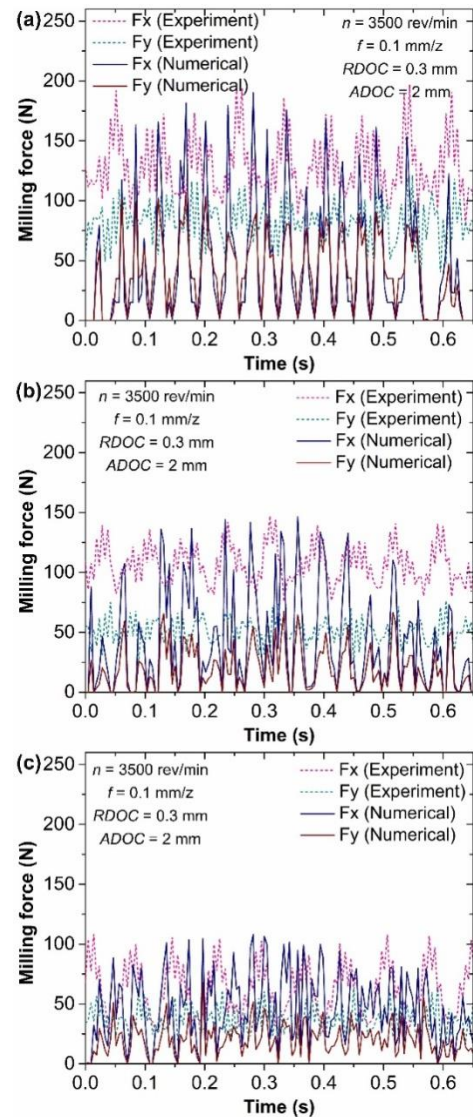


Figure 3. Milling force components vs. helix angle, (a) 35° end mill, (b) 45° end mill, (c) 55° end mill.

3.2. Wall Deflection

In thin-wall machining, in-process deflection results in a loss of form accuracy. Therefore, the in-process deflection was simulated by the developed model. Figure 4 displays the in-process deflection for different helix angles. The deflection magnitude is denoted to decrease with increasing helix angle. The variation is attributed to the normal milling force component (F_x). Higher helix end mill produced lower milling force, resulting in a lower deflection magnitude. Thus end mills with high helix angles are desirable to machine aluminum thin-wall parts with minimum wall deflection. From the plot, it can be seen that the magnitude of deflection obtained experimentally was higher than the values obtained by numerical simulations. The average error between the experimental and numerical values using tools with 35°, 45°, and 55° helix angles was 15%, 16.52%, and 11%, respectively. However, the trends were very well matching.

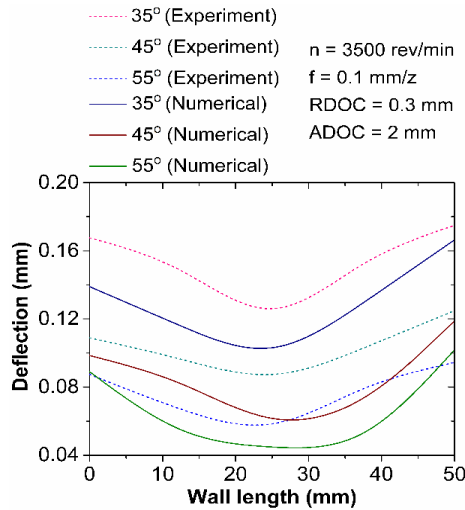


Figure 4. Variation in wall free-end deflection error for different end mill helix angle.

Figure 5 compares form error obtained numerically with the experimental one. Higher in-process deflection during the machining process resulted in a form error. Due to the wall deflection, the material remains uncut (see Figure 6) at the wall free end, producing the wall with a thicker top.

3.3. Formation of Chip and Distribution of Stresses

Figure 7 illustrates the formation of chip and stress distribution during thin-wall milling process. Simulation of chip formation requires fine mesh to provide the desired output, but it increases the simulation time. Therefore, for simulating the chip formation, small portion of the workpiece was finely meshed. The formation of a highly localized primary deformation zone near the tool-workpiece contact region can be noted when the engaging tooth digs into the workpiece. The maximum stress can be observed occurring in the primary deformation zone. Moreover, Figure 7(b-d) gives insight into the post-machining residual stress. As a concluding remark, it can

be said that 3D FEM model is a capable tool for simulating the residual stress and complex chip formation phenomenon.

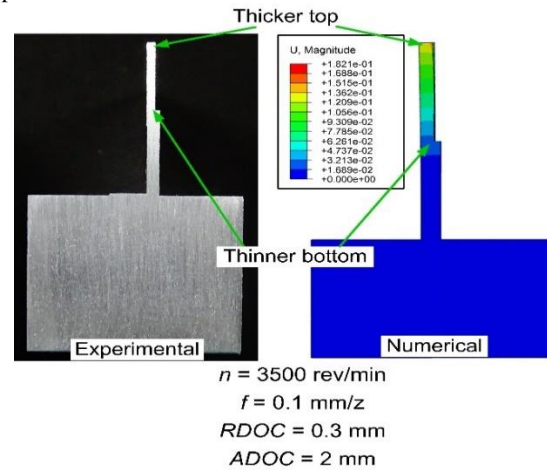


Figure 5. Comparison of form error.

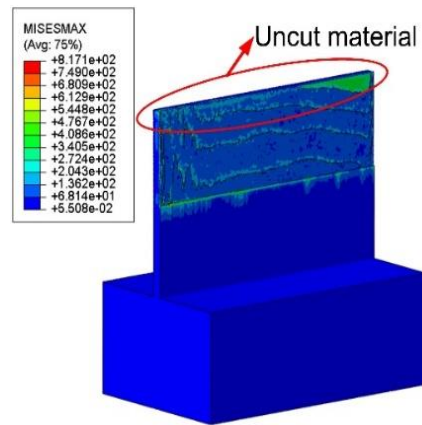


Figure 6. Presence of uncut material after machining.

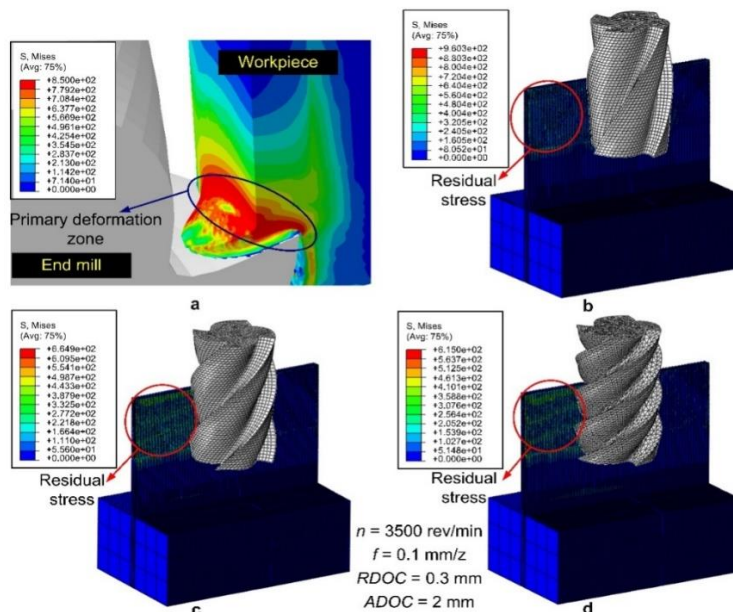


Figure 7. (a) Chip formation and primary deformation zone, (b) Stress developed for 35° tool, (c) Stress developed for 45° tool, (d) Stress developed for 55° tool.

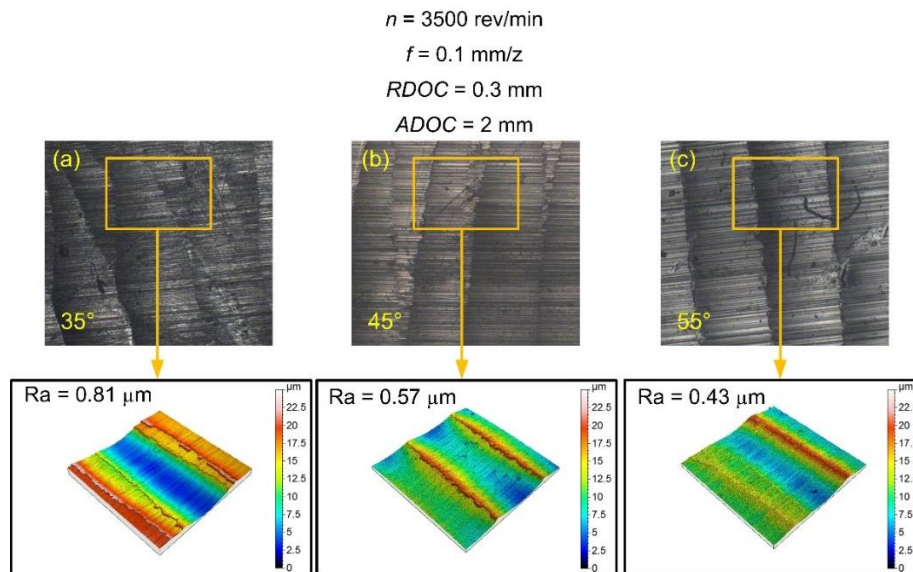


Figure 8. Machined surface topology vs. helix angle (a) 35° helix angle, (b) 45° helix angle, (c) 55° helix angle.

3.4. Experimental Surface Roughness Investigation

The surface of three workpieces experimentally machined using different helix angles was analyzed. Figure 8 displays the topography of surfaces machined using cutters of different helix angles. There was the presence of lay marks on the machined surfaces of all three workpieces, which is typical of the milling operation. The work sample machined with an end mill having a 35° helix angle showed deformed lay marks due to the excessive force developed. An enhancement in the machining surface finish was noted as the tool helix angle increased. Use of end mills having helix angles varying between 45°–55° produced surface with uniform lay marks, which can be attributed to the effective shearing action by the sharp cutting edges.

4. Conclusions

In the presented work, a realistic 3D transient FE model was developed to evaluate the effect of tool helix angle during thin-wall milling. The developed model incorporated material constitutive model, material damage criterion, and contact model to develop a realistic 3D FE simulation for the complex thin-wall milling process. The developed model predicted the milling force components F_x (normal) and F_y (feed). The results clearly show that the helix angle was influencing the normal force component F_x . The magnitude of force component was higher with the use of a cutter with 35°. Moreover, the value of force components predicted using FE model augured well with experimental results. Results also indicate that the helix angle of the end mills influences the wall deflection. Deflection magnitude along the free end of the wall was higher in the case where the 35° helix tool was used. The lower deflection was observed with the use of higher helix cutters (45° and 55°). Using tools with a high helix tool generated a lower force value, resulting in a lower magnitude of wall deflection. The use of end mills having helix angles varying between 45°–55° helped in an effective shearing action, thereby producing a machined

surface with an improved finish. The results confirmed that FE tool is adept in predicting the milling force, wall deflection, and form error. It is also successful in simulating the chip formation phenomenon with the assistance of J-C material and the damage model. The model can be further advanced to include the phenomenon of heat generation and study the influence of tool geometry parameters viz. rake angle and tool diameter of wall deflection and milling force.

References

- [1] M. Farouk, R. Mohamed, S. Fethi, "Development of A New Technique for Modeling and Optimizing Manufacturing Errors for Cn Machine Tools". Jordan Journal of Mechanical & Industrial Engineering, Vol. 14, 2020, 381–386.
- [2] S. Ratchev, W. Huang, S. Liu, A.A. Becker, "Modeling and simulation environment for machining of low-rigidity components". Journal of Materials Processing and Technology, Vol. 153–154, 2004, 67–73.
- [3] T. Aijun, L. Zhanqiang, "Deformations of thin-walled plate due to static end milling force". Journal of Materials Processing and Technology, Vol. 206, 2008, 345–351.
- [4] R. Izamshah, J.P.T. Mo, S. Ding, S. "Hybrid deflection prediction on machining thin-wall monolithic aerospace components". Proceedings of the Institution of Mechanical Engineers, Part B: Journal of Engineering Manufacture, Vol. 226, 2012, 592–605.
- [5] H. Qi, Y. Tian, D. Zhang, "Machining forces prediction for peripheral milling of low-rigidity component with curved geometry". The International Journal of Advanced Manufacturing Technology, Vol. 64, 2013, 1599–1610.
- [6] Z. Du, D. Zhang, H. Hou, S.Y. Liang, S. Y. "Peripheral milling force induced error compensation using analytical force model and APDL deformation calculation". The International Journal of Advanced Manufacturing Technology, Vol. 88, 2017, 3405–3417.
- [7] Z.L. Li, O. Tuysuz, L.M. Zhu, Y. Altintas, "Surface form error prediction in five-axis flank milling of thin-walled parts". International Journal of Machine Tools and Manufacture, Vol. 128, 2018, 21–32.
- [8] Y. Altintas, O. Tuysuz, M. Habibi, Z.L. Li, "Virtual compensation of deflection errors in ball end milling of flexible blades". CIRP Annals, 67, 2018, 365–368.
- [9] N. Arora, A. Agarwal, K.A. Desai, "Modelling of static surface error in end-milling of thin-walled geometries".

- International Journal of Precision Technology, Vol. 8, 2019, 107–123.
- [10] Z. Chen, C. Yue, S.Y. Liang, X. Liu, H. Li, X. Li, “Iterative from error prediction for side-milling of thin-walled parts”. The International Journal of Advanced Manufacturing Technology, Vol. 107, 2020, 4173–4189.
- [11] M. Batista, A. Morales, A. Gómez-Parra, J. Salguero, F.J. Puerta, M. Marcos, “3D-FEM Based Methodology for Analysing Contour Milling Processes of Ti Alloys”. Procedia Engineering, Vol. 132, 2015, 1136–1143.
- [12] C. Ji, Y. Li, X. Qin, Q. Zhao, D. Sun, Y. Jin, “3D FEM simulation of helical milling hole process for titanium alloy Ti-6Al-4V”. The International Journal of Advanced Manufacturing Technology, Vol. 81, 2015, 1733–1742.
- [13] H.B. Wu, S.J. Zhang, “3D FEM simulation of milling process for titanium alloy Ti6Al4V”. The International Journal of Advanced Manufacturing Technology, Vol. 71, 2014, 1319–1326.
- [14] C. Yue, C. Huang, X. Liu, S. Hao, J. Liu, “3D FEM Simulation of Milling Force in Corner Machining Process”. Chinese Journal of Mechanical Engineering. Vol. 30, 2017, 286–293.
- [15] W. Zhang, C. Cheng, X. Du, X. Chen, “Experiment and simulation of milling temperature field on hardened steel die with sinusoidal surface”. International Journal on Interactive Design and Manufacturing. Vol. 12, 2018, 345–353.
- [16] X. Chen, L. Xie, X. Xue, X. Wang, “Research on 3D milling simulation of SiCp/Al composite based on a phenomenological model”. The International Journal of Advanced Manufacturing Technology, Vol. 92, 2017, 2715–2723.
- [17] W. Zhang, F. He, T. Wu, C. Du, H. Liu, “3D numerical simulation on thermal-stress distribution of hardened steels workpiece assembled with different hardness”. International Journal on Interactive Design and Manufacturing, Vol. 11, 2017, 559–568.
- [18] S.E.M. Chien, M.M. Reddy, V.C.C. Lee, D. Sujan, “The Study of Coated Carbide Ball End Milling Tools on Inconel 718 Using Numerical Simulation Analysis to Attain Cutting Force and Temperature Predictive Models at the Cutting Zone”. Materials Science Forum, Vol. 882, 2017, 28–35.
- [19] Y. Gao, J.H. Ko, H.P. Lee, “3D coupled Eulerian-Lagrangian finite element analysis of end milling”. The International Journal of Advanced Manufacturing Technology, Vol. 98, 2018, 849–857.
- [20] R.A. Izamshah, J. Mo, S.L. Ding, “Finite Element Analysis of Machining Thin-Wall Parts”. Key Engineering Materials, Vol. 458, 2010, 283–288.
- [21] K.H. Cui, C.Z. Ren, G. Chen, “Numerical Simulation for Peripheral Milling of Aero-Aluminum Alloy Based on 3D FE Model”. Key Engineering Materials, Vol. 589-590, 2013, 3–7.
- [22] X. Huang, J. Sun, J. Li, “Finite element simulation and experimental investigation on the residual stress-related monolithic component deformation”. The International Journal of Advanced Manufacturing Technology, Vol. 77, 2015, 1035–1041.
- [23] S.N. Joshi, G. Bolar, “Three-Dimensional Finite Element Based Numerical Simulation of Machining of Thin-Wall Components with Varying Wall Constraints”. Journal of The Institution of Engineers (India): Series C, Vol. 98, 2017, 343–352.
- [24] G. Bolar, S.N. Joshi, “Three-dimensional numerical modeling, simulation and experimental validation of milling of a thin-wall component”. Proceedings of the Institution of Mechanical Engineers, Part B: Journal of Engineering Manufacture. Vol. 231, 2017, 792–804.
- [25] P. Bałon, E. Rejman, A. Świątoniowski, B. Kielbasa, R. Smusz, J. Szostak, J. Cieślak, L. Kowalski, “Thin-walled Integral Constructions in Aircraft Industry”. Procedia Manufacturing, Vol. 47, 2020, 498–504.
- [26] N. Gharaibeh, M. AlAjlouni, A. Al-Rousan, “Olive Mill Wastewater as Cutting Fluids: Effect on Surface Roughness of Aluminum”. Jordan Journal of Mechanical & Industrial Engineering, Vol 12, 2018, 161–166.
- [27] Y. Liu, L. He, L., S. Yuan, “Wear Properties of Aluminum Alloy 211z.1 Drilling Tool”. Jordan Journal of Mechanical & Industrial Engineering, Vol. 15, 2021, 59–63.
- [28] A. Gariépy, F. Bridier, M. Hoseini, P. Bocher, C. Perron, M. Lévesque, “Experimental and numerical investigation of material heterogeneity in shot peened aluminium alloy AA2024-T351”. Surface and Coatings Technology, Vol. 219, 2013, 15–30.
- [29] C.A. Rodopoulos, A.T. Kermanidis, E. Statnikov, V. Vityazev, O. Korolkov, “The effect of surface engineering treatments on the fatigue behavior of 2024-T351 aluminum alloy”. Journal of Materials Engineering and Performance, Vol. 16, 2007, 30–34.
- [30] O.S. Zaroog, A. Ali, B.B. Sahari, R. Zahari, “Modeling of residual stress relaxation of fatigue in 2024-T351 aluminium alloy”. International Journal of Fatigue, Vol. 33, 2011, 279–285.
- [31] G.R. Johnson, W.H. Cook, (1983) “A constitutive model and data for materials subjected to large strains, high strain rates, and high temperatures”. Proceedings of the 7th International Symposium on Ballistics, Hague, the Netherlands, 1983.
- [32] T. Mabrouki, F. Girardin, M. Asad, J.F. Rigal, “Numerical and experimental study of dry cutting for an aeronautic aluminium alloy (A2024-T351)”. International Journal of Machine Tools and Manufacture, Vol. 48, 2008, 1187–1197.
- [33] G.R. Johnson, W.H. Cook, “Fracture characteristics of three metals subjected to various strains, strain rates, temperatures and pressures”. Engineering fracture mechanics, Vol. 21, 1985, 31–48.
- [34] M. Madaj, M. Piška, “On the SPH orthogonal cutting simulation of A2024-T351 alloy”. Procedia CIRP, Vol. 8, 2013, 152–157.
- [35] P. Baowan, C. Saikaew, A. Wisitsoraat, “Influence of helix angle on tool performances of TiAlN- and DLC-coated carbide end mills for dry side milling of stainless steel”. The International Journal of Advanced Manufacturing Technology, Vol. 90, 2017, 3085–3097.

Flood Risk Map Using a Multi-Criteria Evaluation and Geographic Information System: Wadi Al-Mafraq Zone

Akram AlSukker^{1,2*}, Marah Al-Saleem¹, Morad Etier¹

¹Department of Industrial Engineering, Faculty of Engineering, The Hashemite University, Jordan

²Risk Management Centre, The Hashemite University, Jordan

Received 29 JULY 2021

Accepted 30 JAN 2022

Abstract

This study aims to explore and identify the flood hazard vulnerability zones in Wadi Al-Mafraq (a Valley located in Jordan) using Geographic Information System (GIS) and Multi-criteria Design Analysis (MCDA). Six factors were taken into consideration to build a flood risk map in the study area. These factors include: distance from main channels, slope, elevation, land use/land cover, rainfall and drainage density. Different weights were assigned to each criterion based on its importance. MCDA was then employed to integrate these criteria to evaluate the study area based on its flood hazard characteristics. The study area was classified into five zones based on potential flood hazard vulnerability. The very-high flood hazard vulnerability represents 4% of the study area while high flood hazard vulnerability represents 9%. Very-low, low, and moderate flood hazard vulnerability represents 43%, 29% and 15%, respectively. It was found that the city center is located in the high and very-high flood hazard vulnerability zone. Results from this study provide a crucial input in disaster management process for local planning authorities. Appropriate decisions can be made based on the produced flood risk map in a timely manner ultimately leading to better disaster management and the protection of residents and properties.

© 2022 Jordan Journal of Mechanical and Industrial Engineering. All rights reserved

Keywords: Geographic Information System; Multi-Criteria Decision Analysis; Flood Risk Management, Flood Hazard Map.

1. Introduction

Flood is considered as the most severe natural disaster in the world during the past decades, resulting in many environmental and socio-economic consequences within the affected flood plain. A flood is an influx of water that overflows land, and can destroy agricultural land, urban areas, and may lead to loss of life. Geographic Information System (GIS), Remote Sensing (RS), and Multi Criteria Decision Analysis (MCDA) are tools used in extracting models for flood threat tracking, risk analysis, and flood risk area recognition. This allows for adequate plan and control of this natural hazard (Youssef et al., 2011; Latu, 2009; Tran et al., 2009).

In 2004, Jordan's National Disaster Response Master Plan (NDRMP) described flash floods as one of the major hazards and potential threats (Farhan and Anaba, 2016). In the past half century, flash flooding incidents in Jordan have claimed the lives of 345 persons and affected 24,321 lives. Additionally, floods usually leave vast agricultural areas covered with mound water. Historical records show that flash floods threatened Petra, Dead Sea and Jordan Valley. This highlights the need for flood control and mitigation measures to protect visitors and the historical monuments (Farhan and Anaba, 2016).

Geographical Information System (GIS) is an organized system consisting of computer hardware and software, along with geographic data and trained staff (Ahn and Chon, 1999). It is designed to handle different data sets for specific geographic areas using the coordinates as the basis for an information system. The main function of a GIS is to input, store, organize,

combine and analyze the ground referenced data and then to integrate these data with data from satellite imagery and other sources (Baban and Al-Ansari, 2001). Additionally, GIS is used to create maps, create 3D views, employ spatial analysis, retrieve data by location, class or attribute and handle visualization. GIS spatial analysis is a rapidly changing area, and GIS packages increasingly provide analytical tools as standard integrated facilities, as optional tool sets, as add-ins or as analysts (De Smith et al., 2007).

Multi-Criteria Decision Analysis (MCDA) is used in a GIS context to combine spatial data layers that reflect the criteria and determine how the layers are combined. In the 1960's, MCDA was designed to help decision-makers incorporate multiple alternatives that reflect the views of the actors involved into a future or retrospective structure. To help spatial decision-making, MCDA is used to incorporate qualitative and quantitative criteria and to define the degree and significance of the relationships between those parameters (Ocampo & Clark 2015; Abdelmoneim 2008; Massam 1988; Malczewski 1999). Decision-making is a systematic process of analysis of complex issues. The strategy is to divide a problem into small parts, analyze and aggregate each part to achieve a meaningful solution. The decision-making process is characterized as a choice of alternatives like GIS (Malczewski, 1999).

GIS applications in hazard mapping and evaluation have been important scientific fields in most world countries since the 1960's. Various GIS-based models were used in flood simulation, including the use of specialized GIS software such as SOBEK (Alkema, 2004a; Alkema, 2004b; Haile and Rientjes, 2005a), HEC-RAS (Rivera et al., 2007; Samarasinghe et al., 2010; Shamaomaet al., 2006), MIKE II, LISFLOOD, One-

* Corresponding author e-mail: akramalsukker@hu.edu.jo.

Dimensional Two-Dimensional (1D2D) hydraulic (Koivumäki et al., 2010) and TUFLOW (Evans, et al., 2007). Topographic maps have been used extensively to delineate the severity of floods (Evans et al., 2007; Forte et al., 2005; Ishaya et al., 2009). The used maps scale ranged from 1:50,000 to 1:250,000. It is popular to apply hydrodynamic physical modeling in flood hazard studies. Popular applications of models requiring many stringent controls (sensitivity analysis, scientist calibration and validation) (e.g., Alkema (2004); Haile and Rientjes (2005a,2005b)). These models require field and data checks, some of these studies use GIS, RS, MCDA in flood risk management and assessment. Studies conducted by Doorga et al. (2022), Msabi & Makonyo (2021), Abu El-Magd et al. (2020), Shafapour et al. (2019), Argaz et al. (2019), and Mundhe (2019), Syed et al. (2017), Rahmati et al. (2016), Danumah et al. (2016) and Franci et al. (2016) highlight the importance of flood profiling and risk management in all regions of the world.

2. Materials and Methods

2.1. Description of Study Area

Jordan is a developing country located off the Mediterranean Sea's South-Eastern coast between 35° and 39° East longitudes and 29° and 33° North latitudes. It is situated in an arid to semi-arid region where about 90% of its land receives an average rainfall of less than 100 mm/year, while only 3% of the land receives an average annual rainfall of 300 mm (Zeyad et al., 2008). The study area is located in the Northern part of Jordan to the west of Mafraq city. The study area selected for this research covers 317.242 km². Several studies were reviewed to obtain a good overall understanding of the study area regarding groundwater, land use and land cover, climate, rainfall, evaporation, temperature, topography, soil, surface hydrology and geology (AL Abbadi and Smadi, 2000; Department of Meteorology, 2015; Allison et al., 1998; Rimawi et al., 1999; Al-Ansari and Baban, 2001; Al-Adamat et al., 2007; Dutton and Shahbaz, 1999; Millington et al., 1999; Salameh et al., 1997; Waddingham, 1994; Allison et al., 2000).

2.2. Data Collection

To describe the study area, several GIS layers were gathered. The major GIS layers used to map spatial data include (a) rainfall, (b) geology, (c) soil, (d) climate and (f) hydrology. The secondary data were collected from various national organizations working in Jordan. Data includes digital maps in addition to integration of physical and socio-economic aspects of the study area.

2.3. Criteria for Flood Hazard Vulnerability Mapping

Criteria identification is useful for determining the degree of significance of topographic variables in flood hazard vulnerability (Malczewski, 1999). After consideration of previous studies assessing the associations between multiple criteria and flood risk, six were selected, namely, rainfall, slope, channels, drainage density, elevation and land use and land cover (Müller et al., 2011;

Mmom and Ayakpo, 2014; Sowmya et al., 2015, Mundhe, 2018). Table 1 summarizes the criteria, weight and rating for flood hazard vulnerability within the study area based on literature review.

In this study, a simple modeling framework was adapted, where the model of a flood hazard vulnerability consists of two components. The first component discusses the upstream hydrology of the watershed, where a hydrological model is built to determine how much runoff is generated during a rainfall event. This will determine the behavior of water coming from the upstream watershed as it enters the main Wadi and downstream towards the city center. The second component deals with the Wadi and flood hazard vulnerability which aims to determine the criteria that affect the flood hazard vulnerability by using MCDA in GIS environment in the study area.

Based on these two combined components, a flood hazard forecasting tool was developed, which can be used to predict many flood-related problems. Insights into the possibility of flooding following runoff produced by rainfall, location and timing of flooding, and the depth of water during flooding may be gained.

Figure 1 shows the methodology of this research which involves: image pre-processing, image classification, data collection and verification, multi-criteria decision analysis. All data that has been collected in this study are processed, analyzed and integrated through GIS and MCDA to create a database of spatial and hydrological data. This database was then utilized in the development and calibration of the flood model to generate flood hazard vulnerability map in the study area.

2.4. Data Analysis

Digital Elevation Models (DEMs) were used to determine drainage networks and outflows of basins. Generating drainage networks from DEMs is dependent on gravity; using the steepest descent, water can flow from higher to lower elevation and no accumulation, evapotranspiration and groundwater depletion are expected. Automated extraction methods are the most effective approaches when the size of the DEM cells is significantly smaller than the dimensions of the watershed. In addition, GIS and remote sensing have been incorporated in the assessment of geo-environmental hazards in recent years.

Data employed in this study include: (1) Shuttle Radar Topography Mission (SRTM) data with a spatial resolution of 30 m, to verify the drainage networks derived from the SRTM; (2) Geological and topographical maps with a working scale of 1:50,000 used to understand the various unit distribution in the study area.

Arc Hydro tools (ArcGIS 10.4.1) were used to establish a framework for obtaining a deeper understanding of the drainage and watershed network in the region under review. Pre-processing of the landscape was used in the processing and development of the study area watershed basin. The DEM derived from SRTM data is used as a pre-processing reference for the terrain. Methods for removing the drainage network from DEM are well documented (Band 1986; Morris and Heerdegen 1988; Tarboton et al. 1991; Ghoneim and El-Baz 2007).

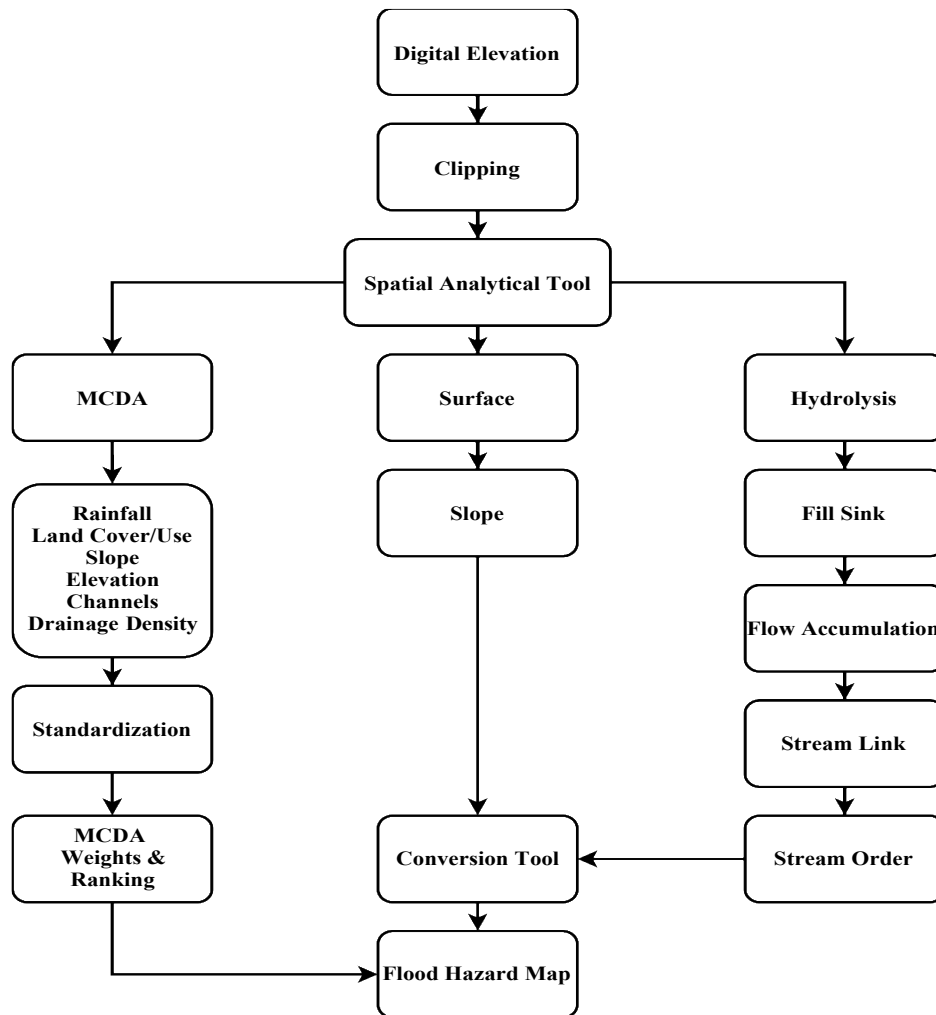


Figure 1. Analysis flowchart.

Table 1. The criteria associated with flood hazard vulnerability and their weights and ratings (Mundhe, 2018).

Criteria	Weight	Rating	
Landuseand Land cover.	31.00	Canal / Rivers and Lakes	4
		Built Up	3
		Agriculture/Scrub/Fallow	2
		Vegetation	1
Distance from Main Channels	24.90	<500	4
		500-1000	3
		1000-1500	2
		>1500	1
Drainage Density	16.68	>15	4
		15-7.5	3
		7.5-2.8	2
		<2.8	1
Rainfall (mm)	14.41	>300	4
		250-200	3
		200-150	2
		<150	1
Elevation	7.71	<560	4
		560-570	3
		570-580	2
		>580	1
Slope	5.14	<1.1	4
		1.1-3.0	3
		3.1-6.0	2
		>6.0	1

The following functions (in sequential order) are involved in Watershed pre-processing adapted from Fairfield and Leymarie (1991): DEM, Fill, Slope, Flow Direction, Flow Accumulation, Stream Link, Stream Order, Snap Power Point, Water Shed, Flood Hazard Vulnerability Map.

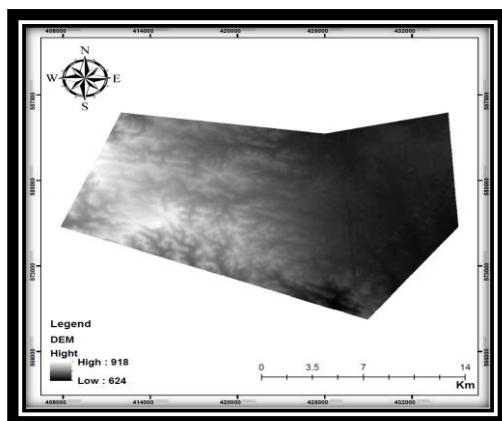
Image pre-processing and classification-in addition to data collection and verification- were processed, analyzed and integrated through GIS and MCDA to create a database of spatial and hydrological data. This database was then utilized in the development and calibration of the flood model to generate flood hazard vulnerability map in the study area.

2.4.1. Surface Hydrology Analysis

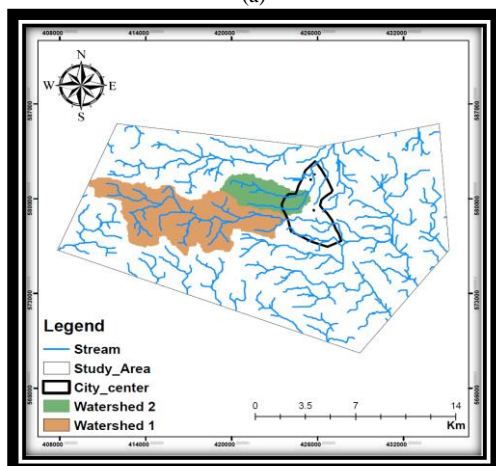
ArcGIS toolbox provided the approach and process needed to build flood simulation models. DEMs, SRTM, spatial analyst tool and management analyst tool on the ArcGIS toolbox were used to provide slope, contour, dimension, watershed etc.

GIS was used to determine the watershed map and runoff computation of the Wadi Al-Mafraq area (Figure 2(b) based on DEM map Figure 2(a)). This was achieved through the following steps:

1. Generate the Sink Fill map from digital elevation map
2. Generate the Slope map of the study area
3. Generate the Aspect map of the study area
4. Generate the Flow Direction map of the study area.
5. Generate the Flow Accumulation map of the study area
6. Generate the Watershed map of the study area.



(a)



(b)

Figure 2. (a) DEM Map; (b) Watershed for main Wadi.

2.4.2. Flood Hazard Vulnerability Mapping

There are two main Wadies (valleys) in the study area selected to calculate each of flow direction, flow accumulation, basin and watershed. The main aim of the surface analysis was to extract the catchment area of two main streams thus determining the amount of water in this basin which may cause flash flooding. The basin for the two Wadies is 53 km² with average rainfall amount of 300mm/year. The amount of water that accumulates in the basin toward the city center is about 15.9*10⁶m³.

Flood hazard vulnerability mapping focused on the six criteria: Distance from Main Channels, Slope, Elevation, Land use/land cover, Rainfall and Drainage density. Spatial maps were constructed and integrated using GIS and MCDA method.

Risk of flash flood hazard is higher in zones close to the Wadi's main channel and decreases moving further away. At the time of flooding, the surrounding area of the Wadies will be more affected. In the study area there are two main Wadies, the direction of these Wadies is coming from the Northwest of study area and converges both streams at the city center. Multiple ring buffers were created based on the distance from the Wadies' channel, then buffers were divided into four classes: high (distance <500m), moderate (distance from 500m to 1000m), low (distance from 1000m to 1500m) and very low (distance >1500m) (Figure 3(a)).

Drainage density is considered as one of the indicators for flash flooding, it is inversely related to permeability. The drainage density indirectly indicates the flood hazard to an area because of its relationship with surface runoff and permeability. The drainage density map was prepared using the line density analysis tool in ArcGIS. Drainage density map of the study area was classified into four categories based on flood hazard i.e.: very low (< 2.8), low (2.8 to 7.4), moderate (7.5 to 15) and high (> 15) and weights assigned them as 1, 2, 3, and 4, respectively (Figure 3(b)).

Rainfall plays a major role in flooding, with areas receiving more rainfall potentially under a greater risk of flash flood hazards than those with low rainfall. Rainfall map was prepared in ArcGIS environment. The rainfall map was classified into four classes: very low rainfall (<150mm), low rainfall (150mm to 200mm), moderate (200mm to 250mm) and high rainfall (>250mm) and weights assigned them as 1, 2, 3, and 4, respectively (Figure 3(c)). Maximum rainfall occurred in the Southwest part of study area.

Water runoff always flows from the high elevated areas to low elevated ones, causing floods to occur in lower areas. Higher elevation is found in Northwest and Southern part of the study area. Elevation mapping was created from DEM using spatial Analyst tool in ArcGIS. Based on flood hazard guideline, elevation map was classified into the four classes: very low elevation (<560m), low (560m to 570m), moderate (570m to 580m) and high elevation (>580m) (Figure 3(d)). Low elevation area was assigned the highest weights and high elevation region assigned the lowest weights.

Water velocity after rainfall is directly related to the angle of the slope over land. The output slope dataset can be calculated in percent or degree of slope (Jensen, 2004). There are four categories of the slope that can be identified and calculated using degree unit. The areas having a slope of < 2° were assigned higher values, and the areas that had a slope between 2-4° were considered as moderate. The areas that had a slope between 4-8°, and more than 8° were

considered as low and very low consecutively (Figure 3(e)).

Land cover and use refer to the natural vegetation, water bodies, rock, soil, or artificial cover due to manmade activities. The Land sat 8 satellite images at a spatial resolution of 30m taken and made available by USGS in July 2019. They were used to collect data about the land use/land cover in the study area. This was made possible using the remotely sensed True Colors Composition (TCC), blue, green and red. All the layers that have been applied were integrated and supervised, and classification for the image was obtained using ArcGIS.

The classified land use and land cover map of the study area was classified based on flood hazard in four categories: urban, agriculture, bare soil and vegetation. The weights are assigned to these criterion as 4, 3, 2, and 1, respectively (Figure 3(f)).

3. Results

The flood models obtained in this study can be used to reconstruct flood events caused by heavy/torrential rains, and in mapping areas that were flooded. If an area previously experienced flooding, it is more likely that it will be flooded again in the near future. Then it is easy to determine which areas are to be avoided should heavy/torrential rains will pour over the area.

The flood hazard vulnerability map was generated by integrating the thematic maps of Channels, Slope, Elevation, Land use/land cover, Rainfall and Drainage density by the MCDA method. There are five class of potential flood hazard vulnerability in the study area. These include very low, low, moderate, high and very high flood hazard vulnerability as shown in Figure (4). The very high flood hazard vulnerability represents 4% of the study area, high flood hazard vulnerability represents 9% of study area. The very low flood hazard vulnerability represents 43% of the study area, the low for flood hazard vulnerability is 29%, and the moderate flood hazard vulnerability represents 15% of study area.

4. Discussion

In this study, the GIS and MCDA were applied to generate a flood hazard vulnerability areas map. Criteria affecting the flood hazard were defined based on literature reviews. MCDA and surface analysis indexes were used to

identify and check the vulnerability of areas for flood hazard in the study area.

DEMs from the Shuttle Radar Topographic Mission (SRTM) was used to generate flood simulation model as an approach and process that was used to create these different models. Using spatial analyst tool and management analyst tool on the Arc toolbox to create each of slope map, aspect map, flow direction, flow accumulation, stream order and watershed.

Research results can be summarized as follow:

1. Slope: it is one of the main criteria that affects the flash flood where, water velocity is directly related to the angle of the slope over land. Areas with a high slope have a greater opportunity for create flash flood than areas with a low slope. The slope classes variations between 0 to 30 degrees, where the slope value that close to 0, is the city center area, this poses a risk of floodwater accumulation in city center.
2. Flow Direction: Creates a flow direction from Fill-DEM, from each cell to its steepest downslope neighbor. The output of the Flow Direction tool is an integer raster whose values range from 1 to 128. Flow Direction is one of the main parameters that affects the flow of flash flood trend.
3. Flow Accumulation: Creates an accumulated flow into each cell from the flow direction map. The flow accumulation result is a raster of accumulated flow to each pixel, as determined by accumulating the weight for all pixel that flow into each downslope cell.
4. Stream Order: Assigns a numeric order to stream a raster representing linear network branches. Stream Order output will be of higher quality if the raster for the input stream and the raster for the input flow direction is generated from the same surface. If the stream raster is extracted from a rasterized stream data set, the output may not be available because the direction will be on a cell-by-cell basis.
5. Watershed: A watershed is the set of cells whose downstream flow path passes through a selected cell (outlet). The main aim of the watershed to extract the catchment area of two main streams thus determining the amount water in this basin which cause of flash flood. The areas of basin for two wadies are 53 km² with average rainfall amount is 300mm/year. The amount of water that accumulation in basin toward the city center is about 15.9Mmc.

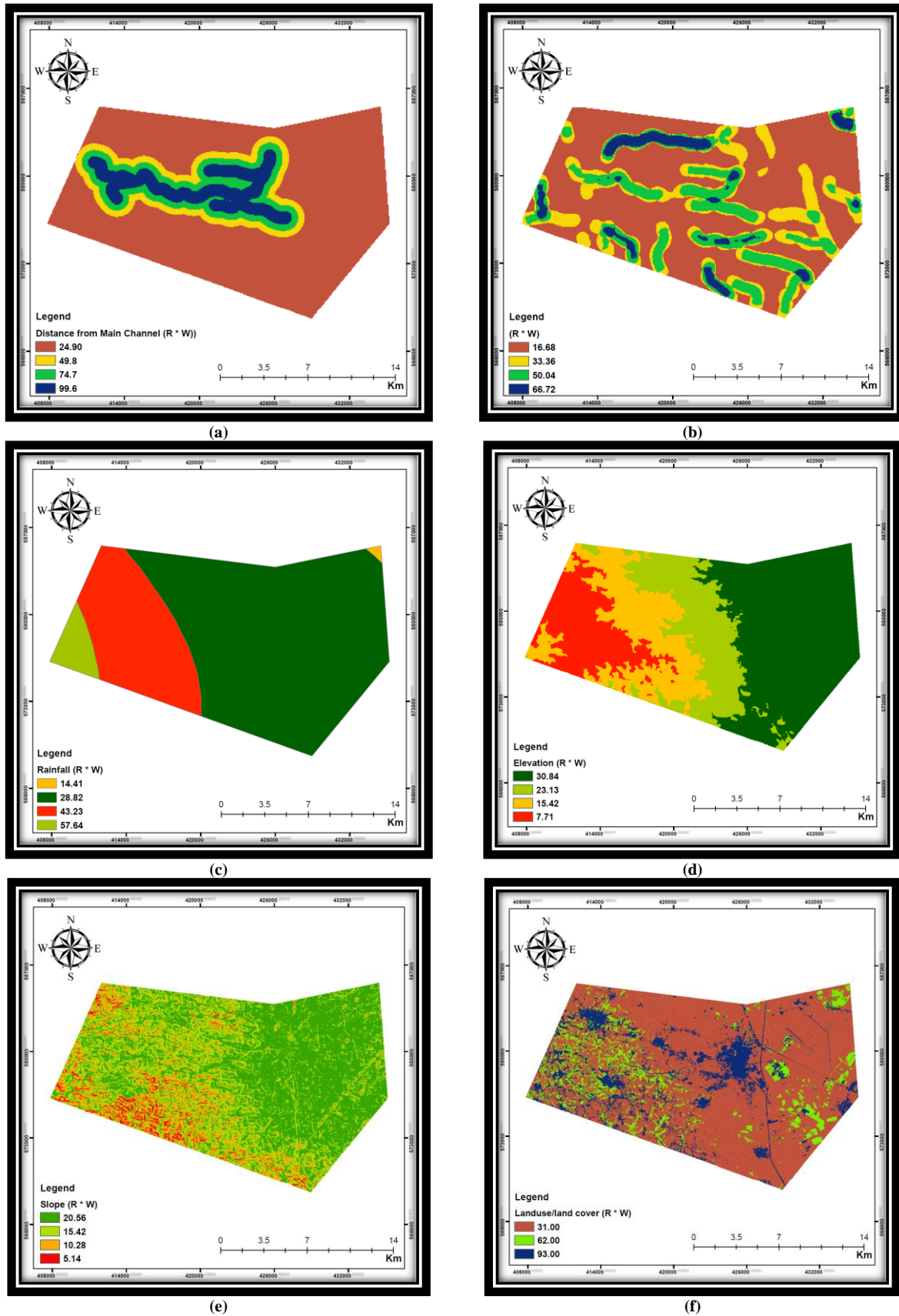


Figure 3. (a) Distance from Main Channels; (b) Drainage Density; (c) Rainfall; (d) Elevations; (e) Slope; (f) Land cover/land use maps.

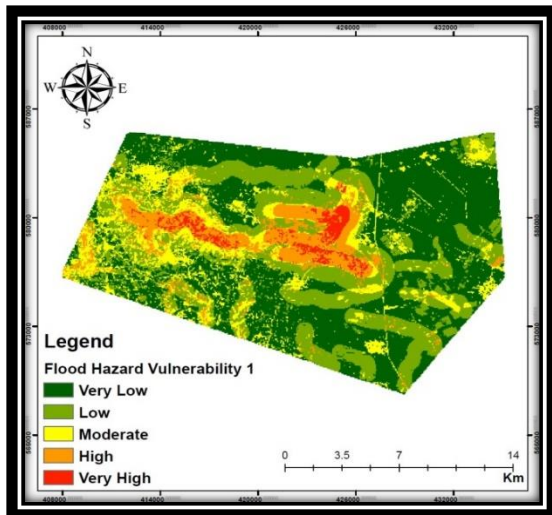


Figure 4. Flood Hazard Vulnerability Map.

4.1. Discussion of flood hazard vulnerability Results

Six thematic maps were added by the GIS and MCDA method. The flood hazard vulnerability map generated by integrating the thematic maps these are: Channels, Slope, Elevation, Land use/land cover, Rainfall and Drainage density. The criteria affecting the flood area and their weights assigned are based on literature reviews.

Based on Figure 3(a), the risk of flash flood hazard is more in zones close to the Wadi's main channel and its decrease the increasing distance. At the time of the flood, firstly the surrounding area of the Wadies is more affected. In the study area there are two main wadies, these wadies are coming from the Northwest, and the confluence of both streams is at City Centre.

Based on Figure 3(b), the drainage density indirectly indicates the flood hazard to an area because of its relationship with surface runoff and permeability. The drainage density map was prepared using the line density analysis tool in ArcGIS. Drainage density map of study area is classified into four categories based on flood hazard i.e.: very low (<2.8), low (2.8 to 7.4), moderate (7.5 to 15) and high (>15) and weights assigned them as 1,2,3, and 4, respectively.

According to Figure 3(c), the rainfall plays a major role in creating a flood situation because it determines the amount of water that falls. The rainfall map is reclassified into four classes: very low rainfall (<150mm), low rainfall (150mm to 200mm), moderate (200mm to 250mm) and high rainfall (>250mm) (Figure 2(d)). Lowest weight 1 assigned to very low rainfall category and highest weight 4 assigned to class of higher rainfall. Maximum rainfall occurs in the Southwest part of study area.

According to Figure 3(d), the Elevation criterion affects the flood situation. water runoff always flows from the high elevated area to low elevated area. Flood situation probably created in lower elevated flat areas compare to a higher elevation. Higher elevation is found in Northwest and Southern part of the study area. On the basis flood hazard guideline, Elevation map is classified into the four classes: high elevation (<560m), moderate (560m to 570m), low (570m to 580m) and very low altitude (>580m). Low elevation area was assigned the highest weights, and high elevation region was assigned the lowest weights.

Based to Figure 3(e), Slope is one of the main factors responsible for flood. Water velocity is directly related to the angle of the slope over land. There are four categories of the slope are identified and calculated as degree unit. The areas having a slope lower than two were assigned higher values and the areas, which had a slope among 2-4%, were considered as moderate. The areas that had a slope more between 4-8 % and more than 8% were considered as low and very low. This is summarized in Table 1, and the map shown in Figure 7.

Based to Figure 3(f), Land cover/land use is an essential factor for flood hazard mapping. Land use refers to man's activities and various uses which are carried on land. The classified land use and land cover map of the study area reclassified based on flood hazard in four categories: (urban, agriculture, bare soil and vegetation). The weights are assigned to these criterion as 4, 3, 2, and 1, respectively.

Based on Figure 4, there are five classes of potential flood hazard vulnerability in the study area. These include very low for flood hazard vulnerability, low for flood hazard vulnerability, moderate for flood hazard vulnerability, high for flood hazard vulnerability and the very high one. The very high flood hazard vulnerability represents 4% of the study area, high flood hazard vulnerability represents 9% of study area. The very low flood hazard vulnerability represents 43% of the study area, the low for flood hazard vulnerability is 29% and the moderate flood hazard vulnerability represents 15% of study area.

4.2. Flood Risk Assessment in Urban Areas Based on flood hazard vulnerability map

In the recent years, flash floods are considered one of the most important destructive natural hazards in Jordan. In the last years, the study area experienced floods with a semi-arid to arid climate and rainfall characterized by falls in the form of high intensity, short duration and irregular storms. Urban development is one of the most important human factors affecting flood occurrence. The flood risk map was created by combining the flood hazard vulnerability map with the land use map (urban map). It was found that the study area (city center) is located within high and very high categories of the possibility of a flood water accumulation. This is a serious indication of the possibility of a flood in any season in the study area. Based on the Figure 5, decision-makers must take all safety measures in the flood management to avoid a disaster by taking some of the recommendations contained in this research.

5. Conclusions

In this study, flood hazard vulnerability areas have been identified using GIS and MCDA methods. At first, a flood inventory map containing flood areas was prepared in the Wadi Al-Mafraq using MCDA, GIS and RS. The surface parameters analysis was used to understand hydrology analysis for study area. These represents of extract each of slope parameter, aspect parameter, flow direction, flow accumulation and watershed. Then, six spatial maps (Destines Channels, Slope, Elevation, Land use/land cover, Rainfall and Drainage density) were derived from the spatial database using MCDA. Using the mentioned conditioning criteria, flood hazard vulnerability

maps were produced from map index calculated using MCDA method, and the results were plotted in ArcGIS.

Results from this research shows that there are five class of potential flood hazard vulnerability in the study area. The very high for flood hazard vulnerability represents 4% and high for flood hazard vulnerability represents 9% of study area. The very low for flood hazard vulnerability represents 43% of the study area, the low for flood hazard vulnerability is 29% and moderately for flood hazard vulnerability represents 15% of study area.

Based on flood Risk Assessment map in Urban Areas, the city center of study area is located in the high and very high for potential flood hazard vulnerability. This will pose a risk to the city's residents from the risk of flooding. Decision makers must take safety measures in disaster management to protect residents and property. These results are helpful for local planning authorities and planners to identify risk areas and make appropriate decisions in good time. The derived flood vulnerability map can provide a valuable tool for assessing flood risk for giving planers to insurance and emergency services.

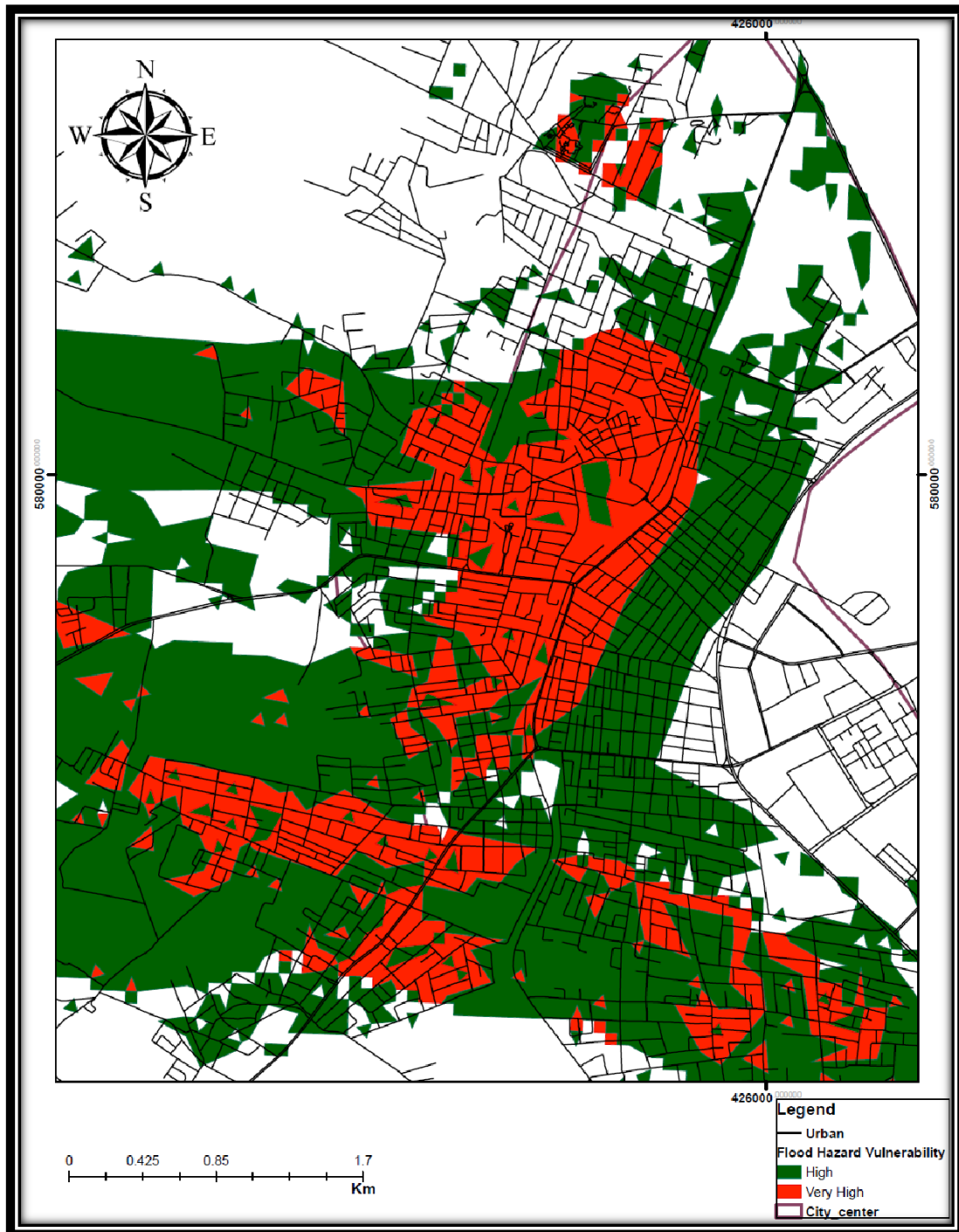


Figure 5. Flood Risk Assessment in Urban Areas.

References

- [1] Abdelmoneim, A. (2008). Fuzzy Genetic Prioritization in Multi-Criteria Decision Problems. *Jordan Journal of Mechanical & Industrial Engineering*, 2(4), 175–182.
- [2] Abu El-Magd, S. A., Amer, R. A., & Embaby, A. (2020). Multi-criteria decision-making for the analysis of flash floods: A case study of Awlad Toq-Sherq, Southeast Sohag, Egypt. *Journal of African Earth Sciences*, 162, 103709.
- [3] Adeoye, N. O., Ayanlade, A., & Babatimehin, O. (2009). Climate change and menace of floods in Nigerian cities: Socio-economic implications. *Advances in Natural and Applied Sciences*, 3(3), 369–377.
- [4] Ahn, H., & Chon, H. (1999). Assessment of groundwater contamination using geographic information systems. *Environmental Geochemistry and Health*, 21(3), 273–289.
- [5] Al Abbadi, K., & Smadi, S. A. (2000). Genital abnormalities and groin hernias in elementary-school children in Aqaba: An epidemiological study. *Eastern Mediterranean Health Journal*, 6(2–3), 293–298.
- [6] Al-Adamat, R., Rawajfih, Z., Easter, M., Paustian, K., Coleman, K., Milne, E., Falloon, P., Powlson, D. S., & Batjes, N. H. (2007). Predicted soil organic carbon stocks and changes in Jordan between 2000 and 2030 made using the GEFSOC Modelling System. *Agriculture, Ecosystems & Environment*, 122(1), 35–45.
- [7] Al-Amoush, H., Al-Shabeeb, A. R., Al-Adamat, R., Al-Fugara, A., Al Ayyash, S., Shdeifat, A., Al-Tarazi, E., & Abu Rajab, J. (2017). The Use of GIS Techniques and Geophysical Investigation for Flood Management at Wadi Al-Mafraq Catchment Area. *Journal of Earth and Environmental Sciences*, 8(2), 97–103.
- [8] Alkema, D. (2004). RS and GIS applications in flood forecasting. *Proceedings of the National Workshop on Flood Disaster Management : Space Inputs, India*, 57–59.
- [9] Allison, R. J., Grove, J. R., Higgitt, D. L., Kirk, A. J., Rosser, N. J., & Warburton, J. (2000). Geomorphology of the eastern Badia basalt plateau, Jordan. *The Geographical Journal*, 166(4), 352–370.
- [10] Allison, R., Higgitt, D., Kirk, A., Whrburton, J., Al-Homoud, A., Sunna, B., & White, I. (1998). *Geology, Geomorphology, Hydrology, Groundwater and Physical Resources*. In *Arid Land Resources & Their Mana* (1st ed., pp. 21–46).
- [11] Argaz, A., Ouahman, B., Darkaoui, A., Hassna, B., Ayouch, E., & Lazaar, R. (2019). Flood Hazard Mapping Using remote sensing and GIS Tools: A case study of Souss Watershed. *Journal of Materials and Sciences*, 10(2), 411–421.
- [12] Authority of Aqaba Special Economic Zone. (2010). *Disaster risk management profile for Aqaba special economic zone*. Aqaba Special Economic Zone Authority.
- [13] Baban, S., & Al-Ansari, N. (2001). A Research Agenda to Minimise Environmental Degradation in the Badia Region, Using Remote Sensing and GIS. In *Living with water scarcity: Water resources in Jordan Badia Region, the way forward* (pp. 136–158). Al Al- Bayt University, Jordan.
- [14] Band, L. E. (1986). Topographic Partition of Watersheds with Digital Elevation Models. *Water Resources Research*, 22(1), 15–24.
- [15] Danumah, J. H., Odai, S. N., Saley, B. M., Szarzynski, J., Thiel, M., Kwaku, A., Kouame, F. K., & Akpa, L. Y. (2016). Flood risk assessment and mapping in Abidjan district using multi-criteria analysis (AHP) model and geoinformation techniques, (cote d'ivoire). *Geoenvironmental Disasters*, 3(1), 10.
- [16] De Smith, M. J., Goodchild, M. F., & Longley, P. A. (2007). *Geospatial Analysis: A Comprehensive Guide to Principles, Techniques and Software Tools* (2nd edition). Troubador Publishing Ltd.
- [17] Doorga, J. R. S., Magerl, L., Bunwaree, P., Zhao, J., Watkins, S., Staub, C. G., Rughooputh, S. D. D. V., Cunden, T. S. M., Lollchund, R., & Boojhawon, R. (2022). GIS-based multi-criteria modelling of flood risk susceptibility in Port Louis, Mauritius: Towards resilient flood management. *International Journal of Disaster Risk Reduction*, 67, 102683.
- [18] Dutton, R., & Shahbaz, M. (1999). The Badia programme: Defining and overcoming constraints on sustainable development. *Applied Geography*, 19(4), 275–281.
- [19] Evans, S., Gunn, N., & Williams, D. (2007). *Use of GIS in Flood Risk Mapping*. National hydrology seminar, Tullamore, Ireland.
- [20] Fairfield, J., & Leymarie, P. (1991). Drainage networks from grid digital elevation models. *Water Resources Research*, 27(5), 709–717.
- [21] Farhan, Y., & Anaba, O. (2016). Flash Flood Risk Estimation of Wadi Yutum (Southern Jordan) Watershed Using GIS Based Morphometric Analysis and Remote Sensing Techniques. *Open Journal of Modern Hydrology*, 6(2), 720–726.
- [22] Forte, F., Pennetta, L., & Strobl, R. O. (2005). Historic records and GIS applications for flood risk analysis in the Salento peninsula (southern Italy). *Natural Hazards and Earth System Science*, 5(6), 833–844.
- [23] Franci, F., Bitelli, G., Mandanici, E., Hadjimitsis, D., & Agapiou, A. (2016). Satellite remote sensing and GIS-based multi-criteria analysis for flood hazard mapping. *Natural Hazards*, 83(1), 31–51.
- [24] Ghoneim, E., & El-Baz, F. (2007). The application of radar topographic data to mapping of a mega-paleodrainage in the Eastern Sahara. *Journal of Arid Environments*, 69(4), 658–675.
- [25] Haile, A. T., & Rientjes, T. H. M. (2005). Effects of LIDAR DEM resolution in flood modelling: A model sensitivity study for the city of Tegucigalpa, Honduras. *ISPRS WG III/3, III/4, V/3 Workshop "Laser Scanning 2005"*, Enschede, Netherlands, 168–173.
- [26] Heywood, S. C. and S. C. I. (2006). *An Introduction to Geographical Information Systems* (3rd ed.). Prentice Hall.
- [27] Ishaya, S., Ifatimehin, O. O., & Abaje, I. B. (2009). Mapping flood vulnerable areas in a developing urban centre of Nigeria. *Journal of Sustainable Development in Africa*, 11(4), 180–194.
- [28] Koivumäki, L., Alho, P., Lotsari, E., Käyhkö, J., Saari, A., & Hyypä, H. (2010). Uncertainties in flood risk mapping: A case study on estimating building damages for a river flood in Finland. *Journal of Flood Risk Management*, 3(2), 166–183.
- [29] Latu, S. (2009). Sustainable Development: The Role of GIS and Visualisation. *The Electronic Journal of Information Systems in Developing Countries*, 38(5), 1–17.
- [30] Malczewski, J. (1996). A GIS-based approach to multiple criteria group decision-making. *International Journal of Geographical Information Systems*, 10(8), 955–971.
- [31] Malczewski, J. (1999). *GIS and Multicriteria Decision Analysis*. John Wiley and Sons.
- [32] Massam, B. H. (1988). Multi-Criteria Decision Making (MCDM) techniques in planning. *Progress in Planning*, 30, 1–84.
- [33] Millington, A., Al-Hussein, S., & Dutton, R. (1999). Population dynamics, socioeconomic change and land colonization in northern Jordan, with special reference to the Badia Research and Development Project area. *Applied Geography*, 19(4), 363–384.
- [34] Mmom, P., & Akpi, A. (2014). Spatial analysis of flood vulnerability levels in Sagbama Local Government Area using geographic information systems (GIS). *International Journal of Research in Environmental Studies*, 1, 1–8.

- [35] Morris, D. G., & Heerdegen, R. G. (1988). Automatically derived catchment boundaries and channel networks and their hydrological applications. *Geomorphology*, 1(2), 131–141.
- [36] Müller, A., Reiter, J., & Weiland, U. (2011). Assessment of urban vulnerability towards floods using an indicator-based approach—A case study for Santiago de Chile. *Natural Hazards and Earth System Sciences*, 11(8), 2107–2123.
- [37] Mundhe, N. (2019). Multi-Criteria Decision Making for Vulnerability Mapping of Flood Hazard: A Case Study of Pune City. *Journal of Geographical Studies*, 2(1), 41–52.
- [38] Msabi, M. M., & Makonyo, M. (2021). Flood susceptibility mapping using GIS and multi-criteria decision analysis: A case of Dodoma region, central Tanzania. *Remote Sensing Applications: Society and Environment*, 21, 100445.
- [39] Nortcliff, S., Carr, G., Potter, R., & Darmame, K. (n.d.). Jordan's water resources: Challenges for the future (Geographical Paper No. 185; pp. 1–24).
- [40] Ocampo, L., & Clark, E. (2015). A Sustainable Manufacturing Strategy Decision Framework in the Context of Multi-Criteria Decision-Making. *Jordan Journal of Mechanical & Industrial Engineering*, 9(3), 177–186.
- [41] Rahmati, O., Haghizadeh, A., & Stefanidis, S. (2016). Assessing the Accuracy of GIS-Based Analytical Hierarchy Process for Watershed Prioritization; Gorganrood River Basin, Iran. *Water Resources Management*, 30(3), 1131–1150.
- [42] Rivera, S., Hernandez, A., Ramsey, R., Suarez, G., & Rodriguez, S. A. (2007). Predicting flood hazard areas: A SWAT and HEC-RAS simulations conducted in aguan river basin of honduras, central America. *ASPRS*, Tampa, Florida, 594–603.
- [43] Salameh, E., Al-Ansari, N., & Al-Nsoor, I. (1997). Water and environment in the area East of Mafraq and their developmental potentials (No. 1). Strategic environment and water resources unit, AL Al-Bayt University, Jordan.
- [44] Samarasinghe, S. M. J. S., Nandalal, H., Weliwitiya, D. P., Fowze, J. s., Hazarika, M., & Samarakoon, L. (2010). Application of remote sensing and gis for flood risk analysis: A case study at Kalu-Ganga River, Sri Lanka. *International Archives of the Photogrammetry, Remote Sensing and Spatial Information Sciences - ISPRS Archives*, 38, 110–115.
- [45] Shafapour Tehrany, M., Kumar, L., Neamah Jebur, M., & Shabani, F. (2019). Evaluating the application of the statistical index method in flood susceptibility mapping and its comparison with frequency ratio and logistic regression methods. *Geomatics, Natural Hazards and Risk*, 10(1), 79–101.
- [46] Shamaoma, H., Kerle, N., & Alkema, D. (2006). Extraction of flood-modelling related base-data from multi-source remote sensing imagery. *SPRS mid-term symposium 2006 remote sensing: from pixels to processes*, Enschede, Netherlands.
- [47] Sowmya, K., John, C. M., & Shrivasthava, N. K. (2015). Urban flood vulnerability zoning of Cochin City, southwest coast of India, using remote sensing and GIS. *Natural Hazards*, 75(2), 1271–1286.
- [48] Syed, N. H., Rehman, A. A., Hussain, D., Ishaq, S., & Khan, A. A. (2017). Morphometric analysis to prioritize sub-watershed for flood risk assessment in Central Karakoram National Park using GIS/RS approach. *ISPRS Annals of Photogrammetry, Remote Sensing and Spatial Information Sciences*, IV-4/W4, 367–371.
- [49] Tarboton, D. G., Bras, R. L., & Rodriguez-Iturbe, I. (1991). On the extraction of channel networks from digital elevation data. *Hydrological Processes*, 5(1), 81–100.
- [50] Tran, P., Shaw, R., Chantry, G., & Norton, J. (2009). GIS and local knowledge in disaster management: A case study of flood risk mapping in Viet Nam. *Disasters*, 33(1), 152–169.
- [51] Waddingham, J. (1994). Water demand in the north-east Badia, Jordan [Unpublished MSc Thesis]. University of Newcastle Upon Tyne, UK.
- [52] Youssef, A. M., Pradhan, B., & Hassan, A. M. (2011). Flash flood risk estimation along the St. Katherine road, southern Sinai, Egypt using GIS based morphometry and satellite imagery. *Environmental Earth Sciences*, 62(3), 611–623.

Optimal Response of a Quarter Car Vehicle Model with Optimal Skyhook Damper Based on Preview Control

L.V.V. Gopala Rao^{a*}, Rakesh Chandmal Sharma^b, V.S.V. Satyanarayana^a

^aVignana's Institute of Information Technology, Duvvada, Visakhapatnam, India

^bMaharishi Markandeshwar (Deemed to be University) Mullana Ambala

Received 4 JUNE 2020

Accepted 3 FEB 2022

Abstract

In this paper, a two degree of freedom(dof) quarter car vehicle model with skyhook damper passing through a rough road is considered. The skyhook damper control parameters namely the spring constant and the damping coefficient which determine the optimal performance of the skyhook damper. The optimal parameters of the skyhook damper are obtained by equating the control force of LQR with preview stochastic optimal control to that of skyhook damper. The parameters of the skyhook damper suspension are optimized to improve the vehicle performance to the level of active suspension system with preview control given by a performance index which is a weighted integral of the mean square acceleration, road holding, suspension stroke and control force.

© 2022 Jordan Journal of Mechanical and Industrial Engineering. All rights reserved

Keywords: Active suspension, Preview control, Optimization, Quarter car, Random road.

1. Introduction

Road induced excitation is the major source of vibration of an automobile which causes the discomfort to the occupants. Researchers have been working to achieve a better ride comfort for the passengers (1-3). Mostafizur Rahman Md and Arafat Rahman (4) applied potential energy theorem to design a driver seat suspension for improving the ride comfort. They added a double negative suspension spring to the suspension system and obtained a significant reduction of seat suspension magnitude. The active suspension system enhances vehicle performance by generating control force through an actuator to counteract road stimulation. Semi-active systems are being developed in view of overcoming the limitations, like low robust, time lag and high cost, associated with the active systems. In this context, Crosby and Karnopp[5] introduced the concept of skyhook damper based semi active suspensions. The sky-hook logic is based on an ideal design of a passive damper connected between the suspension mass and a notional point fixed in the sky. In the case of a passive suspension of a spring and damper in parallel between the sprung mass and the un-sprung mass corresponding to a two degree of freedom vehicle model, or between the sprung mass and the wheel corresponding to a single degree of freedom vehicle model increases the passive damping ratio that leads to a harsher ride. Karnopp et al.,[6] used the skyhook concept in a moving vehicle and compared the performance of skyhook damper with conventional passive suspension system. In subsequent years, many authors have done research work in the area of skyhook damper design, but the performance of skyhook damper depends on the damper parameters. Sammier et al.,[7] used the skyhook damper type suspension to improve the road holding and ride comfort of vehicle model. Hamrouni et al.,[8] compared the

performance of skyhook controller with the performance of CRONE Controller and simulation results and showed better performance compared to the skyhook controller. In the design of skyhook damper, selection of damper parameter values are important to enhance the performance of skyhook damper suspension system.

Different optimization methods have been developed to improve the vehicle suspension performance and applied to quarter car, half car and full car vehicle models. Vladimir and Marian[9] optimized the half car model suspension parameters, such as the spring stiffness and damping coefficients using Genetic Algorithm optimization method. Quantum- behaved particle Swarm optimization method has been used by Lee and Cheng[10] to optimize the 14-dof nonlinear railway suspension parameters. Xu et al.,[11] used Artificial Fish Swarm Algorithm to optimize the hydro pneumatic and Mechanical Elastic Wheel suspension of quarter car vehicle model and results shown the improvement of vehicle ride comfort. Mustafa et al.,[12] introduced a new model-free fuzzy logic controller based on particle swarm optimization (PSO-MFFLC) for the nonlinear active suspension systems and compared the performance of PSO-MFFLC with the time-delay estimation control, intelligent PID and classical PID. Rajagopal and Ponnusamy[13] improved the performance of active vehicle suspension system using the hybrid DEBBO algorithm by tuning the parameters of PID controller.

Even the LQR control gives satisfactory performance, it can be further improved using preview control. In addition to the potential improvements in performance, preview control requires lower power, reduced requirements for internal sensors, and simplified feed back control structure. The objective of the preview control in

* Corresponding author e-mail: lvgrao@gmail.com.

the vehicle suspension system is to get the oncoming road undulations information, and to use this measured information in the active control strategy. Preview control is based on the feedback force that depends on system state, and it also includes feed forward force that requires the information of the road ahead of the vehicle. The performance of *rms* stroke and *rms* road holding improve with increasing preview distance up to a particular distance. The preview time depends on vehicle velocity and preview distance. As the velocity of the vehicle increases the preview distance is covered in quick time.

Vehicle suspension with active elements can give better results in case of ride comfort. But design and maintenance costs are more compared to those used in passive suspension elements like spring and viscous damper. Optimization of the parameters of the vehicle passive suspension and skyhook damper for all road conditions and speeds is a difficult task. So far many researchers have optimized vehicle suspension parameters for a particular speed for better performance. These optimal suspension parameters may not give uniformly better performance at all speeds.

In this work, the steady state random response control of a quarter vehicle model moving on a uneven road is considered. The parameters of the skyhook damper are obtained in an optimal way by equating the control forces of skyhook damper and the optimal preview control in a statistical sense and minimizing the square root of the sum of mean square difference between the relevant control responses of the LQR - preview and skyhook damper.

2. Problem Formulation

2.1. Mathematical modeling

In this section, an active suspension quarter car model with LQR control is presented. The road input information is assumed to be available by measurement at a preview distance of "L" in front of the vehicle. The direct calculation of the optimal control force for LQR model with preview is presented. The model is stated as the LQR model without preview when the preview distance is taken as zero.

Equations of motion of quarter car model with preview control shown in Figure 3 are,

$$m_1 \ddot{y}_1 + k_1(y_1 - y_2) - U = 0 \tag{1}$$

$$m_2 \ddot{y}_2 + k_1(y_2 - y_1) + k_2(y_2 - h) + U = 0, \tag{2}$$

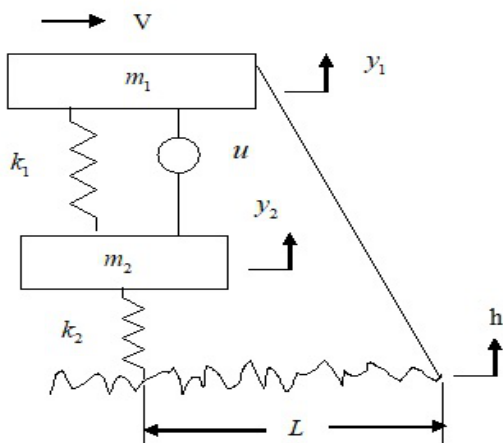


Figure 1. Quarter-car with preview suspension

where m_1 and m_2 are sprung and unsprung masses, k_1 and k_2 are the stiffnesses of the primary suspension and the tyre respectively, h is the random road input and U is the control force. The random road is approximated as Power spectral density of the is given as [14],

$$S_h(\omega) = \frac{\sigma^2}{\pi} \frac{\alpha_r V}{(\omega^2 + (\alpha_r V)^2)^2} \tag{3}$$

where σ^2 is variance of the road undulations, V is forward velocity and α_r is road surface coefficient. The random road profile equation [15] is given by

$$\dot{h}(t) + \alpha_r V h(t) = w(t), \tag{4}$$

where $w(t)$ is a Gaussian white noise,

$$E[w(t)w^T(t + \tau)] = 2\sigma^2 V \alpha_r \delta(\tau),$$

where system state variables are, $x_1 = y_1, x_2 = \dot{y}_1, x_3 = y_2, x_4 = \dot{y}_2, x_5 = h$ and equations (1), (2) and (4) are written as,

$$\dot{x} = Fx + gU(t) + dw(t), \tag{5}$$

U, F, x, g, d are control force vector, system matrix, state vector, control distribution vector and excitation distribution vector respectively.

$$F = \begin{bmatrix} 0 & 1 & 0 & 0 & 0 \\ -\frac{k_1}{m_1} & 0 & \frac{k_1}{m_1} & 0 & 0 \\ 0 & 0 & 0 & 1 & 0 \\ \frac{k_1}{m_2} & 0 & -\frac{k_1+k_2}{m_2} & \frac{k_2}{m_2} & 0 \\ 0 & 0 & 0 & 0 & -\alpha_r V \end{bmatrix}; \quad g = \begin{bmatrix} 0 \\ 0 \\ 0 \\ 0 \\ 1 \end{bmatrix}; \quad d = \begin{bmatrix} 0 \\ 0 \\ 0 \\ 0 \\ 1 \end{bmatrix} \tag{6}$$

2.2. Performance Criterion

The optimal suspension is designed based on stochastic optimal control.

The overall performance index,

$$J = \rho_1 J_1 + \rho_2 J_2 + \rho_3 J_3 + \rho_4 J_4, \tag{7}$$

where $J_1 = E[\dot{y}_1^2]$; $J_2 = E[(y_1 - y_2)^2]$; $J_3 = E[(y_2 - h)^2]$; $J_4 = E[U^2]$ where $E[.]$ denotes expectation operator. ρ_1, ρ_2, ρ_3 and ρ_4 being the weighting factors. Equation (7) can be written as

$$J = E \left[[x(t)^T \quad U(t)^T] \begin{bmatrix} A & n \\ n^T & B \end{bmatrix} \begin{bmatrix} x(t) \\ U(t) \end{bmatrix} \right], \tag{8}$$

where A and B are positive semi definite and definite matrices respectively, and are given by

$$A = \begin{bmatrix} \frac{\rho_1 k_1^2}{m_1^2} + \rho_2 & 0 & -\frac{\rho_1 k_1^2}{m_1^2} - \rho_2 & 0 & 0 \\ 0 & 0 & 0 & 0 & 0 \\ -\frac{\rho_1 k_1^2}{m_1^2} - \rho_2 & 0 & \frac{\rho_1 k_1^2}{m_1^2} + \rho_2 + \rho_3 & 0 & -\rho_3 \\ 0 & 0 & 0 & 0 & 0 \\ 0 & 0 & -\rho_3 & 0 & \rho_3 \end{bmatrix};$$

$$n = \begin{bmatrix} \frac{\rho_1 k_1}{m_1^2} \\ 0 \\ \frac{\rho_1 k_1}{m_1^2} \\ 0 \\ 0 \end{bmatrix}; \quad B = \begin{bmatrix} \rho_1 \\ \rho_1 + \rho_4 \end{bmatrix}$$

The optimal control force is,

$$u(t) = -c_1(t)x(t) + c_2r(t), \tag{9}$$

where $c_1(t) = B^{-1}[n^T(t) + g^T S(t)]$, $c_2 = B^{-1}g^T$ are feed back and feed forward control gain vectors respectively, and S matrix can be solved using the following equation,

$$SF_N + F_N^T S - SgB^{-1}g^T S + A_N = 0 \tag{10}$$

and $r(t)$ is given by

$$r(t) = \int_0^{t_p} \exp[F_G^T \sigma] S d w(t + \sigma) d \sigma, \tag{11}$$

where $A_N = A - nB^{-1}n^T$; $F_N = F - gB^{-1}n^T$ and $F_G = F - gB^{-1}(n^T + g^T S)$.

Substituting equation (9) in equation (5) yields

$$\dot{x} = F_G x + g c_2 + d w(t). \tag{12}$$

The response of system described by covariance matrix as $P(t) = E[x x^T]$ which is obtained by solving the below Liapunov equation.

$$[F - g c_1] P(t) + P(t) [F - g c_1]^T + g c_2 E[r(t) x^T(t)] + E[x(t) r^T(t)] (g c_2)^T + d E[w(t) x^T(t)] + E[x^T w^T(t)] d^T = 0 \tag{13}$$

where

$$E[x(t) r^T(t)] = P_1 + P_2 \tag{14}$$

P_1 and P_2 can be obtained as,

$$P_1 = \int_0^{t_p} \int_0^{t_p} \phi(t, t - (\sigma - \sigma_1)) g c_2 \exp[F_G \sigma] S d \left(\frac{Q}{2}\right) d^T S \exp[F_G^T \sigma_1] d \sigma d \sigma_1; \sigma \geq \sigma_1 \tag{15}$$

otherwise $P_1 = 0$; for $\sigma < \sigma_1$

$$P_2 = \int_0^p \phi(t, t + \sigma) d(Q/2) d^T S^T \exp[F_G^T \sigma]^T d \sigma \tag{16}$$

and

$$E[x(t) w^T(t)] = d(Q/2) + \int_0^{t_p} \phi(t, t - \sigma) g c_2 \exp[F_G^T \sigma] S d(Q/2) d \sigma. \tag{17}$$

By substituting equation (14) and equation (17) in equation (13), we get $P(t)$ which is the response of system. Since the steady state closed loop system matrix F_g is stable, F_g^T is also stable and the exponential function in equation (11) also decreases with time. Hence the effect of knowledge of the future inputs on $r(t)$ will diminish with time and the knowledge of inputs from the distant future will not effect on the system performance. This concept is first observed by Tomizuka[16] and later by Hac [17].

3. Skyhook control

3.1. Quarter car model-skyhook damper

Passive suspension systems are restricted to generate forces in response to local relative motions, that is, between attachment points of contiguous bodies. In this section, a sky hook damper control quarter car model (Figure. 2) is presented. The equations of motion are given by

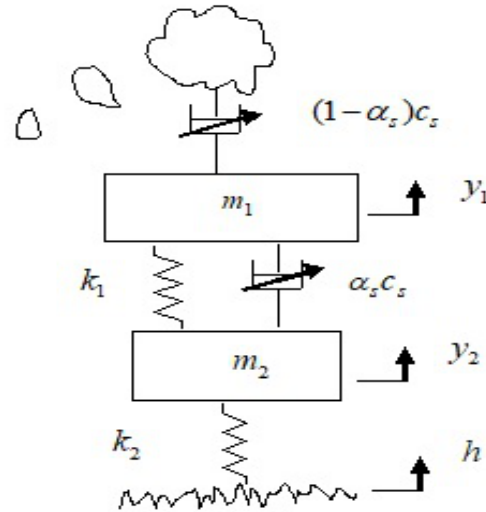


Figure 2. Quarter car model with skyhook damper

$$m_1 \ddot{y}_1 + k_1(y_1 - y_2) + c_s(\dot{y}_1) - \alpha_s c_s \dot{y}_2 = 0, \tag{18}$$

$$m_2 \ddot{y}_2 + k_1(y_2 - y_1) + \alpha_s c_s(\dot{y}_2 - \dot{y}_1) + k_2(y_2 - h) = 0, \tag{19}$$

where α_s and c_s are the skyhook damper parameters. For $\alpha_s=1$, equations ((18)) and ((19)) reduce to passive suspension equations. The skyhook control force can be defined as,

$$U_s = c_s(y_2 - \dot{y}_1) - (1 - \alpha_s)c_s \dot{y}_2. \tag{20}$$

Equations ((4)), ((18)) and ((19)) can be written as matrix differential equations using state space form,

$$\dot{x} = Fx + Dw(t), \tag{21}$$

where $x = [x_1 \ x_2 \ x_3 \ x_4 \ x_5]^T$ and $x_1 = y_1, \ x_2 = \dot{y}_1, \ x_3 = y_2, \ x_4 = \dot{y}_2, \ x_5 = h,$

$$F = \begin{bmatrix} 0 & 1 & 0 & 0 & 0 \\ -\frac{k_1}{m_1} & -\frac{c_s}{m_1} & \frac{k_1}{m_1} & \frac{\alpha_s c_s}{m_1} & 0 \\ 0 & 0 & 0 & 1 & 0 \\ \frac{k_1}{m_2} & \frac{\alpha_s c_s}{m_2} & -\frac{(k_1 + k_2)}{m_2} & -\frac{(\alpha_s c_s)}{m_2} & \frac{k_2}{m_2} \\ 0 & 0 & 0 & 0 & -\alpha_r V \end{bmatrix}, \quad d = \begin{bmatrix} 0 \\ 0 \\ 0 \\ 0 \\ 1 \end{bmatrix} \tag{22}$$

The vehicle response described by covariance matrix $P(t) = E[xx^T]$ is obtained by solving the below Liapunov equation.

$$\dot{P} = FP + PF^T + dQd^T \tag{23}$$

3.2. Optimal skyhook damper parameters

For obtaining the optimal skyhook damper control parameters α_s and c_s at a particular velocity the following new optimization strategy is adopted. In this strategy, the value of α_s is varied from 0 to 1 and for each value of α_s , the corresponding value of c_s is found by equating optimal control effort of the preview control algorithm as per the equation (9) to sky-hook damper control force as per the equation (20). This value of c_s is given by

$$c_s = \sqrt{\frac{E[U^2]}{E[\dot{y}_1 - \alpha_s \dot{y}_2]^2}}. \tag{24}$$

Thus for each value of α_s there is corresponding value of c_s for a specific vehicle velocity. Calculate the overall performance of vehicle with each set of skyhook

damper parameters. Thus there is a need to chose one combination of α_s and c_s for sky hook damper which matches the vehicle performance as the LQR with preview control performance. This can be effected by minimizing the square root of the sum of the difference between the mean square vehicle responses obtained by LQR with preview control and the skyhook damper control. The values of α_s and c_s are thus obtained corresponding to the minimum rms difference given by

$$\min \sqrt{\sum_{i=1}^3 (J_i)_{SH} - (J_i)_{LQRP}}, \quad (25)$$

the subscript LQRP denotes LQR with preview, SH denotes skyhook control and j_i 's are obtained by equation (7).

In this process, one suitable set of (α_s, c_s) for a specific velocity is obtained in view of vehicle overall performance. Since the skyhook damper parameters, once chosen, cannot be varied, the optimal values α_s and c_s obtained for a specific velocity will not be optimal for other vehicle velocities, which is the reason behind choosing other sets of optimal values α_s and c_s for other vehicle velocities. It has been observed that the variation of α_s and c_s values is not very much and the average values of the optimal α_s and c_s are calculated for a velocity range. These average values are considered to be suitable for the skyhook damper to equal the performance of LQR with preview control. Best possible response of the vehicle and optimal control force are obtained by substituting the optimal values of α_s and c_s into equations (18) and (19) and solving the lyapunov equation (23).

The detailed step wise optimization procedure is given below.

- Step 1: Obtained optimal response of quarter car model using LQR with preview control.
- Step 2: Calculated control force of the LQR-preview control.
- Step 3: Control force term is taken from equations of motion of quarter vehicle model with LQR with preview control (Equation 9). This control force is reference force.
- Step 4: From equation of motion of sky-hook model, the control force is taken (Equation 20).
- Step 5: To obtain the optimal response of quarter car sky-hook model close to the optimal response of quarter car-LQR with preview control, both models suspension system forces must be equal.
- Step 6: Equated the control force (reference force) of the LQR model-preview (Equation 9) with control force of sky-hook damper quarter car model (Equation 20) as shown in Equation (24).
- Step 7: There are two unknowns (α_s and c_s) and one equation(Equation (24)).
- Step 8: So for each velocity, fixed the range of α_s as 0 to 1 and corresponding c_s value is obtained using equation (24).
- Step 9: Calculated average of all the α_s and c_s values to find the optimum set of the parameters suitable for all vehicle velocities.

4. Results and Discussion

This section shows the response of the vehicle models, quarter car passive suspension, optimal sky-hook damper, LQR-preview and LQR without preview. The vehicle and road model parameters and the weights of performance index are $m_1 = 1000kg$, $m_2 = 100kg$, $k_1 = 36000N/m$, $k_2 = 360000N/m$, $\alpha_r = 0.15rad/m$, $\sigma^2 = 9 * 10^{-6}m^2$, $\rho_1 = 1$, $\rho_2 = 10^4$, $\rho_3 = 10^4$, $\rho_4 = 10^{-6}$. For the quarter car model, the vehicle parameters and the weighting factors are chosen as in [14]. The optimum values of the skyhook damper parameters obtained using the procedure explained in section 3.2 are $\alpha_s = 0.17$ and $c_s = 7518.5Ns/m$. The response statistics for the different control schemes, LQR control with a preview distance of $P_d = 2$ m, LQR control with $P_d = 0$, skyhook damper control with optimum parameters and the passive system are shown in Figures 3 to 6 respectively.

Figure 3 gives a picture of the variation of sprung mass acceleration with vehicle velocity for the passive suspension, LQR model with preview, LQR model without preview and optimum Sky hook damper model. The performance of the Optimal sky hook model is equal to the performance of the LQR with preview control, marginally better than the LQR without preview, and substantially better than the passive suspension.

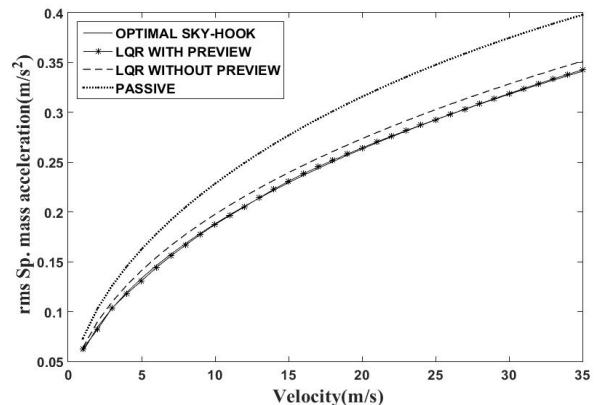


Figure 3. Variatin of sprung mass acceleration with velocity

In Figure 4 the *rms* stroke response is plotted for the four cases of passive, fully active(LQR) suspension without and with preview and semi-active suspension with skyhook damper with the optimal parameters. In this case, it is observed that the optimal skyhook damper performs almost same as the preview control at high velocity while at lower velocity its performance is not matched with that of the preview control. The suspension stroke performance of both of the fully active suspension with preview and the semi-active suspension with optimal skyhook damper is slightly better than the LQR without preview and obviously superior to the passive system. The stroke response of LQR-without preview is slightly worse, implying that the preview helps to improve the performance of the active suspension which is also reflected in the skyhook damper performance.

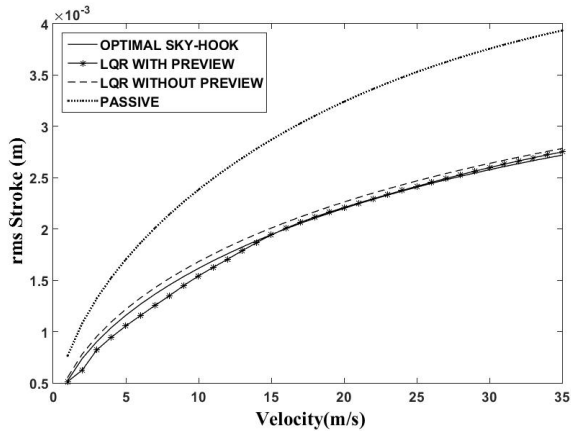


Figure 4. Suspension stroke response for different velocities

Figure 5 shows the road holding characteristics for the different vehicle suspension models. The active suspensions (LQR-preview and LQR-without preview control) performance is superior to the passive suspension. However, LQR with preview control shows better performance when compared to the LQR control without preview. The optimal skyhook damper performance is same as the performance of LQR-preview, and it is marginally superior to LQR model without preview.

From Figure 6, it is observed that the overall performance index, with respect to sprung mass acceleration, road holding and suspension stroke, the LQR with preview control performs the best and the performance in this case is significantly better than that corresponding to the passive suspension and marginally better than the LQR control without preview and the skyhook damper suspension with optimum parameters. The skyhook control with optimum parameters obtained by equating the control force corresponding to the LQR control with preview performs slightly improved when compared to the LQR control without preview.

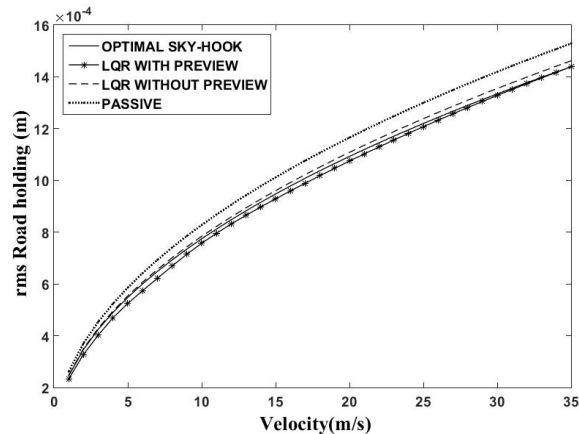


Figure 5. Road holding response for different velocities

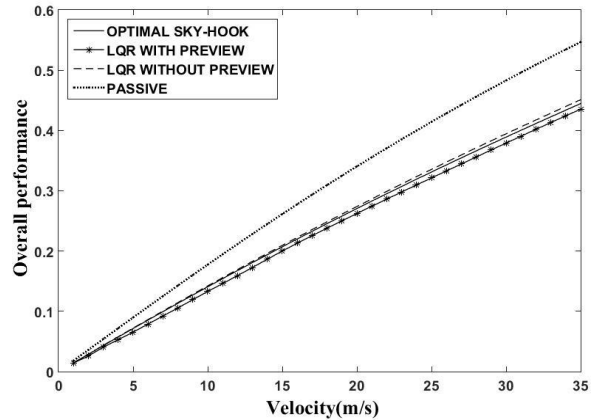


Figure 6. Overall response for different velocities

Figure 7 depicts the control effort required by the three different models. The rms control force of LQR- preview control matches with skyhook damper control and more than the LQR without preview control for most of the velocity range considered as expected.

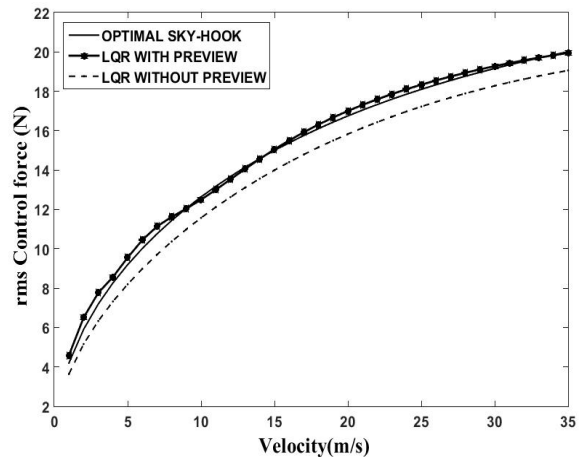


Figure 7. Variation of control force

As a further exercise, sprung mass acceleration, road holding, suspension stroke and overall performance index for different preview distances are plotted in Figures 8 to 11. It is seen from the figures that the performances of acceleration, road holding and suspension stroke improve with increasing preview distance up to a certain preview distance. Therefore, there is a limit preview distance beyond which the benefit of the preview control is not obtained.

From Figure 8 it is seen that the *rms* acceleration response improves with increasing preview distance up to certain preview distance say approximately 2 m beyond that the effect is only marginal. In case of stroke, road holding and overall performances also, as shown in figures 9,10 and 11, improvement is only up to a particular preview distance. Because of this saturation effect, the preview distance is taken as 2 m for the study.

As a further exercise, sprung mass acceleration, road holding, suspension stroke and overall performance index for different preview distances are plotted in Figures 8 to 11. It is seen from the figures that the performances of acceleration, road holding and suspension stroke improve with increasing preview distance up to a certain preview distance. Therefore, there is a limit preview distance beyond which the benefit of the preview control is not obtained.

From Figure 8 it is seen that the *rms* acceleration response improves with increasing preview distance up to certain preview distance say approximately 2 m beyond that the effect is only marginal. In case of stroke, road holding and overall performances also, as shown in figures 9,10 and 11, improvement is only up to a particular preview distance. Because of this saturation effect, the preview distance is taken as 2 m for the study.

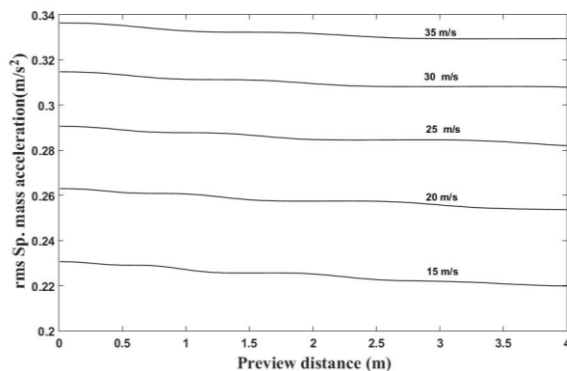


Figure 8. Sprung mass acceleration for different preview distances.

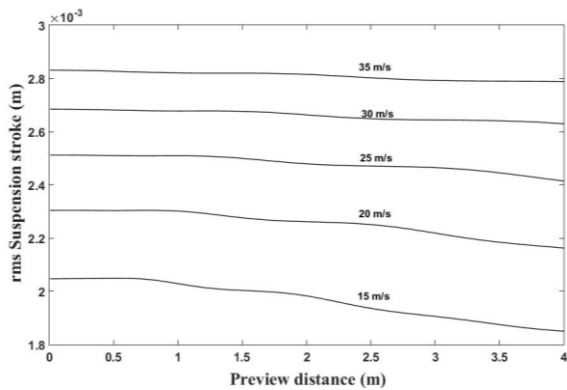


Figure 9. Suspension stroke for different preview distances.

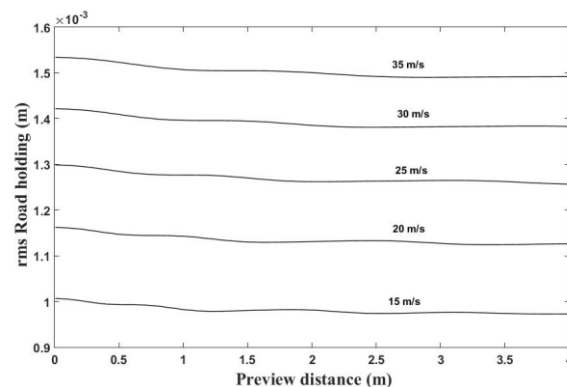


Figure 10. Road holding response for different preview distances.

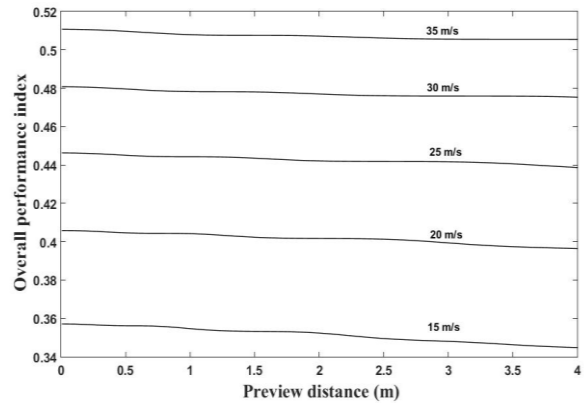


Figure 11. Overall response for different preview distances.

5. Conclusions

In this paper, a new optimization method is proposed for choosing optimal parameters of skyhook damper of quarter car model moving over a random path to obtain optimal response with respect to the ride comfort, road holding, suspension deflection and control force. The skyhook damper parameters are optimized on the basis of minimization of the total *rms* error which is the sum of errors of *rms* road holding, *rms* acceleration and *rms* stroke compared to LQR with preview control. This ensures that the mean square control force obtained by the skyhook damper is equal to the control force of LQR preview control. As a result, the sky hook damper’s performance with optimal parameters is improved to the levels compared to the LQR with preview control. It can be concluded from the results of the skyhook damper suspension system and the LQR with preview control suspension system that the quarter car model performance with optimal skyhook damper is comparable to the vehicle model with preview optimal control and significantly superior to the passive suspension system. Error between the overall performance index of the optimal sky hook damper and the LQR control with preview is observed to be 1.5%. The sprung mass acceleration of the sky hook damper control exactly coordinates with the response of the system with LQR preview.

References

- [1] Meng, Q., Chen, C.C., Wang, P., Sun, Z.Y. and Li, B., 2021. Study on vehicle active suspension system control method based on homogeneous domination approach. *Asian Journal of Control*, 23(1), 561–571. <https://doi.org/10.1002/asjc.2242>
- [2] Ovalle, L., Ríos, H. and Ahmed, H., 2021. Robust Control for an Active Suspension System via Continuous Sliding-Mode Controllers. *Engineering Science and Technology, an International Journal*. <https://doi.org/10.1016/j.jestch.2021.06.006>
- [3] Huang, Y., Na, J., Wu, X., Gao, G.B. and Guo, Y., 2018. Robust adaptive control for vehicle active suspension systems with uncertain dynamics. *Transactions of the Institute of Measurement and Control*, 40(4), pp.1237-1249. <https://doi.org/10.1177%2F0142331216678312>
- [4] Rahman, M. and Rahman, M., 2021. Application of Potential Energy Method for Driver Seat Suspension System Using Quasi-Zero Stiffness: A Numerical and Experimental

- Study. *Jordan Journal of Mechanical & Industrial Engineering*, 15(5). ISSN 1995-6665, pp. 431-439.
- [5] Crosby, M.J., Karnopp, D., 1973. The Active damper- a new concept for shock and vibration control. *Shock and Vibration Bulletin*, 43.
- [6] Karnopp, D., Crosby, M.J., Harward, R.A., 1974. Vibration control using semi-active force generators. *ASME Journal of Manufacturing Science and Engineering*, 96(2), 619-626. <https://doi.org/10.1115/1.3438373>
- [7] Sammier, D., Oliver, S., Dugard, L., 2003. Skyhook and H_{∞} control of semi-active suspensions: some practical aspects. *Vehicle System Dynamics*. 39(4), 279-308. <http://dx.doi.org/10.1076/vsd.39.4.279.14149>
- [8] Hamrouni, E., Moreau, X., Benine-Neto, A., Hernette, V., 2019. Skyhook and CRONE active suspensions: A comparative study. *IFAC-PapersOnLine*. 52-5, 243-248. <https://doi.org/10.1016/j.ifacol.2019.09.039>
- [9] Vladimir, G., Klucik, M., 2012. Optimization of vehicle suspension parameters with use of evolutionary computation. *Procedia Engineering*. 48, 174-179. <https://doi.org/10.1016/j.proeng.2012.09.502>
- [10] Lee, C.K., Cheng, Y.C., 2014. Application of Uniform Design and Quantum-Behaved Particle Swarm Optimization in Solving the Sensitivity Problem a Railway Vehicle System. *Procedia Engineering*. 79, 427-436. <https://doi.org/10.1016/j.proeng.2014.06.364>
- [11] Xu, H., Zhao, Q.Y., Ye, Chao., Lin, F., 2019. Integrated optimization for mechanical elastic wheel and suspension based on an improved artificial fish swarm algorithm. *Advances in Engineering Software*. 137, 1-8. <https://doi.org/10.1016/j.advengsoft.2019.102722>
- [12] Mustafa, G.I.Y., Wang, H.P., Tian, Y., 2019. Vibration control of an active vehicle suspension systems using optimized model-free fuzzy logic controller based on time delay estimation. *Advances in Engineering Software*. 127, 141-149. <https://doi.org/10.1016/j.advengsoft.2018.04.009>
- [13] Rajagopal, K., and Ponnusamy, L., 2015. Hybrid DEBBO Algorithm for Tuning the Parameters of PID Controller Applied to Vehicle Active Suspension System. *Jordan Journal of Mechanical & Industrial Engineering*. 9(2), 85-102.
- [14] Hac, A., 1985. Suspension optimization of a two dof vehicle model using stochastic optimal control technique. *Journal of Sound and Vibration*. 100, 343-357. [https://doi.org/10.1016/0022-460X\(85\)90380-3](https://doi.org/10.1016/0022-460X(85)90380-3)
- [15] Narayanan, S., Senthil, S., 1998. Stochastic optimal active control of a 2-DOF quarter car model with non-linear passive suspension elements. *Journal of Sound and Vibration*, 211(3), 495-506. <https://doi.org/10.1006/jsvi.1997.1396>
- [16] Tomizuka, M., 1976. Optimal linear preview control with application to vehicle suspension- revisited. *ASME Journal of Dynamical Systems, Measurement and Control*. 98(3), 309-315. <https://doi.org/10.1115/1.3427040>
- [17] Hac, A., 1992. Optimal linear preview control of active vehicle suspension. *Vehicle System Dynamics*, 21, 167-195. <https://doi.org/10.1080/00423119208969008>

Effect of Inlet Swirl on Combustion Performance and Soot Formation of a Turbulent Methane-Air Non-Premixed Flame

Tarak Kumar Sahoo, Prakash Ghose*

School of Mechanical Engineering, KIIT Deemed to be University, Bhubaneswar-24, INDIA

Received 11 OCT 2021

Accepted 7 FEB 2022

Abstract

In the present study, the effect of swirl intensity on flame temperature, radiation heat flux, soot formation, dispersion, and other major species concentrations were investigated for methane-air non-premixed combustion. Harwell standard furnace has been chosen for computational modeling. Eddy dissipation combustion model is used to evaluate reaction rate considering one-step global combustion reaction mechanism for methane. Standard k- ϵ turbulent model, Discrete ordinate (DO) radiation model, and Moss-Brookes soot models are used for simulation. The weighted-sum-of-gray-gases model (WSGGM) is employed to calculate the radiation absorption coefficient. A fair agreement has been observed between published experimental and simulation results. The numerical results show that as the swirl intensity increases, the radial component of the flow increases, hence the flame becomes wider. Consequently, the temperature distribution, soot formation, and the species mass concentration are also strongly influenced by the swirl intensity. It has also been observed that the flame temperature decreases with the consideration of soot generation due to an increase in radiation heat loss of eight percent. Incomparable to any swirl, the average wall heat flux increases to 62.72% when the swirl number is 5.

© 2022 Jordan Journal of Mechanical and Industrial Engineering. All rights reserved

Keywords: Swirl number, Radiation heat flux, Soot formation, Species mass fraction.

1. Introduction

At present, a major part of the total energy across the globe depends on fossil fuels such as; coal, oil, and natural gas. Natural gas is primarily composed of methane which is mostly used as fuel for homes, kilns, automobiles, turbines, and other machinery. Methane combustion emits unburned hydrocarbons, carbon dioxide, oxides of nitrogen, etc.[1]. These emissions are exhausted into surroundings, pollute the atmosphere, and are responsible for climate change. To minimize fuel loss and pollution, researchers mainly focused on the finding of maximum combustion efficiency with minimum harmful emissions.

Emissions can be minimized with the complete combustion of fuel. To enhance the combustion efficiency, air feed into the combustion chamber through a swirler is a well-adapted methodology. Because of the swirling action of air, the unburnt fuel is pulled back into the flame region due to adverse pressure gradient, hence the combustion efficiency increases. The effect of swirl has been studied by many researchers both experimentally and numerically. Swirler is also called a flame holding device because it provides stability to the flame by minimizing the flame blowout possibility [2], [3]. Reverse flows are the reasons for the larger residence time of the air-fuel mixture to be present in the flame zone and enhanced combustion as well [4]. Swirl increases the turbulent intensity inside the combustor and thereby affects the scalar variable distribution. It also helps in stabilizing the complex turbulent flames[2]. Iyogun et al.[5] experimentally found that, with the increase in swirl number, a relatively larger recirculation zone is formed with a rectangular nozzle as

compared to a circular counterpart. Saediamiri et al.[6] investigated the effect of low swirl intensity of co-flow air and nozzle diameter on flame stability. It has been reported that swirl has a significant effect on moderate to high co-flow air velocity, but it is not much significant when co-flow air velocity is very less. Sellan et al.[7] implemented swirlers both in the outer and inner air stream where the inner airflow velocity is 2-3 times than the outer air stream. It has been observed that the combined arrangement of the swirler is more effective in flame holding rather than a single inner swirler. Yoon et al.[8] experimentally exhibited the effect of swirl intensity on the combustion and its emission characteristics. They found that by increasing the swirl intensity, the particulate matter and carbon monoxide emissions can be reduced, but the NOx emissions will increase.

The formation of soot particles during combustion is one of the major environmental pollutions as it can damage the respiratory system of any living being. Soot emission is also a primary cause of global warming. Hence, proper prediction of soot in combustion through computational modeling is very much necessary. Ogawa et al.[9] investigated the effect of the swirl ratio on the NOx and soot emissions with the help of the KIVA code. They found that relatively stronger swirl intensity reduces soot emissions up to an optimum limit and further increases in swirl intensity, soot emissions increase. Bonatesta et al.[10] have computationally investigated the soot in an internal combustion engine and found that, in the cylinder, the fuel distribution and the location of combustion are the most influential parameters for the soot formation. An increased

* Corresponding author e-mail: pghosefme@kiit.ac.in.

level of swirl intensity downgrades the combustion by increasing soot formations. Chong et al.[11] studied the combustion behavior of a model aircraft combustor, where a Large-eddy simulation modeling approach is used to incorporate the turbulent effects in the flow field. They found that a very high amount of soot formation occurs on and around the fuel jet. A small set of fuel trajectories deposition on the fuel jets is the prime reason for soot deposition in this part, and that happens due to the swirling action. Zhou et al.[12] experimentally studied the soot emissions in a separated swirl combustion system (SSCS) and compared with a double swirl combustion system (DSCS). They found SSCS produces less incipient soot particles than DSCS, and SSCS has a faster surface soot oxidation. The relationships between soot distribution, flame structure, and the flow field were experimentally investigated for diffusion flames of methane and air by Wang et al.[13]. They observed that the reduction in soot particles with airflow rate is correlated with high-intensity turbulence and elevated oxidation rate in the recirculation zone.

In numerical studies, Keramida et al.[14] used two different radiation models, such as the Discrete transfer model and the Six-flux model, to predict the effect of radiation models on combustion characteristics. They perceived the importance of the thermal radiation effect even in a low-temperature flame. However, to check the performance prediction of both the radiation model, simulated results were verified against the experimental work of Wilkes et al.[15]. Ghose et al.[16] numerically simulated a kerosene fuel spray combustor to speculate the soot formation and effects of thermal radiation at various swirl intensities. The Brookes and Moss[17] augmented soot model for kerosene flames which has been used to evaluate the radiant heat flux on the combustor wall and fuel injector. They found incident heat flux on the wall decreases as the swirl intensity is reduced. Moreover, a uniform temperature distribution in the exhaust gas is obtained in the combustor exit with higher swirl intensity. Yilmaz[18] used AnsysFluent code for numerical simulations of natural gas non-premixed combustion. He used the Eddy dissipation model with one step combustion reaction mechanism, Standard k-ε turbulence model for turbulent closure, and P-1 radiation model flame radiation inside the combustor to verify the effect of the swirl number on flame temperature and the gas concentrations such as CH₄, O₂, CO₂, and H₂O. He found the intensity of the swirl changes the fluid dynamics characteristics of a diffusion flame, such as axial velocity distribution, central recirculation zone, and the external circulation zone.

Yang et al.[19] used Harwell combustor model, and simulated the turbulence radiation interaction (TRI) to acknowledge the radiation characteristics with oxy-combustion conditions. They observed that it strongly affects the temperature fields. Moreover, with increasing the swirl intensity, the TRI effect decreased.

RANS (Reynolds average Navier-Stokes) equations are solved to simulate the turbulent flow. By time averaging of Navier-Stokes equations, RANS equations are derived. The additional terms during averaging of Navier-Stokes equation are evaluated from the Boussinesque hypothesis. RANS has a minimal computational need. Therefore, it is generally used in highly complex geometry where the mesh number is very high. Many researchers used RANS-based turbulent models (various k-ε models) [20][21] and observed that the flow variables are properly predicted by those models.

Seeing the vital role of swirling the combustor, and consequently, the combustion behaviors, it is obligatory to determine its accurate intensity for modeling combustion phenomena. In the light of the above discussions, the present study focuses on the effect of swirl on comprehensive combustion performance. The effect of various levels of swirl intensities on radiant heat flux and soot generation has been investigated; as it was rarely explored in previous articles. The existing experimental data are compared with similar computational and experimental results.

2. The details of models:

2.1. Combustor geometry and boundary conditions

In this paper, the Harwell furnace[15] has been chosen to investigate the swirling effect and the combustion characteristics of methane-air diffusion flame. The length and the radius of the combustion chamber are 900 mm and 150 mm respectively as shown in Figure-1. The air is supplied through the annular hole at a velocity of 12.8 m/s and the fuel is supplied through the central hole at a velocity of 0.15 m/s and temperature of 295 K. The equivalence ratio is maintained constant for all swirl numbers and equal to 0.83. The parameters of boundary and the operational conditions are enlisted in Table-1. The swirling action of flow is given to the airstream only. Swirling causes the flame to be widespread within the combustion chamber, and improves the combustion. In the present study, the dimensionless parameter as swirl number (S) shown in equation (1) is calculated as;

$$S = \frac{2}{3} \left(\frac{v_t}{v_a} \right) \left[\frac{1 - \left(\frac{r_i}{r_o} \right)^3}{1 - \left(\frac{r_i}{r_o} \right)^2} \right] \tan \beta \quad (1)$$

Swirl number is the ratio of the tangential and axial momentum fluxes. In the above equation, v_t and v_a represent the tangential and the axial components of the velocity of airflow, while r_i and r_o represent the internal and external swirl generator radius. In addition, β represent the angle of the swirlervane[22].

Table 1. Operational conditions of Harwell combustor.

Geometry:

Fuel inlet zone (mm)	$r_i=0.0,$	$r_o= 6.0$
Air inlet zone (mm)	$r_i=16.5,$	$r_o= 27.5$
Furnace radius (mm)	150	
Furnace length (mm)	900	
Inlet boundary conditions for fuel and air:	Fuel (m/s)	Air (m/s)
Axial velocity	15	12.8
Radial velocity	0	0
Swirl no.	0	0.4
Turbulent kinetic energy (m^2/s^2)	2.26	1.63
Turbulent dissipation rate (m^2/s^3)	1131.8	692
Temperature	295	
Composition (mass fraction) Fuel Air:	Fuel	Air
Oxygen	0	0.2315
Nitrogen	0	0.7685
Methane	1	0

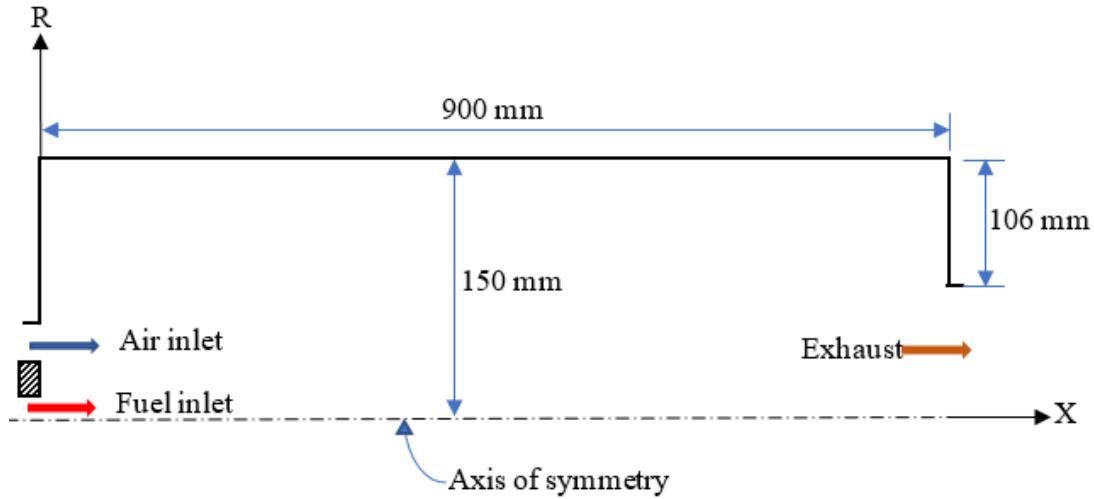


Figure 1. Combustion chamber geometry

2.2. Mathematical modeling

In the present study, a two-dimensional axisymmetric geometry is prepared, and the governing equations for the polar coordinate system are discretized with the help of the finite volume discretization method. Ansys Fluent 19.2 is used for simulation. The universal forms of Reynolds averaged governing equations are expressed as follows:

Continuity equation

$$\frac{\partial}{\partial x_i} \rho \bar{u}_i = 0 \tag{2}$$

Where, ρ represents the gas density and \bar{u}_i is the time average flow velocity vector.

Momentum conservation equation

$$\frac{\partial}{\partial x_i} (\rho \bar{u}_i \bar{u}_j) = \frac{\partial \bar{p}}{\partial x_i} + \frac{\partial}{\partial x_j} (\bar{\tau}_{ij} - \rho \overline{u'_i u'_j}) \tag{3}$$

Where \bar{p} is the time average mean static pressure, $\bar{\tau}_{ij}$ is the stress tensor expressed as

$$\bar{\tau}_{ij} = \left[\mu \left(\frac{\partial \bar{u}_i}{\partial x_j} + \frac{\partial \bar{u}_j}{\partial x_i} \right) \right] \text{ and } -\rho \overline{u'_i u'_j} \text{ is the time-averaged Reynold's stress.}$$

Energy conservation equation

$$\frac{\partial}{\partial x_i} (\rho \bar{u}_j \bar{h}) = \frac{\partial}{\partial x_i} \left(\frac{\mu}{\sigma} \frac{\partial \bar{h}}{\partial x_i} - \rho \overline{h' u'_i} \right) + S_{rad} + S_E \tag{4}$$

Where $\rho \overline{h' u'_i} = \left(\frac{\mu_t}{\sigma_{ht}} \frac{\partial \bar{h}}{\partial x_i} \right)$ is the turbulent flux for enthalpy. Here μ_t is the turbulent viscosity and σ_{ht} is the turbulent Prandtl number. S_{rad} is the radiative source term and S_E is the combustion reaction heat generation term.

Species mass conservation equation

$$\frac{\partial}{\partial x_i} (\rho \bar{u}_j \bar{Y}_k) = \frac{\partial}{\partial x_i} \left(\frac{\mu}{Sc} \frac{\partial \bar{Y}_k}{\partial x_i} - \rho \overline{Y'_k u'_i} \right) + \dot{\omega}_k \tag{5}$$

where, $\rho \overline{Y'_k u'_i} = \left(\frac{\mu_t}{Sc_t} \frac{\partial \bar{Y}_k}{\partial x_i} \right)$ is the turbulent flux for species. Here Sc_t is the turbulent Schmidt number and $\dot{\omega}_k$ represents the net rate of production of species in the species conservation equation. Reynolds stresses and all other turbulent fluxes are evaluated with the help of the Boussinesq hypothesis. k-ε turbulent model [23] is used to evaluate the turbulent quantities inflow field.

2.3. Radiation Model

Radiation is an important phenomenon in hydrocarbon fuel combustion as the products such as; H₂O and CO₂ diligently participate in radiation heat transfer. Moreover, due to the higher emissivity of soot, soot formation enhances the radiation heat loss [16]. DO model [16] can

calculate the effect of participating media and soot in radiation. The radiation transport equation (RTE) is expressed as;

$$\frac{dI(\vec{r}, \vec{s})}{ds} = \kappa I_b(\vec{r}) - \kappa I(\vec{r}, \vec{s}) \tag{6}$$

In the above equation, I is the radiation intensity, I_b is the black body radiation intensity, \vec{r} and \vec{s} are the position vector and direction vector respectively. κ is the bulk gas absorptivity including absorption coefficient of soot ($\kappa = \kappa_{gas} + \kappa_{soot}$).

Weighted sum grey gas model (WSSGM) model is used to evaluate absorptivity of bulk gas is expressed as;

$$\kappa_{gas} = - \frac{\ln \left[1 - \sum_{k=0}^{k=1} a_k (1 - e^{-\kappa_k p_k}) \right]}{z} \tag{7}$$

In the above equation, κ_k is the gray gas absorption coefficient for kth participating gray gas. z is the path length which depends upon mesh size, p_k is the partial pressure of kth gray gas, (a_k) is the emissivity weighing factor for kth gray gas. It is a polynomial function of temperature which is expressed as;

$$a_k = \sum b_{k,j} T^j \tag{8}$$

The absorption coefficient of soot which is contributed to overall absorptivity is expressed as;

$$\kappa_{soot} = 1232.4 \rho_{soot} [1 + 4.8 \times 10^{-4} (T - 2000)] \tag{9}$$

The source term in the energy equation due to radiation which is described as the divergence of radiative heat flux $q(\vec{r})$ is expressed as;

$$\dot{S}_{rad} = \nabla \cdot q(\vec{r}) = \kappa \left[4\pi \frac{\sigma T_g^4}{\pi} - \int_0^{4\pi} I(\vec{r}, \vec{s}) d\Omega \right] \tag{10}$$

In the above equation, Ω is the solid angle.

2.4. Soot model

Hydrocarbon fuel produces soot during combustion at high temperatures. Soot is formed through four stages, such as nucleation, coagulation of hydrocarbons, surface growth, and soot also depletes through oxidation [24]. The nucleation and oxidation rate of soot are relatively slow as compared to the combustion process. Therefore, it requires different transport equations to solve the soot mass concentration and soot density in the computational domain [25]. Moss and Brookes [26], is an appropriate model to predict soot in a methane-air diffusion flame. This model has two soot transport equations. One is to find the number density and another is to find the mass concentration of the soot. The source term for number density can be written as

$$\frac{dN}{dt} = \underbrace{C_\alpha N_A \left(\frac{X_{C_2H_2} P}{RT} \right) \exp\left(-\frac{T_\alpha}{T}\right)}_{\text{Nucleation}} - \underbrace{C_\beta \left(\frac{24 RT}{\rho_{soot} N_A} \right)^{1/2} d_{soot}^{1/2} N^2}_{\text{Coagulation}} \quad (11)$$

and the source term for soot mass fraction can be expressed as;

$$\frac{dM}{dt} = \underbrace{C_\alpha M_p \left(\frac{X_{C_2H_2} P}{RT} \right) \exp\left(-\frac{T_\alpha}{T}\right)}_{\text{Nucleation}} + \underbrace{C_\gamma \left(\frac{X_{C_2H_2} P}{RT} \right) \exp\left(-\frac{T_\gamma}{T}\right) \left[(\pi N)^{\frac{1}{3}} \left(\frac{6M}{\rho_{soot}} \right)^{\frac{2}{3}} \right]^n}_{\text{Surface Growth}} - \underbrace{C_{oxid} C_\omega \eta_{coll} \left(\frac{X_{OH} P}{RT} \right) \sqrt{T} (\pi N)^{\frac{1}{3}} \left(\frac{6M}{\rho_{soot}} \right)^{\frac{2}{3}}}_{\text{Oxidation}} \quad (12)$$

It can be observed that the entire source term equation is a function of pressure, temperature, the universal gas constant, and mole fraction of precursor species C_2H_2 in nucleation and surface growth term and mole fraction of OH in oxidation term. Since the single-step global methane reaction mechanism is used in this work, the precursor species C_2H_2 species is absent in the chemistry. Therefore, to determine the soot precursor C_2H_2 within the computational domain, a relation between the mole fraction of C_2H_2 and mixture fraction ξ has been used. It is given as [27];

$$0 < \xi \leq 0.0575$$

$$X_{C_2H_2} = 5.277237 \times 10^{-2} \xi^2 - 1.920161 \times 10^{-5} \xi + 3.797003 \times 10^{-6} \quad (13)$$

$$0.0575 < \xi \leq 0.128$$

$$X_{C_2H_2} = 1599627 \xi^6 - 932192 \xi^5 + 223543.4 \xi^6 - 28182.59 \xi^3 + 1964.038 \xi^2 - 71.3474 \xi + 1.0513 \quad (14)$$

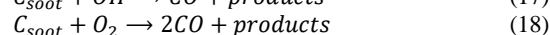
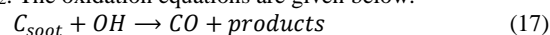
$$0.128 < \xi \leq 1$$

$$X_{C_2H_2} = 4.273195 \times 10^{-4} \xi^2 - 8.440912 \times 10^{-3} \xi + 7.988928 \times 10^{-3} \quad (15)$$

In the above equations ξ is mixture fraction inside the computational domain is expressed as;

$$\xi = \frac{\bar{Y}_{fu}}{\bar{Y}_{fu} + \bar{Y}_{ox}} \quad (16)$$

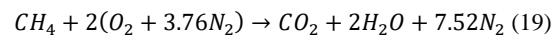
where, \bar{Y}_{fu} is the mass fraction of fuel and \bar{Y}_{ox} is the mass fraction of oxidizer (air) inside the computational domain. When $\xi = 1$, there is only fuel and no other species and for $\xi = 0$, there is an only oxidizer and no other species. The various constants used in equations 8 and 9 are taken from [27]. The turbulence effect on soot production or oxidation has been obtained through coupling with time-averaged temperature/species within the computational domain. A partial equilibrium oxidation model proposed by Fenimore-jones [27] is used to simulate soot oxidation. In the oxidation process, soot is oxidized with OH radical for methane fuel and partly with O_2 . The oxidation equations are given below.



However, in this model, only OH radical is considered for soot oxidation. The reaction rate is determined by the last term of the soot mass fraction source term.

2.5. Numerical Modeling

In the current investigation, the commercial ANSYSFluent 19.2 [28] has been used for computational analysis. The combustor geometry is prepared by following the work of Wilkies et al. [15]. SIMPLE algorithm is used for the coupling of pressure and velocity. All equations are solved with a second-order upwind scheme. The convergence residual value is kept as 10^{-6} for the energy equation, whereas it is set to 10^{-4} for all other governing equations. The standard k- ϵ model has been selected for turbulent flow modeling in the present work. The Eddy dissipation combustion model [29] is used for turbulent chemistry interaction. One step global reaction mechanism has been used for the combustion of methane-air.



DO radiation model is used in this study. This model has the potential to consider the radiation heat exchange between the gaseous phase and the soot present in the flame [30]. However, the P-1 and DO radiation model predicts equally. Habibi et al. [31] compared the prediction performance of the P-1 and DO radiation model on flame and reported that both models predict equally. Moreover, by using the weighted-sum-of-gray-gases model (WSGGM) [32], the absorption coefficient of the radiation is evaluated.

The thermophysical properties of all species used for the simulations are taken from the Fluent database, which is well verified. The specific heat for the mixed gas is evaluated as the mass-weighted averaging method. Moreover, it is taken as the polynomial function of temperature. The density of mixed gas is evaluated following incompressible ideal gas law. However, the conductivity is taken as constant because it does not vary significantly with temperature. The approximate dilution method is used for mass diffusion, where a constant diffusivity between all gases and the mixture is used. The viscosity of individual gas and the mixture gas is also taken as a polynomial function of temperature.

3. Grid Independence and model validation

3.1. Grid independency test and model validation

To reduce the computational cost and enhance the accuracy, the grid independence test has been performed. To investigate the mesh size effect, the test has been conducted for four different mesh sizes including 12,245, 34,542, 67,050 and 1,21,545 nodes before the actual numerical simulations start. The comparison has been done based on the axial temperature distribution inside the combustion chamber. The numerical results were compared with experimental results by Wilkies et al. [15] to determine the optimum mesh size for the numerical simulations. According to figure-2 (a), the mesh sizes of 67050 nodes and 121545 nodes are very much compatible with the experimental data and there is not much significant difference between the results with nodes 67050 and 121545. However, the grid with 67050 nodes is chosen for simulation to obtain fair results in the minimum possible time.

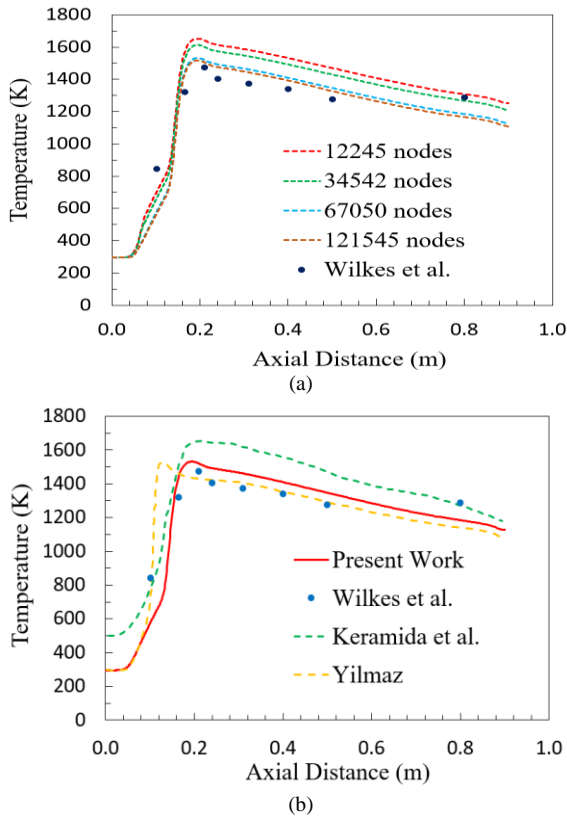


Figure 2. (a) The comparison for grid independence and (b) Numerical result validation: Yilmaz et al. [18]

The figure-2 (b) represents the axial temperature distributions. The predicted axial temperature has a good agreement with the experimental data of Wilkes et al.[15]. Moreover, the overall prediction of the current simulation is somehow better as compared to Keramida et al.[14] and Yilmaz [18].

4. Result and discussion

The effect of swirl intensity on flow behavior is illustrated through streamlines in figure-3. In the present study, the simulations are performed with swirl numbers 0.0, 0.1, 0.2, 0.3, 0.4, 0.5 and 0.6. Irrespective of swirl number a corner recirculation zone (CRZ) is formed due to the sudden expansion of air and fuel into the combustion

chamber. From the figure, it is observed that, with no swirl(SN= 0.0), the re-attachment length becomes maximum. With a further increase in the swirl intensity, the reattachment length for the CRZ decreases due to an increase in the radial component of the flow variable. When the swirl number is increased to 0.4, a central toroidal recirculation zone (CTRZ) is formed closer to the inlet of the combustion chamber. The formation of CTRZ is caused by a stronger swirl. Due to the formation of CTRZ, an adverse pressure gradient pulls the flame back. Hence, the flame becomes stable with increased swirl number, and the possibility of the flame blow out decreases.

Figure-4 (a) illustrates the axial temperature distribution on the symmetry axis for different swirl numbers. It can be seen that the maximum flame temperature location is shifted towards the inlet of the combustion chamber as we increase the intensity of the swirl. It is also observed that with the increase in swirl intensity, the maximum temperature on the axis of symmetry decreases. When the swirl number is higher than 0.3, a stronger CTRZ forms, hence the flame breaks as shown in figure 5. As a result, the highest flame temperature with these higher swirl numbers does not fall on the axis, rather shifts towards the wall region. For no swirl, the flame temperature is higher as compared to swirled flow, and the peak is observed at the farthest position from the inlet region because the flame is not pulled back due to the absence of an adverse pressure gradient. With the increase in swirl intensity, the flame length decreases, and flame width increases due to the presence of an adverse pressure gradient. Figure-4 (b) illustrates the radial distribution of temperature along the radial direction at the exit of the combustor. It is observed that, with strong swirls (swirl number greater than 0.3), the temperature distribution across the exit plane is uniform, which can also be observed in figure 5. It happens due to the CTRZ formation, which widens the flame and protects the flame from stretching. On the other hand, elongated flame produces a non-uniform temperature distribution across the exit plane due to weak swirl or no swirl. Also, the axial temperature at the exit is high.

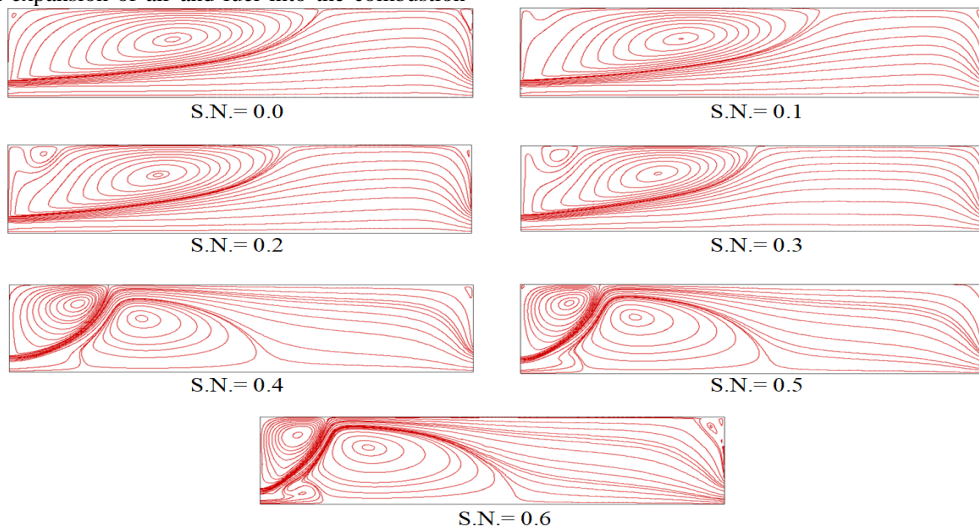


Figure 3. Streamlines flow for different swirl numbers.

The widening of flame and flame breakdown due to high swirling action causes heat loss from the flame through the combustor wall. The peak flame temperature region becomes closer to the combustor wall due to swirling action. As a result, the radiative heat losses increase. However, the lower flame temperature due to

higher swirling action decreases the formation rate of thermal NO_x. This is an advantage of swirling as well. Moreover, the uniformly distributed temperature is very much needed in the case of heating and baking furnaces to improve the quality of the product.

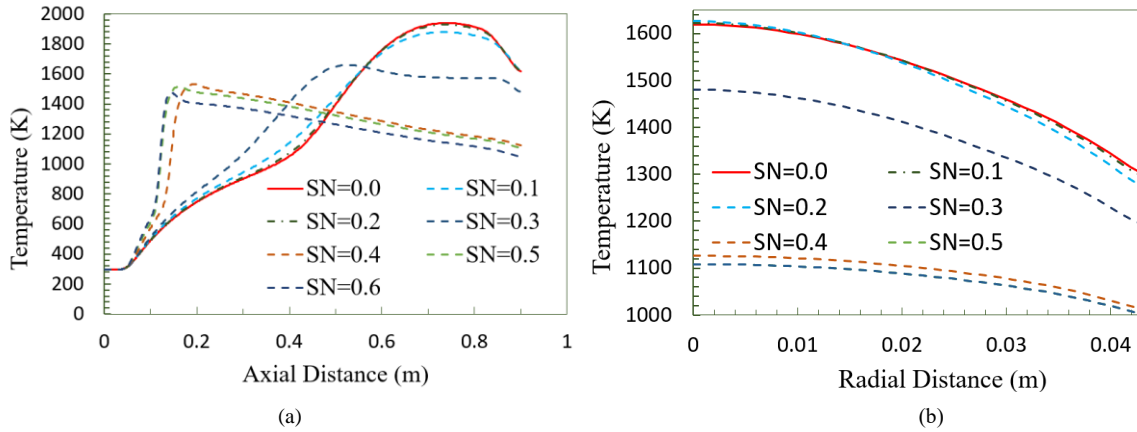


Figure 4. Variation of (a) axial temperature and (b) exhaust temperature with different swirl numbers.

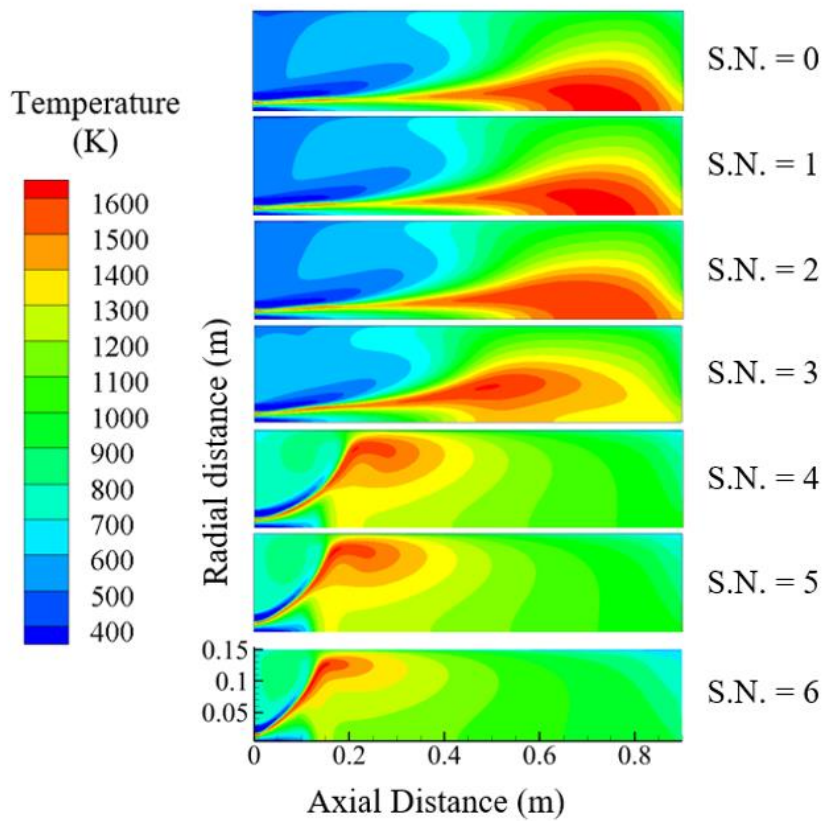


Figure 5. Temperature distribution contours for different swirl numbers.

Figure-6 (a) illustrates the effect of swirl intensity on radiation heat flux along the combustor wall. From the diagram, it is clear that the swirl intensity strongly affects the radiative heat transfer along the combustor wall. It has been observed that, for a strong swirl (swirl number greater than 0.3), the maximum wall radiative heat flux is observed at a little ahead of the inlet region. This wall heat flux depends on the flame position and flame temperature. Figure 5 reveals that, for a stronger swirl, the high-temperature zone of flame is closer to the wall and also is closer to the inlet. As swirl strength decreases, the flame becomes stretched and a high-temperature zone of the flame exists at the downstream region. Thus higher radiative heat transfer occurs from the flame to the combustor wall at the downstream region. Figure-6(b) shows the area-weighted average heat flux at the combustor wall for different swirl numbers. The temperature field near the entire combustor wall is very high with a higher swirl number. As a result average wall heat flux is higher for higher swirl number cases.

Figure 7 illustrates the soot volume fraction along the axis at different inlet swirls. Soot formation rate is directly related to the local equivalence ratio within the reaction zone. Soot formation rate becomes higher within the reaction zone, where the air-fuel mixture is relatively richer. Figure 9a. and 9b. (SN=0 and 0.3), clearly show a significant fuel mass fraction throughout the length of the combustor along the axis. It indicates that in this region relatively richer mixture causes the formation of a higher

amount of soot. As a result, for low inlet swirls (SN=0.0 to 0.3), a relatively higher soot volume fraction is observed along the entire length of the flame on the axis of symmetry as shown in figure 7. On the other hand, for a higher swirl (SN=0.4 to 0.6), significant fuel concentration is observed up to 0.15 m from the inlet as shown in figure 9c (for SN=0.6). Therefore, a higher amount of soot is observed in this region for higher inlet swirl cases. Beyond this region, soot volume fraction significantly decreases up to the exit of the combustor due to the absence of a rich mixture.

From figure-5, it has been observed that the flame structures are pretty similar for the SN 0.0, 0.1, and 0.2. Similarly, the flame structures are pretty similar for SN 0.4, 0.5, and 0.6. However, with SN 0.3, the flame structure is different than others; hence it is a transition kind of structure, where the flame is neither too stretched nor too short. It is well known that soot mass concentration is a strong function of temperature along with precursor species concentration. From the equations 13-15, if a graph will be drawn for $X_{C_2H_2}$ Vs ξ , it can be noticed that for the value of $\xi=0.15$, $X_{C_2H_2}$ is maximum. Most probably for the SN=0.3, the value of ξ is closer to 0.15 in most of the regions. However, the value of ξ depends upon the mixing of fuel and oxidizer. Here probably the mixing of fuel and oxidizer is much better than other swirl number cases. This may be the reason for the difference in soot volume fraction distribution for SN = 0.3.

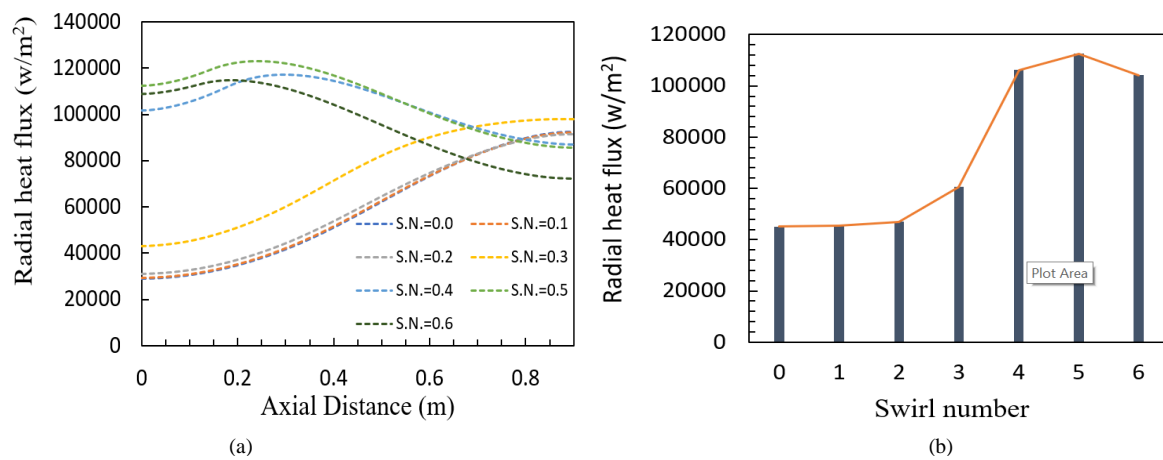


Figure 6. (a)Variation of radiation heat flux at the wall with different swirl numbers and (b) Average of radiation heat flux at the wall with different swirl numbers

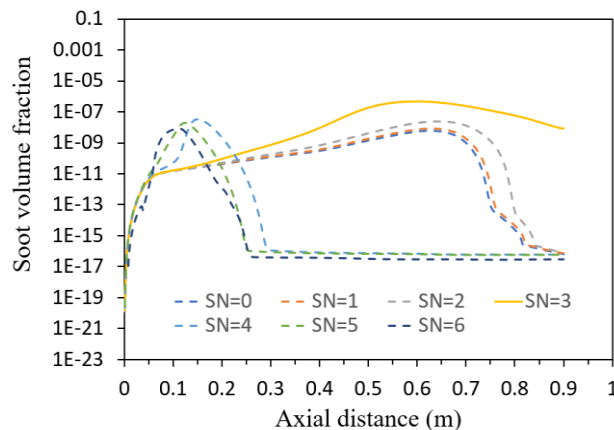


Figure 7. Soot volume fraction along the axis at different inlet swirl

Figure-8 shows the effect of soot on wall radiation heat flux at different swirl strengths. The comparison is made for non-swirling state (swirl number = 0.0) and swirl numbers 0.3 and 0.6. From the diagram, it is clear that the formation of soot enhances the radiation heat transfer irrespective of inlet swirl intensity. Soot is a black body, hence a considerable amount of heat is emitted when soot presents in flame. As a result flame temperature decreases and wall heat flux increases, when soot presents in flame. However, maximum wall heat flux differences are observed in between the conditions; flame with soot and flame without soot at a particular position along the wall length. This maximum difference position can be identified by comparing figure 7 and figure 8 simultaneously. It is obvious that where the soot concentration is the highest, the wall radiative heat flux difference becomes highest at this location along the combustor length.

Figure-9 illustrates the major species (CH_4 , O_2 , CO_2 , and N_2) mass fraction along the axis of symmetry for a non-swirling state (SN = 0.0), swirl number 0.3, and swirl number 0.6. Since the fuel stream is aligned with the axis of symmetry, therefore at the inlet, there is only fuel. Hence, here (at $x = 0$ m) mass fraction of fuel is 1

irrespective of the swirl number. After a certain distance (around $x = 0.05$ m), fuel concentration decreases and CO_2 formation starts. It confirms that the reaction zone starts from here along the axis. When there is no swirl or very low swirl intensity, the fuel is consumed completely far away from the inlet along the axis. This is due to stretched flame and thicker reaction zone. On the other hand, when the swirl intensity is 0.6, fuel is consumed completely closer to the inlet along the axis. This is due to the short flame and thinner reaction zone. However, it is observed that, when the swirl number is 0.6, beyond the reaction zone, the products are well diffused. As a result, no variations of species are observed along the axis, beyond the reaction zone. comparing the species mass fraction graph with the temperature distribution contours, figure-5, it is found that the peak for CO_2 mass fraction and zero fuel concentration is observed with the location of maximum temperature in the combustion chamber. When swirl intensity is increased, this point on the symmetry axis comes closer to the inlet of the furnace. Similarly, the mass fraction of other species (O_2 , N_2) also reach their peak values at the location of maximum temperature. This represents the occurrence of the true combustion process.

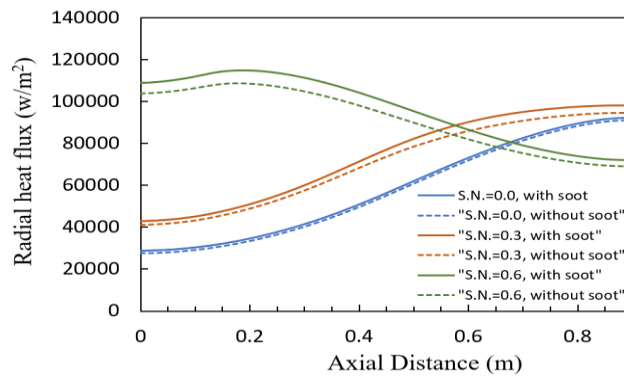


Figure 8. Variation of radiation heat flux at the wall with and without soot at different swirl numbers

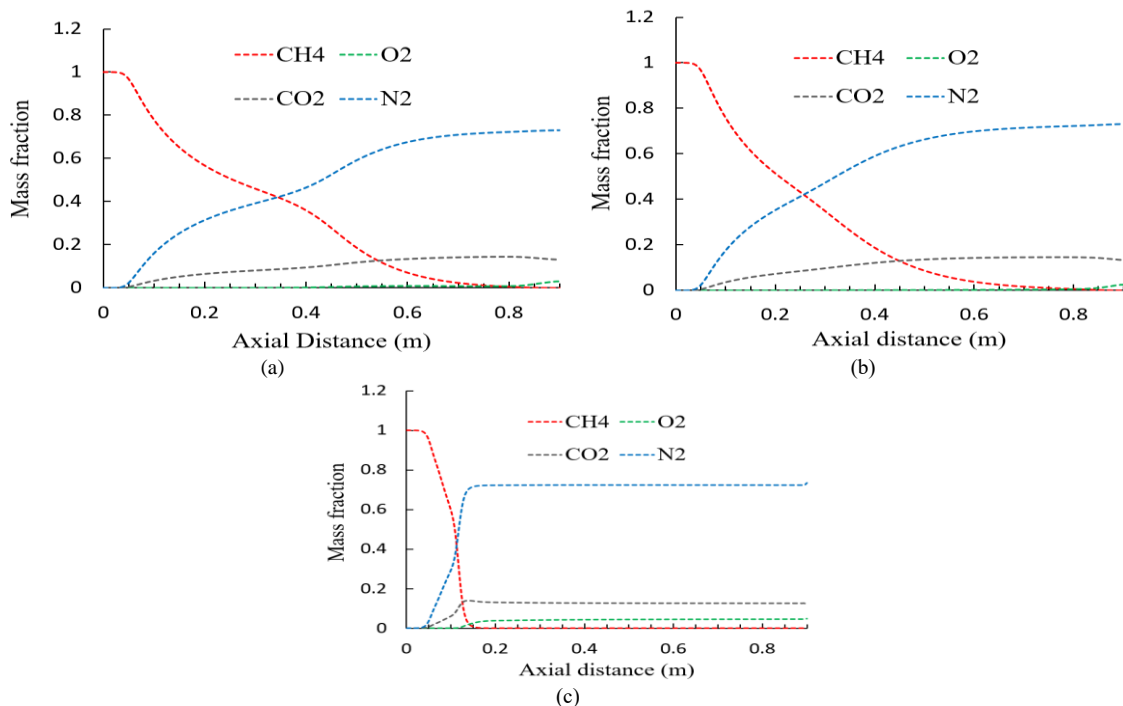


Figure 9. Species mass fraction on axis of symmetry for different swirl numbers. (a) Swirl number = 0.0, (b) Swirl number = 0.3 and (c) Swirl number = 0.6

5. Conclusion

In the present study, numerical simulations have been performed on the Harwell furnace model to assess the effect of swirl intensity on combustion characteristics, such as dynamic flow behavior, temperature distribution contours, heat transfer flux at furnace wall, soot formation, and species mass fraction distribution. The main conclusions are summarized as follows.

- A central toroidal circulation zone forms closer to the inlet of the air-fuel region as the swirl number increases beyond 0.3, and thereby a better air-fuel mixture is prepared. Moreover, the central circulation zone enhances the backflow movement in the flow field and thus the residence time for the fuel inside the combustion zone is increased. This results in an incomplete combustion of fuel and hence the possibility of pollutant formation becomes minimum.
- With increasing swirl intensity, it is found that the fluid flow pattern is widened radially in the combustion chamber and the temperature distribution throughout the furnace is uniformly distributed. Particularly at the outlet, the temperature distribution becomes more uniform and lower. As a result, the possibility of formation thermal NO_x becomes minimum.
- The soot formation is 45.65% higher, at the exit when the swirl number is greater than 0.3 as compared to the no swirl case.
- The radiant heat transfer flux increases as the swirl intensity increases. When the swirl number is more than 0.3, the heat transmission rate nearly doubles. It is consistently distributed along the furnace wall. The heat transfer rate is further enhanced by eight percent with the formation of soot in the fuel-rich region of the flame. As compared to no swirl, the average wall heat flux increases to 62.72% when the swirl number is 5.
- During combustion, the fuel mass fraction is properly utilized and its distribution along the centerline of the furnace becomes uniform with the rise of the swirl intensity.

References

- [1] K. Schofield, *Combustion emissions: Formation, reaction, and removal of trace metals in combustion products*. Elsevier, 2020.
- [2] L. X. Zhou, X. L. Chen, and J. Zhang, "Studies on the effect of swirl on NO formation in methane/air turbulent combustion," *Proc. Combust. Inst.*, vol. 29, no. 2, pp. 2235–2242, 2002, doi: 10.1016/s1540-7489(02)80272-3.
- [3] N. Merlo et al., "Combustion characteristics of methane-oxygen enhanced air turbulent non-premixed swirling flames," *Exp. Therm. Fluid Sci.*, vol. 56, pp. 53–60, 2014, doi: 10.1016/j.expthermflusci.2013.11.019.
- [4] N. Syred and J. M. Beér, "Combustion in swirling flows: A review," *Combust. Flame*, vol. 23, no. 2, pp. 143–201, 1974, doi: 10.1016/0010-2180(74)90057-1.
- [5] C. O. Iyogun, M. Birouk, and J. A. Kozinski, "Experimental investigation of the effect of fuel nozzle geometry on the stability of a swirling non-premixed methane flame," *Fuel*, vol. 90, no. 4, pp. 1416–1423, 2011, doi: 10.1016/j.fuel.2010.12.033.
- [6] M. Saediamiri, M. Birouk, and J. A. Kozinski, "On the stability of a turbulent non-premixed biogas flame: Effect of low swirl strength," *Combust. Flame*, vol. 161, no. 5, pp. 1326–1336, 2014, doi: 10.1016/j.combustflame.2013.11.002.
- [7] D. Sellan and S. Balusamy, "Experimental study of swirl-stabilized turbulent premixed and stratified LPG/air flames using optical diagnostics," *Exp. Therm. Fluid Sci.*, vol. 121, no. August 2020, 2021, doi: 10.1016/j.expthermflusci.2020.110281.
- [8] S. Yoon, S. Lee, H. Kwon, J. Lee, and S. Park, "Effects of the swirl ratio and injector hole number on the combustion and emission characteristics of a light duty diesel engine," *Appl. Therm. Eng.*, vol. 142, no. June, pp. 68–78, 2018, doi: 10.1016/j.applthermaleng.2018.06.076.
- [9] H. Ogawa, Y. Matsui, S. Kimura, and J. Kawashima, "Three-dimensional computation of the effects of the swirl ratio in direct-injection diesel engines on NO_x and soot emissions," *SAE Tech. Pap.*, no. 412, 1996, doi: 10.4271/961125.
- [10] F. Bonatesta et al., "The Influence of Swirl Ratio on Soot Quantity and Distribution in the Cylinder of a Diesel Engine," *Third Eur. Combust. Meet. ECM*, no. November, pp. 1–6, 2007.
- [11] S. T. Chong, M. Hassanaly, H. Koo, M. E. Mueller, V. Raman, and K. P. Geigle, "Large eddy simulation of pressure and dilution-jet effects on soot formation in a model aircraft swirl combustor," *Combust. Flame*, vol. 192, pp. 452–472, 2018, doi: 10.1016/j.combustflame.2018.02.021.
- [12] H. Zhou, X. Li, and F. Liu, "Soot formation and oxidation mechanisms in a diesel engine separated swirl combustion system," *Fuel*, vol. 257, no. August, p. 115955, 2019, doi: 10.1016/j.fuel.2019.115955.
- [13] L. Y. Wang, S. Chatterjee, Q. An, A. M. Steinberg, and Ö. L. Gülder, "Soot formation and flame structure in swirl-stabilized turbulent non-premixed methane combustion," *Combust. Flame*, vol. 209, pp. 303–312, 2019, doi: 10.1016/j.combustflame.2019.07.033.
- [14] E. P. Keramida, H. H. Liakos, M. A. Founti, A. G. Boudouvis, and N. C. Markatos, "Radiative heat transfer in natural gas-fired furnaces," *Int. J. Heat Mass Transf.*, vol. 43, no. 10, pp. 1801–1809, 2000, doi: 10.1016/S0017-9310(99)00244-6.
- [15] S. Wilkes, N.S.; Guilbert, P.W.; Shepherd, C.M.; Simcox, "The application of Harwell-Flow 3D to combustion models," *At. Energy Auth. Report*, Harwell, UK, Pap. No. AERE-R-13508, pp. 1–17, 1989, [Online]. Available: <http://www.opengrey.eu/item/display/10068/630809>.
- [16] P. Ghose, J. Patra, A. Datta, and A. Mukhopadhyay, "Prediction of soot and thermal radiation in a model gas turbine combustor burning kerosene fuel spray at different swirl levels," *Combust. Theory Model.*, vol. 20, no. 3, pp. 457–485, 2016, doi: 10.1080/13647830.2016.1147607.
- [17] P. Ghose, A. Datta, R. Ganguly, A. Mukhopadhyay, and S. Sen, "Modelling of Soot Formation in a Kerosene Spray Flame," in *Modeling and Simulation of Turbulent Combustion*, Springer, Singapore, 2018, pp. 363–394.
- [18] İ. Yılmaz, "Effect of Swirl Number on Combustion Characteristics in a Natural Gas Diffusion Flame," *J. Energy Resour. Technol.*, vol. 135, no. 4, pp. 1–8, 2013, doi: 10.1115/1.4024222.
- [19] X. Yang, Z. He, Q. Niu, S. Dong, and H. Tan, "Numerical analysis of turbulence radiation interaction effect on radiative heat transfer in a swirling oxyfuel furnace," *Int. J. Heat Mass Transf.*, vol. 141, pp. 1227–1237, 2019, doi: 10.1016/j.ijheatmasstransfer.2019.07.060.
- [20] L. K. Moey, M. F. Kong, V. C. Tai, T. F. Go, and N. M. Adam, "Effect of Gable Roof Angle on Natural Ventilation for an Isolated Building," *Jordan J. Mech. Ind. Eng.*, vol. 15, no. 3, pp. 291–300, 2021.
- [21] C. Ghenai, T. Salameh, and I. Janajreh, "Modeling and simulation of shrouded Horizontal Axis Wind Turbine using

- RANS method,” *Jordan J. Mech. Ind. Eng.*, vol. 11, no. Specialissue, pp. 235–243, 2017.
- [22] Ø. Spangelo, “Experimental and Theoretical Studies of a Low NO_x Swirl Burner,” *The Norwegian University of Science and Technology*, 2004.
- [23] A. J. Lew, G. C. Buscaglia, and P. M. Carrica, “A Note on the Numerical Treatment of the k-epsilon Turbulence Model,” *Int. J. Comput. Fluid Dyn.*, vol. 14, no. 3, pp. 201–209, 2001, doi: 10.1080/10618560108940724.
- [24] M. R. Busupally and A. De, “Numerical modeling of Soot formation in a turbulent C₂H₄/air diffusion flame,” *Int. J. Spray Combust. Dyn.*, vol. 8, no. 2, pp. 67–85, 2016, doi: 10.1177/1756827716638814.
- [25] I. M. Kennedy, “Models of soot formation and oxidation,” *Prog. Energy Combust. Sci.*, vol. 23, no. 2, pp. 95–132, Jan. 1997, doi: 10.1016/S0360-1285(97)00007-5.
- [26] S. J. Brookes and J. B. Moss, “Predictions of soot and thermal radiation properties in confined turbulent jet diffusion flames,” *Combust. Flame*, vol. 116, no. 4, pp. 486–503, 1999, doi: 10.1016/S0010-2180(98)00056-X.
- [27] C. P. Fenimore and G. W. Jones, “Soot by Hydroxyl Radicals,” *J. Phys. Chem.*, vol. 71, no. 3, pp. 593–597, 1967.
- [28] ANSYS Fluent User’s Guide Release 15.0. Canonsburg: ANSYS Incorporation, 2013.
- [29] B. F. Magnussen and B. H. Hjertager, “On mathematical modeling of turbulent combustion with special emphasis on soot formation and combustion,” *Symp. Combust.*, vol. 16, no. 1, pp. 719–729, 1977, doi: 10.1016/S0082-0784(77)80366-4.
- [30] R. Siegel and J. R. Howell., *Thermal Radiation Heat Transfer*. Washington DC: Hemisphere Publishing Corporation, 1992.
- [31] A. Habibi, B. Merci, and G. J. Heynderickx, “Multiscale Modeling of Turbulent Combustion and NO_x Emission in Steam Crackers,” *AIChE J.*, vol. 53, no. 9, pp. 2384–2398, 2007, doi: 10.1002/aic.11243.
- [32] M. F. Modest, “The weighted-sum-of-gray-gases model for arbitrary solution methods in radiative transfer,” *J. Heat Transfer*, vol. 113, no. 3, pp. 650–656, 1991, doi: 10.1115/1.2910614.

Optimization of Injection Molding Simulation of Bioabsorbable Bone Screw Using Taguchi Method and Particle Swarm Optimization

Azizah Hadny Qurrota Ayun¹, Joko Triyono², Eko Pujiyanto^{1,*}

¹Department of Industrial Engineering, Faculty of Engineering, Universitas Sebelas Maret, Surakarta, Indonesia.

²Department of Mechanical Engineering, Faculty of Engineering, Universitas Sebelas Maret, Surakarta, Indonesia.

Received 27 OCT 2021

Accepted 5 FEB 2022

Abstract

Application of metal bone screws for internal fixation has many risks, including infection, temperature sensitivity, and radiologic imaging disturbance. Bioabsorbable bone screws appear to overcome the disadvantages of metal bone screws. Many researchers have developed numerous bioabsorbable bone screws using various kinds of polymers. In this research, polylactic acid (PLA) and polyglycolic acid (PGA) were used as the materials for the bone screw. The injection molding method was used to produce the screws as it is one of the most effective methods in polymer or plastic production. This study aims to understand the effect of injection molding simulation parameters on shrinkage and warpage of bone screw, and to discover the best parameters combination to obtain optimal responses, and compare PLA and PGA bone screws. Injection molding simulation experiments used the Taguchi method, and the optimization process used particle swarm optimization. The results showed that melt temperature, injection time, and packing time had significant effects on shrinkage and warpage of PLA bone screws. Meanwhile, the significant factors for PGA bone screws were mold temperature, melt temperature, and injection time. After the optimization process, the shrinkage and warpage value improved to 2.4233% and 0.0928 mm for PLA bone screws and 8.9592% and 0.4646 mm for PGA bone screws.

© 2022 Jordan Journal of Mechanical and Industrial Engineering. All rights reserved

Keywords: Bone screw, injection molding simulation, Taguchi, PSO.

1. Introduction

Several bone fracture fixation methods are used to aid the healing process, including the conventional method, external fixation, and internal fixation. From these methods, the most commonly used one is internal fixation using a metal implant. The advantages of this method include reduction of malunion and nonunion risk of broken bones, shortening of the length of stay in a hospital, and increasing the rate of recovery. One of the various kinds of implant used for internal fixation is bone screw. Bone screw as an independent implant is usually applied on femoral neck fracture, femoral head dislocation, distal femur fracture, tibial plateau fracture, and also on cure ankle, elbow, and shoulder fracture [1]. This screw is usually made of metal, such as stainless steel, titanium, or cobalt, and has to be removed after recovery throughout the surgical process. The risks involved in this process include atrophy, infection, and bone complication due to discharge of metal ions [2]. Furthermore, the application of metal as bone screw material has some disadvantages, such as temperature sensitivity, growth disturbance in children [3] and also disturbing radiologic imaging [4].

Because of the disadvantages of metal bone screws, several researchers have attempted to develop a bioabsorbable bone screw that is degradable inside the human body over time [5]. This kind of bone screw is advantageous because it does not involve any surgical

process for its removal. It also does not disturb radiologic imaging owing to the characteristic of the material used, which can be passed through X-ray [6]. Bioabsorbable bone screw is usually made of a biodegradable polymer such as polylactic acid (PLA), polyglycolic acid (PGA), polylactic-co-glycolic acid, polycaprolactone (PCL), and polydioxanone PDS [7]. Additionally, previous studies proved that the screw has good osseointegration and excellent biocompatibility based on in vivo evaluation [8]. Their study showed that the strength retention of the screws is sufficient for safe fixation [9].

One of the various methods that can be used to produce bioabsorbable bone screws is injection molding. This method is widely applied in polymer and plastic industries because of the highly accurate products with fast cycle time. It is also one of the most important polymer-processing operations in plastic industries [10]. Nevertheless, some parameters, such as melt temperature, pressure limit, packing time, injection pressure, injection speed, injection time, cooling time, and mold temperature, must be considered, which affect the result of injection molding. A bad setting of these parameters will lead to a defective product because of shrinkage and warpage [11]. Thus, this study aimed to investigate the best parameter combination that yields a minimum shrinkage and warpage value. Moreover, the effect of these

* Corresponding author e-mail: ekopujiyanto@staff.uns.ac.id.

parameters was analyzed toward the shrinkage and warpage value and compared between PLA and PGA bone screws.

Several studies have been conducted by some researchers to obtain an optimal parameters combination of injection molding. These studies focused on different parameters of injection molding, and the result varied on the material, dimension, and shape of products. Several parameters, that is, the effect of melt temperature, mold temperature, injection speed, injection time, cycle time, packing time, packing pressure, and coolant temperature, have been investigated [12, 13, 14].

Moreover, different optimization methods were used in optimizing the injection molding process. Kiatcharoenpol [15] and Othman [16] used the Taguchi method to optimize their injection molding results, such as shrinkage, total displacement, and warpage. Conversely, several multiresponse optimization methods were utilized by some researchers to obtain simultaneous optimization results such as gray relational analysis, which was applied by Wang [10], particle swarm optimization by Abuzeid [17] and artificial neural network, which was implemented by Oliaei [18].

Various studies of optimizing shrinkage and warpage of a product have been conducted. Nevertheless, studies on the optimization of the bioabsorbable bone screw injection molding process are still limited. Thus, this study aims to investigate the optimal parameter combination of injection-molded bone screws to obtain minimum shrinkage and warpage. Additionally, this study compared PLA and PGA bone screws in terms of injection molding quality or mechanical strength. This study also aims to understand the effect of the parameters, such as melt temperature, mold temperature, injection time, cooling time, and packing time on the responses such as shrinkage and warpage. A modified ISO 5835:1991 cancellous bone screw with an interlocking thread system has been proposed [19].

2. Material and Method

The experiment preparation was conducted by creating a bone screw design in Autodesk Inventor Software. The design created was a 6.5 mm ISO 5835:1991 cancellous bone screw with thread modification using fastener thread, which can withstand multidirectional force and bending moment so it can limit the movement and radial forces of the bone screw [19]. Cancellous screws have various lengths depending on their purpose. A 75-mm-long cancellous bone screw was chosen for the design, which can be applied for Schatzker type 1 tibial plateau fracture fixation [20]. This study used two different materials for the screw such as PLA and PGA. Table 1 shows the properties of the material used in this simulation. Figure 1 shows the design of the bone screw for tibial plateau fracture fixation.

The responses of this experiment are shrinkage and warpage of injection-molded bone screw. These responses were chosen because they are the common defects that affect the quality of the injection-molded part [21]. This study used five factors, namely, melt temperature, mold temperature, injection time, cooling time, and packing time. Table 2 shows the levels of each factor. This study used the Taguchi method for the experiment, which was conducted on the basis of the orthogonal array [22]. This experiment used five parameters with five levels each. Thus, the orthogonal array $L_{25}(5^5)$ was chosen for the experiment.

Table 1. Properties of material

Properties	PLA	PGA
Young modulus (MPa)	3500	6500
Poisson	0.36	0.453
Shear modulus (MPa)	1287	6000
Density (kg/m ³)	1251.5	1500
Tensile strength (MPa)	60	220
Yield strength (MPa)	60	220

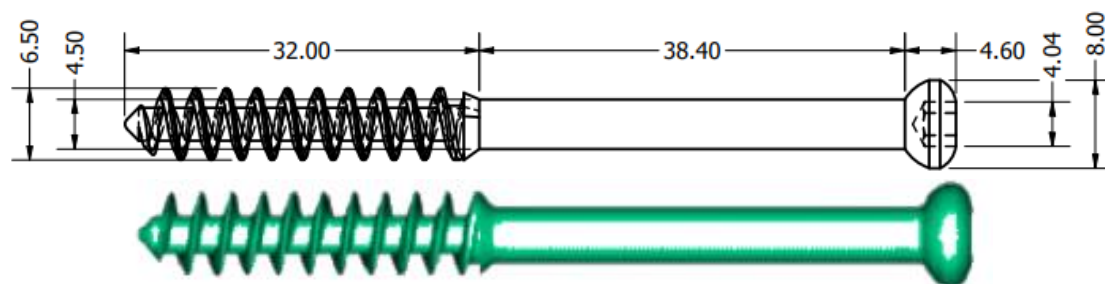


Figure 1. Bone screw design

Table 2. Factors and levels

Code	Factor	Material	Level				
			1	2	3	4	5
A	Mold Temperature (°C)	PLA	10	17	24	31	38
		PGA	60	85	110	135	160
B	Melt Temperature (°C)	PLA	170	185	200	215	230
		PGA	220	232.5	245	257.5	270
C	Injection Time (second)	PLA	1	1.5	2	2.5	3
		PGA	1	1.5	2	2.5	3
D	Cooling Time (second)	PLA	17	19	21	23	25
		PGA	17	19	21	23	25
E	Packing Time (second)	PLA	10	12.5	15	17.5	20
		PGA	10	12.5	15	17.5	20

An experiment was carried out using injection molding simulation software. Various kinds of injection molding simulation software have been widely used in several studies because it can reduce the cost of the experiment, such as in Wang [23], which used Moldex 3D Software for the simulation, and in Martowibowo [24], which utilized Mold Flow software. This study used Autodesk Moldflow Adviser to simulate the injection molding process on the basis of the orthogonal array. Before simulation commenced, the mold cavity of injection molding was designed. Figure 2 shows the cavity mold design. This design was chosen after some trials and errors to avoid any defect due to injection location such as short shots or gate marks. After simulation, shrinkage and warpage value for each level setting was obtained. This value will be analyzed and optimized in the next step.

Shrinkage and warpage data were obtained from the simulation process. These data were analyzed using analysis of variance (ANOVA), which was used to understand the effect of factors on responses and interpretation of experimental data [25, 26]. Afterward, a regression equation was generated to predict the value of shrinkage and warpage after optimization.

This study used the particle swarm optimization (PSO) method to optimize shrinkage and warpage value. PSO is an optimization method that searches the optimal solution using an agent called particle, the track of which is controlled by deterministic and stochastic components. This method was chosen because it can solve continuous problems such as investigating optimal parameters in a machine, and it can optimize some responses simultaneously. When compared with other methods, PSO also has some advantages, such as a faster optimization process, fewer parameters used, and a maintained balance

between global and local searching in its optimization process.

After obtaining the optimum value, the next stage was study validation, which was performed through experimental confirmation and mechanical simulation. Experimental confirmation was conducted to compare the optimum predicted shrinkage and warpage value from the regression equation and the simulated shrinkage and warpage using the optimal setting level. Mechanical simulation was used to understand the strength of bone screws when applied to fix the bone fracture.

Results and Discussion

Shrinkage and warpage value can be measured by choosing “Fill+Pack+Warp” analysis in Autodesk Moldflow Adviser. Table 3 shows the result of the experiment. Furthermore, the results of the experiment were analyzed using ANOVA with Minitab 17. The effect of a factor on responses can be determined based on its P-value. Table 4 presents the P-value result of each factor.

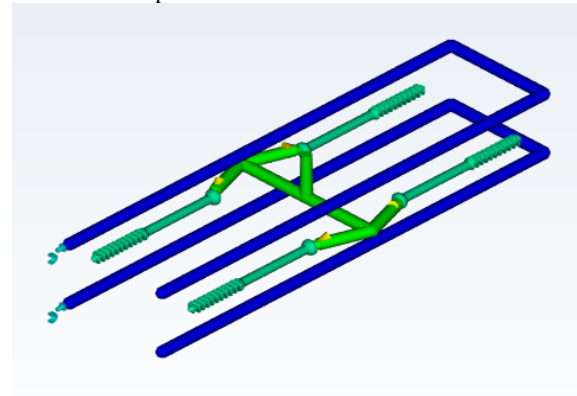


Figure 2. Cavity mold design

Table 3. Experiment results

Exp. No.	PLA		PGA	
	Shrinkage (%)	Warpage (mm)	Shrinkage (%)	Warpage (mm)
1	4.924	0.1114	9.642	0.4612
2	4.685	0.1182	10.2	0.4794
3	6.96	0.1461	10.88	0.4933
4	7.964	0.1632	12.26	0.5041
5	8.639	0.175	13.6	0.5128
6	3.077	0.1066	10.83	0.468
7	5.122	0.1201	10.89	0.4838
8	7.097	0.1484	11.39	0.4966
9	8.086	0.1652	13.12	0.5071
10	7.177	0.1503	11.76	0.5043
11	4.459	0.1118	11.62	0.4726
12	4.819	0.1211	11.59	0.4877
13	7.088	0.1485	11.72	0.5001
14	6.361	0.139	11.32	0.4978
15	9.632	0.1644	13.83	0.5099
16	2.707	0.1052	12.14	0.4779
17	6.407	0.1379	12.23	0.4926
18	6.161	0.1305	12.24	0.4897
19	7.196	0.1505	12.32	0.504
20	8.055	0.1675	13.76	0.5141
21	4.143	0.1115	12.87	0.4852
22	4.451	0.1135	10.65	0.4822
23	5.292	0.128	11.97	0.4972
24	8.218	0.1601	14.19	0.509
25	8.388	0.1735	15.41	0.5174

The results of the experiment were modeled using regression and were used to predict the shrinkage and warpage value after optimization. Furthermore, Minitab 17 was used to build the regression model. Table 5 shows the regression model.

All of the regression equations generated great R-square values, which means that the model explained the response variability well. Additionally, the differences between adjusted R-square and predicted R-square are less than 20%, indicating a strong correlation between the prediction model and simulation result [27]. The next step was optimization using PSO. This study used an equal weight of 0.5 for the scalarization of each response. Equal weightage was used because this study did not prioritize any responses and assumed that the importance of both responses is equal. Before combining two responses as one,

the data must be normalized first to give a sense of fairness for each response. This normalization was conducted by rescaling the data value to between 0 and 1.

The regression model of combined objectives was built using regression in Minitab 17, after obtaining the data. This regression equation was used for optimization, using PSO. Table 6 showed the regression equation of combined objectives PLA and PGA bone screw. Afterward, PSO optimization was conducted using xOptimizer. Several parameters needed adjustment before the optimization process. Table 7 shows the parameters used in this optimization. Figures 3 and 4 show the best fitness graph of the optimization process. Table 8 shows the optimal level combination obtained after the optimization process using PSO and its predicted response values.

Table 4. P-value result of ANOVA

		P-value				
		Mold Temp. (A)	Melt Temp. (B)	Injection Time (C)	Cooling Time (D)	Packing Time (E)
PLA	Shrinkage	0.2700	0.0000	0.0330	0.3320	0.0030
	Warpage	0.1700	0.0000	0.0001	0.3880	0.0109
PGA	Shrinkage	0.0020	0.0000	0.0040	0.6300	0.3540
	Warpage	0.0000	0.0000	0.0000	0.6740	0.4190

Table 5. Regression equation

Response		Regression equation	R-sq (adj)	R-sq (pred)
PLA	Shrinkage (%)	-8.46 - 0.0154 A + 0.07667 B + 0.467 C + 0.0448 D - 0.1397 E	92.40%	89.28%
	Warpage (mm)	-0.0631 - 0.000153 A + 0.000981 B + 0.00922 C + 0.000194 D - 0.000878 E	96.35%	94.87%
PGA	Shrinkage (%)	83.3 + 0.01737 A - 0.658 B + 0.780 C + 0.0108 D - 0.0488 E + 0.001440 B*B	88.53%	83.49%
	Warpage (mm)	0.28253 + 0.000079 A + 0.000774 B + 0.006016 C + 0.000038 D + 0.000022 E	98.35%	97.37%

Table 6. Regression equation of combined objectives

Material	Regression equation	R-sq (adj)	R-sq (pred)
PLA	-2.012 - 0.00221A + 0.012562B + 0.0998C + 0.00462D - 0.01637E	95.59%	93.68%
PGA	-2.659 + 0.002210A + 0.011066B + 0.1211C + 0.00127D - 0.00403E	96.08%	94.62%

Table 7. Parameters in PSO

Parameter	Value
Number of Particle	20
Inertia Weight (ω_0)	0.8
C_1	2
C_2	2
$X_{lowerlimit}$ PLA	[10 170 1 17 10]
$X_{upperlimit}$ PLA	[38 230 3 25 20]
$X_{lowerlimit}$ PGA	[60 220 1 17 10]
$X_{upperlimit}$ PGA	[160 270 3 25 20]

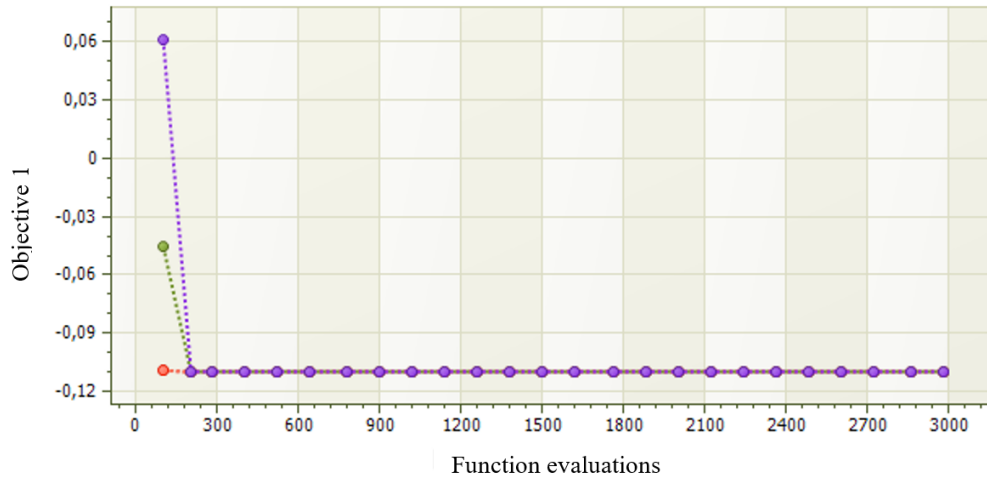


Figure 3. Best fitness graph of PLA bone screw optimization

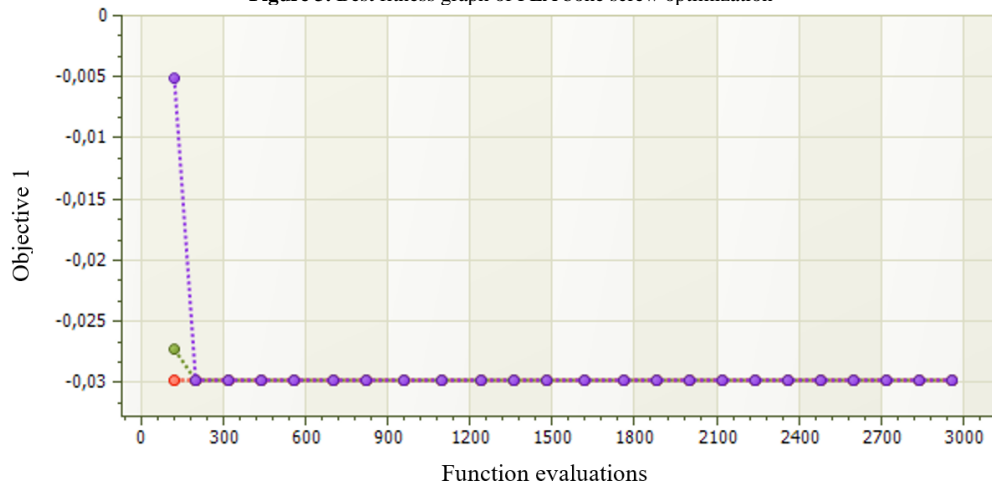


Figure 4. Best fitness graph of PGA bone screw optimization

Table 8. Optimal parameter and predicted responses

Material	A	B	C	D	E	CO	Predicted shrinkage (%)	Predicted warpage (mm)
PLA	38	170	1	17	20	-1.095	2.4233	0.0928
PGA	60	220	1	17	20	-0.0297	8.9592	0.4646

Based on the result, the optimal parameter setting for PLA bone screw includes 38°C mold temperature, 170°C melt temperature, 1 s injection time, 17 s cooling time, and 20 s packing time. For PGA bone screw, the optimal parameter setting includes 60°C mold temperature, 220°C melt temperature, 1 s injection time, 17 s cooling time, and 20 s packing time. Furthermore, PLA bone screw is preferable to PGA bone screw in terms of injection molding quality because the former had a smaller value of optimized shrinkage and warpage. The next step was study validation using experiment confirmation and mechanical simulation. Experiment confirmation was conducted by simulating the optimal parameters setting that have been previously obtained. Table 9 shows the result of experiment confirmation and its comparison to predicted values.

Based on the results shown above, the error rate of the predicted value can be measured by comparing its value with the simulated value. For PLA bone screw, the error rate of shrinkage and warpage are 6% and 10%,

respectively. Conversely, the error rate for PGA bone screw shrinkage and warpage is 7% and 1%, respectively.

Mechanical simulation was performed using Autodesk Inventor to analyze von Mises stress. The von Mises stress is equivalent to the combination of three principal stresses [28]. This value was compared with the tensile strength to judge the failure of the material. Schatzker type 1 tibial plateau fracture that had been fixated using PLA and PGA bone screw was given 2560 N load on the bone. This value was determined on the basis of a total contact force of 80 kg individual’s knee, in walking position [29]. Figures 5 and 6 show the von Mises stress analysis results of PLA and PGA bone screws.

Table 9. Experiment confirmation results and predicted value

Material	Predicted Shrinkage (%)	Predicted Warpage (mm)	Simulated Shrinkage (%)	Simulated Warpage (mm)
PLA	2.4233	0.0928	2.278	0.0842
PGA	8.9592	0.4646	9.642	0.4612

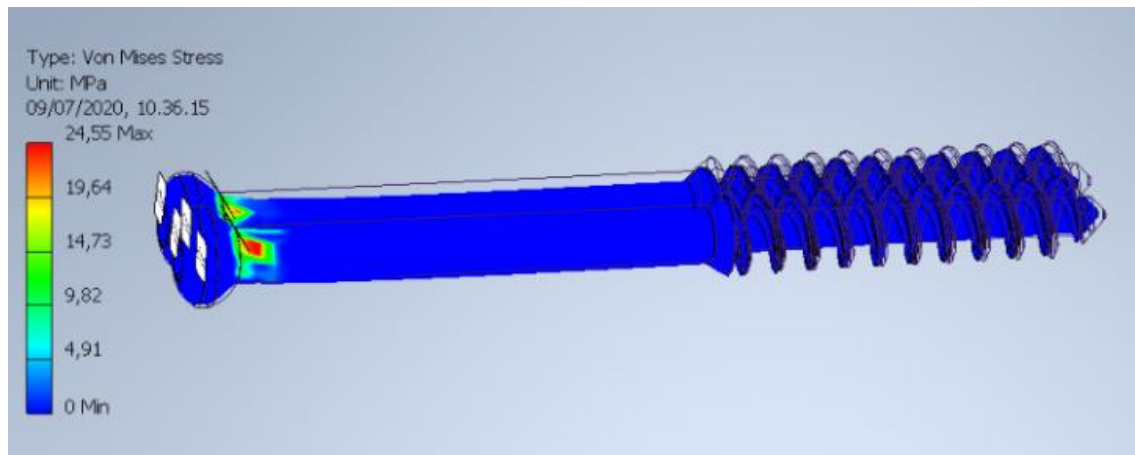


Figure 5. Von mises stress of PLA bone screw

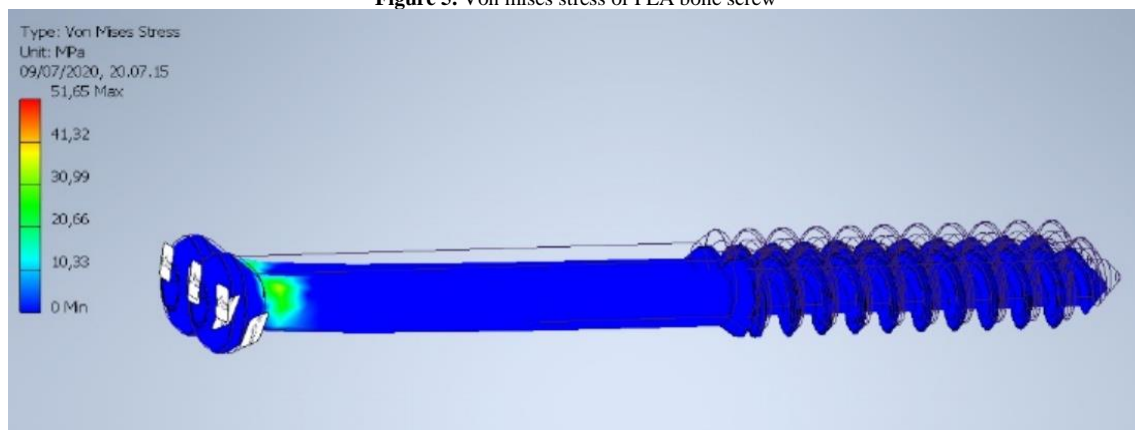


Figure 6. Von mises stress of PGA bone screw

The results show that the maximum von Mises stress of PLA and PGA bone screws was 24.55 and 51.65 MPa, respectively. These values are less than their tensile strength, which indicates that the screws can resist the load. PGA bone screw has greater von Mises stress because it has greater tensile strength too. Thus, it can be concluded that PGA bone screw had better mechanical strength than PLA bone screw.

Conclusion

This study optimized the simulation of the PLA and PGA bone screw injection molding process to minimize its shrinkage and warpage and further compared the quality of both screws. It also investigated the effect of melt temperature, mold temperature, injection time, cooling time, and packing time on shrinkage and warpage. Hence, two sets of experiments based on Taguchi orthogonal array using PLA and PGA were conducted, and the results were analyzed using ANOVA. The result of ANOVA showed that melt temperature, injection time, and packing time affected the shrinkage and warpage of PLA bone screw, whereas the parameters that have a significant effect on PGA bone screw are mold temperature, melt temperature, and injection time. The shrinkage and warpage of both screws were optimized using PSO. After the optimization process, the shrinkage and warpage value improved to 2.4233% and 0.0928 mm for PLA bone screw and 8.9592% and 0.4646 mm for PGA bone screw. Experiment confirmation shows that there were some errors between predicted and simulated values. The mechanical simulation

conducted proved that both screws resisted the applied load when implemented to fix Schatzker type 1 tibial plateau fracture. Nevertheless, both screws had their own superiority toward each other. PGA bone screw had better mechanical strength than PLA bone screw based on the mechanical simulation, whereas PLA bone screw had preferable injection molding quality when compared with PGA bone screw because of its better value of shrinkage and warpage.

Acknowledgement

This work was supported by PU-UNS PNBPN under Grant 452/UN27.21/PN/2020.

References

- [1] Gefen, "Computational simulations of stress shielding and bone resorption around existing and computer-designed orthopaedic screws". *Med. Biol. Eng. Comput.*, vol. 40, no. 3, 311–322, 2002.
- [2] N. Ashammakhi, A. M. Gonzalez, P. Törmälä and I. T. Jackson, "New resorbable bone fixation. Biomaterials in craniomaxillofacial surgery: present and future". *Eur. J. Plast. Surg.*, vol. 26, no. 8, 383–390, 2004.
- [3] M. S. Ibrahim, P. G. L. Koolen, K. Kim, G. S. Perrone, D. L. Kaplan, and S. J. Lin, "Absorbable biologically based internal fixation". *Clin. Podiatr. Med. Surg.*, vol. 32, no. 1, 61–72, 2015.
- [4] G. J. Buijs, B. Stegenga, and R. R. M. Bos, "Efficacy and safety of biodegradable osteofixation devices in oral and

- maxillofacial surgery: a systematic review". *J. Dent. Res.*, vol. 85, no. 11, 980–989, 2006.
- [5] L. Eppley, "Resorbable PLA-PGA plate and screw fixation in paediatric craniofacial surgery: Clinical experience in 1883 patients". *Plastic and Reconstructive Surgery*, vol. 114, no. 4, 850–856, 2004.
- [6] P. B. Maurus and C. C. Kaeding, "Bioabsorbable implant material review". *Oper. Tech. Sports Med.*, vol. 12, no. 3, 158–160, 2004.
- [7] Pertici, G. Bioresorbable polymers for biomedical applications. Woodhead Publishing, 2017.
- [8] M. Cai, H. Liu, Y. Jiang, J. Wang, and S. Zhang, "A high-strength biodegradable thermoset polymer for internal fixation bone screws: Preparation, in vitro and in vivo evaluation". *Colloids Surf. B Biointerfaces*, vol. 183, no. 110445, 1-10, 2019.
- [9] J. Vasenius, P. Helevirta, H. Kuisma, P. Rokkanen, and P. Törmälä, "Absorbable self-reinforced polyglycolide (SR-PGA) screws for the fixation of fractures and osteotomies: strength and strength retention in vitro and in vivo". *Clin. Mater.*, vol. 17, no. 3, 119–123, 1994.
- [10] M. W. Wang, F. Arifin, and V. H. Vu, "The study of optimal molding of a LED lens with grey relational analysis and molding simulation". *Period. Polytech. Mech. Eng.*, vol. 63, no. 4, 278 – 294, 2019.
- [11] E. Hakimian and A. B. Sulong, "Analysis of warpage and shrinkage properties of injection-molded micro gears polymer composites using numerical simulations assisted by the Taguchi method". *Mater. Eng.*, vol. 42, 62–71, 2012.
- [12] C.-P. Chen, M.-T. Chuang, Y.-H. Hsiao, Y.-K. Yang, and C.-H. Tsai, "Simulation and experimental study in determining injection molding process parameters for thin-shell plastic parts via design of experiments analysis". *Expert Syst. Appl.*, vol. 36, no. 7, 10752–10759, 2009.
- [13] N. Sateesh, S. Devakar Reddy, G. Praveen Kumar, and R. Subbiah, "Optimization of injection moulding process in manufacturing the top cap of water meter". *Mater. Today*, vol. 18, 4556–4565, 2019.
- [14] S. Heidari et al., "Optimization simulated injection molding process for ultrahigh molecular weight polyethylene nanocomposite hip liner using response surface methodology and simulation of mechanical behavior". *J. Mech. Behav. Biomed. Mater.*, vol. 65, 160 – 176, 2018.
- [15] T. Kiatcharoenpol and T. Vichiraprasert, "Optimizing and Modeling for Plastic Injection Molding Process using Taguchi Method". *Journal of Physics: Conference Series*, vol. 1026, 2018.
- [16] M. H. Othman et al., "Optimisation of Injection Moulding Parameter towards Shrinkage and Warpage for Polypropylene-Nanoclay-Gigantochloa Scortechinii Nanocomposites". *Procedia Engineering*, vol. 184, 673-680, 2017.
- [17] O. Abuzeid, A. Daoud, and M. Barghash, "Optimal off-grid hybrid renewable energy system for residential applications using particle swarm optimization," *Jordan Journal of Mechanical and Industrial Engineering*, vol. 13, 117–124, 2019.
- [18] Oliaei et al., "Warpage and Shrinkage Optimization of Injection-Molded Plastic Spoon Parts for Biodegradable Polymers Using Taguchi, ANOVA and Artificial Neural Network Methods". *J. Mater. Sci. Technol.*, vol. 32, 710 – 720, 2016.
- [19] P. F. Stahel, "Introducing the bone-screw-fastener for improved screw fixation in orthopaedic surgery: A revolutionary paradigm shift". *Patient Safety in Surgery*, vol. 11, no. 6, 2017.
- [20] Salduz, et al, "The effect of screw thread length on initial stability of Schatzker type I tibial plateau fracture fixation: A biomechanical study". *J. Orthop. Surg. Res.*, vol. 11, 2016.
- [21] S. J. Liao, "Optimal process conditions of shrinkage and warpage of thin-wall part". *Polymer Engineering Science*, vol. 44, 917–928, 2004.
- [22] V. R. Rao, N. Ramanaiah, and M. M. M. Sarcar, "Optimization of volumetric wear rate of Aa7075-Tic metal matrix composite by using taguchi technique," *Jordan Journal of Mechanical and Industrial Engineering*, vol. 10, 189–198, 2016.
- [23] M. W. Wang et al., "Study on micromoulding of a high viewing angle LED lens". *Plast. Rubber Compos.*, 2020.
- [24] S. Y. Martowibowo and A. Kaswadi, "Optimization and Simulation of Plastic Injection Process using Genetic Algorithm and Moldflow". *Chinese J. Mech. Eng. (English Ed.)*, vol. 30, 398 – 406, 2017.
- [25] M. Gopalsamy, "Taguchi method and anova: An approach for process parameters optimization of hard machining while machining hardened steel". *Journal of Scientific and Industrial Research*, vol. 68, 686–695, 2009.
- [26] G. V. S. S. Sharma, P. S. Rao, and B. S. Babu, "Establishing Process Capability Indices in a Sugar Manufacturing Industry - an Industrial Engineering Perspective," *Jordan Journal of Mechanical and Industrial Engineering*, vol. 15, 319–328, 2021.
- [27] M. Mourabet, "Removal of fluoride from aqueous solution by adsorption on hydroxyapatite (HAp) using response surface methodology". *Journal of Saudi Chemical Society*, vol. 19, no. 6, 603–615, 2015.
- [28] Bai, Q. and Bai, Y. *Subsea Pipeline Design, Analysis, and Installation*. Oxford, England: Gulf Professional Publishing, 2014.
- [29] T. W. Lu, "Influence of muscle activity on the forces in the femur: An in vivo study". *Journal of Biomechanics*, vol. 30, 1101–1106, 1997.



الجامعة الهاشمية



المملكة الأردنية الهاشمية

المجلة الأردنية
للمهندسة الميكانيكية والصناعية

JJIMIE

مجلة علمية عالمية محكمة
تصدر بدعم من صندوق البحث العلمي

<http://jjmie.hu.edu.jo/>

ISSN 1995-6665

المجلة الأردنية للهندسة الميكانيكية والصناعية

المجلة الأردنية للهندسة الميكانيكية والصناعية: مجلة علمية عالمية محكمة تصدر عن الجامعة الهاشمية بالتعاون مع صندوق دعم البحث العلمي والابتكار- وزارة التعليم العالي والبحث العلمي في الأردن.

هيئة التحرير

رئيس التحرير

الأستاذ الدكتور علي جوارنه

مساعد رئيس التحرير

الدكتور احمد المقدادي

الدكتور مهند جريسات

الأعضاء

الأستاذ الدكتور طارق العزب

جامعة البلقاء التطبيقية

الأستاذ الدكتور محمد الوديان

جامعة العلوم والتكنولوجيا الاردنية

الأستاذ الدكتور جمال جابر

جامعة البلقاء التطبيقية

الأستاذ الدكتور محمد تيسير هياجنه

جامعة العلوم والتكنولوجيا الاردنية

الأستاذ الدكتور محمد الطاهات

الجامعة الاردنية

فريق الدعم

المحرر اللغوي

الدكتور بكر محمد بني خير

تنفيذ وإخراج

م . علي أبو سليمة

ترسل البحوث إلى العنوان التالي

رئيس تحرير المجلة الأردنية للهندسة الميكانيكية والصناعية

الجامعة الهاشمية

كلية الهندسة

قسم الهندسة الميكانيكية

الزرقاء - الأردن

هاتف : 00962 5 3903333 فرعي 4147

Email: jjmie@hu.edu.jo

Website: www.jjmie.hu.edu.jo